AWARD NUMBER: W81XWH-14-1-0191

TITLE: New Diagnostic and Therapeutic Approaches to Eradicating Recurrent

Breast Cancer PRINCIPAL INVESTIGATOR: Sandra McAllister, Ph.D.

CONTRACTING ORGANIZATION: The Brigham and Women's Hospital, Inc.

Boston, MA 02115

REPORT DATE: SEPTEMBER 2018

TYPE OF REPORT: Annual Technical Report

PREPARED FOR: U.S. Army Medical Research and Materiel Command

Fort Detrick, Maryland 21702-5012

DISTRIBUTION STATEMENT: Approved for Public Release;
Distribution Unlimited

REPORT DOCUMENTATION PAGE

Form Approved
OMB No. 0704-0188

1. REPORT DATE	2. REPORT TYPE	3. DATES COVERED
SEPTEMBER 2018	Annual	1SEP2017 - 31AUG2018

4. TITLE AND SUBTITLE

New Diagnostic and Therapeutic Approaches to Eradicating Recurrent Breast Cancer

5a. CONTRACT NUMBER
W81XWH-14-1-0191

5b. GRANT NUMBER

5c. PROGRAM ELEMENT NUMBER

6. AUTHOR(S)

Sandra McAllister, Ph.D.

E-Mail: smcallister1@bwh.harvard.edu

5d. PROJECT NUMBER

5e. TASK NUMBER

5f. WORK UNIT NUMBER

7. PERFORMING ORGANIZATION NAME(S) AND ADDRESS(ES)

The Brigham and Women's
Hospital, Inc.
75 Francis Street
Boston, MA 02115-6110

8. PERFORMING ORGANIZATION REPORT NUMBER

9. SPONSORING / MONITORING AGENCY NAME(S) AND ADDRESS(ES)

U.S. Army Medical Research and Materiel Command
Fort Detrick, Maryland 21702-5012

10. SPONSOR/MONITOR'S ACRONYM(S)

11. SPONSOR/MONITOR'S REPORT NUMBER(S)

12. DISTRIBUTION / AVAILABILITY STATEMENT

Approved for Public Release; Distribution Unlimited

13. SUPPLEMENTARY NOTES

14. ABSTRACT

Some breast cancer patients have no evidence of metastatic disease when they are first diagnosed, yet many patients later return to the clinic with cancer that has spread throughout the body. It is thought less than 1% of the cells that disseminate are able to form overt tumors. The reasons why certain disseminated tumor cells remain inconsequential and others form life-threatening tumors after long periods of time are unknown. During the past year, support from the Era of Hope Scholar Award enabled us to continue progress on 3 fronts. First, we continued our work using sensitive new technologies to tag individual tumor cells, each with it's own unique label, and trace the individual cells in our breast cancer metastasis models. Our detection methods are enabling us for the first time to isolate and study the consequential cells (those that formed metastases). Second, we have uncovered novel mechanisms by which disseminated tumor-initiating cells are affected by bone marrow derived immune cells to either remain dormant or form aggressively growing tumors. In this area, we discovered that bone-modulating drugs, bisphosphonates, render bone marrow cells tumor suppressive. Third, we continued testing and published our findings that bisphosphonates inhibit bone metastases via previously unknown mechanisms. By distinguishing consequential from inconsequential breast cancer cells, and finding new ways to target the most malignant cells, we hope to provide a foundation for future work to determine whether the disseminated tumor cells isolated from breast cancer patients have similar features. Success in these endeavors would mean that breast cancer patients harboring potentially life-threatening disseminated tumor cells could be identified and treated *before* they experience disease relapse.

15. SUBJECT TERMS NONE LISTED

16. SECURITY CLASSIFICATION OF:			17. LIMITATION OF ABSTRACT	18. NUMBER OF PAGES	19a. NAME OF RESPONSIBLE PERSON
a. REPORT	b. ABSTRACT	c. THIS PAGE			USAMRMC
Unclassified	Unclassified	Unclassified	Unclassified	101	19b. TELEPHONE NUMBER *(include area code)*

Table of Contents

Page

ABSTRACT
Some breast cancer patients have no evidence of metastatic disease when they are first diagnosed, yet many patients later return to the clinic with cancer that has spread throughout the body. It is thought less than 1% of the cells that disseminate are able to form overt tumors. The reasons why certain disseminated tumor cells remain inconsequential and others form life-threatening tumors after long periods of time are unknown. During the past year, support from the Era of Hope Scholar Award enabled us to continue progress on 3 fronts. First, we continued our work using sensitive new technologies to tag individual tumor cells, each with it's own unique label, and trace the individual cells in our breast cancer metastasis models. Our detection methods are enabling us for the first time to isolate and study the consequential cells (those that formed metastases). Second, we have uncovered novel mechanisms by which disseminated tumor-initiating cells are affected by bone marrow derived immune cells to either remain dormant or form aggressively growing tumors. In this area, we discovered that bone-modulating drugs, bisphosphonates, render bone marrow cells tumor suppressive. Third, we continued testing and published our findings that bisphosphonates inhibit bone metastases via previously unknown mechanisms. By distinguishing consequential from inconsequential breast cancer cells, and finding new ways to target the most malignant cells, we hope to provide a foundation for future work to determine whether the disseminated tumor cells isolated from breast cancer patients have similar features. Success in these endeavors would mean that breast cancer patients harboring potentially life-threatening disseminated tumor cells could be identified and treated *before* they experience disease relapse.

1. **INTRODUCTION:** Narrative that briefly (one paragraph) describes the subject, purpose and scope of the research.

Our ultimate goal in conducting this Era of Hope Scholar Award study is to develop new non-invasive tests that will allow oncologists to more accurately identify breast cancer patients who are likely to suffer from disease relapse and to identify new treatment therapies that can be given to those patients *before* disease recurs. **We hypothesize that certain disseminated tumors are endowed with properties that enable them to respond to specific systemic and microenvironmental cues to become malignant metastases and that neutralizing these tumor-promoting processes will provide a therapeutic strategy to save lives**. To rigorously test this hypothesis, we proposed the following:
Aim 1: Define a set of DTC biomarkers that predict risk of breast cancer recurrence
Aim 2: Develop a low-cost, non-invasive test for breast cancer recurrence risk stratification
Aim 3: Identify existing drugs that prevent malignant conversion of DTCs
Our studies are being performed using breast cancer cells, mouse models of breast cancer, and breast cancer patient blood samples and tumor tissues in order to test these new strategies before trying them in patients. We are using a new, highly innovative and sensitive technology that enables us to study rare events related to metastatic outgrowth in vivo, which was previously impossible to do. Our studies are designed to provide us with the first precise identity of life-threatening human cancer cells before they convert to a malignant state. We are also using a unique co-culture assay, developed in our laboratory, to identify mechanisms by which indolent cells convert to malignancy and to identify existing drugs that can prevent their conversion. For this project, we have brought together a team of clinical oncologists, breast pathologists, patient/research advocates, computational biologists, and veterinary oncologists in order to leverage opportunities for immediate clinical translation of our research findings.

2. **KEYWORDS:** Provide a brief list of keywords (limit to 20 words).

Breast cancer, metastasis, dissemination, tumor-initiating cells, recurrence, therapeutic resistance, systemic instigation, microenvironment, bone marrow cells, canine, mouse models

3. **ACCOMPLISHMENTS:** The PI is reminded that the recipient organization is required to obtain prior written approval from the USAMRAA Grants Officer whenever there are significant changes in the project or its direction.

A. What were the major goals of the project?

The original goals of the project as outlined in the statement of work, which was amended and approved in FY3 reporting, are as follows:

<u>Task 1: Define tumor cell hallmarks that predict risk of breast cancer recurrence</u>

a. Identify human breast cancer barcoded DTCs that convert to malignancy in xenograft mouse model of metastasis to bone
b. Identify mouse Her2+ barcoded DTCs that convert to malignancy in model of metastasis to bone
c. Test select human and mouse barcoded DTCs individually *in vivo*
d. Define molecular profile of mouse and human barcoded DTCs via L1000 technology
e. Characterize mouse and human barcoded DTCs *in vitro*
f. Analyze data and build prediction signatures (not yet initiated)
g. Establish predictive power of molecular/cellular signatures using other cell lines and human tumor specimens (not yet initiated)
h. Meet with project team to discuss findings and potential for clinical translation

Task 2: Develop a low-cost, non-invasive test for breast cancer recurrence risk stratification

a. Determine ability of various human and mouse BMDC populations to induce malignant conversion of a test set of DTCs *in vitro*
b. Validate findings from "a" *in vivo*
c. Validate findings using expression databases from large cohort of breast cancer patients
d. Determine response of various barcoded DTCs from human and mouse and human DTC samples to pro-and anti-tumorigenic factors *in vivo* (not yet intiated)
e. Meet with project team to discuss findings and potential for clinical translation

Task 3: Identify existing drugs that prevent malignant conversion of otherwise indolent tumors

a. Determine ability of various drugs/compounds to prevent malignant conversion of human and mouse DTCs *in vitro*
b. Validate select drugs from "a" *in vivo*
c. Perform proteomic analyses and ELISAs on candidate tumor-promoting factors
d. Determine BMDCs and other factors that confer resistance to anti-cancer drugs *in vitro*
e. Validate select findings from "d" *in vivo*
f. Perform proteomic analyses and ELISAs on candidate tumor-resistance factors
g. Meet with project team to discuss findings and potential for clinical translation

B. What was accomplished under these goals?

Task 1: Define tumor cell hallmarks that predict risk of breast cancer recurrence

As a basis for our goal to elucidate tumor-intrinsic molecular and functional properties that increase the risk of breast cancer recurrence, we conducted studies that resulted in both biological and technical insights. Biologically, we were interested in the effects on metastasis of the secreted cytokine, osteopontin (OPN), a protein that we have studied previously and that is relevant for breast cancer metastasis (McAllister, et al., Cell, 2008). We hypothesized that OPN affects response/resistance to chemotherapy. From the technical aspect, we had proposed performing gain- and loss-of-function studies using gene editing techniques to address the problem of recurrence. Typical gene editing protocols require a subcloning step to isolate successfully edited cells, the behavior of which is then compared to the original parental population and/or other non-edited subclones. We hypothesized that the inherent functional heterogeneity present in all breast cancer cell lines could render these populations inappropriate controls, resulting in erroneous interpretations of experimental findings.

We addressed these questions in models of pulmonary metastasis using two murine mammary carcinoma cell lines that are critical to the overall studies originally proposed in our Era of Hope grant: McNeuA, a HER2+ breast cancer cell line derived from a spontaneously arising mammary carcinoma in a MMTV-neu transgenic mouse, and Met-1, an estrogen receptor-negative (ER-) breast cancer cell line derived from a mammary carcinoma in a MMTV-PyMT transgenic mouse (FVB/N-Tg(MMTV-PyVmT). (Please note: the following narrative contains excerpts from our work published as Olive, et al., PLoSOne, 2018; Appendix 1).

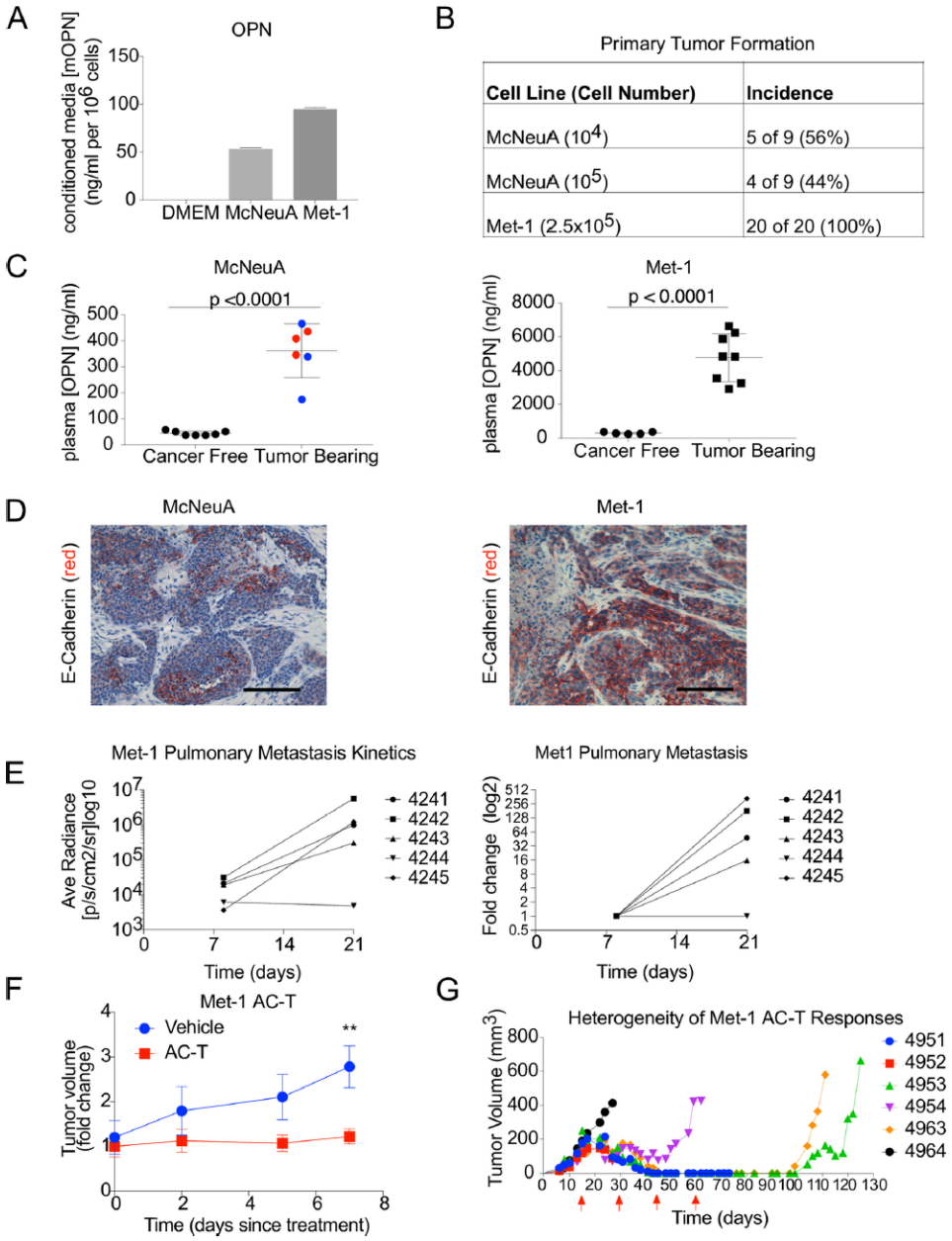

Fig 1. Phenotypic and functional heterogeneity of McNeuA and Met-1 breast cancer cells. (A) Concentration of murine OPN (mOPN; ng/ml per 106 cells) in 24-hr conditioned medium of McNeuA and Met-1 murine mammary carcinoma cells represented as mean +/- SD. There was no detectable mOPN in the control cell-free medium (DMEM) (2 technical replicates per group). (B) Incidence of tumor formation following injection of indicated numbers of McNeuA or Met-1 cells into cohorts of FVB mice. (C) Plasma mOPN concentration (ng/ml) in indicated cohorts of mice at experimental end points of 84 days (McNeuA) and 30 days (Met-1). For McNeuA tumor-bearing mice, blue data points represent 10,000 cells injected, red data points represent 100,000 cells injected; n = 6-7 for McNeuA cohorts; n = 5-8 for Met-1 cohorts. Error bars represent SD; statistical significance evaluated using unpaired, two-tailed Student's t-test. (D) Representative images of immunohistochemical staining for murine E-cadherin (red) on recovered McNeuA and Met-1 tumors. Cell nuclei were counterstained with hematoxylin (blue). Scale bars = 100 μm. (B-D) representative of 3 independent experiments per cell line. (E) Average radiance (log10) per mouse (n = 5) as measured by bioluminescence imaging over 21-day time course following intravenous injection of 106 Met-1 tumor cells into FVB mice (left graph). Fold-change (log2) in pulmonary metastatic burden per mouse (right graph). Representative of 2 independent experiments. (F) Response of orthotopic Met-1 GFP/Luc tumors to single dose combination doxorubicin (5 mg/kg), paclitaxel (10 mg/kg) and cyclophosphamide (120 mg/kg) (AC-T), n = 5±8 tumors/group. Ordinate represents time (days) following treatment. Error bars represent SEM; two-way ANOVA Sidak's multiple comparisons test; $p<0.01$. Representative of 3 independent experiments. (G) Growth kinetics of individual orthotopic Met-1 Luc/GFP tumors in mice injected with 2.5 x 105 tumor cells at the experiment initiation, subsequently receiving 4 biweekly AC-T doses (red arrows). Numbers and colors represent individual mice. From Olive, et al., ***PLoS One*** 2018 Jun 13; 13(6):e0198790. PMID: 29897959

Both McNeuA and Met-1 cell lines secreted detectable levels of OPN in culture (**Fig 1A**) and efficiently formed primary tumors following injection into FVB mice (**Fig. 1B**). Plasma levels of OPN relative to cancer-free cohorts were significantly elevated in both models, whereby average OPN levels were 8-fold and 15-fold higher in the McNeuA and Met1 tumor-bearing mice, respectively, at end stage (**Fig 1C**). The recovered tumors were heterogeneous for the epithelial marker E-cadherin (**Fig 1D**). We were particularly interested in the Met-1 cell line, as women with metastatic ER- breast cancer most often experience pulmonary metastases. The Met-1 cells formed pulmonary metastases, with increasing metastatic burden occurring over the experimental time course (**Fig. 1E**).

We next tested responsiveness of Met-1 mammary carcinoma to combination doxorubicin (A), cyclophosphamide (C), and paclitaxel (T) chemotherapy (AC-T), a standard of care chemotherapy regimen for breast cancer patients with ER-negative disease. In vitro, treatment with both doxorubicin and paclitaxel significantly decreased viability of Met-1 cells (**See Figs. S1E and S1F from Olive, et al., PlosOne 2018**). Cyclophosphamide, a pro-drug, requires activation into cytotoxic metabolites by liver enzymes in vivo and was therefore not tested in vitro. In vivo, a neoadjuvant combination dose of doxorubicin (5 mg/kg), paclitaxel (10 mg/kg), and cyclophosphamide (120 mg/kg) was well tolerated and had a cytostatic effect on Met-1 tumor growth (**Fig. 1F**). To more closely emulate the clinical dosing regimen of AC-T chemotherapy, mice with Met1 mammary carcinoma were administered neoadjuvant AC-T every 2 weeks for 4 cycles. Interestingly, individual mice bearing Met-1 tumors exhibited differential responses to treatment, and in some cases, mice that initially experienced complete tumor regression eventually experienced local recurrence (**Fig 1G**).

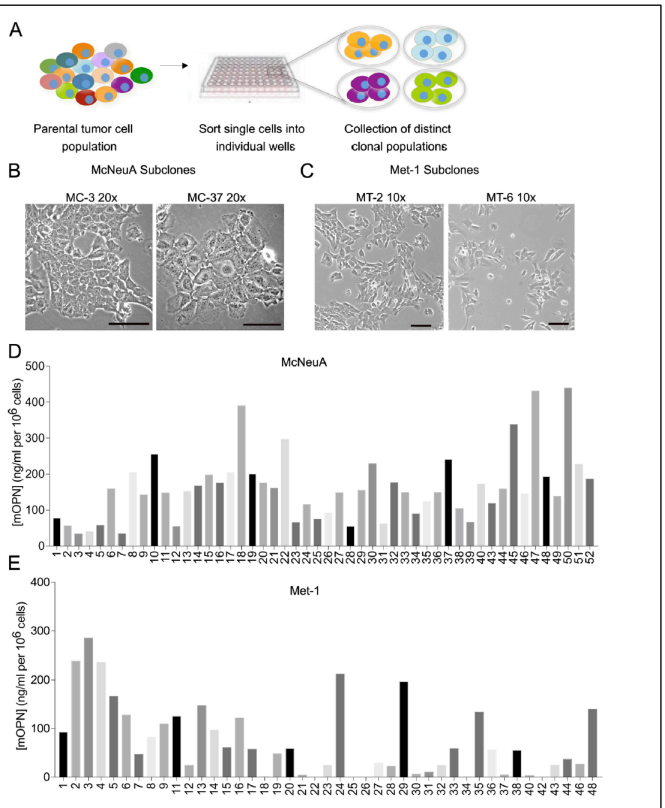

Fig 2. Phenotypic heterogeneity of McNeuA and Met-1 subclonal populations. (A) Schematic of subclone derivation from breast cancer cell lines. (B,C) Phase contrast images of representative McNeuA (B) and Met-1 (C) subclones to demonstrate morphologic variability. Scale bars = 100 µm. (D,E) Concentration of murine osteopontin (mOPN; ng/ml per 106 cells) in 24-hr conditioned media from McNeuA (MC) sublcones (D) and Met-1 (MT) subclones (E). From Olive, et al., ***PLoS One*** 2018 Jun 13; 13(6):e0198790. PMID: 29897959

To determine whether the inherent phenotypic heterogeneity of the McNeuA and Met-1 cells lines would confound the results of an OPN-knockout study, we generated single cell-derived subclonal populations from both the McNeuA (50 clones) and Met-1 (42 clones) parental cell lines (**Fig 2A**). The various subclonal populations exhibited morphological heterogeneity, displaying a range of epithelial and mesenchymal phenotypes in culture (**Fig 2B and 2C**). The McNeuA subclones secreted a range of OPN from 37.5±442.1 ng/ml per 10^6 cells (**Fig 2D**), while the Met-1 subclones exhibited a range from no detectable OPN to 287.6 ng/ml per 10^6 cells (**Fig 2E**). Importantly, a number of individual subclones secreted levels of OPN that differed significantly from their respective parental population. For example, OPN secretion was 6-8-fold higher in some McNeuA subclones (MC-18, MC-22, MC-45, MC-47, MC-50) and 2.5-3-fold higher in some Met-1 subclones (MT-2, MT-3, MT-4) than their respective parental populations (**Figs 1A, 2D and 2E**). Likewise, OPN was undetectable in some of the Met-1 cells (MT-18, MT-22, MT-25, MT-26, MT-40, MT-42) (**Fig 2E**). Taken together, these results highlighted the phenotypic heterogeneity that exists within tumor-derived breast carcinoma populations in vitro.

We next injected cohorts of FVB mice orthotopically with various McNeuA or Met-1 subclonal populations to determine whether heterogeneity could also be observed in vivo. We selected five subclones from each cell line that secreted high levels of OPN (MC-18, MC-22, MC-45, MC-47, MC-50 and MT-2, MT-3, MT-4, MT24, MT-29) (**Fig 2D and 2E**). Two McNeuA subclones (MC-22 and MC-50) formed tumors with 100% incidence, while another subclone (MC-47) failed to form tumors, and incidence was only slightly higher when more cells were injected (**Fig 3A**). Met-1subclones also exhibited variable tumor incidence with 4 of 5 subclones (MT-2, MT-4, MT-24, and MT-29) forming tumors with ~100% incidence. One subclone (MT-3) had reduced incidence to 50±66%, depending on the numbers of cells injected (**Fig 3B**). Those clones that formed tumors displayed variability in latency and growth kinetics (**Fig 3D**);

however, growth kinetics differed significantly between these clones when injected at higher numbers ($p < 0.0001$, **Fig 3C**). The subclonal populations also exhibited differences in latency and growth kinetics (**Fig 3D-F**). A number of individual subclonal populations had different tumor formation capabilities than their respective bulk parental population. For example, while the parental Met-1 tumor cell line formed orthotopic tumors with 100% incidence, the MT-3 subclonal cell line formed tumors with only 60% incidence when the same number of cells was injected (**Figs 1B and 3B**). This was also true of a human xenograft model (**See Olive, et al., *PLoS One* 2018, Fig. S2B**). These observations revealed the considerable subclonal heterogeneity that exists within human carcinoma and murine mammary carcinoma cell lines and that the behavior of individual subclones differs from their respective parental populations.

We next provided evidence that identification of proper controls is necessary for correct interpretation of experimental findings. Traditional CRISPR/Cas9 editing protocols begin with infection or transfection of the bulk parental population. For this reason, the unedited or mock-infected parental cell line is typically used as a control. Due to the inefficiency of infection and/or editing in certain cell lines, there is often a subclonal selection step that follows the initial infection and then a validated, edited subclone is used for subsequent experimentation. Our initial characterizations of the McNeuA and Met-1 parental and subclonal populations demonstrate why one must use caution when considering this commonly used approach. In some scenarios, subclonal heterogeneity could confound interpretation of knockout efficiency. For example, 23% of the Met-1 subclones have low or no detectable secreted OPN (**Fig 2E**). Hence, if one randomly selected one of these clones (e.g. MT-42) and evaluated the functional success of the OPN KO by comparing its OPN secretion levels to that of the parental Met-1 cell line, a failed knockout attempt or false positive result could be overlooked. In another scenario, if the clonal population that was selected after CRISPR/Cas9 OPN knockout happened to be clone MT-3 and its orthotopic tumor penetrance was compared to that of the parental Met-1 population, then one could erroneously interpret the necessity of OPN for primary tumor formation, when in fact this clone, prior to OPN knockout, already inherently forms tumors with lower incidence (~66%) than the parental population (100%) (**Figs 1B and 3B**). Likewise, comparing two subclonal populations, even those that secrete similar levels of OPN and form tumors with the same incidence, could also lead to spurious results. For example, if one randomly selected MT-29 as an OPN KO clone and MT-4 as a control, then incorrect conclusions could be drawn about the role of OPN in tumor growth. This is because prior to OPN KO, both clones express similar levels of OPN (~225 ng/ml; **Fig 2E**) and form tumors with similar incidence (Fig 3B) but MT-29 inherently exhibits significantly longer latency and reduced growth kinetics than MT-4 (**Fig 3E and 3F**). The same holds true for MC-18 and MC- 50, which secrete similar levels of OPN (~400 ng/ml; **Fig 2D**), but incidence of tumor formation after injecting 10^6 cells is ~17% for MC-18 and 100% for MC-50 (**Fig 3A**). Hence, the chances of randomly selecting functionally equivalent clones±such as MC-22 and MC-50, which secrete similar levels of OPN (> 250 ng/ml; **Fig 2D**), form tumors with similar incidence (100%; **Fig 3A**), and display similar growth kinetics (**Fig 3B**) are low without extensive characterization of individual clones prior to gene editing. Our results provided evidence that neither the parental population nor other subclones would represent an

A

McNeuA

Clone ID (no. cells)	Tumor Incidence
MC-18 (10^5)	3/6
MC-18 (10^6)	4/6
MC-22 (10^5)	6/6
MC-22 (10^6)	6/6
MC-45 (10^5)	2/6
MC-45 (10^6)	3/6
MC-47 (10^5)	0/6
MC-47 (10^6)	2/6
MC-50 (10^5)	4/6
MC-50 (10^6)	6/6

B

Met-1

Clone ID (no. cells)	Tumor Incidence
MT-2 (25K)	6/6
MT-2 (250K)	6/6
MT-3 (25K)	2/6
MT-3 (250K)	4/6
MT-4 (25K)	6/6
MT-4 (250K)	6/6
MT-24 (25K)	5/6
MT-24 (250K)	6/6
MT-29 (25K)	6/6
MT-29 (250K)	6/6

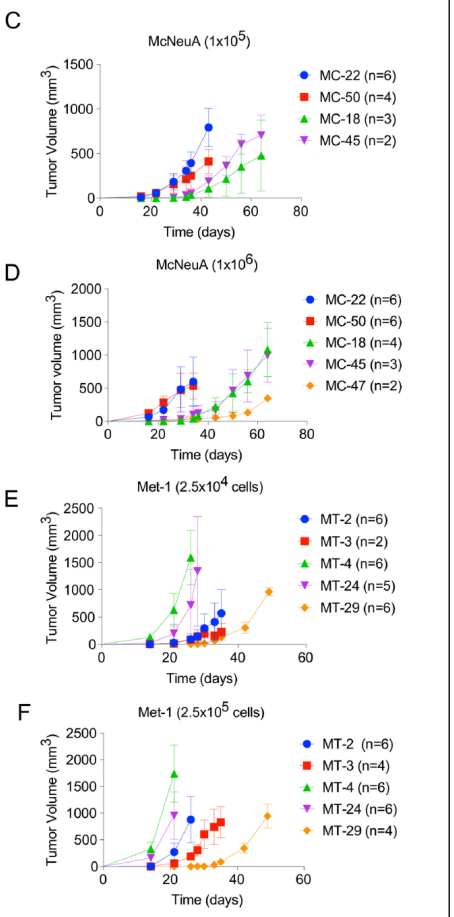

Fig 3. McNeuA and Met-1 subclonal populations are functionally heterogeneous in tumor incidence, latency and growth kinetics. (A,B) Primary tumor incidence of indicated McNeuA (105 or 106 cells; A) and Met-1 (2.5x104 or 2.5x105 cells; B) clonal populations that were injected orthotopically into FVB mice. (C,D) Tumor growth kinetics of indicated McNeuA clones that were orthotopically injected into FVB mice at 105 (C) or 106 (D) cells. Error bars represent SD; statistical significance evaluated using 2way-ANOVA. (E,F) Tumor growth kinetics of indicated Met-1 clones that were orthotopically injected into FVB mice at 2.5x104 (E) or 2.5x105 (F) cells. Error bars represent SD; statistical significance evaluated using 2way-ANOVA. From Olive, et al., ***PLoS One*** 2018 Jun 13; 13(6):e0198790. PMID: 29897959

appropriately matched wild-type control for a CRISPR/Cas9 knockout cell line that was selected after the gene editing step. The only appropriate control would be to compare the behavior of edited and unedited cells derived from the same clonal population. We therefore concluded that a modified strategy should be developed to account for heterogeneity and enable the generation of appropriately matched cell lines.

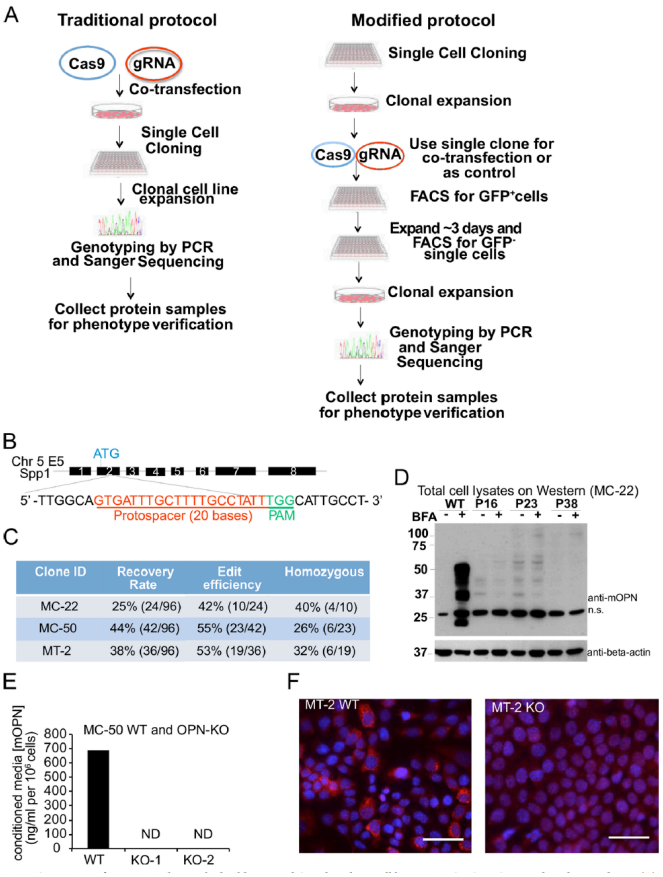

Fig 4. Generation of appropriately matched wild-type and OPN knockout cell lines using CRISPR-Cas9 mediated gene editing. (A) Schematic of traditional and modified CRISPR/Cas9 based gene editing protocols. (B) Schematic diagram of sgRNA targeting the spp1 gene loci. Protospacer sequence is highlighted in red. Protospacer adjacent motif (PAM) sequences are presented in green. (C) Recovery rates, gene editing efficiency, and rate of homozygous targeting of the OPN gene in indicated subclones. (D) Western blot for OPN protein in MC-22 WT and edited clones (P16, P23, and P38) cultured in the presence or absence of brefeldin A (BFA). Expected multiple Osteopontin isoforms were detected between ~37±50 kD. A non-specific band was detected in each sample, indicated by [a]n.s[o]. From Olive, et al., ***PLoS One*** 2018 Jun 13; 13(6):e0198790. PMID: 29897959

One would not have known a priori about differences in subclonal biological phenotypes and experimental outcomes by taking traditional approaches to gene editing. Therefore, we developed a modified CRISPR-Cas9 editing protocol for generating matched control and knockout cells (**see Fig. 4A-C from Olive, et al., *PLoS One* 2018 Jun 13; 13(6):e0198790. PMID: 29897959** for full details of protocol). We validated loss of OPN protein expression in each of the OPN KO clones compared to its appropriately matched control using western blotting, ELISA of conditioned media, or immunocytochemistry. We observed no detectable OPN protein (**Fig 4D-F**), demonstrating that our CRISPR/Cas9 editing strategy was successful and we had generated authentic OPN KO subclonal cell lines.

Most studies, including our own, report that OPN is dispensable for primary tumor growth, but is critical for metastasis due to its effects on tumor cells, the host systemic environment, and the tumor microenvironment. Therefore, we tested the tumor formation capabilities of the matched clones. WT and OPN KO MC-50 cells, MC-22 cells or MT-2 cells were orthotopically injected into FVB mice and were allowed to grow until tumors reached ~1 cm^3. Loss of tumor-derived OPN did not significantly affect growth kinetics or the final mass of any of the tumors derived from matched subclonal cell lines (**See Fig 5A-D from Olive, et al., PlosOne, 2018**). As expected, mOPN plasma levels were elevated in the mice bearing WT tumors relative to the cancer-free cohort, and plasma OPN levels were significantly reduced in the mice bearing KO tumors relative to WT (**See Fig 5A-D from Olive, et al., PlosOne, 2018**).

Osteopontin is considered a biomarker for tumor progression and is detected at higher levels in more aggressive tumors than their low-grade counterparts, is elevated in the serum of patients with metastatic disease and is included in gene lists predicting poor prognosis for many cancer types. Although OPN is most often dispensable for primary tumor growth, OPN is necessary for metastasis. To address this question, we labeled the MT-2 WT and MT-2 OPN KO cell lines with a dual GFP/luciferase reporter and injected the labeled cells intravenously via the tail vein into cohorts of mice (**Fig 6A**). Metastatic burden was decreased in the MT-2 OPN KO cohort relative to that of the MT-2 WT cohort (**Fig 6B, C**). There were significantly fewer total and multifocal pulmonary metastases in mice that had been injected with the OPN KO cells compared to mice that had been injected with OPN WT cells (**Fig 6D-F**). Collectively, our results established that by using appropriately matched cells, we could confidently conclude that OPN is necessary for metastatic colonization and that our CRISPR/Cas9 protocol is useful for pre-clinical metastasis studies.

Resistance to standard chemotherapies remains a significant clinical problem, particularly for triple-negative breast cancer. In order to interrogate whether OPN contributes to chemoresistance in breast cancer models, we tested the MT-2 WT and KO cell lines for sensitivity to AC-T chemotherapy in vivo. We injected MT-2 WT or matched OPN KO tumor

cells into the mammary fat pads of FVB mice. When established tumors reached ~60±80 mm3 in volume (14 days), animals were randomized based on tumor volume and enrolled into either vehicle control (PBS) or AC-T chemotherapy treatment cohorts (**Fig 7A**). MT-2 WT and MT-2 KO tumors exhibited sensitivity to AC-T treatment relative to their respective vehicle-treated cohorts (Fig 7B). However, in response to AC-T, the MT-2 KO tumors exhibited reduced growth kinetics compared to their MT-2 WT counterparts in three independent trials (**Fig 7B**). Likewise, final tumor mass was significantly lower in the MT-2 KO treatment cohorts compared to the MT-2 WT treatment cohorts (not shown). Together, these data established that elimination of OPN expression enhances chemosensitivity of the MT-2 breast cancer population.

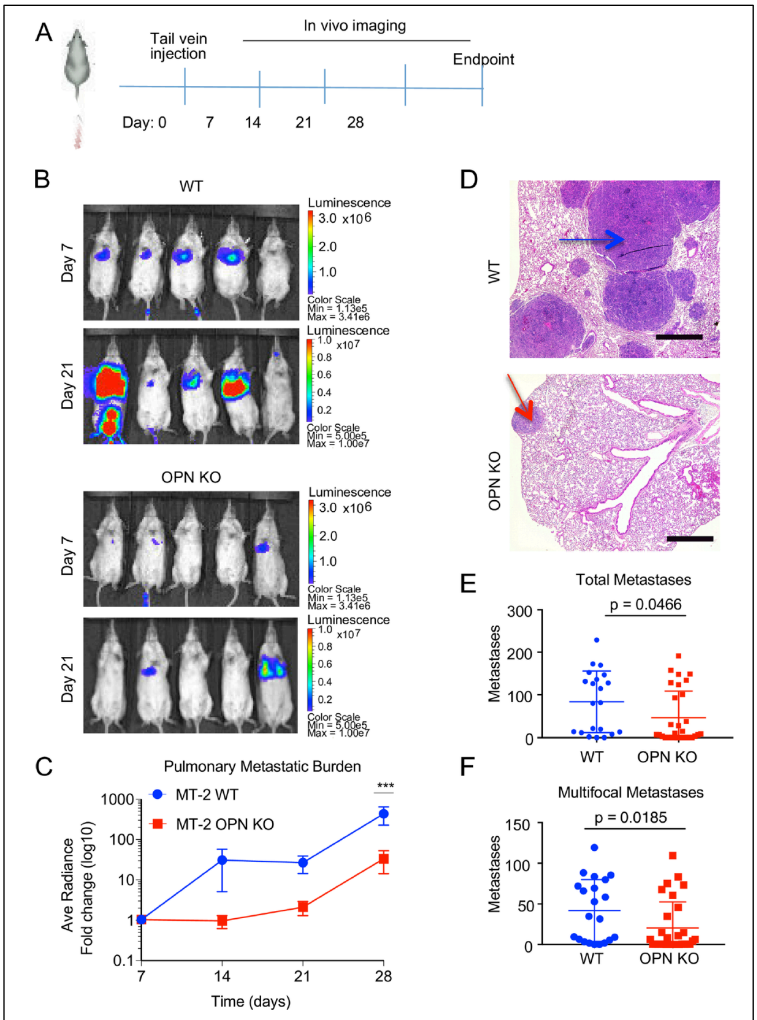

Fig 6. OPN is necessary for pulmonary metastasis. (A) Experimental schema for metastasis assay. (B) Representative in vivo bioluminescent images of mice injected with MT-2 WT or MT-2 OPN KO after 7d and 21d. (C) Average fold change of bio-luminescent signal (radiance (p/sec/cm2/sr), log10, normalized for differences in Luciferase expression between cell lines) from mice with MT-2 WT (blue) or MT-2 OPN KO (red) at indicated time points. (unpaired, two tailed t-test: p = 0.000067). Error bars represent SEM. (D) Representative hematoxylin & eosin staining of lungs from mice that received tail vein injections of MT-2 WT or MT-2 OPN KO cells. An example of a multifocal metastasis is marked with a blue arrow and an example of a single focus metastasis is marked with a red arrow. Scale = 1000 µm. (E) Quantification of total metastases in MT-2 WT (blue) and MT-2 OPN KO (red) cohorts (WT n = 21, KO n = 30; Mann-Whitney, p = 0.0466). Error bars represent SD. (F) Quantification of multifocal metastases in MT-2 WT (blue) and MT-2 OPN KO (red) cohorts (WT n = 21, KO n = 30; Mann-Whitney, p = 0.0185). Error bars represent SD. From Olive, et al., ***PLoS One*** 2018 Jun 13; 13(6):e0198790. PMID: 29897959

To continue to leverage these single-cell cloning approaches for our overall goal to define tumor cell hallmarks that predict risk of breast cancer recurrence, we continued our molecular barcoding work (described in progress reports years 1-3). We had spent the majority of the previous year overcoming challenges associated with this goal. We found a solution to this problem by re-constructing the barcodes for analysis by multiplex next generation sequencing using PCR-based strategies. This new approach, which we call SunCatcher, significantly cut down on our costs and time. The general approach provided the basis for our original proposal and was described in previous progress reports. Briefly, the basis of SunCather is as follows: We first generate stable single cell-derived monoclonal populations (CPs) from heterogeneous populations of cancer cell lines or patient-derived tumor cells. We tag each individual clonal population with a unique molecular "barcode" sequence using lentiviral vectors to create barcoded clonal populations (BCPs). Upon integration, each vector introduces a unique 24-base pair heritable DNA barcode tag into each cell clone genome; hence, we can precisely follow the progeny of each cell over time. We then mix an equal number of each BCP to create a barcoded polyclonal population of

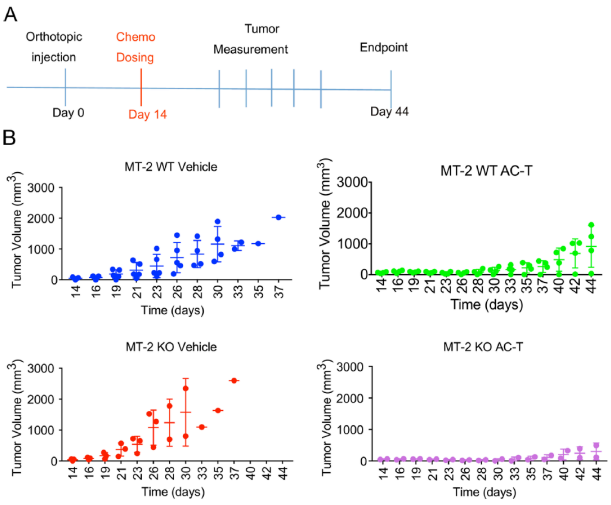

Fig 7. MT-2 OPN-KO tumors exhibit enhanced chemosensitivity. (A) Experimental schema. (B) Tumor growth kinetics for MT-2 WT vehicle (blue; n = 5) and AC-T treated (green; n = 4) and MT-2 OPN-KO vehicle (red; n = 3) and AC-T treated mice (purple; n = 2). Representative of 3 biological repetitions. Error bars represent SD. From Olive, et al., ***PLoS One*** 2018 Jun 13; 13(6):e0198790. PMID: 29897959

cells (BPP). Each variable barcode sequence is flanked by uniform sequences, common to all barcode vectors, which allows for PCR amplification of barcodes from genomic DNA preparations. To identify and quantify relative abundance of each clonal population within a polyclonal mixture of cells, including tumor and non-tumor stromal cells, we now perform PCR-based analysis. We are thereby able to identify and quantify the representation of each individual barcode in a given tissue sample.

Importantly, our barcoding approach is different from others that have been reported in that we generate single cell subclones prior to introducing the barcode tags. Other reported approaches infect heterogeneous parental populations of cells with an entire library of barcodes at low MOI, without the ability to identify which cells are tagged with which barcode. Hence, the advantage of the SunCatcher approach is that by introducing single barcodes into monoclonal populations and then generating the pooled barcoded polyclonal population rather than infecting the bulk parental population with a library of barcodes, we gain the ability to retroactively characterize barcoded monoclonal populations in any given experiment. This approach also allows us to be confident that the same barcode is not unwittingly introduced into multiple unique clonal populations, thus confounding subsequent analyses.

We thus employed the SunCatcher approach in order to identify the cells within a heterogeneous, normally indolent patient-derived cell line that respond to systemic and microenvironmental cues to progress to malignancy. As previously reported in earlier progress reports, we generated 30 single cell-derived subclones from a parental triple-negative human breast cancer cell line (HMLER-HR). To do so, we sorted single cells based on their CD24/44 profiles as an arbitrary way to capture heterogeneity, and expanded these to establish HMLER-derived human breast cancer monoclonal populations (hCPs). Each individual hCP was infected with a unique barcode sequence to generate HMLER barcoded monoclonal populations (hBCPs). The individual hBCPs were morphologically distinct from one another, ranging across a spectrum from epithelial to mesenchymal (reported in earlier progress reports). In addition, the hBCPs differed in their *in vitro* proliferation kinetics and the ability to form tumorspheres in suspension culture. Having established that the hBCPs were phenotypically diverse, we then mixed an equal number of each of the 30 hBCPs to generate the HMLER barcoded polyclonal population (hBPP). We determined that the hBPP is stable in culture over time, with no monoclonal subpopulations becoming dominant or extinct during six passages (reported in earlier progress reports). Importantly, proliferation and tumorsphere forming ability did not significantly differ between the hBPP cells and the parental HMLER cells in vitro (reported in earlier progress reports). As reported in earlier progress reports, we found that an activated systemic environment (A-HSE; marked by enhanced immune inflammation), increased the heterogeneity observed in tumors derived from these barcoded populations, relative to a naïve, non-inflammed systemic environment (N-HSE). Moreover, the reproducibility of BCPs detected across tumors from each given cohort suggested that the systemically driven selection was directed rather than stochastic.

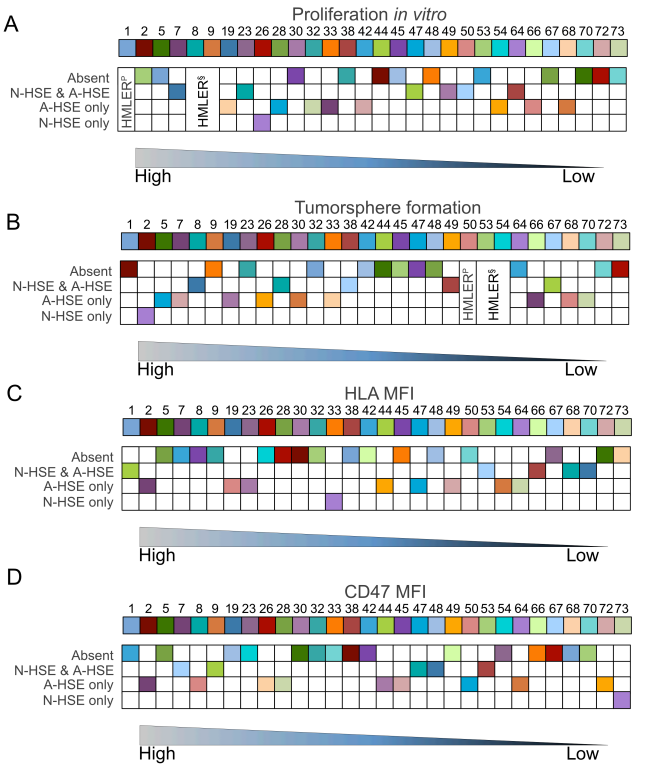

Figure 8. Cell intrinsic properties of individual CPs do not explain selection patterns observed in vivo. A-D: Individual CPs evaluated for their proliferation kinetics rates (A), tumorsphere formation rates (B), HLA-1 expression levels (quantified using median fluorescence intensity, MFI) (C), and CD47 expression levels (D). CP identities are represented using color and are placed in columns arranged from highest to lowest values from left to right. CPs were placed in the row that corresponds to their presence or absence from HMLER tumors in the naïve systemic environment (N-HSE), activated systemic environment (A-HSE), or both environments.

Since the patterns of BCP selection within tumors from the naive and activated nude mouse cohorts did not appear to be stochastic, we analyzed cell intrinsic properties of individual BCPs that might explain their presence or absence in resulting tumors. We found that the *in vitro* proliferation kinetics rates or tumorsphere formation capacity of individual BCPs did not correlate with the observed *in vivo* selection patterns **(Fig. 8).** For example, the most highly proliferative

BCP (BCP 53) and the BCP with the highest rate of tumorsphere formation (BCP 2) both were only detected in 3/29 and 7/29 tumors, respectively **(Fig. 8).** The slowest proliferating BCP (BCP 70) and the BCP with the lowest tumorsphere formation rate (BCP 73) appear in tumors at similar rates, and were detected in 2/29 and 16/29 tumor samples, respectively **(Fig. 8)**.

To test whether the BCPs that had similar *in vivo* behaviors also shared common molecular features, we performed gene expression analysis of each CP using the LINCS L1000 profiling platform. Hierarchical clustering revealed that BCP expression profiles did not correlate with whether or not CPs were selected for in any of the *in vivo* systemic environments **(Fig. 9).** Collectively, these results indicated that none of the individual cell-intrinsic characteristics that we examined *in vitro* explained the differential CP selection patterns that we observed in the N-HSE and A-HSE nude mouse cohorts. And this happened in absence of additional oncogenic genetic mutations

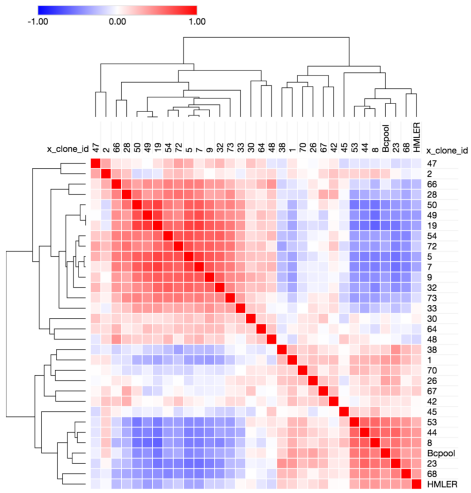

Fig. 9. Hierarchical clustering of gene expression of individual HMLER clones (indicated by numbers), parental population (HMLER), and the barcoded pool (BCPool).

Given that individual cell intrinsic properties were not shared in common, we wondered if *in vivo* behavior of individual BCPs is affected by its interactions with other BCPs. Previous studies have demonstrated the important role that clonal cooperation plays in breast cancer progression, including contributing to immune evasion. We therefore generated different pools of barcoded populations comprised of various BCPs depending on their in vivo outcome - subpools by creating mixtures containing equal numbers of each CP that was detected in HMLER§ tumors in the N-HSE or A-HSE **(Fig. 10,** referred to as N-HSE§ and A-HSE§, respectively). We also generated a subpool that contained CPs that were found exclusively in the A-HSE HMLER§ tumors and were never detected in the naïve systemic environment **(Fig. 10,** A-HSE-exclusive§). Finally, we generated subpools that contained a subset of BCPs or all BCPs that were not detected in any HMLER§ tumors (**Fig. 10**, partial-absent§ (absent^{P§}) and total-absent§ (absent^{T§})).

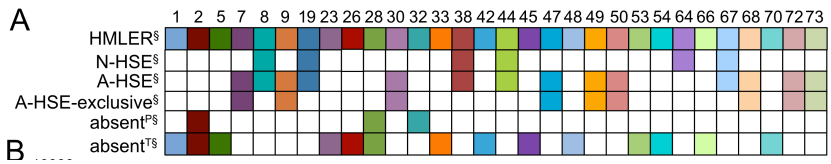

Fig. 10. HMLER subpools that resembled HMLER tumor clonal composition in the experiment were generated by mixing equal numbers of the indicated CPs.

We first performed gene expression profiling of the CP subpools with hierarchical clustering of the resultant gene expression signatures. Despite the fact that the clones contained within N-HSE§ are also present in A-HSE§, these two subpools did not cluster together, suggesting that they have unique molecular profiles **(Fig. 11A).** In contrast, the A-HSE-exclusive§, which also contains CPs that are present in A-HSE§, does cluster with A-HSE§ **(Fig. 11A).** These results suggested that the addition of the CPs in A-HSE-exclusive§ contribute more strongly to the A-HSE§ signature than the CPs in N-HSE§. Interestingly, when hierarchical clustering of the individual gene expression signatures of the CPs present within A-HSE§ was performed, the clones within N-HSE§ clustered together, and the clones within A-HSE-exclusive§ clustered together **(Fig. 11B)**. We also queried the gene expression signatures of the CP subpools for connectivity with gene expression signatures of a group of ~7,000 TCGA breast cancer samples. We found that A-HSE-exclusive§ had notably more high ranking connections with TNBC patient samples than the other pool signatures (**Fig. 11C).** This suggests that A-HSE-exclusive§, which contains CPs that exclusively appear in the TNBC tumor bearing A-HSE, more closely matches TNBC patient samples than the other pools. Gene set enrichment analysis (GSEA) of the L1000 gene signatures revealed several instances where the A-HSE§ and N-HSE§ pool signatures revealed opposite patterns of connectedness to KEGG pathways that are relevant for cancer pathogenesis that were statistically significant **(Fig. 11D)**. For example, whereas the N-HSE§ pool signature exhibited significant connectivity to the KEGG Cell Cycle and KEGG DNA Replication pathways, the A-HSE§ pool signature was negatively enriched for these pathway members (**Fig. 11D)**. Also of interest was that the A-HSE§ and A-HSE-exclusive§ pool signatures differed from one another in these analyses, suggesting that these molecular profiles were the result of cooperation among all of the clones in A-HSE§, and did not merely represent a majority contribution of the signaling pathways active in A-HSE-exclusive§ CPs **(Fig. 11D**).

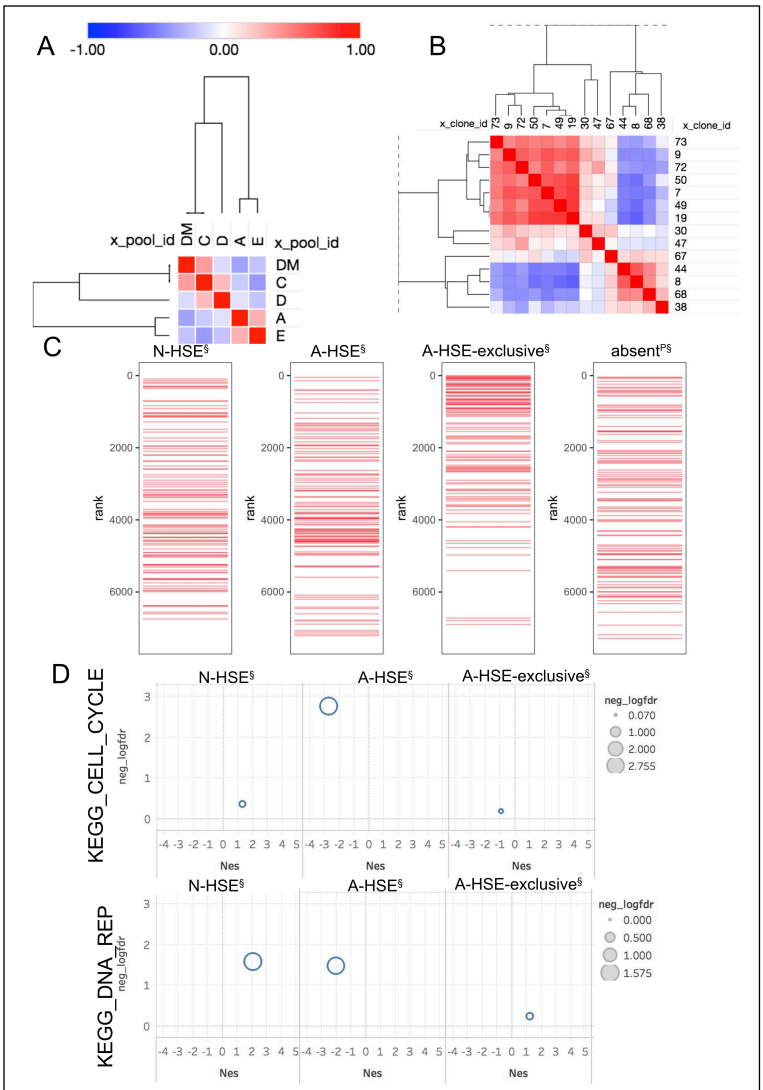

Fig. 11. HMLER‍ subpools have unique gene expression signatures despite containing common CPs. (A) Hierarchical clustering of the HMLER‍ subpools L1000 gene expression signatures. (B) Hierarchical clustering of individual CP L1000 gene expression signatures within A-HSE‍. (C) Tick plots showing the position of each TNBC sample in the ranked list of connectivities between all TCGA breast cancer samples (~7k) and the L1000 gene expression signature of each HMLER‍ pool. (D) Volcano plots showing Normalized enrichment score (Nes) and the corresponding –log(FDR) for the indicated KEGG pathways for various HMLER‍ subpools.

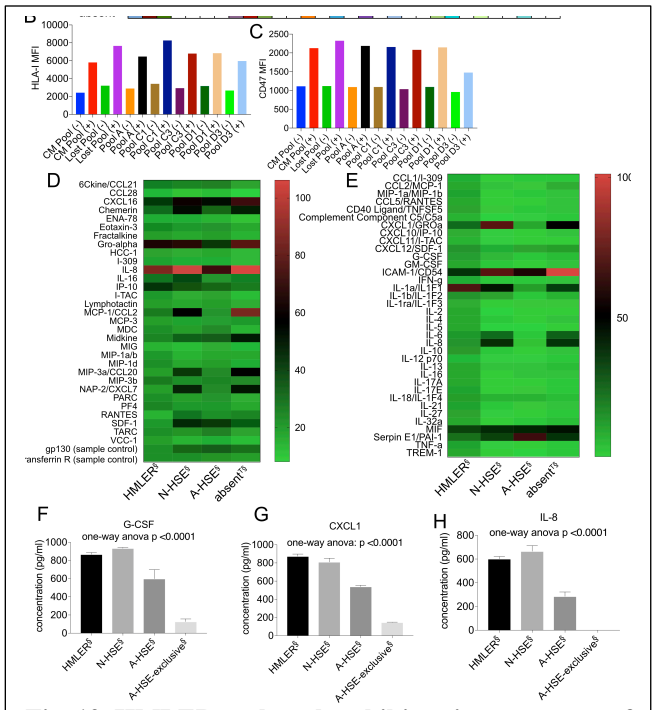

Fig. 12. HMLER‍ subpools exhibit unique patterns of cytokine and chemokine secretion. (B) HLA-I median fluorescence intensity (MFI) values of CP subpools that had been cultured in the absence (-) or presence (+) of IFN-gamma. (C) CD47 median fluorescence intensity (MFI) values of CP subpools that had been cultured in the absence (-) or presence (+) of IFN-gamma. (D) Heat map representing protein array quantifications of chemokine expression levels in conditioned media from the indicated HMLER‍ subpools. (E) Heat map representing protein array quantifications of cytokine expression levels in cell lysates of the indicated HMLER‍ subpools.(F-H) Expression levels G-CSF (F), CXCL1 (G), and IL-8 (H) in conditioned media of the indicated HMLER‍ subpools as measured by ELISA. Error bars represent SD (n = 3 per condition, one-way ANOVA).

We then used flow cytometry to evaluate the expression levels of two cell surface proteins, HLA-1 and CD-47, that could explain innate immune clearance in pool A relative to pool C or D that we also observed in our DEG analysis. We evaluated the expression level of both proteins on each CP in the presence and absence of IFN-gamma. We did not observe any trends in expression levels of either of these proteins that would account for the differential CP selection patterns that we observed *in vivo* **(Figure 8C, D).** Specifically, we did not see significantly higher or lower expression levels of either protein in CPs that were lost during tumor progression, compared to those that were maintained. We also found that all of the CPs were IFN-gamma responsive, suggesting that this characteristic could also not explain their differential behavior *in vivo*. We did not observe any correlation between the *in vivo* behavior of CP subpools and their expression of either HLA-1 or CD-47 or response to IFNg (**Fig. 12B, C**). Cytokine and chemokine protein array analysis of conditioned media or cell lysates from CP subpools revealed that a number of proteins related to immune cell chemotaxis and function were differentially expressed and/or secreted by the HMLER§ and CP subpools N-HSE§ and A-HSE§ **(Fig. 12D, E).** Of particular interest to us was the observation that several factors involved in neutrophil mobilization and chemotaxis were downregulated in A-HSE§ and A-HSE-exclusive§ compared to the other subpools, consistent with our DEG analysis. ELISA analysis of conditioned media samples confirmed that the A-HSE§ and A-HSE-exclusive§ subpools secrete significantly lower levels of G-CSF, CXCL-1 and IL-8 compared to both HMLER§ and N-HSE§ **(Fig. 12F-H)**.

In order to determine whether innate immune components played a role in shaping the unique clonal compositions observed in polyclonal tumors in hosts with naive or activated systemic pathophysiology, a repetition of the *in vivo* selection experiment was performed in which hBPP cells were injected into either naive or activated NSG mice **(Fig. 13A**). Whereas nude mice have a functional innate immune system, NSG mice exhibit dysfunction of a number of innate immune cell components, including macrophages, dendritic cells, and NK cells. Therefore, if the innate immune system was playing a critical role driving the subclonal selection within polyclonal tumors, then we expected to see an abrogation of the differential selection patterns between the naive and activated cohorts in NSG mice.

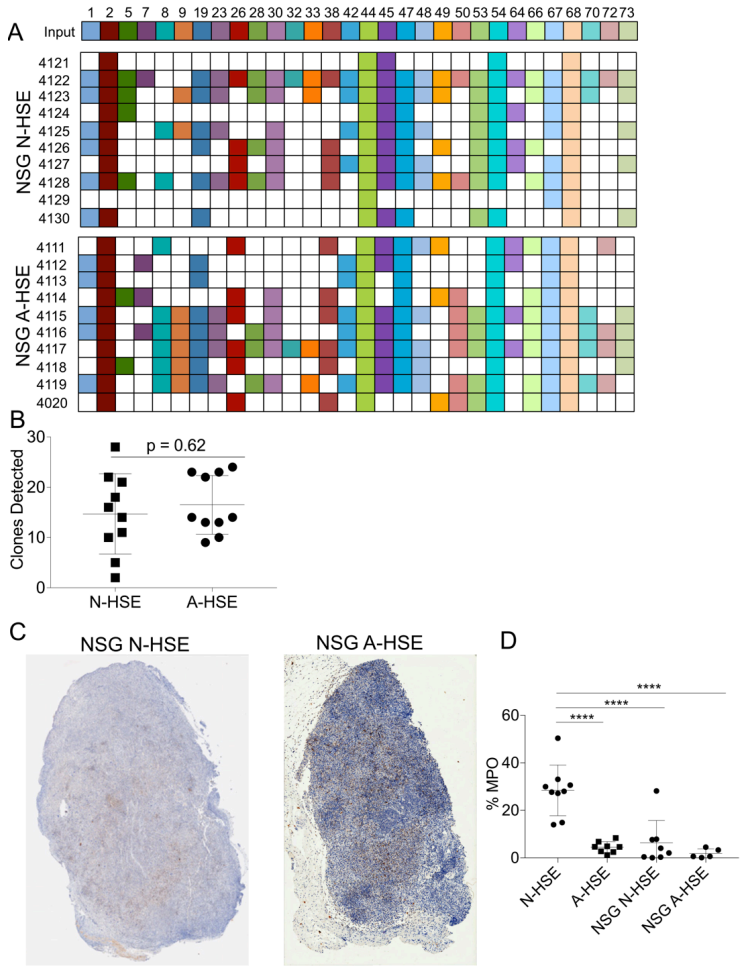

Figure 13. A functional innate immune system is required for enhanced heterogeneity in A-HSE HMLER tumors. (A) Representation of next-generation sequencing detected barcodes in individual HMLER tumors recovered from NSG mice in the N-HSE and A-HSE cohorts. Individual tumors are represented across rows and barcode identity is represented along columns. (B) Number of detected CPs per HMLER tumor. Each point represents an individual tumor. Bars represent mean and SD (N-HSE: n = 10, A-HSE: n = 10; Mann-Whitney test). (C) Representative images of HMLER tumors recovered from NSG N-HSE and NSG A-HSE cohorts stained for MPO (brown) and counterstained with hematoxylin. Images were captured at 20x magnification. (D) Percent of cells that stained positively for MPO in indicated cohorts. Points represent individual tumors. Error bars represent mean and SD (N-HSE: n = 9; A-HSE: n = 8; NSG N-HSE: n = 10; NSG A-HSE: n = 10; **** = $p < 0.0001$, Ordinary one-way ANOVA, Tukey's Multiple Comparisons Test).

In contrast to the nude mouse experiments, there was no significant difference between the number of detected BCPs in the naive (average of 15.4 per tumor) and activated (average of 16.4 per tumor) cohorts when the hBPP tumors were allowed to form in NSG mice **(**p=0.5721, **Fig. 13A, B).** In addition, the selection patterns appeared to be much more stochastic in NSG mice compared to nude mice **(Fig. 13A)**. Whereas in nude mice there were particular subclonal populations that were never detected in any tumors, in the NSG cohort every clone was detected in at least one tumor and there was a large amount of variability among mice within each systemic environment **(Fig. 13A).** Both the naive and activated NSG cohorts exhibited an enhancement of heterogeneity compared to that of the nude activated cohort, with an average of 15.4, 16.4 and 12 clones detected, respectively. Strikingly, similar to the nude activated cohort, tumors recovered from both cohorts of NSG mice also exhibited a reduction in neutrophil infiltration compared to the nude naive cohort **(Fig. 13C, D).**

Together, these data established that a fully functional innate immune system is required to observe a reduction of heterogeneity in the naive cohort compared to the activated cohort and that reduced neutrophil infiltration appears to correlate with enhanced heterogeneity.

We next evaluated whether the unique gene expression patterns among the HMLER§ subpools translated to differences in behaviors by evaluating in their ability to respond to standard of care chemotherapeutics. The chemosensitivity of HMLER§, N-HSE§, and A-HSE§ was evaluated by treating each pool with doxorubicin, 5-FU or paclitaxel for 72 hours and then evaluating the cell viability of each pool using the Cell Titer Glo assay. A-HSE§ exhibited significantly higher rates of survival and decreased chemosensitivity compared to N-HSE§ and this result was replicated in 4 separate repetitions of the experiment **(Fig. 14A).** Strikingly, when the clonal composition of the surviving cells was analyzed, we found that all of the CPs were maintained during treatment with doxorubicin in HMLER§, N-HSE§, and A-HSE§ at the IC50 dose. This suggests that the enhanced survival was not the result of the selection of particular chemoresistant CPs from among A-HSE§, but that there is clonal cooperation taking place among the A-HSE§ CPs that affords enhanced chemoresistance.

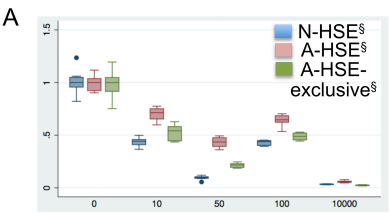

Drug	Lower Survival	p value
5-FU	N-HSE§	5.5 e-11
Paclitaxel	N-HSE§	8.7 e-05
Doxorubicin	N-HSE§	5.4 e-13

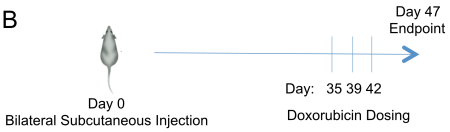

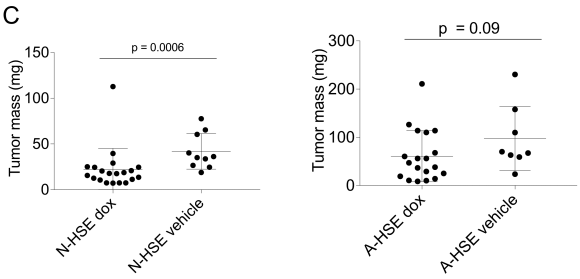

Figure 14. N-HSE⍰ subpool is more chemosensitive than A-HSE⍰ subpool both in vitro and in vivo. (A) Fractional survival (y-axis) of subpools following 72 hours of treatment with doxorubicin (concentrations along x-axis: 0 nM, 10 nM, 50 nM, 100 nM, and 10 uM). A two-sided Wilcoxon rank sum test, stratified for dose, was used to compare fractional survival of N-HSE⍰ to A-HSE⍰. (B) Experimental schema for in vivo doxorubicin study. (C) Final tumor mass for N-HSE⍰ to A-HSE⍰ tumors (N-HSE dox: n=20; N-HSE vehicle: n=10; A-HSE dox: n=19; A-HSE vehicle: n=8; Mann-Whitney test).

We examined whether this differential chemosensitivity was also relevant in an *in vivo* setting by injecting N-HSE§ and A-HSE§ into NSG mice and evaluating their response to treatment with doxorubicin. Treatment was initiated with either doxorubicin (1.5 mg/kg) or vehicle control (saline) when palpable tumors were observed in the majority of mice **(Fig. 14B)**. We found that while the final tumor mass in the N-HSE§ cohort was significantly lower in the doxorubicin treated mice compared to the vehicle treated mice, there was no significant difference between the final tumor mass in the two A-HSE§ cohorts **(Fig. 14C).** This agrees with the *in vitro* observation that A-HSE§ is less chemosensitive than N-HSE§.

Together these results suggest that the directed selection that we observed in the A-HSE in nude mice was functionally consequential and that the enhanced heterogeneity generated in this environment can lead to the development of a more aggressive TNBC tumor.

<u>Task 2a-c and Task 3a-c</u>

As reported in our progress reports from years 1-3, we uncovered mechanisms by which certain primary tumors can prevent disseminated tumor cells (DTCs) from generating metastases. The inhibitory primary tumors elicit a systemic innate immune response involving IL-1β-expressing monocytes that infiltrate the distant DTC microenvironment. These monocytes maintain DTCs in a mesenchymal, non-proliferative state that prevents them from giving rise to differentiated, proliferative epithelial progeny that are critical for forming robustly growing tumor tissue. IL-1R inhibition or surgical resection of the inhibitory primary tumor permits outgrowth of DTC-derived secondary tumors. As reported in year 3, we had submitted this work for publication in Nature Cell Biology. At that time, we were missing clinical data to validate our findings, so during year 4, we investigated that avenue.

Our studies demonstrated that innate immune cells secreting IL-1β, mobilized by the primary tumor, compromise MIC colonization at secondary sites by preventing their differentiation into epithelial progeny, which is essential for forming actively growing tumors (**Fig. 15A**). Given that this cascade of events depends on the continued presence of the primary tumor, clinical validation relied on careful selection of appropriate patient populations. Indeed, hMIC-derived metastases were not inhibited if the IL-1β dependent inflammatory cascade was instigated after MIC dissemination and growth initiation (**Fig. 15B, C**). hMIC tumors that were <2mm (low mitotic index) at the time of HMLER implantation were significantly suppressed; however, if hMIC tumors had already entered an active growth phase (>2mm) at the time of primary tumor implantation, MIC-derived tumors sustained continued growth (**Fig. 15C**). These data provided preliminary indication that HMLER tumors do not cause regression of robustly growing hMIC tumors but instead, exert their inhibitory effects at early stages of secondary tumor establishment when MICs are still in the ZEB1+ state.

We therefore compared primary tumor IL-1β expression in breast cancer patients with lymph node-positive (LN+) and LN-negative disease by retrospective gene set analyses using a database of Affymetrix microarray profiles. Among 508 patients with LN- disease, IL-1β expression did not stratify overall survival (**Fig. 15D**). However, among 215 patients with LN+ breast cancer, those with high IL-1β had improved overall survival relative to those with low IL-1β expression (**Fig. 15E**). Interestingly, patients whose primary tumors expressed high IL-1β had improved outcome (distant metastasis-free survival) when we interrogated the entire cohort of 1,379 patients (**See Supplementary Fig. 8a from Castano, et al, Nat Cell Biol, 2018; Attached as Appendix 2**).

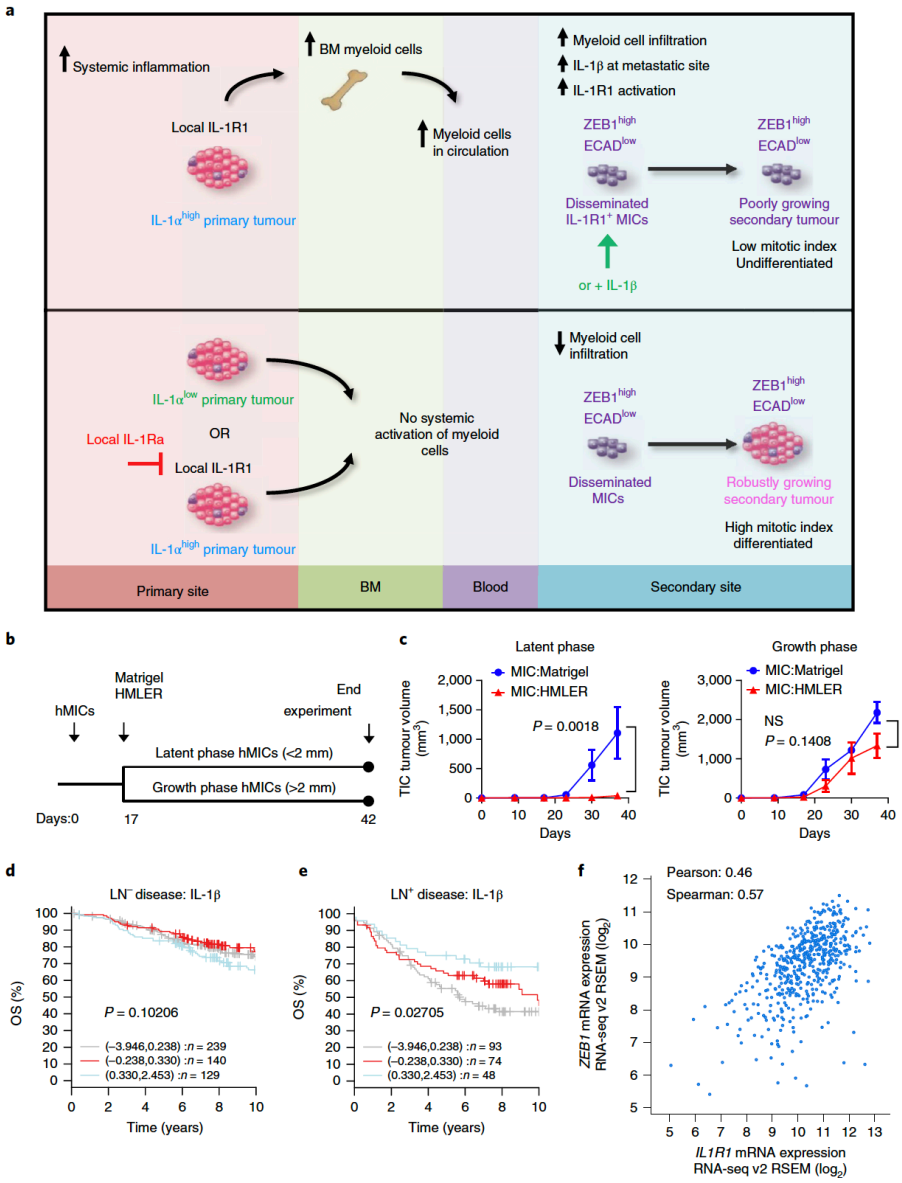

Figure 15. Low primary tumor IL-1β correlates with reduced overall survival in breast cancer
a, Model illustrating systemic mechanism by which primary tumors elicit an IL-1β-dependent inflammatory response to suppress MIC colonization. **Top panel**: Primary tumors that secrete high levels of pro-inflammatory cytokines, e.g., IL-1α, elicit a systemic innate immune response that expands bone marrow and circulating myeloid cells, culminating in increased immune infiltrate into tissues where metastasis-initiating cells (MICs) disseminate. In the metastatic microenvironment, IL-1β acts in a paracrine fashion on IL-1R expressing MICs, causing the MICs to maintain their mesenchymal phenotype of high ZEB1 and/or low E-cadherin (ECAD), thereby preventing MIC differentiation and proliferation. **Bottom panel:** Preventing inflammation at the primary tumor site or inhibiting IL-1R1 with the antagonist, IL-1Ra, in the metastatic microenvironment causes MICs to differentiate, proliferate and thereby establish robustly growing secondary tumors and metastases. **b,** Schematic of experiments to test effect of primary HMLER tumors on established hMIC tumors in Nude mice. **c**, Growth kinetics of hMIC tumors that were either in latent phase (left) or growth phase (right) at day 17 when Matrigel control or HMLER tumor cells were injected contralaterally. (Latent phase: Matrigel n=6 tumors, HMLER n=5 tumors. Growth phase: Matrigel n=4 tumors, HMLER n=5 tumors). One experiment was performed. 2way ANOVA and Sidak's multiple comparisons test. **d, e,** Kaplan-Meier analysis using overall survival (OS) as end point with 10-year censoring, based on *IL1B* gene expression (log2, stratified into three indicated quantiles) in primary tumor tissues from patients with lymph node negative (LN^-; n=508 patients) **(d)** or lymph node positive (LN^+; n=215 patients) **(e)** disease. Logrank p values are shown. Data and analysis obtained from the GOBO database (http://co.bmc.lu.se/gobo/gsa.pl). **f,** Correlation between IL-1R1 and Zeb1 mRNA expression in 818 tumor tissue samples from patients with invasive breast carcinoma. Data and analysis obtained from the cBioPortal database (http://www.cbioportal.org/index.do).

We also analyzed correlations between IL-1R1 and markers of differentiation status that we had observed. In an analysis of 818 tumor tissue samples from patients with invasive breast carcinoma, IL-1R1 expression positively correlated with Zeb1 (**Fig. 15F**).

Therefore, we found that among patients with lymph node-positive breast cancer (i.e., those at high risk for metastasis), high IL-1β was associated with improved overall survival and distant metastasis-free survival. These results suggest opportunities for developing better risk assessment algorithms and therapeutic interventions that could be administered before lethal metastatic disease erupts. During the past year, we published these findings in *Nature Cell Biology*, where it received a lot of press. This manuscript is attached as **Appendix 2.**

Task 2a-c and Task 3a-f

During FY4, we followed up our previously published work (Ubellacker, et al., *Breast Cancer Res*. 2017) to understand the mechanisms by which bisphosphonates generate tumor-suppressive bone marrow cells. In the year 3 progress report, we had reported that the bisphosphonate, zoledronic acid (ZA), modulates hematopoietic myeloid/osteoclast progenitor cell (M/OCP) lineage potential to render the bone marrow metastasis-suppressive. We learned that granulocyte-colony stimulating factor (G-CSF) promotes ZA resistance by re-directing M/OCP differentiation. However, we still did not understand mechanisms by which this occurred and were lacking clinical correlatives. During the past year, we worked to complete this story (please note that the following contains excerpts published as Ubellacker, et al., Cancer Research, 2018).

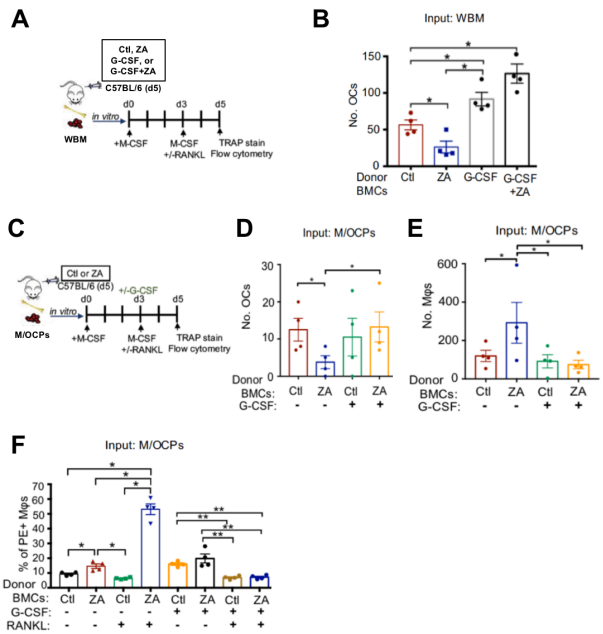

Figure 16. G-CSF counteracts ZA's ability to push differentiation of myeloid/osteoclast progenitors toward phagocytic macrophages (**A**) Experimental scheme for *in vitro* osteoclast differentiation assay using bone marrow from Ctl-, ZA-, G-CSF- or ZA+G-CSF-treated C57BL/6 donors (**B**) Quantification of osteoclasts (OC, TRAP+, multinucleated cells) at endpoint (d5) of *in vitro* osteoclast differentiation assay with 1,000 WBM per well Ctl, ZA, G-CSF or ZA+G-CSF treated C57BL/6 donors (n=4 donor samples/cohort; representative of 3 biological replications). (**C**) Experimental scheme for *in vitro* osteoclast differentiation assay using bone marrow from Ctl- or ZA-treated C57BL/6 donors that were subsequently treated with Ctl or recombinant hG-CSF *in vitro* at d3 (**D**) Quantification of osteoclasts (OC, TRAP+, multinucleated cells) at endpoint (d5) of *in vitro* osteoclast differentiation assay with 250 M/OCPs per well from Ctl or ZA treated C57BL/6 donor mice; M/OCPs were treated *in vitro* with RANKL ± G-CSF (n=4 donor samples per cohort; representative of 3 biological replications). (**E**) Flow cytometric quantification of macrophages (Cd11b+/F4/80 MHCII+) at end point of *in vitro* OC differentiation assay (d5) using sorted M/OCPs from Ctl or ZA treated C57BL/6 mice; M/OCPs were subsequently treated *in vitro* with M-CSF and RANKL ± G-CSF (n=4 donor samples per cohort; representative of 3 biological replications). (**F**) Percent of phycoerythrin (PE)-positive M/OCP-derived macrophages (Cd11b+ F4/80+ MHCII+) at end point (d5), indicating phagocytosis of Did-Cm (PE)-labeled B1 tumor cells (n=4 donor samples per cohort, representative of 3 biological replications).Error bars represent mean ± SEM; two-tailed t-tests (unpaired) were used to determine statistical significance, *p<0.05, **p<0.01

We learned that GCSF counteracts the ability of ZA to push differentiation of myeloid/osteoclast progenitors toward phagocytic macrophages. Our results thus far established that ZA alters the lineage potential of M/OCPs and renders them tumor-suppressive, while G-CSF mediates resistance to their tumor-suppressive effect. We therefore wished to know if G-CSF alters the lineage potential of the M/OCP population.

We first isolated WBM from Ctl-, ZA-, G-CSF, and ZA+G-CSF-treated mice and then treated the cells *in vitro* with MCSF and RANKL (**Fig. 16A**). As we repeatedly observed, in the absence of G-CSF, WBM from the ZA-treated cohort gave rise to significantly fewer osteoclasts than those from the control cohorts (**Fig. 16B**). However, WBM from G-CSF-treated animals gave rise to significantly more osteoclasts, even in the context of ZA treatment (**Fig 16B**).

We also isolated M/OCPs from Ctl- or ZA- treated mice and then treated the cells *in vitro* with M-CSF and RANKL in the presence or absence of G-CSF (**Fig. 16C**). In the presence of G-CSF, M/OCPs from both Ctl- and ZA-treated mice gave rise to increased numbers of osteoclasts and decreased numbers of macrophages *in vitro* relative to M/OCPs in the absence of G-CSF (**Fig 16D, E, and Supplementary Figure S5A, S5B from Ubellacker, et al., Can Res, 2018, Appendix 3**).

Our RNAseq analyses of M/OCPs from Ctl and ZA-treated mice had suggested that ZA induces transcriptional changes consistent with monocyte/macrophage lineage bias. Therefore, to test potential functional consequences of altered M/OCP lineage potential, we added fluorescently labeled B1 tumor cells to the cultures resulting from M/OCP differentiation under various conditions, thus enabling us to assess macrophage phagocytic capacity by scoring their uptake of fluorescence. In the absence of G-CSF, macrophages derived from M/OCPs of ZA-treated mice had significantly enhanced phagocytic capacity relative to those from Ctl-treated mice, irrespective of adding RANKL to the culture (**Fig 16F**). In contrast, G-CSF significantly decreased the phagocytic capacity of the resulting culture from ZA-treated M/OCPs in both the undifferentiated (without RANKL) and differentiated (with RANKL) cultures (**Fig 16F**). Consistent with the phagocytic phenotype, numbers of F4/80 MHCII+ macrophages in the bone marrow of ZA-treated mice was ~3-fold higher than in the control cohort, and G-CSF prevented this increase (**See Supplementary Figure S5C from Ubellacker, et al., Can Res, 2018, Appendix 3**).

Collectively, these findings suggested that G-CSF counteracts the effect of ZA on M/OCP function and lineage potential at least in part by preventing ZA from inducing M/OCP differentiation toward phagocytic macrophages. Moreover, these results provide additional evidence to suggest an association between lineage potential and the tumor-inhibitory function of the bone marrow.

The results from our pre-clinical metastasis models thus far indicated that the status of the bone marrow at the time metastatic tumor cells encounter it has a profound influence on metastatic success. As such, we wanted to gain insights into how the whole bone marrow hematopoietic microenvironment is affected by ZA and how G-CSF may alter the ZA signature. We therefore characterized transcriptional programs (RNA-seq) on whole bone marrow from mice treated with Ctl, ZA, G-CSF, or combination ZA+G-CSF (GSE108250). We first analyzed the RNA-seq data by identifying enriched gene ontology processes within the lists of DEGs from each treatment condition (ZA, G-CSF, or ZA+G-CSF) as compared to Ctl-treated bone marrow (**See Supplementary Figure S6A-C, Supplementary Tables S3A-F from Ubellacker, et al., Can Res, 2018**). In the ZA-treated cohort, significantly enriched processes were related primarily to metabolic process whereas in the G-CSF-treated cohorts, as well as in the ZA+G-CSF-treated cohorts, significantly enriched processes were dominated by immune processes (**Supplementary Figure S6C from Ubellacker, et al., Can Res, 2018, Appendix 3**).

Figure 6

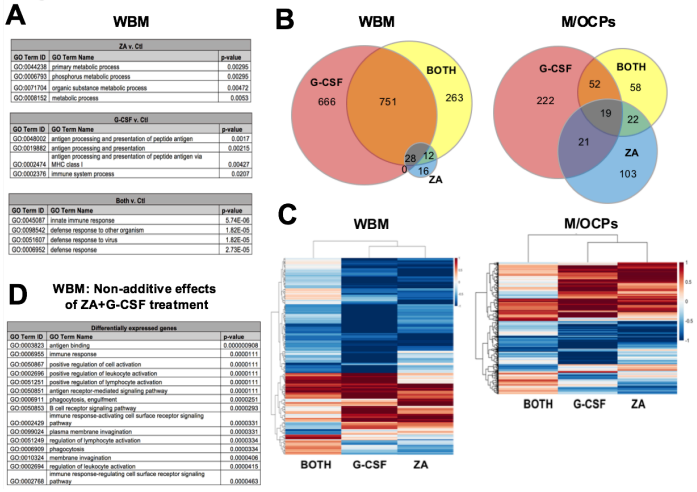

Figure 17. Bone marrow transcriptome and gene ontology processes that correlate with function (A) Table of enriched gene ontology categories from each indicated cohort of whole bone marrow as compared to control using the top 200 significant differentially expressed genes (as ordered by absolute log2 fold change; modified BH adjusted p-value less than 0.01) A list of the top 15 statistically enriched gene ontology (GO) terms for biological processes was generated using g:profiler. Revigo (http://revigo.irb.hr/) was used to simplify the GO output using an algorithm that relies on semantic similarity measures to identify the most representative subset of the terms. **(B)** Venn-Diagrams for distinct and non-distinct differentially expressed genes in the bone marrow (left) or M/OCPs (right) from mice treated with ZA (blue), G-CSF (red) or ZA+G-CSF ("Both", yellow), as normalized to Ctl-treated bone marrow or M/OCPs (modified BH adjusted p-value less than 0.01). **(C)** Heatmap of expression levels of genes identified from a regression analysis of the interaction between G-CSF and ZA effects on gene expression for whole bone marrow (left) or M/OCPs (right). Individual sample expression levels are shown for genes with a modified BH adjusted p-value of less than 0.01 from the regression. Values represent normalized counts after centering on the mean expression levels of the control samples and scaling to the range of gene expression across all samples (so that -1 represents the lowest expression level for all samples and 1 the highest). **(D)** Table of enriched gene ontology categories for genes for which the simultaneous effects of G-CSF and ZA treatment on expression were not additive in a comparative analysis model for whole bone marrow. Categories for each indicated cohort were compared to control using the non-additive genes (as ordered by absolute log2 fold change; modified BH adjusted p-value less than 0.01 A list of the statistically enriched gene ontology (GO) terms for biological processes was generated using the methods described in (A)).

A global analysis of gene expression differences between each of the 3 treatment cohorts (ZA, G-CSF, and ZA+G-CSF) and the control cohort (Ctl) provided insights into the effect size of each treatment on WBM and M/OCPs. For WBM, the comparisons identified 56, 1,445 and 1,054 DEGs (modified BH adjusted p-value <0.01) in the ZA, G-CSF, and ZA+G-CSF cohorts, respectively (**Fig. 17A**). 779 DEGs were common to both the G-CSF and ZA+G-CSF comparisons, only 28 of which were also shared with the ZA comparison (**Fig. 17A**). The 28 DEGs that were affected by all 3 treatments were the only DEGs shared between the ZA and ZA+G-CSF comparisons (**Fig. 17A**). Importantly, 16 DEGs were affected exclusively by ZA treatment (i.e., not identified in the combined treatment comparison) and included genes involved in phagocytosis such as *Slc15a4, Usp37,* and *Ipo13* (Figure 6A and Supplementary Table S4A). Interestingly, ~25% of the DEGs resulting from combination ZA+G-CSF were unique to that treatment cohort (**Fig. 17A**).

In the M/OCPs, 165 DEGs resulted from ZA treatment, 314 from G-CSF treatment, and 151 from combination ZA+G-CSF (**Fig. 17A**). As observed with WBM, a number of DEGs (~38%) were unique to the combination treatment. 103 DEGs were affected exclusively by ZA treatment (**Fig. 17A**). Interestingly, *Mapk8ip2* was one of the most significantly up-regulated DEGs in the ZA-treated cohort ($p=3.39x10^{-14}$) but was down-regulated in both G-CSF-treated ($p<8.48x10^{-4}$), and ZA+G-CSF-treated cohorts ($p=4.31x10^{-6}$). *Mapk8ip2* is involved in monocyte differentiation into macrophages when activated (**See Supplementary Table S5A from Ubellacker, et al., Can Res, 2018**). These analyses revealed that both G-CSF and ZA significantly and uniquely affect transcriptional programs in the WBM and that combined treatment yields yet a different transcriptional profile from either treatment alone. Moreover, ZA treatment had a larger impact on M/OCPs

than on WBM, while G-CSF appeared to dominate the effect on WBM.

We next considered the transcriptional effect sizes that we had observed with each treatment and the fact that ZA treatment generated metastasis-suppressive marrow while G-CSF alone had no effect on metastatic burden, yet G-CSF induced resistance to ZA and increased metastatic burden in the context of ZA treatment. In doing so, we speculated that ZA and G-CSF either affect the marrow in opposing directions or that the effects of combination treatment cannot be explained by contributions of either treatment alone. Our comparative analysis revealed that the DEGs upon combination treatment were not equivalently significant in either the ZA or G-CSF cohorts (**Fig. 17A**). In other words, none of these genes was expressed in an opposing manner. Indeed, 263 DEGs were unique to WBM and 58 genes unique to the M/OCP population in the ZA+G-CSF cohorts (**Fig. 17A**). Hence, we employed a regression approach with an interaction term and identified genes for which the effects of G-CSF and ZA statistically interact (**Fig. 17B**). GO analysis of the non-additive genes from WBM revealed processes significantly enriched by the combination treatment that described the difference in response to ZA in the presence of G-CSF (**Fig. 17C**). The enrichment list represents gene sets that were either enhanced or ablated relative to ZA alone, or newly emerging with combination treatment. Of these, "immune response" and "phagocytosis" were particularly intriguing to us, as these were predominantly suppressed by combination treatment. For example, a number of genes involved in antigen processing and lymphocyte activation, including *B2m, Vav2*, and a number of histocompatibility genes (*H2-K1, H2-D1, H2-Q5, H2-Q7*) were uniquely suppressed with ZA+G-CSF combination treatment relative to Ctl treatment (**See Supplementary Table S6A from Ubellacker, et al., Can Res, 2018**). Moreover, *Axl*, which suppresses myeloid cell immune function and dampens NK cell activity (37), was significantly suppressed by ZA treatment (log2(Fold Change)= -1.20, $p=1.25x10^{-4}$) but significantly enhanced with ZA+G-CSF treatment (log2(Fold Change)=1.68, $p=2.7x10^{-5}$) (**See Supplementary Table S6A from Ubellacker, et al., Can Res, 2018**). Together with our pre-clinical modeling, these analyses indicated that in the marrow of animals treated with combination ZA + G-CSF, the transcriptional effects of ZA are negated and/or significantly changed by G-CSF in a manner that associates with metastatic progression.

Our pre-clinical data established that G-CSF mediates resistance to ZA, and in fact, ZA+G-CSF combination treatment had unexpected effects on the metastatic microenvironment, resulting in enhanced metastasis relative to ZA treatment alone. Hence, we sought to understand if patient plasma G-CSF levels correlate with response to ZA. In the clinical setting, bisphosphonates have suggested benefit, as demonstrated by results from a meta-analysis in which patients who had received adjuvant bisphosphonate treatment observed a significant reduction in breast cancer recurrence in the bone. Nevertheless, responses have been limited for unknown reasons and biomarkers that can be used to guide treatment decisions are lacking.

We analyzed patient plasma samples (n=392) from the AZURE clinical trial in which women with stage II/III breast cancer were randomized to receive standard systemic treatment (>95% of the patients received chemotherapy) with or without adjuvant ZA (**Figure 18A**). In the AZURE trial, postmenopausal (natural or induced with ovarian suppression) patients observed a significant decrease in overall breast cancer recurrence. Importantly, primary G-CSF prophylaxis was not used in these patients. We verified that the magnitude of effect of ZA in reducing the development of bone metastasis

Figure 7

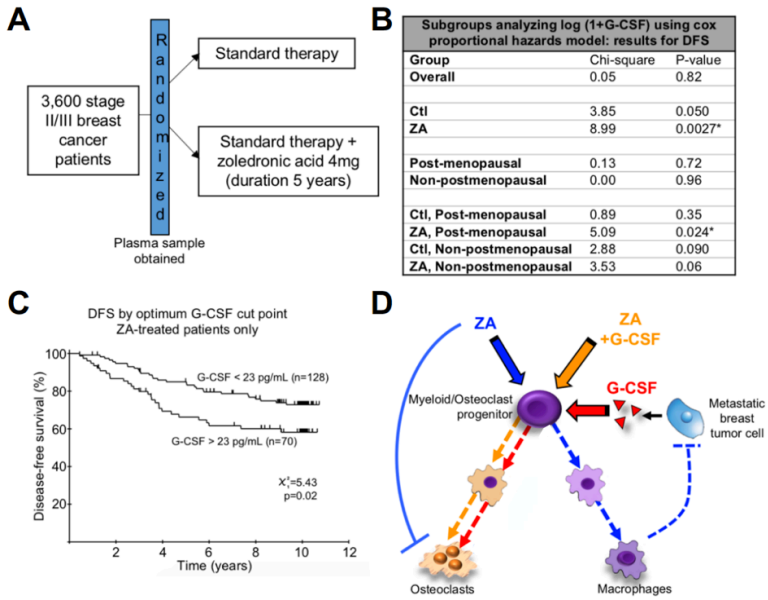

Figure 18. High plasma G-CSF correlates with worse outcome for breast cancer patients treated with adjuvant ZA

(**A**) AZURE clinical trial randomization scheme (Coleman et al., 2014). (**B**) Cox proportional hazards model analysis of subgroup from AZURE trial (n=392) for DFS by Ctl and ZA cohorts, menopausal status, and by menopausal status for treatment group; *p<0.05. (**C**) Disease-free survival (DFS) outcome (derived from cut point analysis—see STAR methods) defined in terms of number of DFS events avoided/saved over the 10-year period post randomization among ZA-treated patients; optimal cut point was at 23 pg/mL for G-CSF. **(D)** Proposed model. ZA inhibits mature osteoclasts and also increases the numbers of M/OCPs in the BM, altering their gene expression profile to drive them toward tumor suppressive phagocytic macrophages. Tumor-derived or systemic G-CSF counteracts the effects of ZA by driving the lineage potential of M/OCPs toward osteoclasts.

at any time during the 10-year follow-up in our patient subset was similar to that of the overall trial (trial total n=3,360, hazard ratio (HR)=0.81, 95% confidence interval (CI) 0.68-0.97 (39); our subset n=392, HR=0.89, 95% CI 0.62-1.3) (**Figure 18B**).

We utilized an analytical approach that adjusts for an optimal plasma G-CSF concentration cut point and enables us to accurately determine DFS and significance levels in an unbiased fashion (**See Methods, Figure S7A-D from Ubellacker, et al., Can Res, 2018**). Based on these previously published methods, we determined that a plasma G-CSF concentration of 23 pg/mL was the optimum cut-point for assessing disease-free survival (DFS) events in ZA-treated patients.

Patients receiving adjuvant ZA whose plasma G-CSF levels were > 23 pg/mL at the time of randomization had significantly reduced DFS when compared with patients with plasma G-CSF levels < 23 pg/mL (p adjusted=0.02) as assessed over a 10-year period (**Figure 18C**). However, in the cohort that did not receive ZA, plasma G-CSF levels did not predict a significant difference in DFS (**Supplementary Figure S7B from Ubellacker, et al., Can Res, 2018**). Cox model analysis demonstrated that the relationship between high plasma G-CSF levels and DFS in ZA-treated patients could not be explained by imbalances in other key prognostic variables, namely number of involved lymph nodes affected, tumor size (T stage), and breast cancer receptor status (ER/PR/Her2). Moreover, in support of the retrospective analyses demonstrating that post-menopausal patients observed significant benefit with adjuvant ZA, plasma G-CSF levels were significantly lower in post-menopausal patients than pre-menopausal patients in our cohort ($p=1.14x10^{-4}$).

This work revealed that bone marrow hematopoietic cell states, particularly M/OCP lineage potential, have a profound impact on breast cancer bone metastasis and that the hematopoietic microenvironment, which serves as a niche for disseminated tumor cells, can be modulated by bone-targeting agents and cytokines to alter disease outcome. Specifically, the bisphosphonate, ZA, directs M/OCP lineage potential toward tumor-suppressive macrophages and prevents metastatic growth in the bone; systemic or tumor-derived G-CSF promotes resistance to the metastasis-suppressive effect of ZA by skewing M/OCP differentiation toward osteoclasts and away from the phagocytic myeloid lineage (**Figure 18D**).

Further studies based on results of the gene expression profiling under these various conditions may reveal factors, pathways, and processes that are necessary and/or sufficient for the tumor inhibitory function of the bone marrow. Some of the newly identified gene products presented here may be considered as candidate targets for future combination therapies and pre-clinical research. Likewise, additional work will be necessary to determine the translatability of G-CSF as a biomarker for selection of patients who should/should not receive ZA treatment, given that many patients also receive G-CSF at the time of chemotherapy and adjuvant ZA treatment (the patients in our study did not receive primary G-CSF prophylaxis and less than 10% received secondary G-CSF treatment). Identifying biomarkers that better stratify patient risk and responses to ZA hold the potential of using bone-modulating drugs to improve patient outcomes.

We published this the entirety of this work in *Cancer Research*, and it is attached as **Appendix 3**

Task 1h, 2e, 3g

We held a project retreat that included members of the lab, one of our clinical collaborators, one of our scientific colleagues/collaborators, and two of the DF/HCC breast cancer research/patient advocates. The retreat was held over a 2-day period in which investigators gave formal presentations of their work in progress and we had dedicated discussion time for feedback and exchange of ideas.

C. What opportunities for training and professional development has the project provided?

Funds from this project enabled postdoctoral associates and the graduate student to attend international scientific conferences, where they gave posters and oral presentations.

D. How were the results disseminated to communities of interest?

1. During the past year, we had a number of opportunities to interact with the Dana Farber/Harvard Cancer Center breast cancer research and patient advocates.
2. I was invited to present our work to the DF/HCC Breast Cancer Advocate group during their monthly meeting.
3. Two of the advocates attended our retreat where they gave presentations about advocacy and patient involvement in research.
4. We published a number of research papers and review articles (please see Accomplishments above)
5. Our work was featured in various news articles where funding from BCRP was acknowledged

E. What do you plan to do during the next reporting period to accomplish the goals?

Task 1 (per SOW):

a. Identify human breast cancer barcoded DTCs that convert to malignancy in xenograft mouse model of metastasis to bone. *We plan to continue our investigation in this line of experimentation*

f. Analyze data and build prediction signatures. *Following the near completion of tasks a-e, we will build these signatures*

g. Establish predictive power of molecular/cellular signatures using other cell lines and human tumor specimens. *We are beginning to identify other cell lines and will test these in the coming year.*

h. Meet with project team to discuss findings and potential for clinical translation. *We will continue to meet as we do each year.*

Task 2 (per SOW):

d. Determine response of various barcoded DTCs from human and mouse and human DTC samples to pro-and anti-tumorigenic factors in vivo. *Cells identified in Task 1 will then be used in these assays in the coming year.*

e. Meet with project team to discuss findings and potential for clinical translation. *We will continue to meet as we do each year.*

Task 3 (per SOW):

a. Determine ability of various drugs/compounds to prevent malignant conversion of human and mouse DTCs in vitro. *Work under this task is nearly completed. Should we identify any new therapeutic candidates during the course of our investigations in Tasks 1 and 2, we will test them in the coming year.*

4. IMPACT: This component is used to describe ways in which the work, findings, and specific products of the project have had an impact during this reporting period. Describe distinctive contributions, major accomplishments, innovations, successes, or any change in practice or behavior that has come about as a result of the project relative to:

- the development of the principal discipline(s) of the project;
- other disciplines;
- technology transfer; or
- society beyond science and technology.

What was the impact on the development of the principal discipline(s) of the project?

****Last year (FY3), we reported that CDK4/6 inhibitors increase anti-tumor immunity and that combination therapy with CDK4/6 inhibitor and an immune checkpoint blockade drug (anti-PD-L1) led to durable response. Based on our findings, a phase 1b trial of Abemaciclilb (CDK4/6 inhibitor) and Pembrolizumab (anti-PD-1) was initiated (clinicaltrials.gov NCT02779751) for patients with metastatic hormone receptor positive breast cancer. Results from the 24-week analysis reported at ASCO indicated 28.6% objective response rate, a significant improvement over standard therapies (Tolaney S et al. *ASCO* 2018).**

What was the impact on other disciplines?

Nothing to report

What was the impact on technology transfer?

We are discussing possibilities for various IP opportunities with our Research Ventures and Licensing office

What was the impact on society beyond science and technology?

Nothing to report

5. CHANGES/PROBLEMS: The Project Director/Principal Investigator (PD/PI) is reminded that the recipient organization is required to obtain prior written approval from the awarding agency Grants Officer whenever there are significant changes in the project or its direction. If not previously reported in writing, provide the following additional information or state, "Nothing to Report," if applicable:

- Changes in approach and reasons for change.
- Actual or anticipated problems or delays and actions or plans to resolve them.
- Changes that have a significant impact on expenditures.
- Significant changes in use or care of human subjects, vertebrate animals, biohazards, and/or select agents.

Changes in approach and reasons for change

Nothing to report

Actual or anticipated problems or delays and actions or plans to resolve them

Nothing to report

Changes that had a significant impact on expenditures

Nothing to report

Significant changes in use or care of human subjects, vertebrate animals, biohazards, and/or select agents

Nothing to report

6. PRODUCTS: List any products resulting from the project during the reporting period.

Publications:

1. Olive JF, Qin Y, DeCristo MJ, Laszewski T, Greathouse F, McAllister SS. Accounting for tumor heterogeneity when using CRISPR-Cas9 for cancer progression and drug sensitivity studies. ***PLoS One*** 2018 Jun 13; 13(6):e0198790. PMID: 29897959.

2. Ubellacker JM, Baryawno N, Severe N, DeCristo MJ, Sceneay J, Hutchinson JN, Haider MT, Rhee CS, Qin Y, Gregory WM, Garrido-Castro AC, Holen I, Brown JE, Coleman RE, Scadden DT, McAllister SS. Modulating bone marrow hematopoietic lineage potential to prevent bone metastasis in breast cancer. ***Cancer Res.*** 2018 Sep 15;78(18):5300-5314. [Epub ahead of print July 31, 2018]. PMID: 30065048

3. Castaño Z, San Juan BP, Spiegel A, Pant A, DeCristo MJ, Laszewski T, Ubellacker JM, Janssen SR, Dongre A, Reinhardt F, Henderson A, Garcia del Rio A, Gifford AM, Herbert ZT, Hutchinson JN, Weinberg RA, Chaffer CL, McAllister SS. IL-1β inflammatory response driven by primary breast cancer prevents metastasis-initiating cell colonization. ***Nat Cell Biol***. 2018 Sep;20(9):1084-1097. PMID: 30154549.

4. Lee JJ, van de Ven RAH, Zaganjor E, Ng MR, Barakat A, Demmers JJPG, Finley L, Gonzalez Herrera KN, Hung YP, Harris IS, Jeong SM, Danuser G, McAllister SS, Haigis MC. Inhibition of epithelial cell migration and

Src/FAK signaling by SIRT3. ***Proc Natl Acad Sci USA***. 2018 Jul 3; 115(27):7057-7062. PubMed PMID: 29915029.

Presentations:

2017 CDK4/6 Inhibition Triggers Anti-Tumor Immunity / Breast Oncology Seminar Series
DF/HCC

2017 Systemic and microenvironmental determinants of cancer progression and metastasis / Special Session
Tumor Microenvironment Town Hall Meeting; AACR Annual Meeting, Washington, DC

2018 Marrow Matters, and other breast cancer related issues / Seminar Series
Hematology Division, BWH

2018 Pharmacological and Physiological Modulators of Response to Immunotherapies in Breast cancer / Breast Immuno-Oncology Program, DF/HCC

2018 Physiological Processes that Affect Breast Cancer Progression and Therapeutic Response / Seminar Series; Seminars in Oncology, DFCI

2018 Physiological Processes that Affect Breast Cancer Progression and Response to Therapy / Seminar Series
Department of Pathology and Laboratory Medicine, Boston University, Boston, MA

2018 Pharmacological and Physiological Processes that Affect Response to Immunotherapy / Symposium
AACR Special Conference on Tumor Immunology and Immunotherapy Meeting; Miami, FL

- **Technologies or techniques**

  Nothing to report

- **Inventions, patent applications, and/or licenses**

US 62/519,312 Implications for Zoledronic Acid In Bone Marrow Cell Mobilization and Breast Cancer Metastasis; Provisional

US 62/683,225 Single Cell Cloning Approaches for Biological Studies; Provisional

- **Other Products**

  Nothing to report

7. PARTICIPANTS & OTHER COLLABORATING ORGANIZATIONS

Provide the following information on participants:

What individuals have worked on the project?

Name:	Sandra McAllister
Role:	Principal Investigator
Nearest person month worked:	10

Contribution to project:	Dr. McAllister oversees all aspects of the project and supervises personnel on the project
Name:	Gregory Goreczny
Role:	Postdoctoral Fellow
Nearest person month worked:	6
Contribution to project:	Dr. Goreczny has performed work on molecular biological and RNAseq methods for the barcoding project (Task 1)
Name:	Qiuchen Guo
Role:	Postdoctoral Fellow
Nearest person month worked:	6
Contribution to project:	Dr. Guo has performed work on method optimization for the barcoding project (Task 1) and testing drugs that inhibit outgrowth of otherwise indolent tumors (Task 3)
Name:	Milos Spasic
Role:	Postdoctoral Fellow
Nearest person month worked:	2
Contribution to project:	Dr. Spasic has performed work on molecular biological aspects of the barcoding project (Task 1) and effects on bone metastasis (Task 2)
Name:	Anna Molineaux
Role:	Research Scientist/Lab Manager
Nearest person month worked:	3
Contribution to project:	Ms. Molineaux provides technical support to the project
Name:	Tyler Laszewski
Role:	Research Technician
Nearest person month worked:	7
Contribution to project:	Mr. Laszewski performs and supports all animal work associated with the project
Name:	Amanuel Bizuayehu
Role:	Research Technician
Nearest person month worked:	1
Contribution to project:	Mr. Bizuayehu performed work to support animal work associated with the project and on canine mammary carcinoma samples

Has there been a change in the active other support of the PD/PI(s) or senior/key personnel since the last reporting period?

No.

Since the activation of this award the following grants have ended:

Nothing to report

What other organizations were involved as partners?

Organization Name: Broad Institute of Harvard and MIT
Location of Organization: Cambridge, Massachussetts
Partner's contribution to the project: Scientific collaboration

Organization Name: Harvard School of Public Health
Location of Organization: Boston, Massachussetts
Partner's contribution to the project: Scientific collaboration – computational biology and data analysis

Organization Name: Dana-Farber Cancer Institute
Location of Organization: Boston, Massachussetts
Partner's contribution to the project: Scientific collaboration

8. SPECIAL REPORTING REQUIREMENTS:

None

9. APPENDICES: Please see attached appendices including:

Appendix 1. JF Olive, et al., 2018; Accounting for tumor heterogeneity when using CRISPR-Cas9 for cancer progression and drug sensitivity studies. ***PLoS One***

Appendix 2. Z Castaño Z, et al., 2018; IL-1β inflammatory response driven by primary breast cancer prevents metastasis-initiating cell colonization. ***Nat Cell Biol***.

Appendix 3. JM Ubellacker, et al., 2018; Modulating bone marrow hematopoietic lineage potential to prevent bone metastasis in breast cancer. ***Cancer Res.***

PLOS ONE

RESEARCH ARTICLE

Accounting for tumor heterogeneity when using CRISPR-Cas9 for cancer progression and drug sensitivity studies

Jessica F. Olive[1,2☯], Yuanbo Qin[1,2☯], Molly J. DeCristo[1,2], Tyler Laszewski[1], Frances Greathouse[1], Sandra S. McAllister[1,2,3,4]*

1 Department of Medicine, Division of Hematology, Brigham and Women's Hospital, Boston, Massachusetts, United States of America, **2** Department of Medicine, Harvard Medical School, Boston, Massachusetts, United States of America, **3** Broad Institute of Harvard and MIT, Cambridge, Massachusetts, United States of America, **4** Harvard Stem Cell Institute, Cambridge, Massachusetts, United States of America

☯ These authors contributed equally to this work.
* smcallister1@bwh.harvard.edu

Citation: Olive JF, Qin Y, DeCristo MJ, Laszewski T, Greathouse F, McAllister SS (2018) Accounting for tumor heterogeneity when using CRISPR-Cas9 for cancer progression and drug sensitivity studies. PLoS ONE 13(6): e0198790. https://doi.org/10.1371/journal.pone.0198790

Editor: Aamir Ahmad, University of South Alabama Mitchell Cancer Institute, UNITED STATES

Received: March 19, 2018

Accepted: May 28, 2018

Published: June 13, 2018

Data Availability Statement: All relevant data are within the paper and its Supporting Information files.

Funding: Financial support provided by NIH-NCI-R01CA166284 (https://www.cancer.gov/about-nci), Presidential Early Career Award for Scientists and Engineers and the Department of Defense BCMRP Era of Hope Scholar Award W81XWH-14-1-0191 (http://cdmrp.army.mil/bcrp/). The funders had no role in study design, data collection and

Abstract

Gene editing protocols often require the use of a subcloning step to isolate successfully edited cells, the behavior of which is then compared to the aggregate parental population and/or other non-edited subclones. Here we demonstrate that the inherent functional heterogeneity present in many cell lines can render these populations inappropriate controls, resulting in erroneous interpretations of experimental findings. We describe a novel CRISPR/Cas9 protocol that incorporates a single-cell cloning step prior to gene editing, allowing for the generation of appropriately matched, functionally equivalent control and edited cell lines. As a proof of concept, we generated matched control and osteopontin-knockout Her2$^+$ and Estrogen receptor-negative murine mammary carcinoma cell lines and demonstrated that the osteopontin-knockout cell lines exhibit the expected biological phenotypes, including unaffected primary tumor growth kinetics and reduced metastatic outgrowth in female FVB mice. Using these matched cell lines, we discovered that osteopontin-knockout mammary tumors were more sensitive than control tumors to chemotherapy *in vivo*. Our results demonstrate that heterogeneity must be considered during experimental design when utilizing gene editing protocols and provide a solution to account for it.

Introduction

CRISPR/Cas9 is a useful tool that has expanded our ability to define the role of particular factors in biological processes, including cancer biology [1, 2]. Oftentimes, studies employ the CRISPR/Cas9 system to generate loss- or gain-of-function mutations in a gene of interest and then look for a corresponding phenotypic change, indicating whether or not the targeted gene is necessary and/or sufficient for a particular behavior. Widely used protocols that employ CRISPR/Cas9 to generate genetically modified cell lines often require a subcloning and/or selection step in order to isolate a particular subpopulation in which the gene of interest was

analysis, decision to publish, or preparation of the manuscript.

Competing interests: The authors have declared that no competing interests exist.

efficiently edited [3–7]. In order to correctly define the role that particular factors play, for example in cancer models, it is essential to use appropriately matched controls to compare to the edited subclone(s); however, such comparisons can be complicated by the widespread heterogeneity present in tumors and cancer cell lines derived from them.

The relevance and pervasiveness of genetic and functional heterogeneity within most cancer types has become particularly appreciated over the past decade [8–10]. It is now known that even supposedly clonal cancer cell lines are composed of subpopulations with widely differing phenotypes and functional characteristics [11–13]. Genetic and phenotypic heterogeneity has also been observed in other disease models, including bacterial antibiotic resistance and in the evolution of antiviral resistance [14–17].

Due to the inherent functional heterogeneity observed in most cancer cell lines, therefore, subcloning and selection steps employed in genetic editing protocols can render the parental population an inappropriate control, as its behavior may differ from that of the selected subclonal population prior to gene editing. For example, if the aim of a study is to evaluate whether a particular gene product (protein) is relevant for primary tumor formation, it is common practice to compare the tumorigenicity of a knockout cell line with that of the parental cell line. However, if the selected subclonal population has an inherently different tumorigenic potential than the bulk parental population, it would be possible to incorrectly conclude that the knockdown of the gene of interest was responsible for any functional differences that are observed in any given biological assay.

Here we report a modified CRISPR/Cas9 targeting strategy to create appropriately matched knockout (KO) and wild-type (WT) control mammary carcinoma cell lines. We used these cell lines for both proof-of-concept and discovery studies. Our results demonstrate that it is critical to generate appropriately matched control and knockout cell lines in order to accurately evaluate the relevance of a protein of interest to cancer cell behaviors.

Materials and methods

Cell lines

McNeu and Met-1 murine mammary carcinoma cells (kind gifts from Drs. Michael Campbell and Johanna Joyce, respectively) were cultured as previously described [18, 19]. Briefly, cells were cultured in DMEM (Gibco) media, supplemented with 10% fetal bovine serum (FBS) and 100 U/ml penicillin-streptomycin at 37˚C under 5% CO_2. Human MDA-MB-435 cells were a generous gift from Dr. Robert Weinberg and were cultured in DMEM:F12 (1:1; Gibco), supplemented with 10% fetal bovine serum and 100 U/ml penicillin-streptomycin at 37˚C under 5% CO_2. All cell lines were validated as mycoplasma-negative. Human cells were validated using short tandem repeat (STR) profiling (Molecular Diagnostics Laboratory at Dana-Farber Cancer Institute, Boston, MA). For mouse cells, the murine strain of origin was confirmed by short tandem repeat analysis (Bioassay Methods Group, NIST).

New gene editing protocol

Clonal subpopulations are generated from parental cell lines by sorting one single cell per well into 96-well plates using a FACSAria II cell sorter (BD Bioscience). Single cell-derived populations are subsequently allowed to proliferate for expansion. A single expanded clone is used for both control and co-transfection with the Cas9/GFP and sgRNA vectors. Select cell populations were seeded into 12-well plates overnight before transfection with 500ng pCas9_GFP and 500ng sgRNA expressing plasmids using FugeneHD (Roche). 48 hours after transfection, successfully transfected single cells are isolated by FACS sorting for GFP-positivity using a FACSAria II cell sorter (BD Bioscience) followed by recovery and expansion in 12-well plates

for 2–3 days. At confluency, cells were collected for a second round of FACS sorting and single GFP-negative cells were sorted into individual wells in a 96-well plate to ensure that random Cas9/GFP integration did not occur. Following clonal expansion editing is validated using Sanger sequencing and phenotype verification is performed.

To generate luciferase/GFP-positive populations, cells were infected with lentivirus generated from pLV-Luc-IRES-GFP viral plasmids (a generous gift from Dr. Robert Weinberg's lab) and then sorted for GFP-positive populations.

Vector construction

The human codon-optimized Cas9 expression plasmid pCas9_GFP was a gift from Kiran Musunuru (Addgene plasmid # 44719). The sgRNA targeting mouse OPN exon 2 (5'-GTGAT TTGCTTTTGCCTATT-3') driven by human U6 promoter was synthesized at Eurofin.

Evaluating target site modification by Sanger sequencing

OPN gene fragments were amplified with the primers OPN-F (5'-GACTTGGTGGTGATCT AGTGG-3') and OPN-R (5'-GCCAGAATCAGTCACTTTCAC-3') using Phire Animal Tissue Direct PCR Kit (Thermo Scientific). The resulting PCR products were then submitted for sanger sequencing (Macrogen USA).

Animals and tumor studies

Female FVB/NJ mice 7 weeks of age were purchased from Jackson Labs (stock no. 001800). NOD/SCID mice were maintained in-house under aseptic sterile conditions. All experiments were conducted in accordance with regulations of the Children's Hospital Institutional Animal Care and Use Committee (protocol 12-11-2308R), the MIT committee on animal care (protocol 1005-076-08), and Brigham and Women's Hospital animal care protocol committee (2017N000056). Mice were 8–9 weeks of age at the time of study initiation. All efforts were made to minimize animal suffering. Animal facility personnel monitored the animals daily, checking for levels of food, water, and bedding in each cage. Mice were also physically checked three times a week by the investigators. The basic animal maintenance included housing the mice in cages (five per cage) with sufficient diet, water and bedding and cages were cleaned and sanitized on a regular basis. Investigators strictly adhered to approved protocols for humane endpoints; if any animal became severely ill prior to an experimental endpoint, that animal would be euthanized. Humane endpoints were defined as follows: $\geq$20% weight loss, rough hair coat, jaundice and/or anemia, coughing, labored breathing, nasal discharge, neurological signs (frequent seizure activity, paralysis, ataxia), prolapse, self-induced trauma, any condition interfering with eating or drinking, excessive or prolonged hyperthermia or hypothermia, tumor size $\geq$1.5 cm^3 in volume. Animals were randomly assigned to treatment groups and no animals were excluded from analysis.

For tumor studies, murine mammary carcinoma cells were injected orthotopically, using a total of 10^5 or 10^6 McNeu cells, or 2.5×10^4 or 2.5×10^5 Met-1 cells implanted into the fourth mammary fat pad of 7–10 week old female FVB mice. Where indicated, either $1x10^5$ or $1x10^6$ cells of the McNeuA parental cell line were implanted subcutaneously. $2.5x10^5$ human MDA-MB-435 cells were injected subcutaneously into 8–10 week old female NOD-SCID mice. Thereafter, tumors were monitored and measured using calipers with volume calculated as $0.5(\text{length} \times \text{width}^2)$.

For the Met-1 metastasis assay, mice received tail vein injections with 10^6 cells of luciferase-labeled Met-1 cells suspended in 100 μl of sterile phosphate-buffered saline. MT-2 WT and OPN-KO clones express different levels of luciferase in vitro because they were labeled

separately. Therefore, we evaluated the in vitro luciferase expression levels of these cells at the start of the experiment, prior to IV injection, and used that reading to normalize the in vivo signals. Pulmonary metastases were monitored weekly by bioluminescent imaging using the Spectrum Imaging System and Living Image software (Caliper Life Sciences, Inc.). Prior to imaging, mice were intraperitoneally administered 150 mg/kg D-luciferin (Perkin-Elmer) and were anesthetized using isoflurane inhalation. Luminescent signal was detected for the regions of interest as radiance (p/sec/cm^2/sr) and analyzed using the Living Image Software Version 4.1 (Caliper Life Sciences). Lungs were fixed and stained using Hematoxylin/Eoisin and metastases were classified as multi- or single-focal and were counted manually on 3 separate sections spaced 50 microns apart per mouse. Total lung area was quantified using Cell Profiler and metastases counts were normalized total lung area.

Chemotherapy

For AC-T chemotherapy trials, 2.5×10^5 Met-1 Luc/GFP cells were injected into the mammary fat pad of 6–8-week-old female FVB mice. Doxorubicin (Teva), paclitaxel (Hospira), and cyclophosphamide (Sigma) were diluted in PBS for *in vivo* experiments. Mice were treated with two to four doses of 5 mg/kg doxorubicin, 10 mg/kg paclitaxel, and 120 mg/kg cyclophosphamide administered every two weeks. Doxorubicin was administered via retro-orbital injection, and paclitaxel and cyclophosphamide were administered via intraperitoneal injection.

For studies investigating the role of OPN in chemotherapeutic response, 2.5×10^4 WT or OPN KO tumor cells were injected into the mammary fat pad of 6–8-week-old female FVB mice. When established tumors reached 60–80 mm^3 in volume, treatment was initiated. Four treatment arms were included: vehicle control (PBS) on WT or OPN KO cohorts or one dose of paclitaxel (10 mg/kg), doxorubicin (5 mg/kg) and cyclophosphamide (120 mg/kg) by intraperitoneal injection (paclitaxel and cyclophosphamide) and retro-orbital injection (doxorubicin) on WT or OPN KO cohorts. Tumor growth was monitored using caliper measurements. Average tumor mass at sacrifice was measured and is presented as the average ± standard error of mean.

Osteopontin ELISAs and western blotting

To assess circulating secreted murine osteopontin (mOPN) or human osteopontin (hOPN) protein levels, whole blood was collected in EDTA-coated tubes (VWR) and centrifuged at 1.5xg for 8 minutes to isolate plasma. mOPN and hOPN concentrations were determined by ELISA according to manufacturer's instructions (R&D) and analyzed using a plate reader (Molecular Device).

To quantify secreted mOPN levels in conditioned medium, cells were grown to 80–90% confluence in growth medium containing 10% FBS. Then the medium was replaced with serum-free medium and was collected 24 hours later. mOPN levels in conditioned media were quantified by ELISA or western blotting.

Whole cell lysates were prepared following culture in the presence or absence of brefeldin A (used to prevent the secretion of OPN and ensure detection of protein expression). Cell lysates or concentrated conditioned medium were subjected to SDS-PAGE on 12% gels and then transferred onto a polyvinylidenedifluoride membrane, which was incubated with mouse anti-OPN (final dilution: 1:200, Clone AKm2A1, Santa Cruz Catalog # sc-21742, mouse monoclonal antibody raised against recombinant OPN of mouse origin, references with validation available on manufacturer's datasheet) antibody at 4C overnight. After being washed, membranes were incubated with horseradish peroxidase-conjugated anti-mouse IgG for 1 hour. The enzyme bound to OPN was visualized using the SuperSignal™ West Pico Chemiluminescent kit (ThermoFisher). The blot was then stripped and

incubated with rabbit anti-mouse β-actin antibody as a loading control (final dilution: 1:1000, Rockland Catalog # 600-401-886, rabbit polyclonal antibody raised against human beta-actin, references with validation available on manufacturer's datasheet).

Immunohistochemistry, immunofluorescence and microscopy

Formalin-fixed, paraffin embedded tissues were sectioned onto ProbeOn Plus microscope slides (Fisher Scientific) and immunohistochemistry was performed as described [20]. For immunohistochemistry studies, anti-OPN (final dilution: 1:200, Maine Biotechnology Services Catalog #MAB197P, mouse monoclonal antibody raised against recombinant OPN of human origin, [21]) or anti-e-Cadherin (final dilution: 1:100, Cell Signaling Technologies Catalog #3195T) were used and were detected using the Vector ABC kit (Vector Laboratories, Burlingame, CA, USA). For immunofluorescence, anti-OPN (final dilution: 1:50, Clone AKm2A1, Santa Cruz Catalog # sc-21742, mouse monoclonal antibody raised against recombinant OPN of mouse origin, references with validation available on manufacturer's datasheet) was used and was detected using a goat anti-mouse IgG AF549 conjugated secondary antibody (final dilution: 1:1000, Invitrogen Catalog # A11032, polyclonal, references with validation available on manufacturer's datasheet). Nuclei were counterstained with DAPI (Invitrogen). Images were captured with identical exposure and gain using a Nikon Eclipse N*i* microscope.

In vitro chemosensitivity studies

4,000 Met-1 cells were plated in quadruplicates in 96-well plates containing growth media. The next day, vehicle (PBS) or chemotherapy (doxorubicin: .33 nM—2.2 μM; paclitaxel: 14 μM–160 μM) was added to the plate and incubated for 72 hours. ATP levels were quantified as a surrogate measure for viability (CellTiter-Glo, Promega) using a luminometer (Perkin-Elmer).

Statistical analyses

Data are represented as mean ± SEM and analyzed by ANOVA, Student's t-test, and/or Mann-Whitney test as indicated using GraphPad Prism 7.0, unless otherwise stated. $P < 0.05$ was considered statistically significant. Error bars represent standard deviation unless otherwise indicated.

Results

Selection of Her2$^+$ and Estrogen receptor-negative mammary carcinoma models

We aimed to design an approach that would enable us to generate appropriately matched control and CRISPR/Cas9 knockout cell lines, while taking into account the inherent functional heterogeneity present in nearly all breast tumors and tumor-derived cancer cell lines. We hypothesized that results from studies employing standard CRISPR/Cas9 approaches, which often require a subcloning and/or selection step, would be confounded by subclonal functional heterogeneity.

As a proof of concept, we chose to study Osteopontin (OPN), a protein that we have studied previously and that is relevant for breast cancer metastasis [20, 22–28]. OPN plays an important role in metastasis and survival in many pre-clinical cancer studies, and is positively associated with metastasis as well as reduced progression-free and overall survival in breast cancer patients [27–29]. Additionally, OPN has been shown to play a role in chemoresistance in some cancer types [22, 24, 25, 30–32], but it is unclear whether this is also true of breast cancer.

Hence, we determined that the breast cancer models that we would employ must meet the following criteria: secretion of detectable levels OPN both *in vitro* and *in vivo*, capacity to form primary and metastatic tumors *in vivo*, evidence of heterogeneity, and responsiveness to chemotherapy.

Transgenic mice that specifically overexpress oncogenic proteins in the mammary fat pad are commonly employed both for the study of spontaneous breast tumors and as a source for murine breast cancer cell lines that can be allografted orthotopically in immunocompetent animals. In this study, we utilized two such murine breast cancer cell lines: McNeuA, a $HER2^+$ breast cancer cell line derived from a spontaneously arising mammary carcinoma in a MMTV-*neu* transgenic mouse [19], and Met-1, an estrogen receptor-negative (ER^-) breast cancer cell line derived from a mammary carcinoma in a MMTV-PyMT transgenic mouse (FVB/N-Tg(MMTV-PyVmT) [18].

Characterization of McNeuA and Met-1 cell lines demonstrated their potential as models for this study, as they secreted detectable levels of OPN in culture as measured by ELISA (Fig 1A). Both cell lines efficiently formed primary tumors following injection into FVB mice (Figs 1B and S1A). While both cell lines formed tumors that had an average mass of 2.3 g at the experimental end points (30 days for Met-1 and 90 days for McNeuA, or when tumors reached 1.5 mm^3, S1B Fig), the McNeuA tumors exhibited more variability in both their tumor incidence and final tumor mass.

In both models, the tumor bearing mice had significantly elevated plasma levels of OPN relative to cancer-free cohorts whereby average OPN levels were 8-fold and 15-fold higher in the McNeuA and Met1 tumor-bearing mice, respectively, at end stage (Fig 1C). Interestingly, plasma OPN levels positively correlated with the final tumor mass in mice bearing the McNeuA tumors (S1C Fig). Immunohistochemical analysis of the recovered tumors revealed intratumoral heterogeneity for the epithelial marker E-cadherin (Fig 1D).

Previous studies have demonstrated that both of these cell lines are capable of forming lung metastases [18, 19]. We were particularly interested in the Met-1 cell line, as women with metastatic ER^- breast cancer most often experience pulmonary metastases [33]. We confirmed that the Met-1 cells formed pulmonary metastases, with 4 of 5 mice experiencing increased metastatic burden (~15-300-fold increases) over the experimental time course (Figs 1E and S1D).

We next tested responsiveness of Met-1 mammary carcinoma to combination doxorubicin (A), cyclophosphamide (C), and paclitaxel (T) chemotherapy (AC-T), a standard of care chemotherapy regimen for breast cancer patients with ER^- negative disease. We first tested the sensitivity of Met-1 cells to doxorubicin and paclitaxel *in vitro* and performed an initial in vivo experiment to identify a therapeutically relevant, well-tolerated combinatorial dose. Cyclophosphamide, a pro-drug, requires activation into cytotoxic metabolites by liver enzymes in vivo and was therefore not tested *in vitro*. Treatment with both doxorubicin and paclitaxel significantly decreased viability of Met-1 cells *in vitro* (S1E and S1F Fig). *In vivo*, a neoadjuvant combination dose of doxorubicin (5 mg/kg), paclitaxel (10 mg/kg), and cyclophosphamide (120 mg/kg) was well tolerated (no weight loss; data not shown) and had a cytostatic effect on Met-1 tumor growth (Figs 1F and S1G).

To more closely emulate the clinical dosing regimen of AC-T chemotherapy, mice with Met1 mammary carcinoma were administered neoadjuvant AC-T every 2 weeks for 4 cycles. Interestingly, individual mice bearing Met-1 tumors exhibited differential responses to treatment, and in some cases, mice that initially experienced complete tumor regression eventually experienced local recurrence (Fig 1G).

Collectively, our analyses indicated that the McNeuA and Met-1 cell lines met our criteria of OPN secretion *in vitro* and *in vivo*, efficient formation of primary orthotopic tumors, and evidence of phenotypic and functional heterogeneity *in vivo*. Moreover, the Met-1 cells met

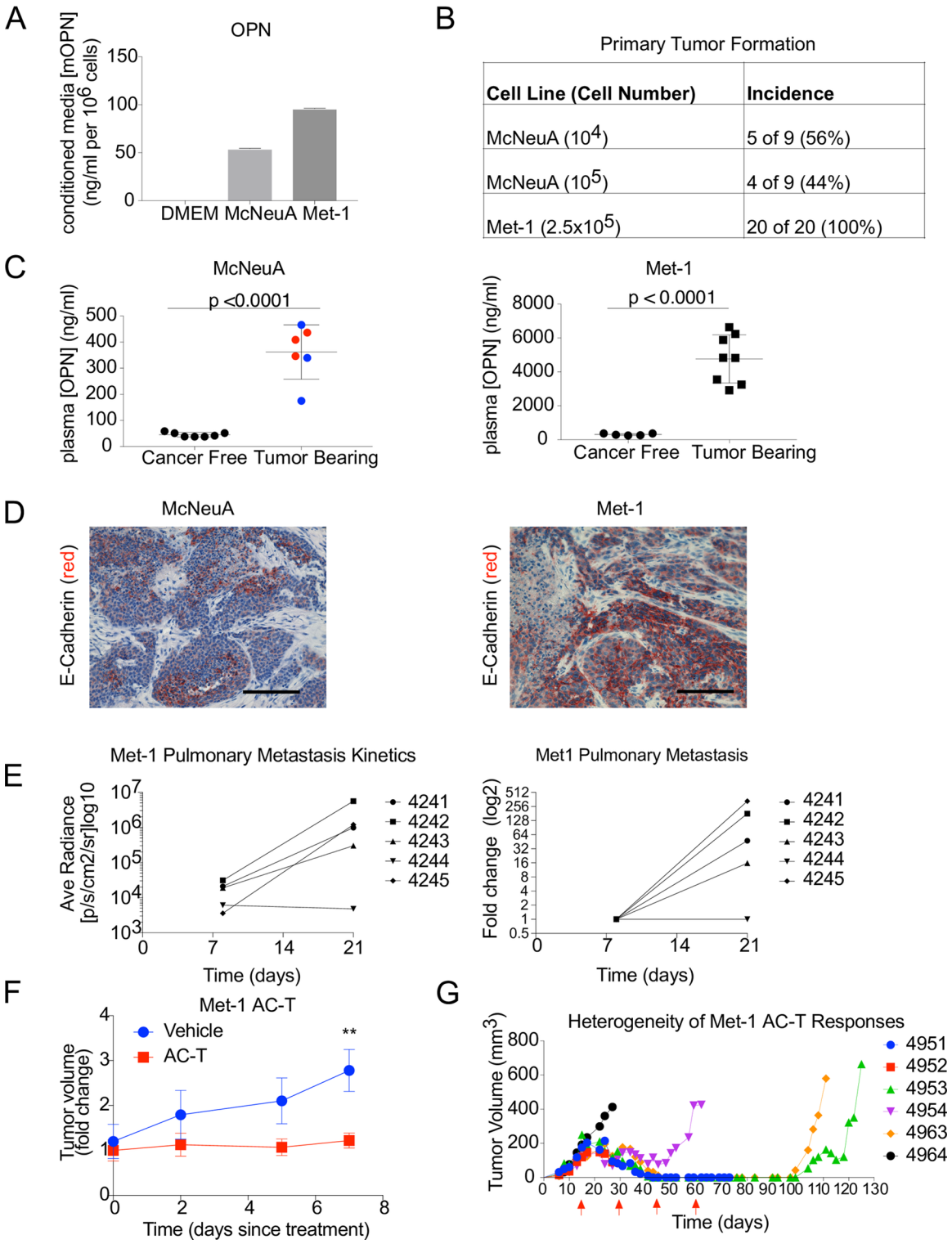

Fig 1. Phenotypic and functional heterogeneity of McNeuA and Met-1 breast cancer cells. (A) Concentration of murine OPN (mOPN; ng/ml per 10^6 cells) in 24-hr conditioned medium of McNeuA and Met-1 murine mammary carcinoma cells represented as mean ± SD. There was no detectable mOPN in the control cell-free medium (DMEM) (2 technical replicates per group). **(B)** Incidence of tumor formation following injection of indicated numbers of McNeuA or Met-1 cells into cohorts of FVB mice. **(C)** Plasma mOPN concentration (ng/ml) in indicated cohorts of mice at experimental end points of 84 days (McNeuA) and 30 days (Met-1). For McNeuA tumor-bearing mice, blue data points represent 10,000 cells injected, red data points represent 100,000 cells injected; n = 6–7 for

McNeuA cohorts; n = 5–8 for Met-1 cohorts. Error bars represent SD; statistical significance evaluated using unpaired, two-tailed Student's t-test. **(D)** Representative images of immunohistochemical staining for murine E-cadherin (red) on recovered McNeuA and Met-1 tumors. Cell nuclei were counterstained with hematoxylin (blue). Scale bars = 100 μm. (B-D) representative of 3 independent experiments per cell line. **(E)** Average radiance (log_{10}) per mouse (n = 5) as measured by bioluminescence imaging over 21-day time course following intravenous injection of 10^6 Met-1 tumor cells into FVB mice (left graph). Fold-change (log_2) in pulmonary metastatic burden per mouse (right graph). Representative of 2 independent experiments. **(F)** Response of orthotopic Met-1 GFP/Luc tumors to single dose combination doxorubicin (5 mg/kg), paclitaxel (10 mg/kg) and cyclophosphamide (120 mg/kg) (AC-T), n = 5–8 tumors/group. Ordinate represents time (days) following treatment. Error bars represent SEM; two-way ANOVA Sidak's multiple comparisons test; $^{**}p<0.01$. Representative of 3 independent experiments. **(G)** Growth kinetics of individual orthotopic Met-1 Luc/GFP tumors in mice injected with 2.5 x 10^5 tumor cells at the experiment initiation, subsequently receiving 4 biweekly AC-T doses (red arrows). Numbers and colors represent individual mice.

https://doi.org/10.1371/journal.pone.0198790.g001

the criteria of metastatic capacity and, chemosensitivity. Hence, the McNeuA and Met-1 cell lines were ideal for our investigation into the effect of tumor heterogeneity on the generation of appropriately matched control and OPN-KO cell lines.

Heterogeneity between subclonal populations derived from McNeuA and Met-1

In order to better understand whether the inherent phenotypic heterogeneity of the McNeuA and Met-1 cells lines would potentially confound the results of an OPN-knockout study, we generated single cell-derived subclonal populations from both the McNeuA (50 clones) and Met-1 (42 clones) parental cell lines (Fig 2A). The various subclonal populations exhibited morphological heterogeneity, displaying a range of epithelial and mesenchymal phenotypes in culture (Fig 2B and 2C). Cell size also appeared to vary between subclones for each given cell line (Fig 2B and 2C).

Levels of OPN secreted *in vitro* by the McNeuA and Met-1 subclones varied considerably. The McNeuA subclones secreted a range of OPN from 37.5–442.1 ng/ml per 10^6 cells (Fig 2D), while the Met-1 subclones exhibited a range from no detectable OPN to 287.6 ng/ml per 10^6 cells (Fig 2E). Importantly, a number of individual subclones secreted levels of OPN that differed significantly from their respective parental population. For example, OPN secretion was 6-8-fold higher in some McNeuA subclones (MC-18, MC-22, MC-45, MC-47, MC-50) and 2.5-3-fold higher in some Met-1 subclones (MT-2, MT-3, MT-4) than their respective parental populations (Figs 1A, 2D and 2E). Likewise, OPN was undetectable in some of the Met-1 cells (MT-18, MT-22, MT-25, MT-26, MT-40, MT-42) (Fig 2E). We observed similar heterogeneity of OPN secretion from clonal populations that we derived from a human melanoma cell line, MDA-MB-435 (S3A Fig), suggesting that this phenomenon is not limited to murine cell lines or breast cancer cell lines.

Taken together, these results highlighted the phenotypic heterogeneity that exists within tumor-derived breast carcinoma populations *in vitro*. We therefore explored if different clones would perform differently *in vivo* as well.

McNeuA and Met-1 derived clonal populations behave differently *in vivo*

To understand whether various subclones that displayed different phenotypes *in vitro* would also display functional heterogeneity with respect to tumorigenesis, we injected cohorts of FVB mice orthotopically with various McNeuA or Met-1 subclonal populations and monitored tumor growth parameters over a course of 64 or 49 days, respectively. We chose to use five subclones from each cell line that secreted high levels of OPN (MC-18, MC-22, MC-45, MC-47, MC-50 and MT-2, MT-3, MT-4, MT24, MT-29) (Fig 2D and 2E). We injected either 10^5 or 10^6 cells of each McNeuA subclone and $2.5x10^4$ or $2.5x10^5$ cells of each Met-1 subclone.

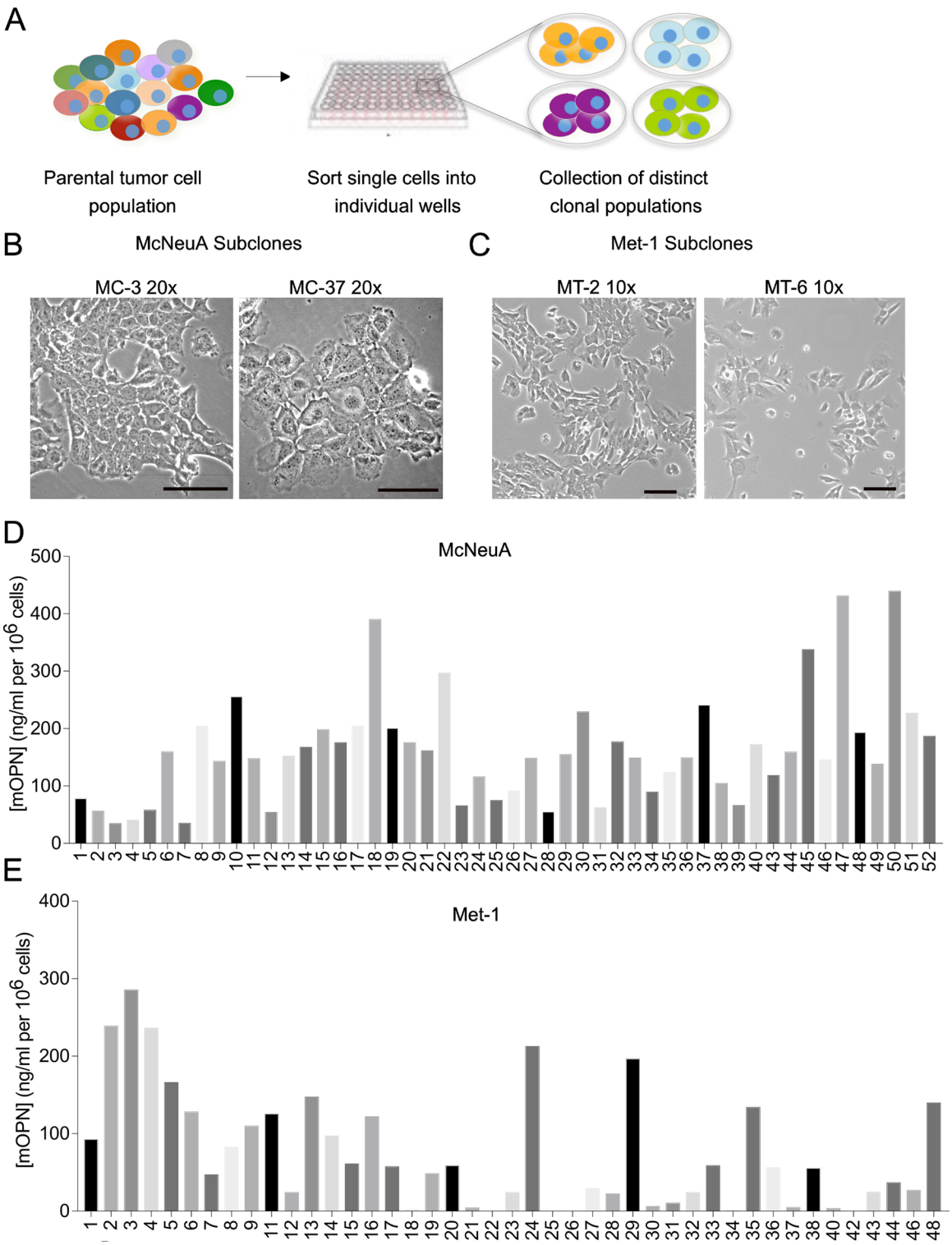

Fig 2. Phenotypic heterogeneity of McNeuA and Met-1 subclonal populations. (A) Schematic of subclone derivation from breast cancer cell lines. **(B,C)** Phase contrast images of representative McNeuA (B) and Met-1 (C) subclones to demonstrate morphologic variability. Scale bars = 100 μm. **(D,E)** Concentration of murine osteopontin (mOPN; ng/ml per 10^6 cells) in 24-hr conditioned media from McNeuA (MC) sublcones (D) and Met-1 (MT) subclones (E).

https://doi.org/10.1371/journal.pone.0198790.g002

Among the McNeuA subclones, a subset of clones (MC-22 and MC-50) formed tumors with 100% incidence, while another subclone (MC-47) failed to form tumors in any mice, and incidence was only slightly higher when more cells were injected (Fig 3A). Similarly, Met-1 subclones also exhibited variable tumor incidence with 4 of 5 subclones (MT-2, MT-4, MT-24, and MT-29) forming tumors with ~100% incidence, while one subclone (MT-3) had reduced incidence to 50–66%, depending on the numbers of cells injected (Fig 3B).

Those clones that formed tumors displayed variability in latency and growth kinetics. For example, latency and growth kinetics were not statistically different between MC-22 and MC-50 when 10^6 cells were injected (Fig 3D); however, growth kinetics differed significantly between these clones at 10^5 ($p<0.0001$, Fig 3C). The subclonal populations also exhibited differences in latency. For example, when 10^6 cells were injected, MC-22 and MC-50 had latencies of ~20 days, MC-18 and MC-45 had latencies of ~40 days, and MC-47 had a latency of ~60 days (Fig 3D).

Similarly, the growth kinetics of the Met-1 subclonal populations was also variable. When $2.5x10^4$ cells were injected, at the 28 day time point (when the MT-4 cohort had reached its endpoint), the growth kinetics of MT-4 were significantly different from the MT-2, MT-3, MT-24 and MT-29 subclones ($p<0.0002$, Fig 3E). The Met-1 subclones also had different latencies, with the MT-4 and MT-24 clones having shorter latencies than the other subclonal populations when either $2.5x10^4$ or $2.5x10^5$ cells were injected (Fig 3E and 3F).

The subclones derived from the human melanoma cell line also varied in incidence of subcutaneous tumor formation in NOD-SCID mice, with some clones (i.e. 11, 28, 29, 30) unable to form tumors *in vivo* (S2B Fig). Moreover, tumor mass at the experimental end point varied considerably among these subclones (S2B Fig).

Critically, a number of individual subclonal populations from each tumor model exhibited different tumor formation capabilities than the respective bulk parental population from which they were derived. For example, while the parental Met-1 tumor cell line formed orthotopic tumors with 100% incidence, the MT-3 subclonal cell line formed tumors with only 60% incidence when the same number of cells was injected (Figs 1B and 3B). This was also true of the human xenograft model (S2B Fig).

These observations revealed the considerable subclonal heterogeneity that exists within human carcinoma and murine mammary carcinoma cell lines and that the behavior of individual subclones differs from their respective parental populations.

Evidence that identification of proper controls is necessary for correct interpretation of experimental findings

Traditional CRISPR/Cas9 editing protocols begin with infection or transfection of the bulk parental population [3–7]. For this reason, the unedited or mock-infected parental cell line is typically used as a control. Due to the inefficiency of infection and/or editing in certain cell lines (especially tumor cell lines that are hyperploid), there is often a subclonal selection step that follows the initial infection and then a validated, edited subclone is used for subsequent experimentation. Our initial characterizations of the McNeuA and Met-1 parental and subclonal populations demonstrate why one must use caution when considering this commonly used approach.

In some scenarios, subclonal heterogeneity could confound interpretation of knockout efficiency. For example, 23% of the Met-1 subclones have low or no detectable secreted OPN (Fig 2E). Hence, if one randomly selected one of these clones (e.g. MT-42) and evaluated the functional success of the OPN KO by comparing its OPN secretion levels to that of the parental Met-1 cell line, a failed knockout attempt or false positive result could be overlooked.

In another scenario, if the clonal population that was selected after CRISPR/Cas9 OPN-knockout happened to be clone MT-3 and its orthotopic tumor penetrance was compared to

A

McNeuA

Clone ID (no. cells)	Tumor Incidence
MC-18 (10^5)	3/6
MC-18 (10^6)	4/6
MC-22 (10^5)	6/6
MC-22 (10^6)	6/6
MC-45 (10^5)	2/6
MC-45 (10^6)	3/6
MC-47 (10^5)	0/6
MC-47 (10^6)	2/6
MC-50 (10^5)	4/6
MC-50 (10^6)	6/6

B

Met-1

Clone ID (no. cells)	Tumor Incidence
MT-2 (25K)	6/6
MT-2 (250K)	6/6
MT-3 (25K)	2/6
MT-3 (250K)	4/6
MT-4 (25K)	6/6
MT-4 (250K)	6/6
MT-24 (25K)	5/6
MT-24 (250K)	6/6
MT-29 (25K)	6/6
MT-29 (250K)	6/6

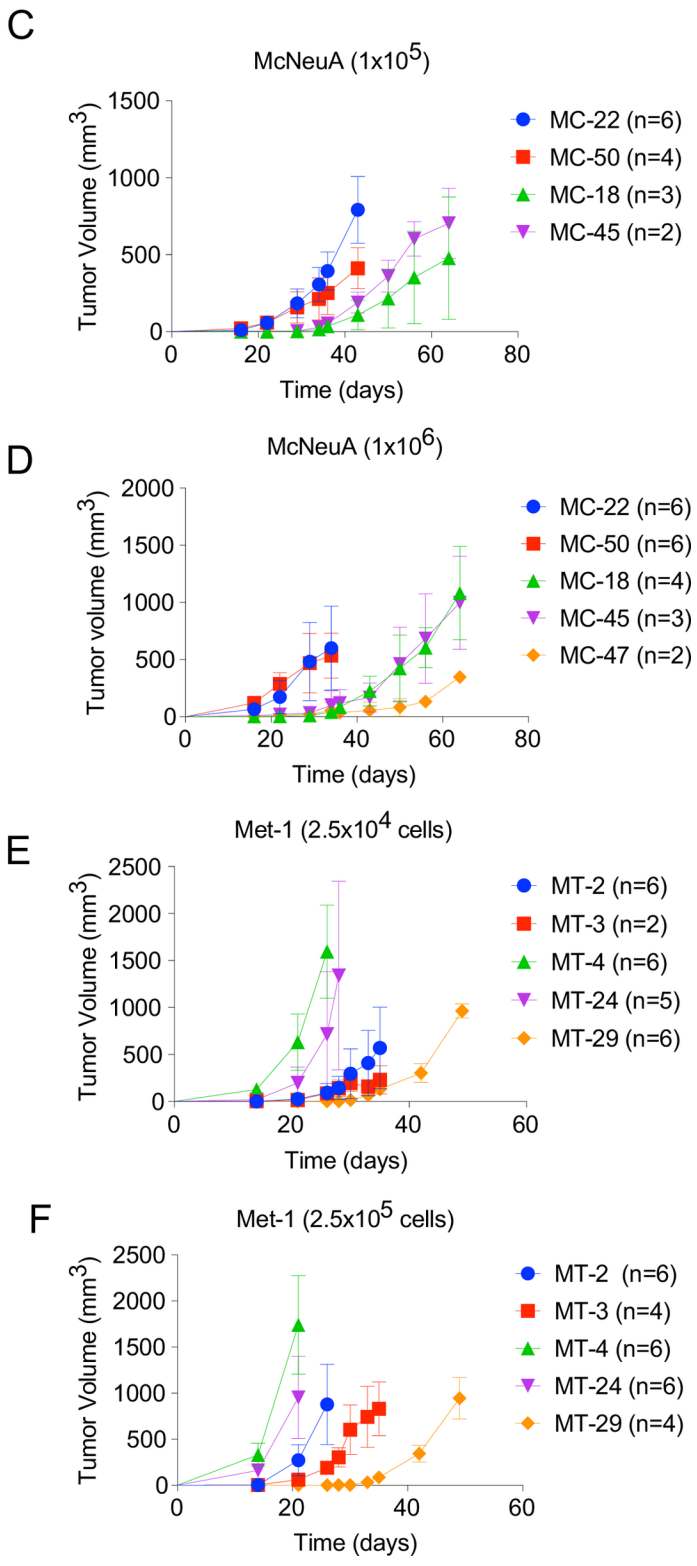

Fig 3. McNeuA and Met-1 subclonal populations are functionally heterogeneous in tumor incidence, latency and growth kinetics. **(A,B)** Primary tumor incidence of indicated McNeuA (10^5 or 10^6 cells; A) and Met-1 ($2.5x10^4$ or $2.5x10^5$ cells; B) clonal populations that were injected orthotopically into FVB mice. **(C,D)** Tumor growth kinetics of indicated McNeuA clones that were orthotopically injected into FVB mice at 10^5 (C) or 10^6 (D) cells. Error bars represent SD; statistical significance evaluated using 2way-ANOVA. **(E,F)** Tumor growth kinetics of indicated Met-1 clones that were orthotopically injected into FVB mice at $2.5x10^4$ (E) or $2.5x10^5$ (F) cells. Error bars represent SD; statistical significance evaluated using 2way-ANOVA.

https://doi.org/10.1371/journal.pone.0198790.g003

that of the parental Met-1 population, then one could erroneously interpret the necessity of OPN for primary tumor formation, when in fact this clone, prior to OPN knockout, already inherently forms tumors with lower incidence (~66%) than the parental population (100%) (Figs 1B and 3B).

Likewise, comparing two subclonal populations, even those that secrete similar levels of OPN and form tumors with the same incidence, could also lead to spurious results. For example, if one randomly selected MT-29 as an OPN KO clone and MT-4 as a control, then incorrect conclusions could be drawn about the role of OPN in tumor growth. This is because prior to OPN KO, both clones express similar levels of OPN (~225 ng/ml; Fig 2E) and form tumors with similar incidence (Fig 3B) but MT-29 inherently exhibits significantly longer latency and reduced growth kinetics than MT-4 (Fig 3E and 3F). The same holds true for MC-18 and MC-50, which secrete similar levels of OPN (~400 ng/ml; Fig 2D), but incidence of tumor formation after injecting 10^6 cells is ~17% for MC-18 and 100% for MC-50 (Fig 3A). Hence, the chances of randomly selecting functionally equivalent clones–such as MC-22 and MC-50, which secrete similar levels of OPN (>250 ng/ml; Fig 2D), form tumors with similar incidence (100%; Fig 3A), and display similar growth kinetics (Fig 3B)–are low without extensive characterization of individual clones prior to gene editing.

Our results provided evidence that neither the parental population nor other subclones would represent an appropriately matched wild-type control for a CRISPR/Cas9 knockout cell line that was selected after the gene editing step. The only appropriate control would be to compare the behavior of edited and unedited cells derived from the same clonal population. We therefore concluded that a modified strategy should be developed to account for heterogeneity and enable the generation of appropriately matched cell lines.

Generating *spp1* knockout clonal populations via CRISPR/Cas9

One would not have known *a priori* about differences in subclonal biological phenotypes and experimental outcomes by taking traditional approaches to gene editing. Therefore, we developed a modified CRISPR-Cas9 editing protocol for generating matched control and knockout cells. Appropriate subclonal populations that we had generated and characterized were chosen for CRISPR/Cas9 gene targeting based on the desired biological properties of high intrinsic levels of OPN secretion and orthotopic tumor incidence of 100%. We identified three clonal populations that fit these criteria: MC-22, MC-50, and MT-2 (Figs 2D, 2E, 3A and 3B). In contrast to traditional CRISPR/Cas9 protocols, we used single cell-derived subclonal populations that we had generated prior to CRISPR/Cas9 gene targeting (Fig 4A).

We used our modified CRISPR/Cas9 editing strategy to delete the *spp1* gene (which encodes Osteopontin) in each subclonal population in order to generate OPN KO cell lines. To do so, the individual subclonal populations were transiently co-transfected with a human codon-optimized spCas9-2A-GFP fusion protein expression plasmid (Addgene plasmid #44719) and a plasmid harboring a sgRNA targeting exon 2 of *spp1* (Fig 4B). After 24 hours, the GFP-positive (and therefore successfully transfected) Cas9-expressing cells from each subclonal population were collected by FACS and allowed to expand in culture for at least six doublings (~3 days) (Fig 4A). By giving transfected cells more time to recover from FACS sorting, we observed improved single cell cloning recovery rates for the MC-22, MC-50, and MT-2 subclones (respectively 42%, 55%, and 53%, Fig 4C) compared to transfected cells that were directly sorted as single cells, in which the recovery rate was ~5% in an initial trial (data not shown). The higher colony recovery rate and enrichment of Cas9 expressing cells during the first sorting step allowed us to achieve both higher editing efficiency and more homozygously edited clones (Figs 4C and S3).

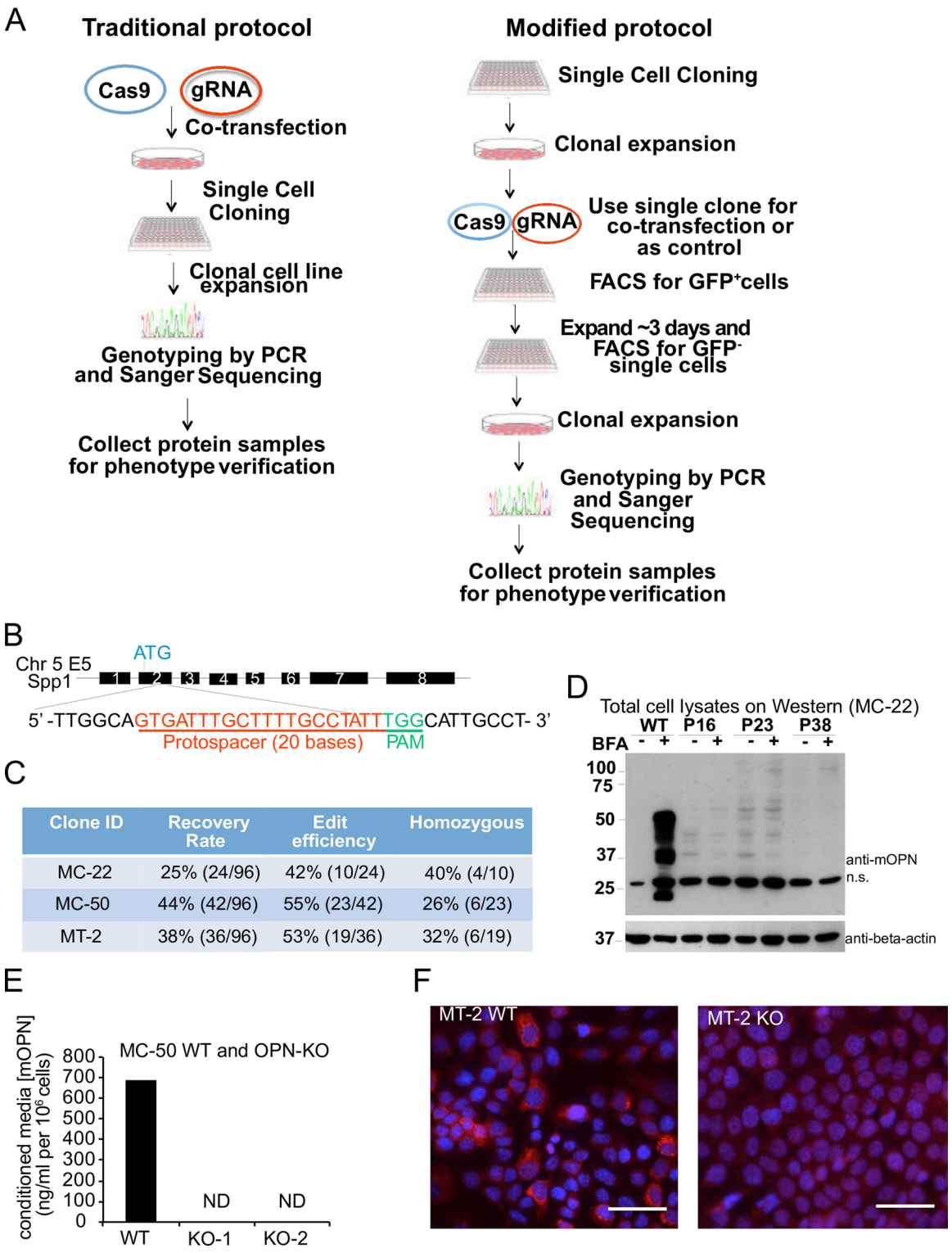

Clone ID	Recovery Rate	Edit efficiency	Homozygous
MC-22	25% (24/96)	42% (10/24)	40% (4/10)
MC-50	44% (42/96)	55% (23/42)	26% (6/23)
MT-2	38% (36/96)	53% (19/36)	32% (6/19)

Fig 4. Generation of appropriately matched wild-type and OPN knockout cell lines using CRISPR-Cas9 mediated gene editing. (A) Schematic of traditional and modified CRISPR/Cas9 based gene editing protocols. **(B)** Schematic diagram of sgRNA targeting the *spp1* gene loci. Protospacer sequence is highlighted in red. Protospacer adjacent motif (PAM) sequences are presented in green. **(C)** Recovery rates, gene editing efficiency, and rate of homozygous targeting of the OPN gene in indicated subclones. **(D)** Western blot for OPN protein in MC-22 WT and edited clones (P16, P23, and P38) cultured in the presence or absence of brefeldin A (BFA). Expected multiple Osteopontin isoforms were detected between ~37–50 kD. A non-specific band was detected in each sample, indicated by "n.s".

(E) Concentration of murine osteopontin (mOPN) in 24-hr conditioned media from MC-50 WT and edited clones (MC-50-KO1 and MC-50-KO2). mOPN levels were normalized to final cell count. Osteopontin was undetected (ND) in conditioned media collected from both edited subclones. **(F)** Immunofluorescence cytochemical staining for mOPN (red) in MT-2 WT and a validated MT-2 OPN-KO clone. Nuclei are counterstained with hematoxylin (blue). Scale = 100 μm.

https://doi.org/10.1371/journal.pone.0198790.g004

Due to the transient nature of our transfection protocol, only cells in which the Cas9-GFP fusion protein had been randomly integrated would maintain GFP expression past this point. In order to avoid random integration of the Cas9 expression plasmid into the genome, a second round of single-cell sorting by FACS was employed to isolate cells that had not undergone a Cas9 integration event by sorting and selecting for GFP-negative cells (Fig 4A). Single cell-derived subclones were then expanded in culture.

We next employed Sanger sequencing to identify the edited subpopulations from among the recovered subclones (S3A Fig). Of the recovered subclones from the MC-22, MC-50, and MT-2 lines, a subset of the single cell clones contained either a hemizygous or homozygous mutation in the *spp1* gene, representing editing efficiencies of 42%, 55%, and 53%, respectively (Fig 4C). We found that MC-50 clone is hyperploid for the chromosome region containing *spp1* based on partially edited clones' sequencing result (S3B Fig) and this observation was further validated by genotyping these clones using TA cloning and Sanger sequencing (data not shown). Between 26–40% of the successfully edited clones contained homozygous mutations (Fig 4C).

We validated loss of OPN protein expression in each of the OPN KO clones compared to its appropriately matched control using western blotting, ELISA of conditioned media, or immunocytochemistry. We observed no detectable OPN protein (Fig 4D–4F), demonstrating that our CRISPR/Cas9 editing strategy was successful and we had generated authentic OPN KO subclonal cell lines.

Osteopontin is dispensable for primary tumor growth

Most studies, including our own, report that OPN is dispensable for primary tumor growth, but is critical for metastasis due to its effects on tumor cells, the host systemic environment, and the tumor microenvironment [20, 23, 26]. Therefore, successful generation of appropriately matched KO and WT cell lines should also reflect these properties (e.g., loss of OPN should have no effect on primary tumor growth, but should alter metastatic ability). This makes OPN an ideal protein to test our concept because its dispensability for primary tumor growth means that WT and OPN KO clones should exhibit similar primary tumor growth kinetics and incidence. Therefore, we tested the tumor formation capabilities of the matched clones.

WT and OPN KO MC-50 cells ($2x10^5$), MC-22 cells ($1x10^5$) or MT-2 cells ($2.5x10^4$) were orthotopically injected into FVB mice and were allowed to grow until tumors reached ~1 cm^3. Loss of tumor-derived OPN did not significantly affect growth kinetics or the final mass of any of the tumors derived from matched subclonal cell lines (Fig 5A–5C). In fact, there were no significant differences in any other tumor growth parameters (Fig 5A–5C) or spleen mass (S4A Fig) between cohorts bearing WT and the respective matched OPN KO tumors.

As a control, we tested the concentration of circulating plasma mOPN in the tumor-bearing mice and cancer-free controls. As expected, mOPN plasma levels were elevated in the mice bearing WT tumors relative to the cancer-free cohort, and plasma OPN levels were significantly reduced in the mice bearing KO tumors relative to WT (Fig 5A–5C). Plasma OPN levels from the cohorts of mice bearing MC-50 and MT-2 OPN KO tumors were not significantly different from their respective cancer-free cohorts (Fig 5A–5C). However, plasma OPN from mice bearing MC-22 KO tumors was significantly higher than the cancer free controls (Fig 5A), suggesting that clone MC-22 may in fact induce an elevation in host-derived OPN.

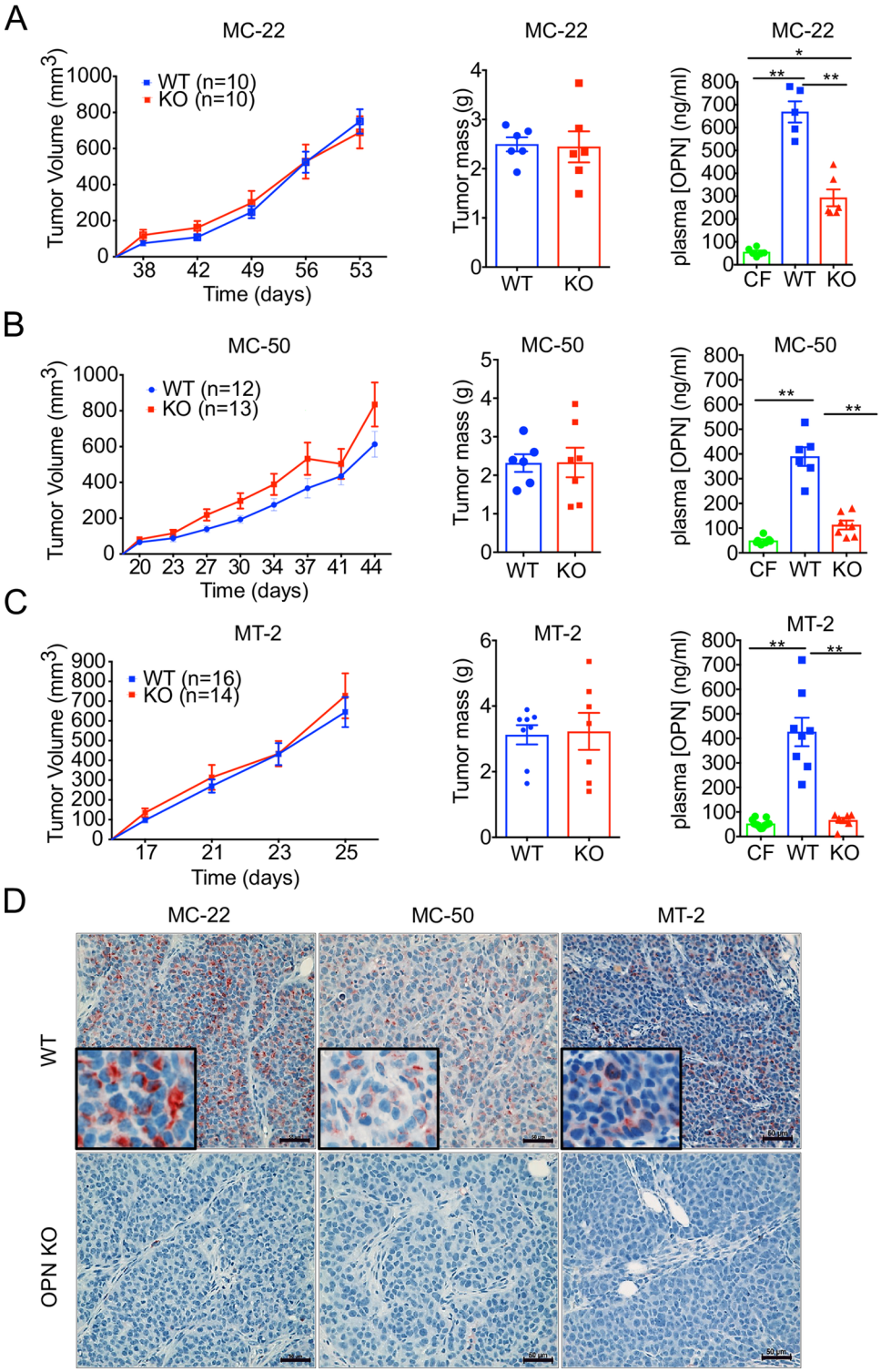

Fig 5. OPN depletion does not affect primary tumor formation in murine models of HER2$^+$ and ER$^-$ breast cancer. (A-C) FVB mice were orthotopically injected with 10^5 MC-22 (A), 10^5 MC-50 (B), or 2.5 x 10^4 MT-2 (C) cells. Growth kinetics (mm^3) of orthotopic tumors of WT (blue lines) and validated OPN-KO clones (red lines). Mass of primary tumors from WT (blue) or OPN-KO (red) cohorts at experimental end points. No statistically significant differences were determined by 2way ANOVA (tumor growth kinetics) or unpaired, two-tailed Students' t-test (tumor mass) statistical analyses. Circulating plasma murine osteopontin (mOPN) levels from cancer-free (green) or tumor bearing mice from the MC-22, MC-50, or MT-2 WT (blue) or OPN-KO (red) cohorts (One-way ANOVA: ***

p = 0.0003, **** p < 0.0001). Error bars represent SD. **(D)** Representative immunohistochemical staining for mOPN (red) in tumors derived from MC-22, MC-50 and MT-2 WT and validated OPN-KO cell lines. Cell nuclei counterstained with hematoxylin (blue). Scale bar = 50 μm.

https://doi.org/10.1371/journal.pone.0198790.g005

It is important to note that if we had used the parental McNeuA cell line as a WT control rather than the appropriately matched WT MC-22 cell line, we would have failed to see a significant difference in the circulating OPN levels between cohorts (S4B Fig). This observation would not have been possible using a traditional CRISPR/Cas9 gene editing protocol, once again highlighting the strength of our system and the necessity of using appropriately matched control cell lines in knockout studies.

Finally, we visualized OPN expression in the tumors that formed in each cohort using immunohistochemical staining. We observed positive staining for OPN in the WT MC-22, MC-50, and MT-2 tumors, but did not detect any OPN^+ cells in the corresponding OPN KO tumors (Fig 5D), confirming that the OPN KO was successful. These observations provided further evidence that any circulating OPN detected in mice injected with the OPN-KO clones (Fig 5A–5C) was host-derived rather than tumor derived.

Together, these results demonstrated that our modified CRISPR/Cas9 gene editing protocol can be successfully used for studies examining the role of a gene in primary tumor outgrowth.

Loss of osteopontin reduces multifocal metastatic outgrowth

Osteopontin is considered a biomarker for tumor progression and is detected at higher levels in more aggressive tumors than their low-grade counterparts, is elevated in the serum of patients with metastatic disease, and is included in gene lists predicting poor prognosis for many cancer types [28, 34–40]. Although OPN is most often dispensable for primary tumor growth, OPN is necessary for metastasis [20, 41–43].

Met-1 cells are highly metastatic [18] (Fig 1E) and therefore serve as an ideal pre-clinical model of ER-negative disease to test whether our CRISPR/Cas9 system is useful for metastasis studies. To address this question, we labeled the MT-2 WT and MT-2 OPN KO cell lines with a dual GFP/luciferase reporter and injected the labeled cells intravenously via the tail vein into cohorts of mice (Fig 6A). Metastasis formation was monitored using bioluminescent *in vivo* imaging at weekly intervals.

Metastatic burden was decreased in the MT-2 OPN KO cohort relative to that of the MT-2 WT cohort, as indicated by the marked reduction in the fold change of bioluminescent signal in the MT-2 OPN KO cohort at day 28 ($p = 0.000067$ at day 28, $p>0.05$ for all other time points; Fig 6B and 6C). As further confirmation, we analyzed H&E lung sections at the experimental end point and quantified the numbers of single and multifocal metastases. There were significantly fewer total and multifocal pulmonary metastases in mice that had been injected with the OPN KO cells compared to mice that had been injected with OPN WT cells (Fig 6D–6F). Additionally, the average number of single-focus metastatic outgrowths was also reduced in mice in the OPN KO cohort compared to the WT cohort (S5 Fig).

Collectively, our results established that by using appropriately matched cells, we could confidently conclude that OPN is necessary for metastatic colonization and that our CRISPR/Cas9 protocol is useful for pre-clinical metastasis studies.

Loss of osteopontin enhances chemosensitivity

Resistance to standard chemotherapies remains a significant clinical problem, particularly for triple-negative breast cancer [44]. In order to interrogate whether OPN contributes to

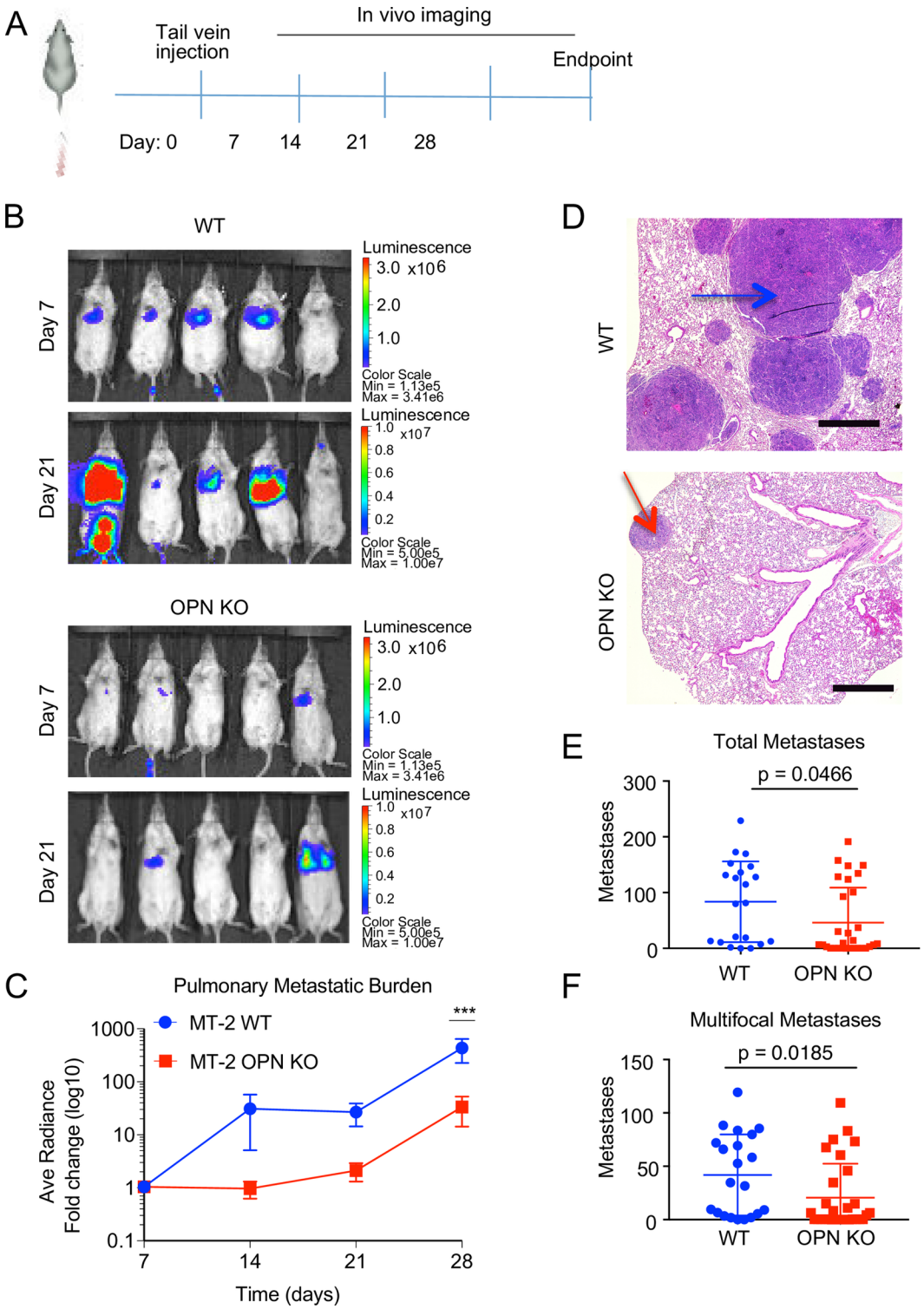

Fig 6. Matched wild type and knockout OPN cell lines can be used for pre-clinical metastasis studies. (A) Experimental schema for metastasis assay. **(B)** Representative *in vivo* bioluminescent images of mice injected with MT-2 WT or MT-2 OPN KO after 7d and 21d. **(C)** Average fold change of bioluminescent signal (radiance (p/sec/cm^2/sr), log10, normalized for differences in Luciferase expression between cell lines) from mice with MT-2 WT (blue) or MT-2 OPN KO (red) at indicated time points. (unpaired, two tailed t-test: *** p = 0.000067). Error bars represent SEM. **(D)** Representative hematoxylin & eosin staining of lungs from mice that received tail vein injections of MT-2 WT or MT-2 OPN KO cells. An example of a multifocal metastasis is marked with a blue arrow and an example of a single focus metastasis is marked with a red arrow.

Scale = 1000 μm. **(E)** Quantification of total metastases in MT-2 WT (blue) and MT-2 OPN KO (red) cohorts (WT n = 21, KO n = 30; Mann-Whitney, p = 0.0466). Error bars represent SD. **(F)** Quantification of multifocal metastases in MT-2 WT (blue) and MT-2 OPN KO (red) cohorts (WT n = 21, KO n = 30; Mann-Whitney, p = 0.0185). Error bars represent SD.

https://doi.org/10.1371/journal.pone.0198790.g006

chemoresistance in breast cancer models, we tested the MT-2 WT and KO cell lines for sensitivity to AC-T chemotherapy in vivo.

We injected 2.5×10^4 MT-2 WT or matched OPN KO tumor cells into the mammary fat pads of FVB mice. When established tumors reached ~60–80 mm^3 in volume (14 days), animals were randomized based on tumor volume and enrolled into either vehicle control (PBS) or AC-T chemotherapy treatment cohorts (Fig 7A).

MT-2 WT and MT-2 KO tumors exhibited sensitivity to AC-T treatment relative to their respective vehicle-treated cohorts (Fig 7B). However, in response to AC-T, the MT-2 KO tumors exhibited reduced growth kinetics compared to their MT-2 WT counterparts in three independent trials (Fig 7B). Likewise, final tumor mass was significantly lower in the MT-2 KO treatment cohorts compared to the MT-2 WT treatment cohorts (Fig 7C). Sensitivity to doxorubicin and paclitaxel was not apparent *in vitro* (S6A and S6B Fig). Hence, the enhanced sensitivity observed *in vivo* could be due to the effects of OPN only on cyclophosphamide resistance, the host microenvironment, or both.

Together, these data established that elimination of OPN expression enhances chemosensitivity of the MT-2 breast cancer population.

Discussion

The ability to genetically edit a cell line to either suppress, knockdown, induce, overexpress, knock-in, or mutate a protein of interest provides an indispensible tool for biological research. However, our work demonstrates that studies designed to test necessity or sufficiency of genes/gene products without choosing appropriately matched unedited controls run the risk of detecting false positive or false negative results due to inherent phenotypic differences in subclonal cellular populations that result from heterogeneity. Our alternative approach to generate subclones and screen for desired phenotypes prior to genetic manipulation provides one solution to this problem.

As we demonstrated through proof-of-concept studies, our approach works well for hypothesis-testing experimentation, when biological phenotypes to be tested are defined. Another benefit to our modified approach is that characterization of subclone phenotypes may enable one to select a range of biological properties that could be tested. Moreover, this approach enables discovery of novel properties for which mechanistic insight could be obtained in a straightforward manner. For example, one of our subclones (MC-22 KO) stimulated elevated host plasma OPN while another clone (MC-50 KO) did not, thereby enabling one to compare properties (e.g., gene expression) of related clones to yield mechanistic insights. While our approach takes added time and expense, it ensures that the real function of a specific protein of interest is uncovered during experimentation.

One caveat of our approach is that isolating particular subclonal populations removes the inherent heterogeneity of a cell line, which could have important biological consequences. This is particularly relevant in circumstances in which the biology is not well understood. If heterogeneity is desirable, then one could employ a clonal pooling approach, thus ensuring that a given experiment is both properly controlled and that the heterogeneous nature of the parental cell line is not lost.

It has been reported that functional heterogeneity can arise even within a 'clonal' cellular population as a result of cell plasticity or epigenetic alteration [13]. Hence, although we did not

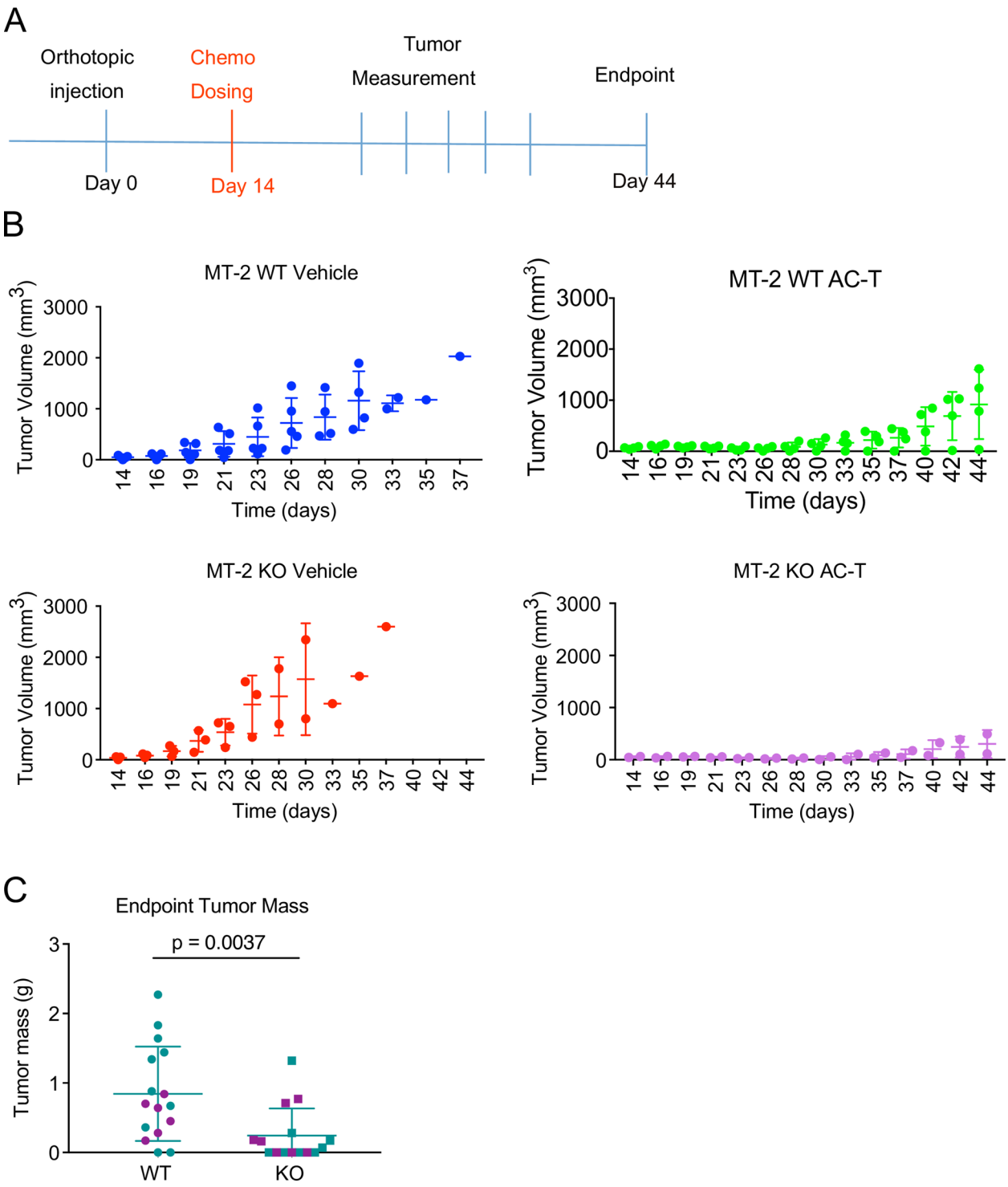

Fig 7. MT-2 OPN-KO derived tumors exhibit enhanced chemosensitivity *in vivo*. **(A)** Experimental schema. 2.5×10^4 MT-2 WT or OPN-KO tumor cells were injected into the mammary fat pads of 6–8-week-old female FVB mice. A single dose of AC-T was initiated at 14 days, when tumors reached ~60–80 mm^3 in volume, and tumor growth was monitored periodically until the end point of 44 days. Error bars represent SD. **(B)** Tumor growth kinetics for MT-2 WT vehicle (blue; n = 5) and AC-T treated (green; n = 4) and MT-2 OPN-KO vehicle (red; n = 3) and AC-T treated mice (purple; n = 2). Representative of 3 biological repetitions. Error bars represent SD. **(C)** Endpoint tumor mass for MT-2 WT and MT-2 OPN-KO AC-T treated mice from 2 separate experiments (Mann-Whitney, p = 0.0037; endpoint tumor mass was not measured during the first of the three experimental repetitions). Data points from individual repetitions are represented with different colors. Error bars represent SD.

https://doi.org/10.1371/journal.pone.0198790.g007

test clonal plasticity in our system, it is reasonable to hypothesize that a high degree of cellular plasticity could cause differences between matched control and edited populations that may not be due to the target gene. Limiting the *in vitro* passage of the cell lines to minimize chances for additional selection and monitoring for unexpected functional changes in control cell lines may help to prevent this added complication.

Our new experimental approach led us to discover an important function of OPN in resistance to a standard breast cancer chemotherapy regimen. Use of our matched wild type and OPN-deficient subclones will enable future studies to determine the mechanism through which OPN acts to promote this chemoresistance in breast cancer. It appears that it may rely on a non-cell intrinsic mechanism, as the reduced chemosensitivity was only observed *in vivo* and not *in vitro*. The matched subclones we report here provide a valuable tool to expand such studies.

Supporting information

S1 Fig. Met-1 and McNeuA parental tumor characteristics. (A) Individual and average tumor growth kinetic rates from FVB mice orthotopically injected with $2.5x10^5$ Met-1 cells. Error bars represent SD. **(B)** Endpoint tumor masses of mice injected with 10^5 (red) or 10^6 (blue) McNeuA cells or $2.5x10^5$ Met-1 cells. Error bars represent SD. **(C)** Circulating plasma osteopontin (OPN) levels were measured using ELISA and were plotted against the primary tumor mass in the corresponding animal. **(D)** Representative hematoxylin & eosin staining of lung tissue from a mouse that received intravenous injection of Met-1 cells. An example of a pulmonary metastasis is marked with a blue arrow. Scale = 1000 μm. Representative of two independent experiments. **(E,F)** Viability of Met1 GFP Luc cells treated in vitro with various doses of doxorubicin and paclitaxel for 72 hours. Representative of three independent experiments. Error bars represent SEM. **(G)** Tumor growth kinetics of the Met-1 Luc/GFP parental cells injected orthotopically into FVB mice at 2.5×10^5 cells treated with two bi-weekly doses of either vehicle (blue, n = 6) or AC-T (red, n = 8). Error bars represent SEM.
(TIF)

S2 Fig. MDA-MB-435 subclonal populations are heterogeneous. (A) Human osteopontin (hOPN) secreted into culture medium by MDA-MB-435 parental cells (P1-3) and single cell clones after 24h, normalized for the number of cells in each well (n = 3 replicates per cell line). **(B)** Average mass (mg) of tumors 60 days after subcutaneous injection of $2.5x10^5$ MDA-MB-435 parental cells (P1-4) or indicated subclones into NOD-SCID (n = 5 mice per cohort).
(TIF)

S3 Fig. Sanger sequencing of matched wild type and CRISPR-Cas9 OPN knockout cell lines. (A) Examples of coding-frame shift confirmed to be homozygous in MT-2, MC-22 and MC-50 clones by Sanger sequencing as reported in Fig 4C**. (B)** Example of coding-frame shift confirmed to be heterozygous as reported in Fig 4C.
(TIF)

S4 Fig. OPN depletion does not affect final primary tumor mass or spleen mass in murine models of $HER2^+$ and ER^- breast cancer. (A) Final spleen mass was measured in mice injected with either MC-22, MC-50, or MT-2 WT or OPN-KO cell lines. No significant difference was observed between WT and KO cohorts for each clone (unpaired, two-tailed Student's t-test). **(B)** Circulating plasma mOPN levels were measured from mice bearing either McNeuA Parental or MC-22 OPN-KO primary tumors using ELISA (unpaired, two-tailed t-test, p = 0.2480). Error bars represent SD.
(TIF)

S5 Fig. OPN knockout results in reduced metastatic burden. Quantification of single focus metastases in MT-2 WT (blue) and MT-2 OPN KO (red) cohorts (WT n = 21, KO n = 30; Mann-Whitney, p = 0.1248). Error bars represent SD.
(TIF)

S6 Fig. Enhanced chemosensitivity of OPN-depleted cell lines to doxorubicin and paclitaxel is not observed *in vitro*. (A,B) MT-2 WT or MT-2 OPN-KO cells were plated in quadruplicate and were treated with various doses of doxorubicin (A) or paclitaxel (B) 24 hours after plating. ATP levels were quantified 72 hours after treatment as a surrogate measure for viability using Cell-Titer Glo and were normalized to vehicle treated. Error bars represent SD.
(TIF)

Acknowledgments

We would like to thank Hanna Starobinets and Zafira Castano for technical assistance; Jessalyn M. Ubellacker and Jaclyn Sceneay for thoughtful discussion. We would like to thank the ARCH veterinary, technical, and management staff.

Author Contributions

Conceptualization: Yuanbo Qin, Sandra S. McAllister.

Data curation: Jessica F. Olive, Yuanbo Qin, Molly J. DeCristo, Tyler Laszewski, Frances Greathouse.

Formal analysis: Jessica F. Olive, Yuanbo Qin, Molly J. DeCristo.

Funding acquisition: Sandra S. McAllister.

Investigation: Yuanbo Qin.

Methodology: Yuanbo Qin.

Supervision: Sandra S. McAllister.

Writing – original draft: Jessica F. Olive.

Writing – review & editing: Jessica F. Olive, Yuanbo Qin, Sandra S. McAllister.

References

1. Guernet A, Grumolato L. CRISPR/Cas9 editing of the genome for cancer modeling. Methods. 2017; 121–122:130–7. https://doi.org/10.1016/j.ymeth.2017.03.007 PMID: 28288827.
2. Doudna JA, Charpentier E. Genome editing. The new frontier of genome engineering with CRISPR-Cas9. Science. 2014; 346(6213):1258096. https://doi.org/10.1126/science.1258096 PMID: 25430774.
3. Yang L, Yang JL, Byrne S, Pan J, Church GM. CRISPR/Cas9-Directed Genome Editing of Cultured Cells. Curr Protoc Mol Biol. 2014; 107:31 1 1–17. https://doi.org/10.1002/0471142727.mb3101s107 PMID: 24984853.
4. Harrod A, Fulton J, Nguyen VTM, Periyasamy M, Ramos-Garcia L, Lai CF, et al. Genomic modelling of the ESR1 Y537S mutation for evaluating function and new therapeutic approaches for metastatic breast cancer. Oncogene. 2017; 36(16):2286–96. https://doi.org/10.1038/onc.2016.382 PMID: 27748765; PubMed Central PMCID: PMCPMC5245767.
5. Neggers JE, Vercruysse T, Jacquemyn M, Vanstreels E, Baloglu E, Shacham S, et al. Identifying drug-target selectivity of small-molecule CRM1/XPO1 inhibitors by CRISPR/Cas9 genome editing. Chem Biol. 2015; 22(1):107–16. https://doi.org/10.1016/j.chembiol.2014.11.015 PMID: 25579209.

6. Mali P, Yang L, Esvelt KM, Aach J, Guell M, DiCarlo JE, et al. RNA-guided human genome engineering via Cas9. Science. 2013; 339(6121):823–6. https://doi.org/10.1126/science.1232033 PMID: 23287722; PubMed Central PMCID: PMCPMC3712628.
7. Ran FA, Hsu PD, Wright J, Agarwala V, Scott DA, Zhang F. Genome engineering using the CRISPR-Cas9 system. Nat Protoc. 2013; 8(11):2281–308. https://doi.org/10.1038/nprot.2013.143 PMID: 24157548; PubMed Central PMCID: PMCPMC3969860.
8. McGranahan N, Swanton C. Clonal Heterogeneity and Tumor Evolution: Past, Present, and the Future. Cell. 2017; 168(4):613–28. https://doi.org/10.1016/j.cell.2017.01.018 PMID: 28187284.
9. Swanton C. Intratumor heterogeneity: evolution through space and time. Cancer Res. 2012; 72 (19):4875–82. Epub 2012/09/25. https://doi.org/10.1158/0008-5472.CAN-12-2217 PMID: 23002210; PubMed Central PMCID: PMC3712191.
10. Burrell RA, McGranahan N, Bartek J, Swanton C. The causes and consequences of genetic heterogeneity in cancer evolution. Nature. 2013; 501(7467):338–45. https://doi.org/10.1038/nature12625 PMID: 24048066.
11. Laughney AM, Elizalde S, Genovese G, Bakhoum SF. Dynamics of Tumor Heterogeneity Derived from Clonal Karyotypic Evolution. Cell Rep. 2015; 12(5):809–20. https://doi.org/10.1016/j.celrep.2015.06.065 PMID: 26212324.
12. Gupta PB, Fillmore CM, Jiang G, Shapira SD, Tao K, Kuperwasser C, et al. Stochastic state transitions give rise to phenotypic equilibrium in populations of cancer cells. Cell. 2011; 146(4):633–44. https://doi.org/10.1016/j.cell.2011.07.026 PMID: 21854987.
13. Kreso A, O'Brien CA, van Galen P, Gan OI, Notta F, Brown AM, et al. Variable clonal repopulation dynamics influence chemotherapy response in colorectal cancer. Science. 2013; 339(6119):543–8. https://doi.org/10.1126/science.1227670 PMID: 23239622.
14. Goldberg DE, Siliciano RF, Jacobs WR Jr. Outwitting evolution: fighting drug-resistant TB, malaria, and HIV. Cell. 2012; 148(6):1271–83. https://doi.org/10.1016/j.cell.2012.02.021 PMID: 22424234; PubMed Central PMCID: PMCPMC3322542.
15. Sanchez-Romero MA, Casadesus J. Contribution of phenotypic heterogeneity to adaptive antibiotic resistance. Proc Natl Acad Sci U S A. 2014; 111(1):355–60. https://doi.org/10.1073/pnas.1316084111 PMID: 24351930; PubMed Central PMCID: PMCPMC3890857.
16. Chait R, Palmer AC, Yelin I, Kishony R. Pervasive selection for and against antibiotic resistance in inhomogeneous multistress environments. Nat Commun. 2016; 7:10333. https://doi.org/10.1038/ncomms10333 PMID: 26787239; PubMed Central PMCID: PMCPMC4735756.
17. Levin-Reisman I, Ronin I, Gefen O, Braniss I, Shoresh N, Balaban NQ. Antibiotic tolerance facilitates the evolution of resistance. Science. 2017; 355(6327):826–30. https://doi.org/10.1126/science.aaj2191 PMID: 28183996.
18. Borowsky AD, Namba R, Young LJ, Hunter KW, Hodgson JG, Tepper CG, et al. Syngeneic mouse mammary carcinoma cell lines: two closely related cell lines with divergent metastatic behavior. Clin Exp Metastasis. 2005; 22(1):47–59. https://doi.org/10.1007/s10585-005-2908-5 PMID: 16132578.
19. Campbell MJ, Wollish WS, Lobo M, Esserman LJ. Epithelial and fibroblast cell lines derived from a spontaneous mammary carcinoma in a MMTV/neu transgenic mouse. In Vitro Cell Dev Biol Anim. 2002; 38(6):326–33. Epub 2003/01/07. https://doi.org/10.1290/1071-2690(2002)038<0326:EAFCLD>2.0.CO;2 PMID: 12513120.
20. McAllister SS, Gifford AM, Greiner AL, Kelleher SP, Saelzler MP, Ince TA, et al. Systemic endocrine instigation of indolent tumor growth requires osteopontin. Cell. 2008; 133(6):994–1005. https://doi.org/10.1016/j.cell.2008.04.045 PMID: 18555776; PubMed Central PMCID: PMCPMC4121664.
21. Plumer A, Duan H, Subramaniam S, Lucas FL, Miesfeldt S, Ng AK, et al. Development of fragment-specific osteopontin antibodies and ELISA for quantification in human metastatic breast cancer. BMC Cancer. 2008; 8:38. https://doi.org/10.1186/1471-2407-8-38 PMID: 18237408; PubMed Central PMCID: PMCPMC2259319.
22. Gu T, Ohashi R, Cui R, Tajima K, Yoshioka M, Iwakami S, et al. Osteopontin is involved in the development of acquired chemo-resistance of cisplatin in small cell lung cancer. Lung Cancer. 2009; 66 (2):176–83. https://doi.org/10.1016/j.lungcan.2009.02.004 PMID: 19285749.
23. Jia R, Liang Y, Chen R, Liu G, Wang H, Tang M, et al. Osteopontin facilitates tumor metastasis by regulating epithelial-mesenchymal plasticity. Cell Death Dis. 2016; 7(12):e2564. https://doi.org/10.1038/cddis.2016.422 PMID: 28032860; PubMed Central PMCID: PMCPMC5261026.
24. Liu G, Fan X, Tang M, Chen R, Wang H, Jia R, et al. Osteopontin induces autophagy to promote chemo-resistance in human hepatocellular carcinoma cells. Cancer Lett. 2016; 383(2):171–82. https://doi.org/10.1016/j.canlet.2016.09.033 PMID: 27702661.

25. Pang H, Cai L, Yang Y, Chen X, Sui G, Zhao C. Knockdown of osteopontin chemosensitizes MDA-MB-231 cells to cyclophosphamide by enhancing apoptosis through activating p38 MAPK pathway. Cancer Biother Radiopharm. 2011; 26(2):165–73. https://doi.org/10.1089/cbr.2010.0838 PMID: 21539449.

26. Sangaletti S, Tripodo C, Sandri S, Torselli I, Vitali C, Ratti C, et al. Osteopontin shapes immunosuppression in the metastatic niche. Cancer Res. 2014; 74(17):4706–19. https://doi.org/10.1158/0008-5472.CAN-13-3334 PMID: 25035397.

27. Singhal H, Bautista DS, Tonkin KS, O'Malley FP, Tuck AB, Chambers AF, et al. Elevated plasma osteopontin in metastatic breast cancer associated with increased tumor burden and decreased survival. Clin Cancer Res. 1997; 3(4):605–11. PMID: 9815727.

28. Tuck AB, Chambers AF, Allan AL. Osteopontin overexpression in breast cancer: knowledge gained and possible implications for clinical management. J Cell Biochem. 2007; 102(4):859–68. https://doi.org/10.1002/jcb.21520 PMID: 17721886.

29. Xu YY, Zhang YY, Lu WF, Mi YJ, Chen YQ. Prognostic value of osteopontin expression in breast cancer: A meta-analysis. Mol Clin Oncol. 2015; 3(2):357–62. https://doi.org/10.3892/mco.2014.480 PMID: 25798267; PubMed Central PMCID: PMCPMC4360850.

30. Luo SD, Chen YJ, Liu CT, Rau KM, Chen YC, Tsai HT, et al. Osteopontin Involves Cisplatin Resistance and Poor Prognosis in Oral Squamous Cell Carcinoma. Biomed Res Int. 2015; 2015:508587. https://doi.org/10.1155/2015/508587 PMID: 26491674; PubMed Central PMCID: PMCPMC4605257.

31. Ding K, Fan L, Chen S, Wang Y, Yu H, Sun Y, et al. Overexpression of osteopontin promotes resistance to cisplatin treatment in HCC. Oncol Rep. 2015; 34(6):3297–303. https://doi.org/10.3892/or.2015.4306 PMID: 26397192.

32. Ng L, Wan T, Chow A, Iyer D, Man J, Chen G, et al. Osteopontin Overexpression Induced Tumor Progression and Chemoresistance to Oxaliplatin through Induction of Stem-Like Properties in Human Colorectal Cancer. Stem Cells Int. 2015; 2015:247892. https://doi.org/10.1155/2015/247892 PMID: 26106421; PubMed Central PMCID: PMCPMC4461767.

33. Kennecke H, Yerushalmi R, Woods R, Cheang MC, Voduc D, Speers CH, et al. Metastatic behavior of breast cancer subtypes. Journal of clinical oncology: official journal of the American Society of Clinical Oncology. 2010; 28(20):3271–7. https://doi.org/10.1200/JCO.2009.25.9820 PMID: 20498394.

34. Wei R, Wong JPC, Kwok HF. Osteopontin—a promising biomarker for cancer therapy. J Cancer. 2017; 8(12):2173–83. https://doi.org/10.7150/jca.20480 PMID: 28819419; PubMed Central PMCID: PMCPMC5560134.

35. Graudens E, Boulanger V, Mollard C, Mariage-Samson R, Barlet X, Gremy G, et al. Deciphering cellular states of innate tumor drug responses. Genome Biol. 2006; 7(3):R19. https://doi.org/10.1186/gb-2006-7-3-r19 PMID: 16542501; PubMed Central PMCID: PMCPMC1557757.

36. Minn AJ, Gupta GP, Siegel PM, Bos PD, Shu W, Giri DD, et al. Genes that mediate breast cancer metastasis to lung. Nature. 2005; 436(7050):518–24. https://doi.org/10.1038/nature03799 PMID: 16049480; PubMed Central PMCID: PMCPMC1283098.

37. Richardson AL, Wang ZC, De Nicolo A, Lu X, Brown M, Miron A, et al. X chromosomal abnormalities in basal-like human breast cancer. Cancer Cell. 2006; 9(2):121–32. https://doi.org/10.1016/j.ccr.2006.01.013 PMID: 16473279.

38. van de Vijver MJ, He YD, van't Veer LJ, Dai H, Hart AA, Voskuil DW, et al. A gene-expression signature as a predictor of survival in breast cancer. N Engl J Med. 2002; 347(25):1999–2009. https://doi.org/10.1056/NEJMoa021967 PMID: 12490681.

39. Ramankulov A, Lein M, Kristiansen G, Meyer HA, Loening SA, Jung K. Elevated plasma osteopontin as marker for distant metastases and poor survival in patients with renal cell carcinoma. J Cancer Res Clin Oncol. 2007; 133(9):643–52. https://doi.org/10.1007/s00432-007-0215-z PMID: 17479289.

40. Shevde LA, Das S, Clark DW, Samant RS. Osteopontin: an effector and an effect of tumor metastasis. Curr Mol Med. 2010; 10(1):71–81. PMID: 20205680.

41. Cook AC, Tuck AB, McCarthy S, Turner JG, Irby RB, Bloom GC, et al. Osteopontin induces multiple changes in gene expression that reflect the six "hallmarks of cancer" in a model of breast cancer progression. Mol Carcinog. 2005; 43(4):225–36. https://doi.org/10.1002/mc.20105 PMID: 15864800.

42. Feng F, Rittling SR. Mammary tumor development in MMTV-c-myc/MMTV-v-Ha-ras transgenic mice is unaffected by osteopontin deficiency. Breast Cancer Res Treat. 2000; 63(1):71–9. PMID: 11079161.

43. Wai PY, Mi Z, Guo H, Sarraf-Yazdi S, Gao C, Wei J, et al. Osteopontin silencing by small interfering RNA suppresses in vitro and in vivo CT26 murine colon adenocarcinoma metastasis. Carcinogenesis. 2005; 26(4):741–51. https://doi.org/10.1093/carcin/bgi027 PMID: 15661802.

44. Wein L, Loi S. Mechanisms of resistance of chemotherapy in early-stage triple negative breast cancer (TNBC). Breast. 2017; 34 Suppl 1:S27–S30. https://doi.org/10.1016/j.breast.2017.06.023 PMID: 28668293.

Figure 1

A

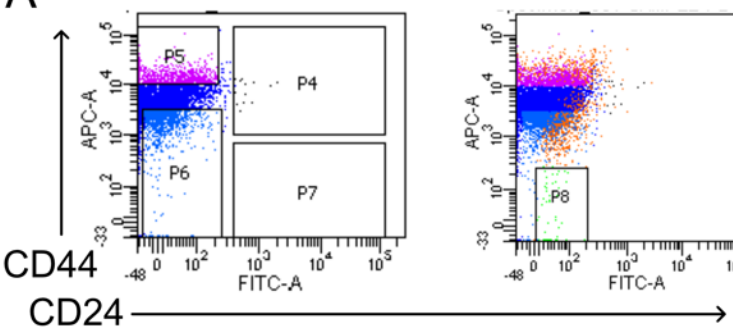

Gate	CD44/CD24 Profile	# of CPs
P4	$CD44^{+}/CD24^{+}$	3
P5	$CD44^{hi}/CD24^{-}$	10
P6	$CD44^{+}/CD24^{-}$	9
P7	$CD44^{-}/CD24^{+}$	0
P8	$CD44^{-}/CD24^{-}$	8

B

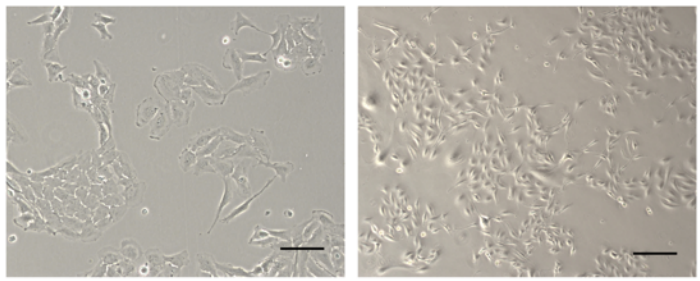

C

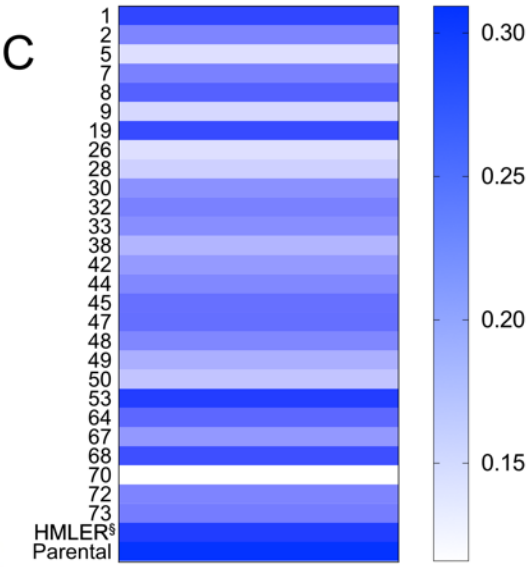

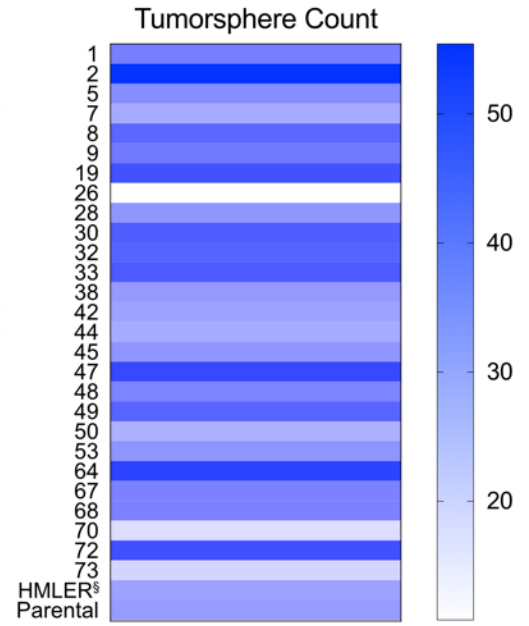

D

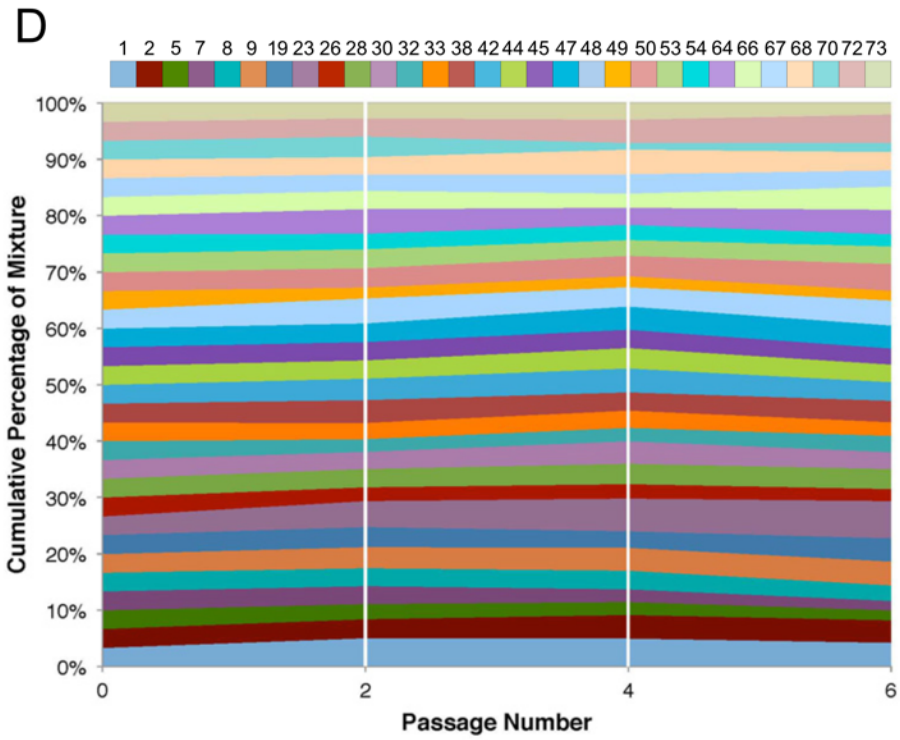

Figure 1. HMLER clonal populations are functional heterogeneous. **(A)** CD44/CD24 gating strategy for FACS to isolate single cell clones that were used to generate thirty clonal populations from the HMLER-HR-tdTomato cell line. **(B)** Phase microscopy images of two CPs with varying degrees of epithelial and mesenchymal morphology. Scale bars = 100 µm. **(C)** Heat maps representing range of proliferation rates and tumorsphere formation rates of individual CPs, HMLER§, and the parental HMLER-HR-tdTomato (HMLER^{P}) cell line. **(D)** Sandplot showing clonal composition of HMLER§ over 6 passages *in vitro*.

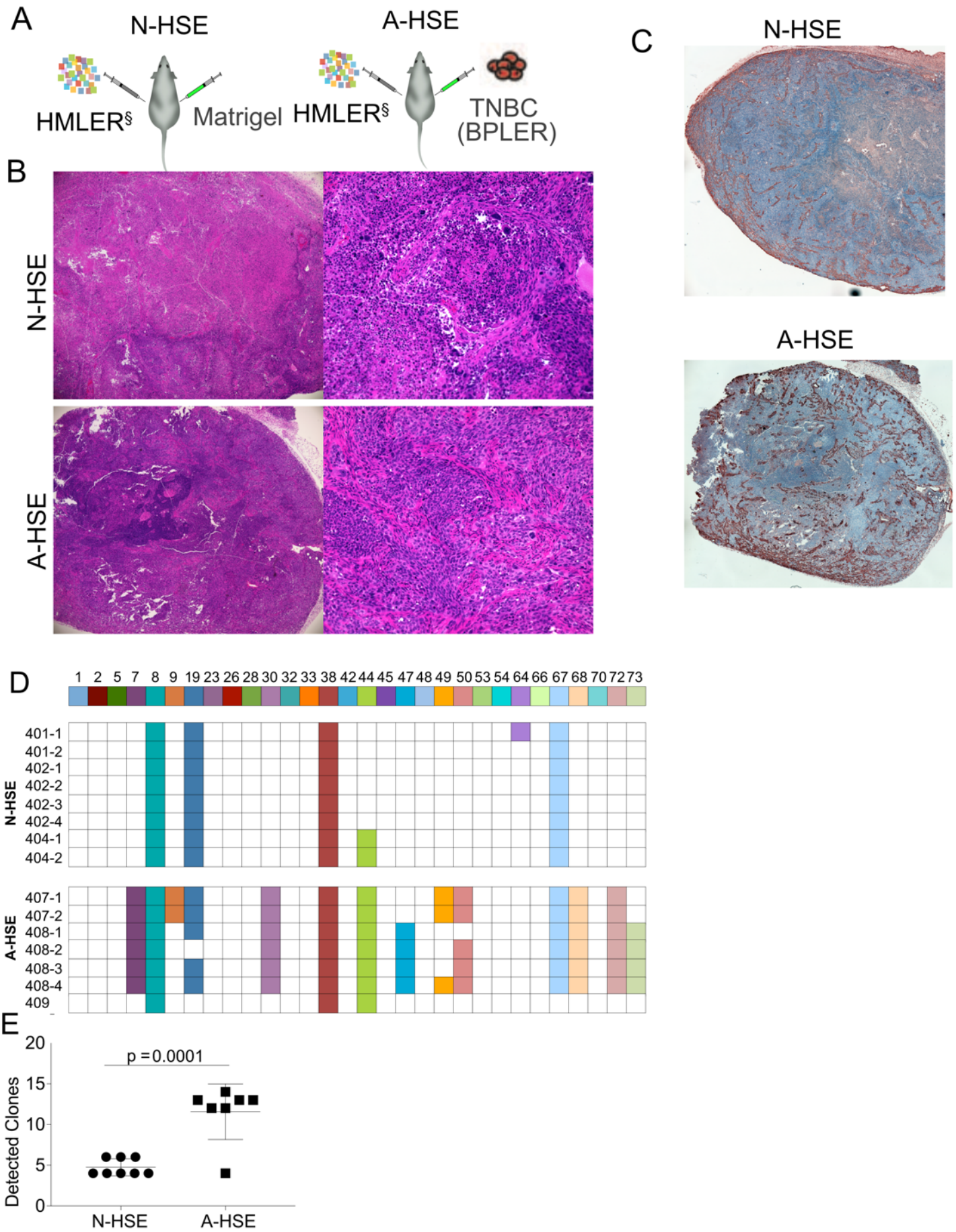
A
N-HSE
A-HSE
HMLER§
Matrigel
HMLER§
TNBC
(BPLER)
B
N-HSE
A-HSE
C
N-HSE
A-HSE
D
1 2 5 7 8 9 19 23 26 28 30 32 33 38 42 44 45 47 48 49 50 53 54 64 66 67 68 70 72 73
N-HSE
401-1
401-2
402-1
402-2
402-3
402-4
404-1
404-2
A-HSE
407-1
407-2
408-1
408-2
408-3
408-4
409
E
p = 0.0001
Detected Clones
20
15
10
5
0
N-HSE
A-HSE

Figure 2. HMLER§ tumors recovered from the activated host systemic environment are more heterogeneous than those in the naïve host systemic environment. (A) Experimental schema for HMLER§ cell line injection into the naïve host systemic environment (N-HSE) and activated host systemic environment (A-HSE). **(B)** Representative images from hematoxylin and eoisin (H&E) stained HMLER§ tumors recovered from N-HSE and A-HSE cohorts. Left panels imaged at 4x, right panels imaged at 20x. **(C)** Representative images from HMLER§ tumors recovered from N-HSE and A-HSE cohorts that were stained for α-SMA (brown) and counterstained with hematoxylin. Tumors imaged at 20x. **(D)** Representation of PRISM detected barcodes in individual HMLER§ tumors recovered from mice in the N-HSE and A-HSE cohorts. Individual tumors are represented across rows and barcode identity is represented along columns. **(E)** Number of detected CPs per HMLER§ tumor. Each point represents an individual tumor. Bars represent mean and SD (N-HSE n = 8, A-HSE n = 7; unpaired, two-tailed t-test).

A

N-HSE

A-HSE

Neutrophils (MPO)

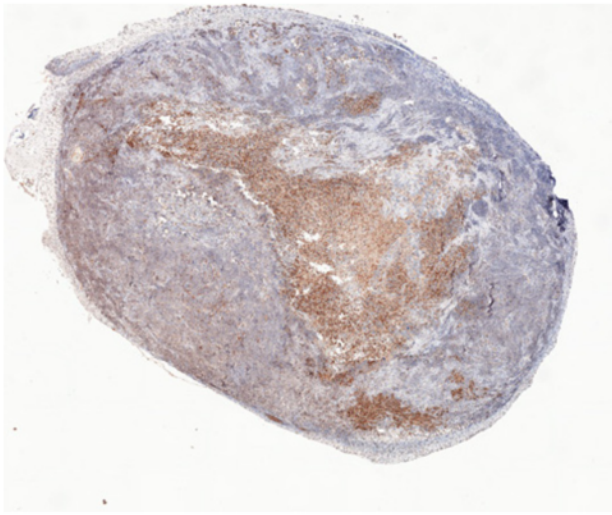

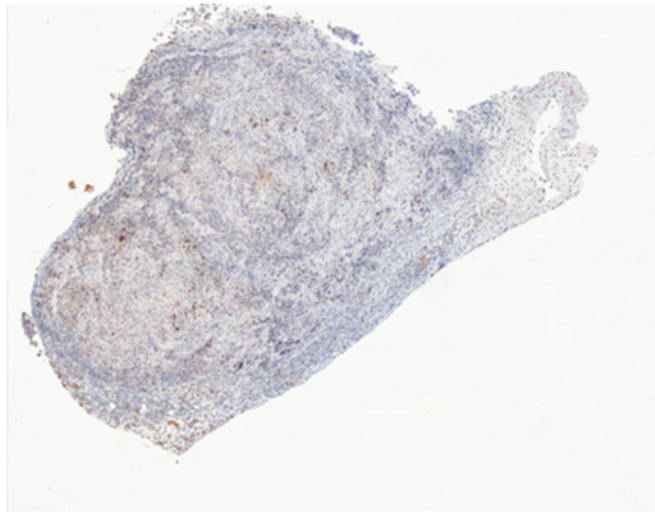

B

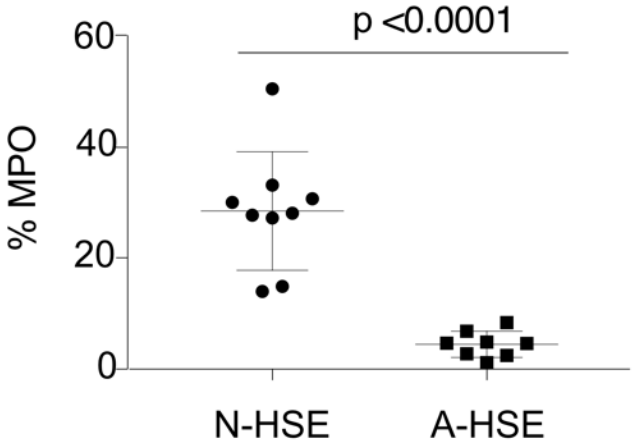

C

N-HSE

A-HSE

Macrophages (F4/80)

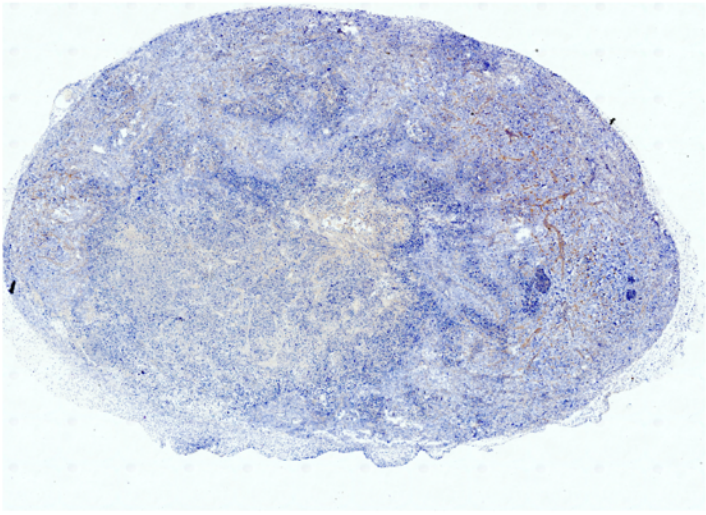

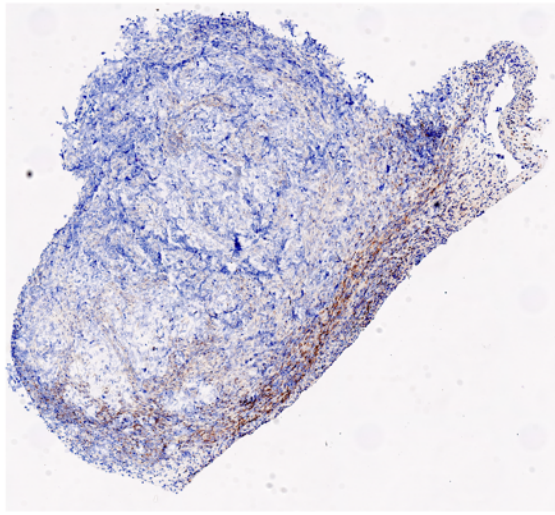

Figure 3. HMLER§ tumors in N-HSE and A-HSE have different patterns of innate immune infiltration. (A) Representative images of HMLER§ tumors recovered from N-HSE and A-HSE cohorts stained for MPO (brown) and counterstained with hematoxylin. Images were captured at 20x magnification. **(B)** Percent of cells that stained positively for MPO. Points represent individual tumors. Error bars represent mean and SD (N-HSE: n = 9; A-HSE: n = 8; unpaired, two-tailed T-test). **(C)** Representative images of HMLER§ tumors recovered from N-HSE and A-HSE cohorts stained for F4/80 (brown) and counterstained with hematoxylin. Images were captured at 20x magnification.

Figure 4

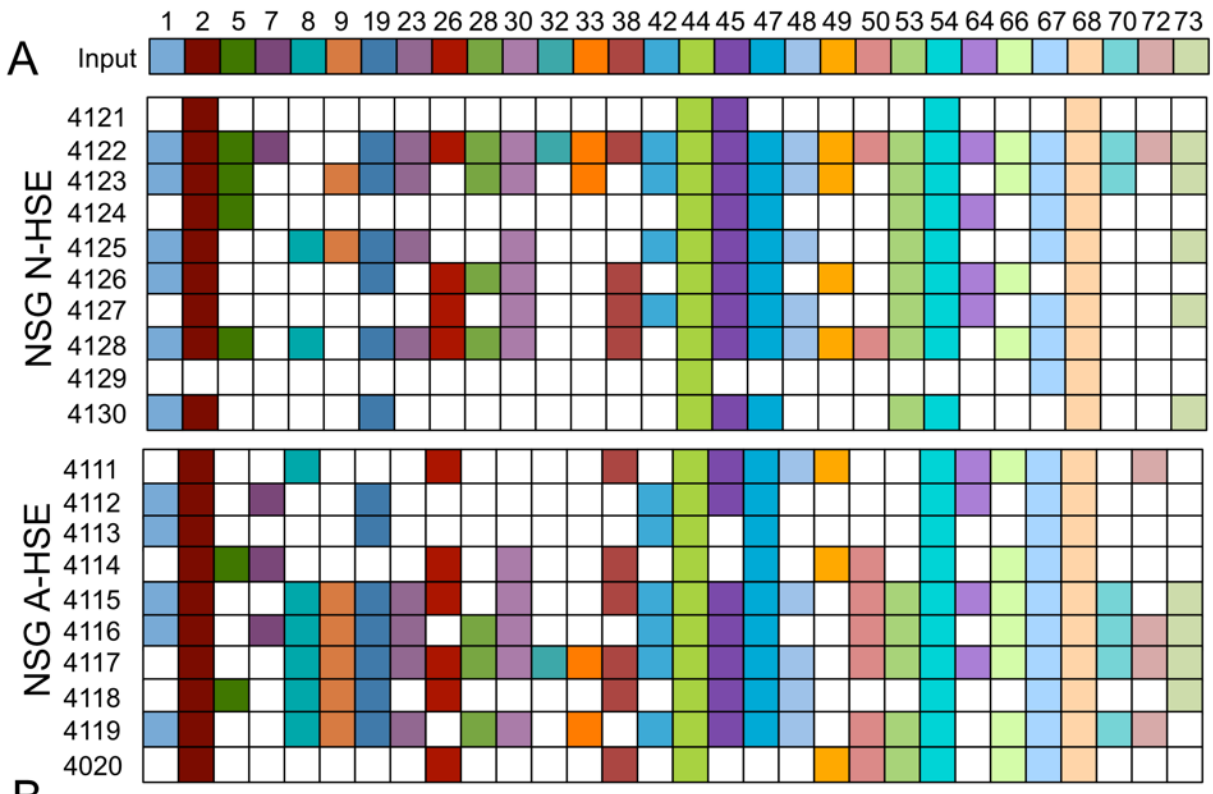
A
Input
1 2 5 7 8 9 19 23 26 28 30 32 33 38 42 44 45 47 48 49 50 53 54 64 66 67 68 70 72 73
NSG N-HSE
4121
4122
4123
4124
4125
4126
4127
4128
4129
4130
NSG A-HSE
4111
4112
4113
4114
4115
4116
4117
4118
4119
4020

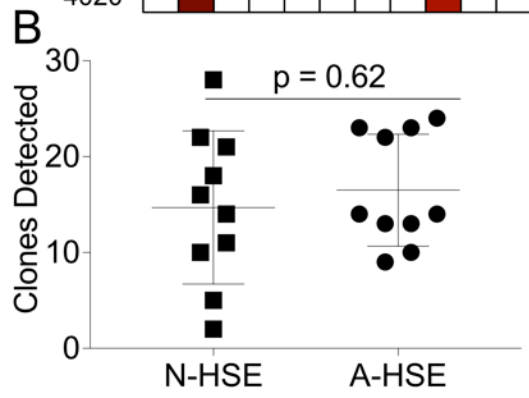
B
p = 0.62
Clones Detected
30
20
10
0
N-HSE
A-HSE

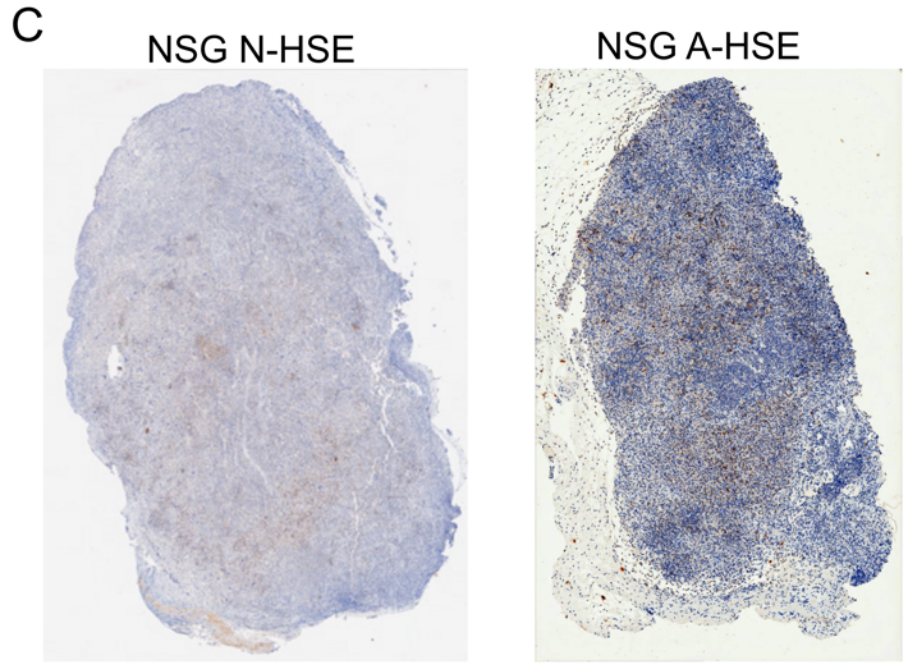
C
NSG N-HSE
NSG A-HSE

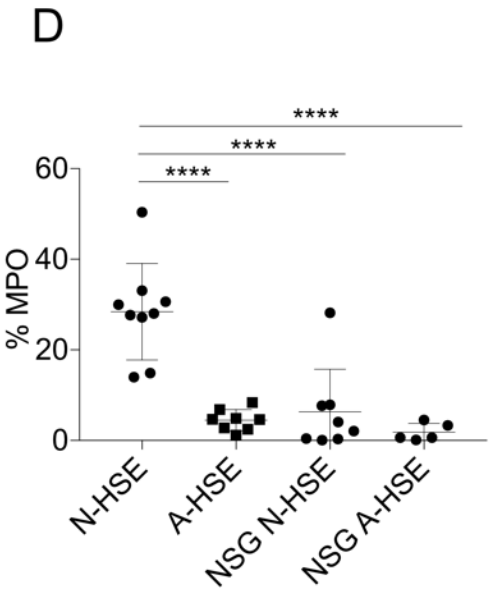
D
****
****
****
% MPO
60
40
20
0
N-HSE
A-HSE
NSG N-HSE
NSG A-HSE

Figure 4. **A functional innate immune system is required for enhanced heterogeneity in A-HSE HMLER§ tumors. (A)** Representation of next-generation sequencing detected barcodes in individual HMLER§ tumors recovered from NSG mice in the N-HSE and A-HSE cohorts. Individual tumors are represented across rows and barcode identity is represented along columns. **(B)** Number of detected CPs per HMLER§ tumor. Each point represents an individual tumor. Bars represent mean and SD (N-HSE: n = 10, A-HSE: n = 10; Mann-Whitney test). **(C)** Representative images of HMLER§ tumors recovered from NSG N-HSE and NSG A-HSE cohorts stained for MPO (brown) and counterstained with hematoxylin. Images were captured at 20x magnification. **(D)** Percent of cells that stained positively for MPO in indicated cohorts. Points represent individual tumors. Error bars represent mean and SD (N-HSE: n = 9; A-HSE: n = 8; NSG N-HSE: n = 10; NSG A-HSE: n = 10; **** = $p < 0.0001$, Ordinary one-way ANOVA, Tukey's Multiple Comparisons Test).

Figure 5

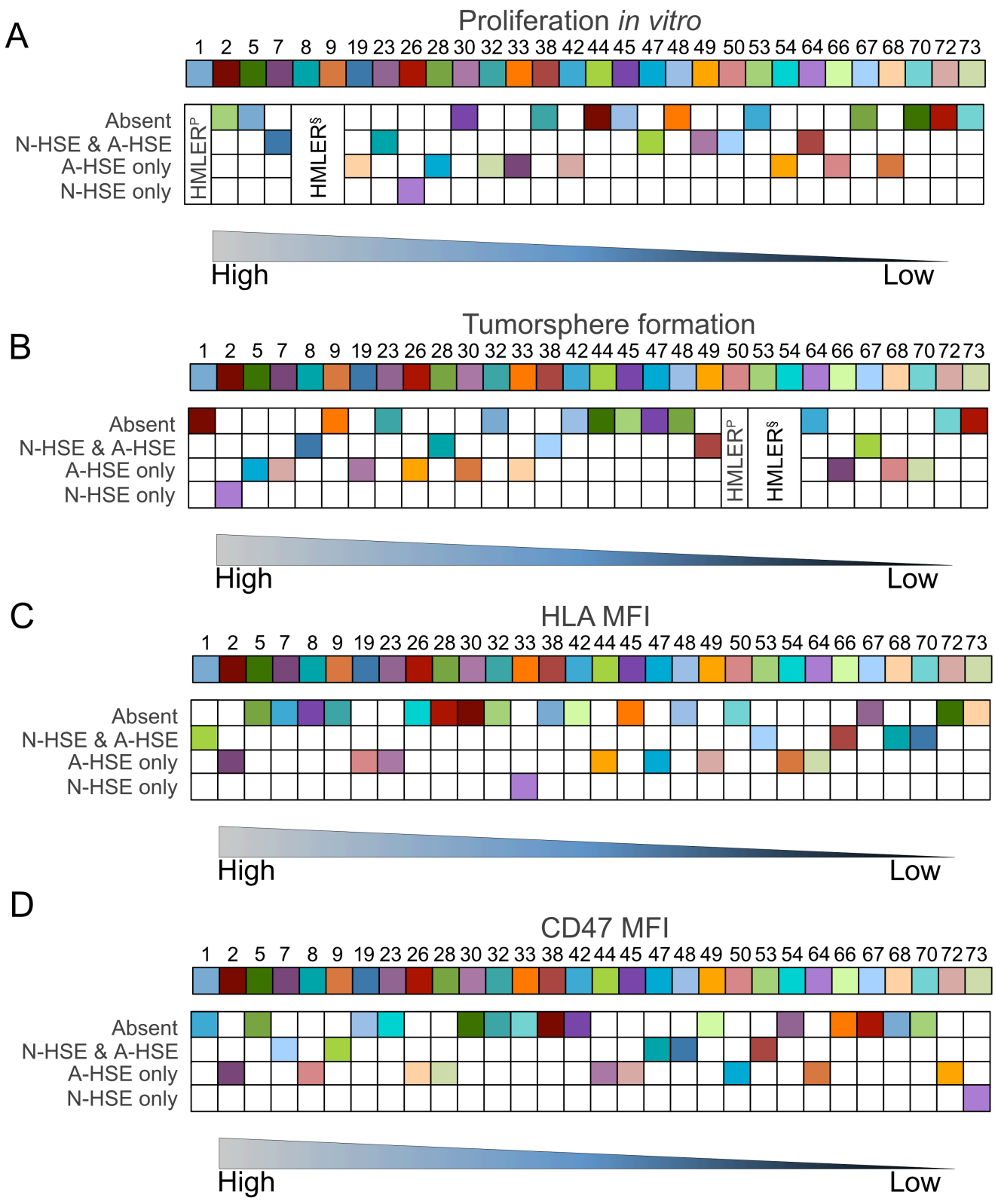
A
Proliferation *in vitro*
1 2 5 7 8 9 19 23 26 28 30 32 33 38 42 44 45 47 48 49 50 53 54 64 66 67 68 70 72 73
Absent
N-HSE & A-HSE
A-HSE only
N-HSE only
HMLER^{P}
HMLER^{S}
High
Low
B
Tumorsphere formation
1 2 5 7 8 9 19 23 26 28 30 32 33 38 42 44 45 47 48 49 50 53 54 64 66 67 68 70 72 73
Absent
N-HSE & A-HSE
A-HSE only
N-HSE only
HMLER^{P}
HMLER^{S}
High
Low
C
HLA MFI
1 2 5 7 8 9 19 23 26 28 30 32 33 38 42 44 45 47 48 49 50 53 54 64 66 67 68 70 72 73
Absent
N-HSE & A-HSE
A-HSE only
N-HSE only
High
Low
D
CD47 MFI
1 2 5 7 8 9 19 23 26 28 30 32 33 38 42 44 45 47 48 49 50 53 54 64 66 67 68 70 72 73
Absent
N-HSE & A-HSE
A-HSE only
N-HSE only
High
Low

Figure 5. Cell intrinsic properties of individual CPs do not explain selection patterns observed *in vivo*. A-D: Individual CPs evaluated for their proliferation kinetics rates (A), tumorsphere formation rates (B), HLA-1 expression levels (quantified using median fluorescence intensity, MFI) (C), and CD47 expression levels (D). CP identities are represented using color and are placed in columns arranged from highest to lowest values from left to right. CPs were placed in the row that corresponds to their presence or absence from HMLER§ tumors in the N-HSE, A-HSE, or both environments in the *in vivo* selection experiment represented in **Figure 2**.

Figure 6

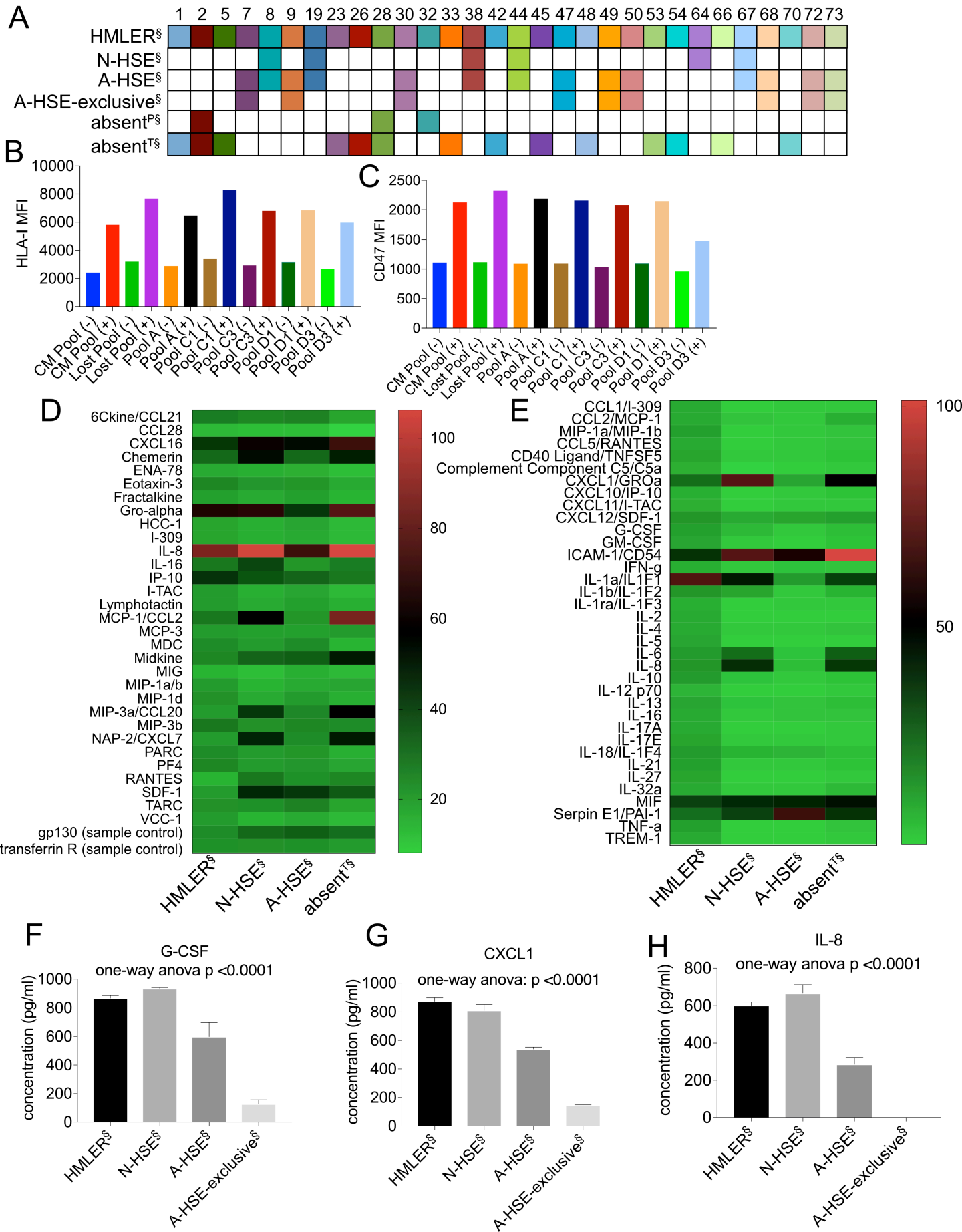
A
1 2 5 7 8 9 19 23 26 28 30 32 33 38 42 44 45 47 48 49 50 53 54 64 66 67 68 70 72 73
HMLER§
N-HSE§
A-HSE§
A-HSE-exclusive§
absentP§
absentT§
B
HLA-I MFI
10000
8000
6000
4000
2000
0
CM Pool (-)
CM Pool (+)
Lost Pool (-)
Lost Pool (+)
Pool A (-)
Pool A (+)
Pool C1 (-)
Pool C1 (+)
Pool C3 (-)
Pool C3 (+)
Pool D1 (-)
Pool D1 (+)
Pool D3 (-)
Pool D3 (+)
C
CD47 MFI
2500
2000
1500
1000
500
0
CM Pool (-)
CM Pool (+)
Lost Pool (-)
Lost Pool (+)
Pool A (-)
Pool A (+)
Pool C1 (-)
Pool C1 (+)
Pool C3 (-)
Pool C3 (+)
Pool D1 (-)
Pool D1 (+)
Pool D3 (-)
Pool D3 (+)
D
6Ckine/CCL21
CCL28
CXCL16
Chemerin
ENA-78
Eotaxin-3
Fractalkine
Gro-alpha
HCC-1
I-309
IL-8
IL-16
IP-10
I-TAC
Lymphotactin
MCP-1/CCL2
MCP-3
MDC
Midkine
MIG
MIP-1a/b
MIP-1d
MIP-3a/CCL20
MIP-3b
NAP-2/CXCL7
PARC
PF4
RANTES
SDF-1
TARC
VCC-1
gp130 (sample control)
transferrin R (sample control)
100
80
60
40
20
HMLER§
N-HSE§
A-HSE§
absentT§
E
CCL1/I-309
CCL2/MCP-1
MIP-1a/MIP-1b
CCL5/RANTES
CD40 Ligand/TNFSF5
Complement Component C5/C5a
CXCL1/GROa
CXCL10/IP-10
CXCL11/I-TAC
CXCL12/SDF-1
G-CSF
GM-CSF
ICAM-1/CD54
IFN-g
IL-1a/IL1F1
IL-1b/IL-1F2
IL-1ra/IL-1F3
IL-2
IL-4
IL-5
IL-6
IL-8
IL-10
IL-12 p70
IL-13
IL-16
IL-17A
IL-17E
IL-18/IL-1F4
IL-21
IL-27
IL-32a
MIF
Serpin E1/PAI-1
TNF-a
TREM-1
100
50
HMLER§
N-HSE§
A-HSE§
absentT§
F
G-CSF
one-way anova p <0.0001
concentration (pg/ml)
1000
800
600
400
200
0
HMLER§
N-HSE§
A-HSE§
A-HSE-exclusive§
G
CXCL1
one-way anova: p <0.0001
concentration (pg/ml)
1000
800
600
400
200
0
HMLER§
N-HSE§
A-HSE§
A-HSE-exclusive§
H
IL-8
one-way anova p <0.0001
concentration (pg/ml)
800
600
400
200
0
HMLER§
N-HSE§
A-HSE§
A-HSE-exclusive§

Figure 6. HMLER§ subpools exhibit unique patterns of cytokine and chemokine secretion. (A) HMLER§ subpools that resembled HMLER§ tumor clonal composition in the experiment represented in **Figure 2** were generated by mixing equal numbers of the indicated CPs. **(B)** HLA-I median fluorescence intensity (MFI) values of CP subpools that had been cultured in the absence (-) or presence (+) of IFN-gamma. **(C)** CD47 median fluorescence intensity (MFI) values of CP subpools that had been cultured in the absence (-) or presence (+) of IFN-gamma. **(D)** Heat map representing protein array quantifications of chemokine expression levels in conditioned media from the indicated HMLER§ subpools. **(E)** Heat map representing protein array quantifications of cytokine expression levels in cell lysates of the indicated HMLER§ subpools.**(F-H)** Expression levels G-CSF (F), CXCL1 (G), and IL-8 (H) in conditioned media of the indicated HMLER§ subpools as measured by ELISA. Error bars represent SD (n = 3 per condition, one-way ANOVA).

Figure 7

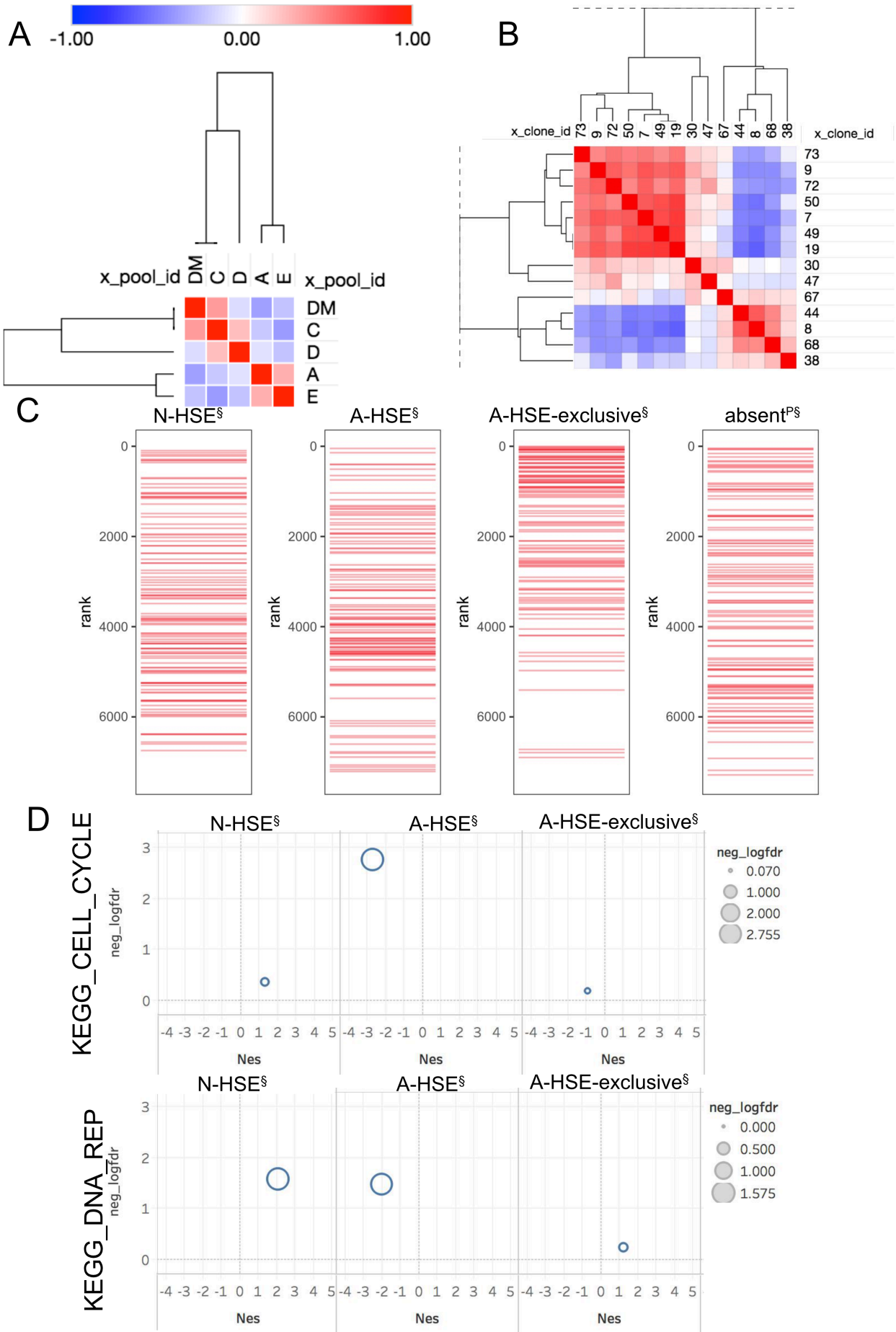
A
-1.00
0.00
1.00
x_pool_id
DM
C
D
A
E
B
x_clone_id
73
9
72
50
7
49
19
30
47
67
44
8
68
38
C
N-HSE§
A-HSE§
A-HSE-exclusive§
absentPS§
rank
0
2000
4000
6000
D
KEGG_CELL_CYCLE
KEGG_DNA_REP
neg_logfdr
Nes
-4 -3 -2 -1 0 1 2 3 4 5
neg_logfdr
0.070
1.000
2.000
2.755
0.000
0.500
1.000
1.575

Figure 7. HMLER§ subpools have unique gene expression signatures despite containing common CPs. (A) Hierarchical clustering of the HMLER§ subpools L1000 gene expression signatures. **(B)** Hierarchical clustering of individual CP L1000 gene expression signatures within A-HSE§. **(C)** Tick plots showing the position of each TNBC sample in the ranked list of connectivities between all TCGA breast cancer samples (~7k) and the L1000 gene expression signature of each HMLER§ pool. **(D)** Volcano plots showing Normalized enrichment score (Nes) and the corresponding –log(FDR) for the indicated KEGG pathways for various HMLER§ subpools.

A

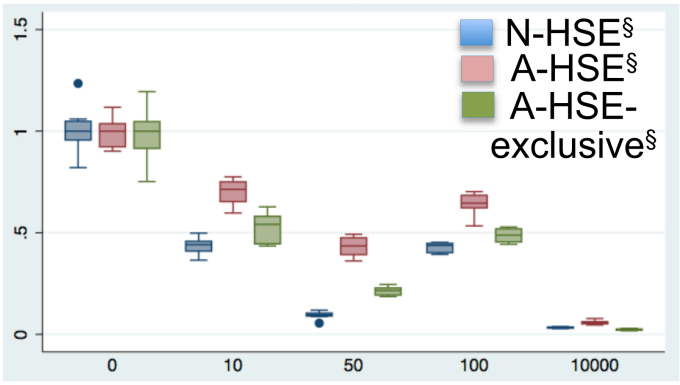

Drug	Lower Survival	p value
5-FU	N-HSE§	5.5 e-11
Paclitaxel	N-HSE§	8.7 e-05
Doxorubicin	N-HSE§	5.4 e-13

B

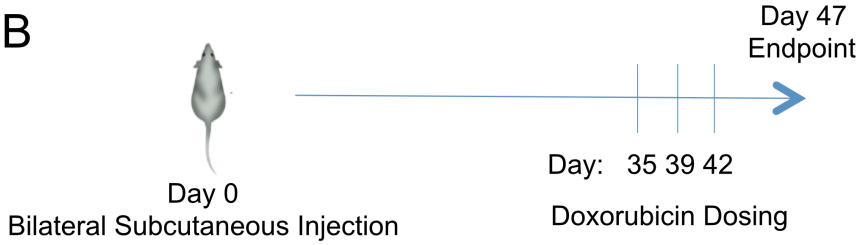

C

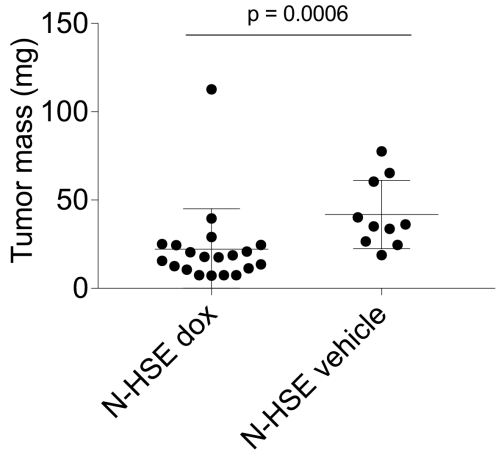

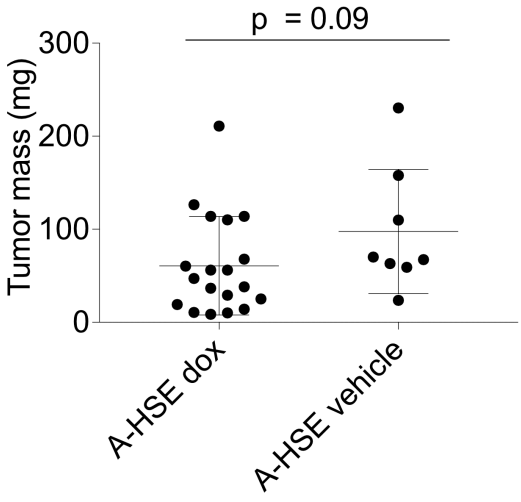

Figure 8. N-HSE§ subpool is more chemosensitive than A-HSE§ subpool both *in vitro* and *in vivo*. (A) Fractional survival (y-axis) of subpools following 72 hours of treatment with doxorubicin (concentrations along x-axis: 0 nM, 10 nM, 50 nM, 100 nM, and 10 uM). A two-sided Wilcoxon rank sum test, stratified for dose, was used to compare fractional survival of N-HSE§ to A-HSE§. **(B)** Experimental schema for *in vivo* doxorubicin study. **(C)** Final tumor mass for N-HSE§ to A-HSE§ tumors (N-HSE dox: n=20; N-HSE vehicle: n=10; A-HSE dox: n=19; A-HSE vehicle: n=8; Mann-Whitney test).

ARTICLES
https://doi.org/10.1038/s41556-018-0173-5
nature cell biology

IL-1β inflammatory response driven by primary breast cancer prevents metastasis-initiating cell colonization

Zafira Castaño[1,2], Beatriz P. San Juan[3], Asaf Spiegel[4], Ayush Pant[4], Molly J. DeCristo[1,2], Tyler Laszewski[1], Jessalyn M. Ubellacker[1,2], Susanne R. Janssen[4], Anushka Dongre[4], Ferenc Reinhardt[4], Ayana Henderson[1,2], Ana Garcia del Rio[1], Ann M. Gifford[4], Zachary T. Herbert[5], John N. Hutchinson[6], Robert A. Weinberg[4,7], Christine L. Chaffer[3,4,10*] and Sandra S. McAllister[1,2,8,9,10*]

Lack of insight into mechanisms governing breast cancer metastasis has precluded the development of curative therapies. Metastasis-initiating cancer cells (MICs) are uniquely equipped to establish metastases, causing recurrence and therapeutic resistance. Using various metastasis models, we discovered that certain primary tumours elicit a systemic inflammatory response involving interleukin-1β (IL-1β)-expressing innate immune cells that infiltrate distant MIC microenvironments. At the metastatic site, IL-1β maintains MICs in a ZEB1-positive differentiation state, preventing MICs from generating highly proliferative E-cadherin-positive progeny. Thus, when the inherent plasticity of MICs is impeded, overt metastases cannot be established. Ablation of the pro-inflammatory response or inhibition of the IL-1 receptor relieves the differentiation block and results in metastatic colonization. Among patients with lymph node-positive breast cancer, high primary tumour IL-1β expression is associated with better overall survival and distant metastasis-free survival. Our data reveal complex interactions that occur between primary tumours and disseminated MICs that could be exploited to improve patient survival.

Patients with breast cancer often exhibit no evidence of disseminated disease at initial diagnosis, yet ~20% of patients ultimately relapse[1]. Metastatic dissemination often begins at early stages[2,3], yielding many latent micrometastases. By some estimates, less than 0.02% of those disseminated tumour cells will form secondary tumours, indicating that successful metastatic colonization is rare[4–6] and ascribed to only specialized minority cancer cells, termed MICs[7].

The seemingly simultaneous emergence of clinically detectable metastases has led to the notion that reactivation of secondary lesions from dormancy is triggered systemically[8,9]. Preclinical modelling has revealed that primary tumours influence metastasis by modulating both systemic and secondary tumour microenvironments before and after dissemination[10–15]. The role of the immune system during these processes is particularly complex[16]. Little is known about the impact of the immune system on MIC colonization or the context in which primary tumour-driven pathophysiology will prove to be pro- or antimetastatic.

Successful metastatic colonization is also largely dependent on the inherent biology of the tumour cell. Cellular plasticity is a fundamental component of several leading metastasis models, including co-option of developmental pathways, the epithelial-to-mesenchymal transition (EMT) and cancer stem cell models[17]. Once MICs reach a distant tissue, the necessity of cellular plasticity to developing overt metastatic lesions remains to be determined. Clinical and preclinical findings therefore provoke the question of whether the success of disseminated MICs is influenced by overall disease pathophysiology.

Results

Identification of primary tumours that inhibit metastatic colonization. To determine whether primary tumours influence colonization of disseminated MICs, we first employed a polyclonal metastatic mammary carcinoma cell line, Met1, derived from a spontaneous lung metastasis in an FVB/N-Tg(MMTV-PyMT) mouse[18]. Met1 cells or PBS vehicle control were injected orthotopically into FVB mice. After 2 weeks, when primary tumours reached ~100 mm^3 (Supplementary Fig. 1a), we synchronized metastasis by injecting the same heterogeneous Met1 population intravenously (Fig.1a), whereby only the MIC subpopulation should be capable of seeding metastases[19]. Lungs were analysed after a subsequent 2-week period.

In three independent experiments, the control cohort developed overt pulmonary metastases while no macrometastases were observed in mice bearing orthotopic Met1 primary tumours (Fig. 1b,c). Importantly, orthotopic Met1 primary tumours did not inhibit the development of Met1 secondary tumours that were injected subcutaneously (Supplementary Fig. 1b), an injection scheme that does not provide selection pressure for murine MIC (mMIC)

[1]Division of Hematology, Department of Medicine, Brigham and Women's Hospital, Boston, MA, USA. [2]Department of Medicine, Harvard Medical School, Boston, MA, USA. [3]The Kinghorn Cancer Centre, Garvan Institute of Medical Research, Darlinghurst, New South Wales, Australia. [4]Whitehead Institute for Biomedical Research, Cambridge, MA, USA. [5]Molecular Biology Core Facilities, Dana-Farber Cancer Institute, Boston, MA, USA. [6]Department of Biostatistics, Harvard T.H. Chan, School of Public Health, Boston, MA, USA. [7]MIT Department of Biology and Ludwig/MIT Center for Molecular Oncology, Cambridge, MA, USA. [8]Broad Institute of Harvard and MIT, Cambridge, MA, USA. [9]Harvard Stem Cell Institute, Cambridge, MA, USA. [10]These authors contributed equally to this work: Christine L. Chaffer, Sandra S. McAllister. *e-mail: c.chaffer@garvan.org.au; smcallister1@bwh.harvard.edu

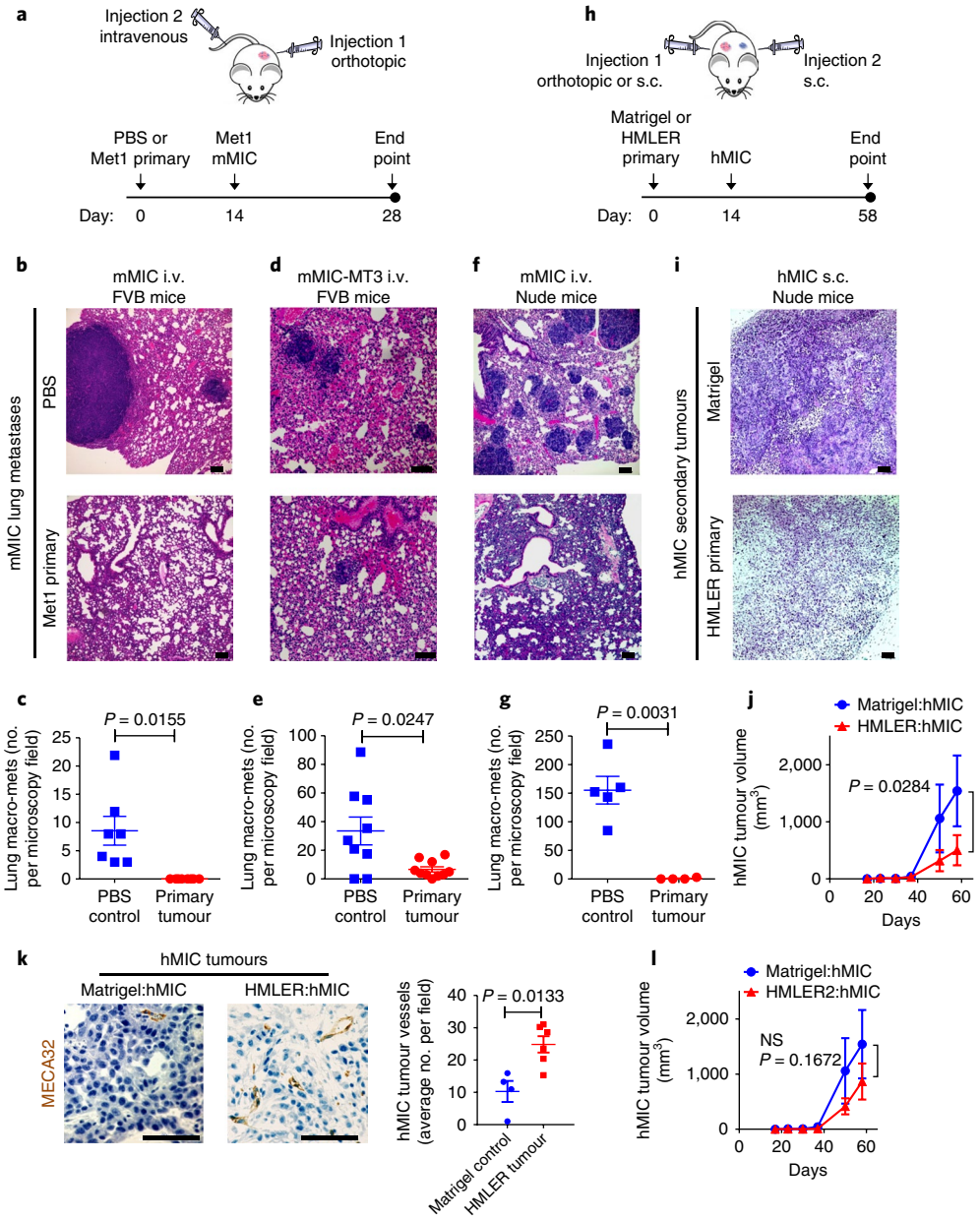

Fig. 1 | Primary tumours inhibit the outgrowth of distant MICs independently of the adaptive immune system. a, Schematic modelling the early stages of mMIC lung colonization in the presence of a Met1 primary tumour in FVB (**b**–**e**) or nude (**f**,**g**) mice. PBS vehicle is the control for primary tumours. Met1 cells (2.5×10^5 per mouse) or PBS control (20 µl) were injected into a single fourth inguinal mammary fat pad at day 0. On day 14, Met1 cells (mMIC) or the Met1-derived clone MT3 (mMIC-MT3) were injected intravenously (i.v.; tail vein) (7.5×10^5 cells per mouse). Primary tumour growth kinetics were monitored from day 0; pulmonary metastases were quantified at experimental end points. **b**,**d**,**f**, H&E images of lungs from mice bearing Met1 primary tumours or PBS control. **c**,**e**,**g**, Macrometastases (macro-mets) >100 µm quantified from microscopy tissue sections from 4 lung lobes per animal for mMIC metastases in FVB mice (PBS, $n=7$ animals; Met1, $n=8$ animals) (**c**), mMIC-MT3 metastases in FVB mice (PBS, $n=9$ animals; Met1, $n=10$ animals) (**e**), and mMIC metastases in nude mice (PBS, $n=5$ animals; Met1, $n=4$ animals) (**g**). **h**, Schematic modelling the early stages of hMIC colonization in the presence of a HMLER primary tumour in nude mice (**i**–**k**). Matrigel vehicle is the experimental control for primary tumours. HMLER cells (5.0×10^5 per mouse) or Matrigel control (100 µl) were injected subcutaneously (s.c.) into one flank at day 0. Two weeks later, hMIC (2.5×10^5 cells per mouse) were injected subcutaneously into the contralateral flank. Growth kinetics were monitored for the duration of the experiment. **i**, H&E images of hMIC tumours from mice bearing HMLER primary tumours or Matrigel control. **j**, hMIC tumour growth kinetics in mice bearing Matrigel control ($n=9$ animals) or HMLER primary tumours ($n=10$ animals). **k**, Left: hMIC tumours opposite Matrigel ($n=25$ images representing 4 tumours) or HMLER primary tumours ($n=25$ images representing 6 tumours), stained for mouse panendothelial cell antigen (MECA32). Right: mean vessel number per microscopy field. **l**, Tumour growth kinetics of hMIC implanted opposite Matrigel control or an HMLER2 primary tumour ($n=10$ animals per cohort), per protocol in 1 h. All scale bars, 100 µm. Source data for **c**, **e**, **g**, **j**, **k** and **l** are provided in Supplementary Table 1. Welch's two-sided *t*-test (**c**, **e**, **g** and **k**); Two-way ANOVA followed by Sidak's multiple comparison test (**j** and **l**).

subpopulations[19]. These results suggested that Met1 primary tumours specifically inhibit growth driven by their MICs and not the bulk, heterogeneous population of tumour cells.

We previously generated a series of single cell-derived clones from the parental Met1 line[20]. To identify a purified population of Met1 mMICs, we tested the metastatic potential of two of

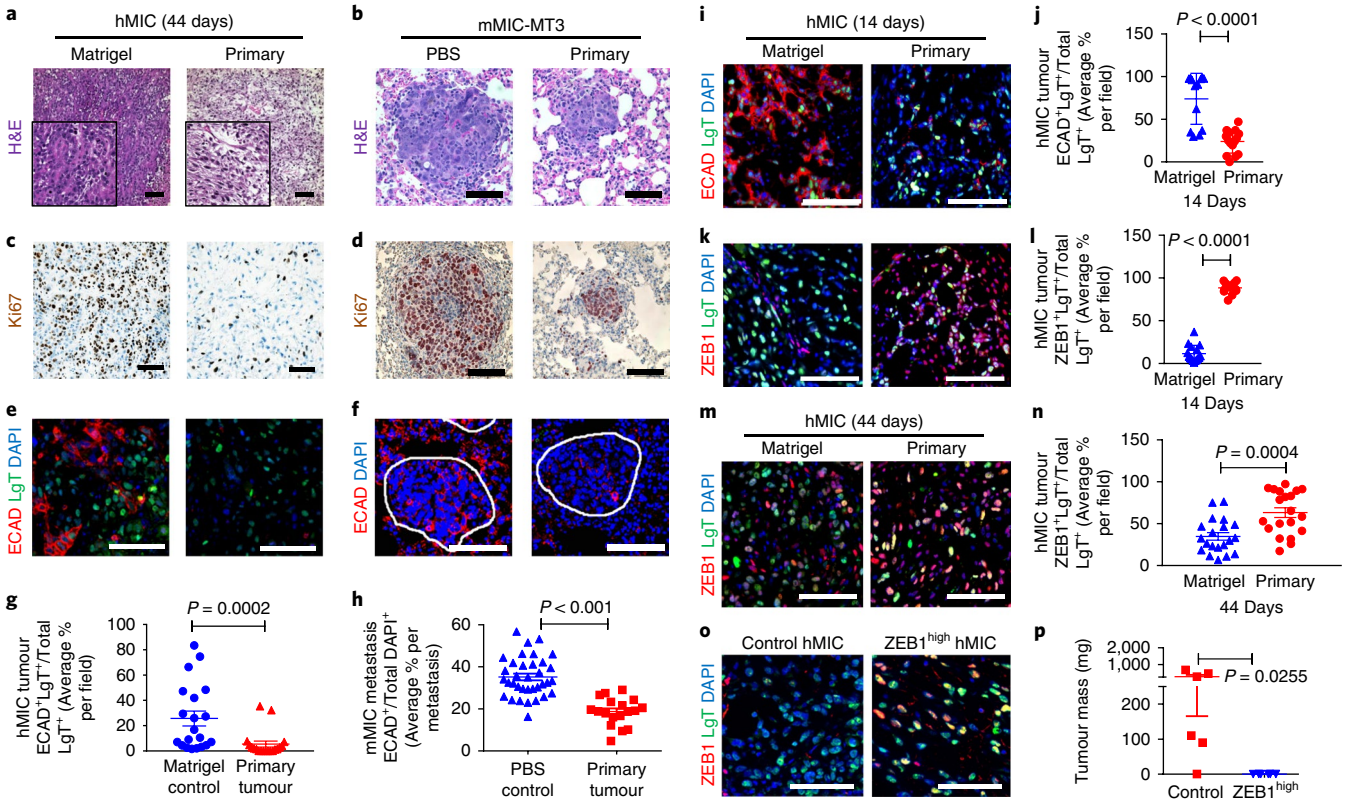

Fig. 2 | Primary tumours prevent the differentiation and proliferation of distant MICs. a–d, hMIC secondary tumours and mMIC-MT3 pulmonary metastases (per the schematics in Fig. 1a,h) stained with H&E. Inset images (black boxes) represent 2× enlargment of image beneath. (**a**,**b**), and Ki67 (brown) and haematoxylin (nuclei; blue) (**c**,**d**). **e**,**f**, Immunofluorescence for E-cadherin (ECAD; red), large T antigen (LgT; green) to identify hMICs, and DAPI (nuclei; blue), with lung metastases circled in white. **g**,**h**, ECAD$^+$ cells as the percentage of the total number of LgT$^+$ tumour cells (**g**) or DAPI$^+$ cells (**h**) per microscopy field (ECAD in hMIC tumours, $n=20$ images representing 5 tumours per cohort; ECAD in mMIC-MT3 metastasis, $n=52$ images representing at least 18 metastases per cohort). **i**-**l**, Immunofluorescence images of hMIC tumours after 14 days of growth stained with ECAD (**i**) and quantified (**j**) (Matrigel cohort, $n=15$ images; HMLER cohort, $n=13$ images) or ZEB1 (**k**) and quantified (**l**) (Matrigel cohort, $n=13$ images; HMLER cohort. $n=16$ images); **j** and **l** are presented as the percentage of the total number of LgT$^+$ hMIC tumour cells. **m**,**n**, hMIC tumours after 44 days of growth (per Fig. 1a). Immunofluorescence images (**m**) and quantification (**n**) of ZEB1 staining (red) in hMIC tumours (positive for LgT antigen; green), as a percentage of the total of LgT$^+$ cells. DAPI (nuclei; blue). Control, $n=20$ independent images representing 3 tumours; HMLER cohort, $n=20$ independent images representing 3 tumours. **o**, ZEB1 (red), LgT$^+$ tumour cells (green), and DAPI (nuclei; blue) in hMIC tumours expressing either doxycycline-inducible control (control hMIC) or ZEB1 cDNA (ZEB1^{high} hMIC). All scale bars, 100 μm. **p**, Final mass of hMIC tumours from (**o**) (Control hMIC, $n=6$ tumours; ZEB1^{high} hMIC, $n=6$ tumours). Source data for **g**, **h**, **j**, **l**, **n** and **p** are provided in Supplementary Table 1. Two-sided Mann–Whitney test (**g**,**l**); Welch's two-sided *t*-test (**h**,**n**); one-sided Welch's t test (**j**,**p**).

these clones, MT2 and MT3. The MT3 subclone was subsequently defined as a mMIC population due to its enhanced metastatic potential (~90 macrometastases per field; 100% incidence) compared to poorly metastatic MT2 cells (~1 macrometastasis per field; 66.6% incidence) (Supplementary Fig 1c). Hence, Met1 primary tumours or control PBS were orthotopically injected into cohorts of FVB mice followed 2 weeks later by intravenous injection of the mMIC-MT3 cells (Fig. 1a). At the experimental end point, mMIC-MT3 pulmonary metastases were reduced by approximately sixfold in the cohort bearing Met1 primary tumours relative to the control cohort (Fig. 1d,e).

To test whether adaptive immunity was necessary for inhibiting mMIC pulmonary metastases, we conducted the same experiments in athymic nude mice. After 2 weeks, when primary tumours reached ~200 mm^3 (Supplementary Fig. 1d), Met1 cells were injected intravenously (Fig.1a). Again, Met1 primary tumours significantly inhibited pulmonary metastases (Fig. 1f,g), indicating that mMIC inhibition was not T cell-dependent.

The results from immunocompromised mice presented us with the opportunity to test human xenografts. Accordingly, we used the polyclonal human mammary carcinoma cell line HMLER, which represents heterogeneous cell populations commonly observed in primary breast cancers. We used a well-characterized clonal MIC subpopulation (hMIC) that had been isolated directly from the HMLER cell line; compared with other HMLER subclones, hMIC is uniquely metastatic[21].

Primary HMLER tumours significantly inhibited the outgrowth of subcutaneous hMIC secondary tumours (Fig. 1h–j) as well as hMIC pulmonary metastases (Supplementary Fig. 1e). We also tested highly metastatic MDA-MB-231 human breast cancer cells, which are enriched for hMICs[22]. These MDA-MB-231-MIC secondary tumours were also significantly inhibited by HMLER primary tumours (Supplementary Fig. 1f–i).

We ruled out the possibility that the primary tumours inhibited hMIC outgrowth through the release of anti-angiogenic factors[23]. In fact, hMIC-derived tumours from mice bearing primary tumours contained ~2.5-fold more blood vessels per section than the control cohort (Fig. 1k).

Importantly, we discovered that primary tumours from another HMLER derivative subpopulation, HMLER2[21], did not inhibit hMIC colonization (Fig. 1l). This finding suggested that there are properties specific to inhibitory primary tumours.

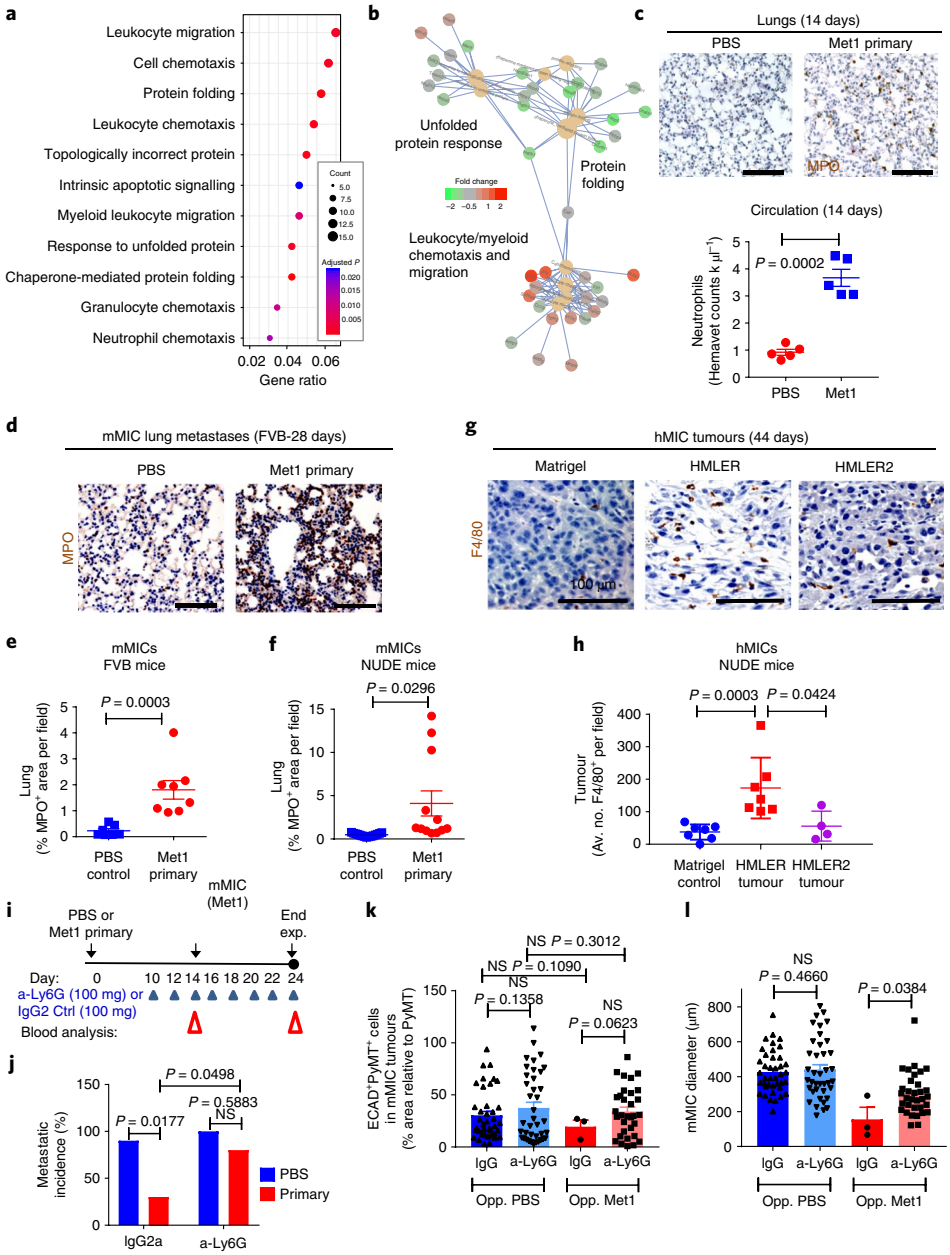

Fig. 3 | Myeloid cells are necessary for preventing MIC differentiation and outgrowth. a, GO terms found in DEGs (DESeq2 adjusted $P<0.05$) between lungs of FVB mice with orthotopic PBS control and Met1 primary tumours ($n=4$ mice per cohort) 14 days after injection. The *y* axis shows the top 11 enriched (adjusted $P<0.01$) categories, with low represented in red and high represented in blue (adjusted *P* value). The dot size represents the number of DEGs within the GO term. The *x* axis shows the ratio of DEGs to total gene number within a GO term. **b**, Connectivity map of the top 10 enriched GO terms and DEGs within them. GO term nodes (beige), fold-change (red, up; green, down) between Met1 primary tumour-bearing and control lungs. **c**, Top: pulmonary neutrophils (myeloperoxidase, MPO; brown) from FVB mice 14 days after orthotopic injection of Met1 primary tumours or PBS control. Haematoxylin (nuclei; blue). Bottom**:** circulating neutrophil counts per microlitre of blood (hemavet). **d**, Pulmonary neutrophils (MPO; brown) from FVB mice 28 days after orthotopic injection of PBS control or Met1 primary tumours (14 days after mMIC intravenous injections per Fig. 1a). Haematoxylin (nuclei; blue). **e**,**f**, Quantification of pulmonary neutrophils from FVB mice (**e**) and nude mice (**f**). For FVB mice: control cohort, $n=21$ independent images representing 7 lungs; Met1 primary tumour cohort, $n=24$ independent images representing 8 lungs. For nude mice: control, $n=15$ independent images representing 5 lungs; Met1 primary cohort, $n=12$ independent images representing 4 lungs. **g**,**h**, Representative immunohistochemistry (**g**) and corresponding quantification (**h**) of hMIC tumours that had grown for 44 days opposite Matrigel, HMLER or HMLER2 tumours (per Fig. 1h). Tissues stained with F4/80 (macrophages; brown); haematoxylin (nuclei; blue). Control, $n=28$ independent images representing 7 tumours; HMLER, $n=24$ independent images representing 7 tumours; HMLER2, $n=16$ independent images representing 4 tumours. **i**, Schematic of neutrophil depletion experiments using 100 µg of either anti-Ly6G (a-Ly6G) or IgG control. **j**, Incidence of pulmonary macrometastases (control IgG2a, $n=4$ mice per cohort; anti-Ly6G, $n=8$ mice per cohort). **k**, ECAD⁺/PyMT⁺ staining in mMIC lung metastases. **l**, average mMIC lung metastasis size. mMIC opposite control PBS: anti-IgG2a, $n=40$ independent images representing 4 mice; anti-Ly6G $n=39$ independent images representing 4 mice. mMIC opposite Met1 primary tumour: anti-IgG2a, $n=3$ independent images representing 5 mice; anti-Ly6G $n=33$ independent images representing 4 mice. Scale bars, 100 µm. Source data for **c**, **e**, **f**, **h**, **j**, **k** and **l** are provided in Supplementary Table 1. One-sided Welch's *t*-test (**c**,**k**); two-sided Welch's *t*-test (**f**); one-sided Mann–Whitney test (**h**,**l**); two-sided Mann–Whitney test (**e**); two-way ANOVA with Sidak's multiple comparison test (**j**).

These data established several important principles. First, primary tumours that inhibited MIC colonization did not prevent the outgrowth of heterogeneous tumour cell populations composed of MICs and non-MICs, suggesting that MIC-specific properties make them susceptible to growth inhibition. Second, systemic growth inhibition of MICs is not tissue-specific, since primary tumours inhibited the outgrowth of both subcutaneous and pulmonary MICs. Third, primary tumours systemically inhibited MICs independently of an adaptive immune system without affecting MIC vascularization, pointing to innate immune mechanisms. Fourth, not all primary tumours inhibited distant MIC colonization.

MIC proliferation and differentiation are mechanistically linked. The histopathology of control cohort hMIC tumours was consistent with that of breast ductal adenocarcinomas observed in the clinic (Fig. 2a). In contrast, cancer cells in hMIC tumours from cohorts bearing primary HMLER tumours appeared mesenchymal-like, resembling breast spindle cell carcinomas (Fig. 2a). Similarly, mMIC-MT3 metastatic foci in primary tumour-bearing mice appeared poorly differentiated (Fig. 2b). hMIC and mMIC proliferation was significantly reduced in cohorts bearing primary tumours relative to their respective control cohorts (Fig. 2c,d).

Evidence from multiple groups has indicated that MICs reside in a partial-EMT state[24]. As MICs generate their non-MIC progeny during secondary tumour formation, mesenchymal properties are lost and epithelial phenotypes are reacquired[7,25]. Our histopathological observations supported the hypothesis that inhibitory primary tumours maintain the MIC mesenchymal state and prevent differentiation into epithelial progeny.

Consistent with MIC traits, both hMICs and mMICs expressed low or undetectable levels of the epithelial marker E-cadherin (ECAD) in vitro at the time of their injection (Supplementary Fig. 2a,b). In vivo, however, MIC-derived metastases and secondary tumours from control cohorts acquired ECAD expression, which was approximately fivefold higher in hMICs and approximately twofold higher in mMICs compared with MICs from primary tumour-bearing mice (Fig. 2e–h). Epithelial phenotypic plasticity was also apparent when we visualized cytokeratin and vimentin (Supplementary Fig. 2c,d).

We next asked whether the blocks in MIC differentiation and growth inhibition were mechanistically related. We reasoned that these responses should be analysed from size-matched MIC-derived tumour tissues. We therefore used the hMIC model and injected either HMLER cells or Matrigel control subcutaneously into mice; 14 days later, we injected hMICs into the contralateral flanks of the mice in each cohort and harvested tumours 14 days later (Supplementary Fig. 2e). At this early time point, hMIC tumours were comparable in size (~50 mm^3) between cohorts, although hMIC tissues from the mice with primary tumours had ~62% fewer proliferating tumour cells with no significant differences in numbers of caspase 3-positive cells (Supplementary Fig. 2e–i).

We examined these small secondary tumours for ECAD and for the human mesenchymal marker ZEB1[26], which is highly expressed in hMICs in vitro (Supplementary Fig. 2b). In the control cohort (no primary tumour), the vast majority of hMICs acquired ECAD expression, with only ~10% of the cells expressing ZEB1 (Fig. 2i–l). In striking contrast, hMICs from the mice bearing primary tumours largely maintained ZEB1 expression (~90%), with only a small fraction of tumour cells acquiring ECAD expression (Fig. 2i–l).

The $ZEB1^{high}$ phenotype persisted through later end points (Fig. 2m,n). We therefore tested the effects of locking MICs in a mesenchymal state by creating and injecting hMICs that stably express either ZEB1 ($ZEB1^{high}$ hMICs) or an empty vector control (control hMICs) (Supplementary Fig. 2j). After 6 weeks, the $ZEB1^{high}$ hMIC tumours were 20-fold smaller than control hMIC tumours and indeed maintained high ZEB1 protein expression (Fig. 2o,p). Hence, maintaining high ZEB1 expression in hMICs, either in the presence of a primary tumour or by *ZEB1* overexpression, severely compromises their tumour-forming ability.

These data demonstrated that proliferation is mechanistically linked to MIC epithelial plasticity, which was critical for robust tumour growth. Specifically, reduced proliferation in the mesenchymal state accounts for the lack of MIC outgrowth when a distantly located primary tumour is present.

Myeloid cells in the metastatic microenvironment prevent MIC differentiation and colonization. A transcriptomic analysis of lung tissues 14 days after control PBS or Met1 primary tumour initiation—the time point at which mMIC metastases typically encounter the lungs (Supplementary Fig. 3a,b)—revealed a list of significantly differentially expressed genes (DEGs) that clustered by cohort (Supplementary Fig. 3c,d; Supplementary Table 2). The MIC-suppressive lung environment was defined by functionally enriched gene ontology (GO) terms and pathways involved in leukocyte (myeloid, neutrophil and granulocyte) migration and chemotaxis and diminished for protein-folding responses (Fig. 3a,b).

In agreement with RNA sequencing (RNA-seq) results, neutrophils were abundant in the lungs and approximately fourfold higher in the circulation of the tumour-bearing cohort than in the tumour-free cohort (Fig. 3c). Increased neutrophil infiltration persisted throughout disease progression to the 28-day experimental end point (Fig. 3d,e and Supplementary Fig. 3e) and was also apparent in the lungs of nude mice (Fig. 3f).

Myeloid cells, including macrophages and neutrophils, can confer either pro- or antitumorigenic functions that are governed in tissue- and microenvironment-specific contexts[10,11,13,27–29]. One particular study reported gene expression signatures of breast cancer metastasis-promoting, immune-suppressive circulating neutrophils ("KEP")[13]. An analysis of the reported KEP and of normal lung neutrophil signatures revealed that the lungs from mice with Met1 primary tumours had a lower KEP:normal ratio (~1.7) compared to the control cohort (ratio of ~2.8) (Supplementary Fig. 3f). Similarly, leukotrienes expressed by pre-metastatic lung neutrophils to expand the MIC pool in a reported study[11] were not differentially expressed in the lungs of the tumour-bearing cohort (see GSE111157). These results suggested that the neutrophils in lungs of Met1 tumour-bearing mice are entrained differently to those of previously described circulating neutrophils.

Similarly, myeloid cells infiltrated the hMIC tumours from mice bearing inhibitory human primary tumours (HMLER) but not those bearing non-inhibitory primary tumours (HMLER2). In these cases, macrophages were ~4.5-fold more abundant in hMIC secondary tumours from mice with primary HMLER tumours than either Matrigel controls or HMLER2 tumour-bearing mice (Fig. 3g,h).

To determine whether neutrophils are necessary for inhibiting mMIC lung colonization, we neutralized $Ly6G^+$ cells. We selected an optimal anti-Ly6G dose that restored circulating $Ly6G^+$ cells to that of the control cohorts, did not affect primary tumour growth and reduced lung neutrophil infiltration (Supplementary Fig. 3g–l). We then orthotopically injected PBS control or Met1 cells and after 10 days, animals were randomized into two additional cohorts to receive either anti-Ly6G or control IgG2a every 2 days. mMIC cells were then injected intravenously into all cohorts at day 14, and the dosing regimens were continued (Fig. 3i).

As expected, pulmonary macrometastases were reduced approximately fourfold in the primary tumour-bearing cohort treated with control IgG2a relative to the control primary tumour-free cohort (Fig. 3j). However, when the primary tumour-bearing cohort was treated with anti-Ly6G and circulating neutrophils were reduced to that of the control cohort without affecting primary tumour mass (Supplementary Fig. 3m,n), metastatic colonization was no longer

inhibited (Fig. 3j). Neutrophil ablation was associated with significantly larger pulmonary metastases that displayed approximately twofold more ECAD expression compared with the control IgG2a cohort (Fig. 3k,l; Supplementary Fig. 3o–q). We confirmed that lung neutrophils were maintained at baseline levels while lung monocytes were unaffected at the experimental end point (Supplementary Fig. 3r).

IL-1β is sufficient to prevent MIC differentiation. We next interrogated candidate DEGs as drivers of MIC suppression. Among the top most-upregulated DEGs in the lungs of mice with primary tumours, we considered pro-inflammatory cytokines common to both neutrophils and macrophages[13,30,31] (Supplementary Fig. 4a). One of the most highly upregulated DEGs in lungs of primary tumour-bearing mice was IL-1β (Fig. 4a), which is known to drive ZEB1 expression[32,33]. IL-1β was significantly more abundant in the lungs of both FVB and nude mice bearing Met1 primary tumours (Fig. 4b,c), and mMICs did not secrete appreciable levels of IL-1β in culture (Supplementary Fig. 4b). We confirmed that murine Met1 cells and derivative clones, MT2 and MT3, expressed IL-1 receptor (IL-1R) and were responsive to IL-1β in a dose-dependent manner (Supplementary Fig. 4c).

We also assessed IL-1 expression in hMIC tumours from HMLER- and Matrigel-bearing mice by species-specific quantitative PCR (qPCR). Human *IL1B* and *IL1A* expression were not different between cohorts (Fig. 4d). In fact, hMICs secrete very low levels of IL-1β (<1 pg ml^{-1}) in culture (Supplementary Fig. 4d). However, relative to Matrigel control mice, murine *Il1b* expression was 2.7-fold elevated in hMIC tumours from mice bearing primary tumours; this was accompanied by a 3.4-fold increase in human *IL1R1* expression (Fig. 4d). Indeed, murine IL-1β can efficiently bind and activate human IL-1R1[34], and IL-1β induces the expression of *IL1R1*, thereby amplifying IL-1 signalling[35,36].

Tumour-associated macrophages (positive for both CD11b and F4/80) equivalently infiltrated hMIC tumours from both cohorts at the early time point (Supplementary Fig. 4e). However, macrophages expressed significantly higher levels of intracellular IL-1β protein per cell in the cohort with primary tumours than those from the control cohort (Fig. 4e).

We directly tested the effects of IL-1β on MIC plasticity by admixing hMICs with Matrigel containing either IL-1β (hMIC + IL-1β) or PBS control (hMIC + PBS) (Fig. 4f). After 2 weeks, the hMIC + IL-1β tumours had significantly fewer ECAD$^+$ tumour cells and more ZEB1$^+$ tumour cells than the hMIC + PBS tumours (Fig. 4g,h). Importantly, hMIC + IL-1β tumours displayed significantly enhanced macrophage infiltration (Fig. 4i), demonstrating that a single dose was sufficient to trigger a sustained inflammatory response and maintain the mesenchymal phenotype.

IL-1R1 signalling is necessary for preventing MIC differentiation. To test whether IL-1R1 signalling is necessary for preventing MIC differentiation, we first generated hMIC cells deficient in IL-1R1 (sh-IL-1R1-hMIC) and scrambled short hairpin RNA (shRNA) control cells (sh-Ctl-hMIC). Only one out of six shRNA constructs provided sufficient suppression of IL-1R1 without significantly affecting cell proliferation (Supplementary Fig. 5a,b); hence, we performed all in vivo experiments with those sh-IL-1R1-hMIC cells only. Cohorts of mice bearing primary HMLER tumours or Matrigel control were injected with sh-IL-1R1-hMIC or sh-Ctl-hMIC cells and tissues were harvested 2 weeks later (Fig. 5a). hMIC tissue mass was not significantly different between cohorts at this time point (Supplementary Fig. 5c).

Echoing earlier results, the sh-Ctl-hMIC tumours from mice with primary tumours had significantly fewer ECAD$^+$ cells and more ZEB1$^+$ cells than those from the Matrigel control cohort (Fig. 5b,c). In stark contrast, the sh-IL-1R1-hMIC tumours from both cohorts expressed similar levels of ECAD and ZEB1, and the majority of tumour cells from both cohorts were in ZEB1^{low}ECAD^{high} state (Fig. 5b,c).

We also treated mMICs in a three-dimensional tumoursphere assay with IL-1β, anakinra (an IL-1R1 antagonist), a combination of IL-1β + anakinra, or vehicle control. IL-1β treatment activated nuclear factor-κB (NF-κB) signalling and significantly reduced tumoursphere size, whereas anakinra reduced NF-κB activation and increased both tumoursphere size and ECAD protein levels (Supplementary Fig. 5d,e).

In addition to dysfunctional adaptive immunity, NOD/SCID (non-obese diabetic/severe combined immunodeficiency) mice have an impaired innate immune system, of which defects in IL-1 signalling are a particular feature[37]. Hence, we injected cohorts of NOD/SCID mice with either Matrigel or HMLER primary tumours. After 10 days, circulating monocytes were not significantly different between cohorts (Supplementary Fig. 5f). At day 14, we then injected either hMICs or hMICs with recombinant IL-1β (hMICs + IL-1β) as secondary tumours and harvested tissues of equivalent mass after an additional 2 weeks (Fig. 5d,e, Supplementary Fig. 5g).

The majority of hMIC tumour cells in the control NOD/SCID mice were ECAD^{high}ZEB1^{low} (Fig. 5f,g). However, unlike nude mice, HMLER primary tumours failed to lock distant hMICs in the ZEB1$^+$ state and these hMIC tumour cells were also ECAD^{high}ZEB1^{low} (Fig. 5f,g). Therefore, ablation of IL-1β-dependent aspects of innate immunity prevented MIC entrapment in the mesenchymal-enriched state, even in the presence of a distant primary tumour. Finally, addition of recombinant IL-1β maintained hMICs in a ZEB1$^+$ECAD^{low} state (Fig. 5f,g), indicating that hMICs were still capable of responding to IL-1β in NOD/SCID mice.

These observations indicated that the ability of primary tumours to systemically maintain secondary hMIC tumours in the ZEB1$^+$ECAD^{low} state critically depended on eliciting systemic inflammation involving IL-1β-secreting innate immune cells and IL-1R pathway activation in the disseminated MICs.

MIC-inhibitory primary tumours elicit a systemic inflammatory response. Our results thus far suggested that MIC-inhibitory primary tumours elicit a systemic pro-inflammatory response. Indeed, myeloid cells infiltrated the Met1 and HMLER primary tumours but not the HMLER2 primary tumours that did not suppress distant hMIC outgrowth (Fig. 6a,b; Supplementary Fig. 6a). Circulating neutrophils were significantly increased 10 days after disease initiation (that is, before mMIC implantation) in the Met1 primary tumour-bearing FVB cohort (Fig. 6c). Moreover, there was a 10% increase in circulating monocytes in HMLER tumour-bearing nude mice after just 14 days (Fig. 6c,d).

In the bone marrow of FVB mice, short-term haematopoietic stem cells (ST-HSCs), common myeloid progenitors (CMPs) and granulocyte–monocyte progenitors (GMPs) expanded 28 days after Met1 tumour establishment while production of haematopoietic stem cells (HSCs), long-term HSCs (LT-HSCs), common lymphoid progenitors (CLPs) and megakaryocyte/erythroid progenitors (MEPs) decreased (Fig. 6e). The shift towards CMPs and GMPs reflected a skewing towards the production of neutrophil and macrophage precursors. Circulating neutrophils were still significantly elevated by the end stage in both FVB and nude mice (Fig. 6f). Similarly, bone marrow monocytes and their expression of intracellular IL-1β were significantly elevated at end-stage of HMLER primary disease (Fig. 6g). These results were indicative of a sustained pro-inflammatory response throughout disease progression.

Inhibiting inflammation at the primary tumour site results in distant MIC differentiation and growth. Our results suggested that inhibiting inflammation at the primary tumour site should affect

a

Gene name	Fold change log_2	Adjusted *P* value
Fos	1.687	9.26×10^{-15}
Csf3r	1.572	8.82×10^{-8}
Egr1	1.502	6.86×10^{-17}
Il1b	1.365	8.09×10^{-5}
Nr4a1	1.309	1.80×10^{-6}
S100a8	1.192	1.64×10^{-5}
Fcho1	1.120	3.58×10^{-4}
Cd180	1.084	0.0023
Ppp4r4	1.070	0.0041
Srsf5	1.013	8.99×10^{-8}

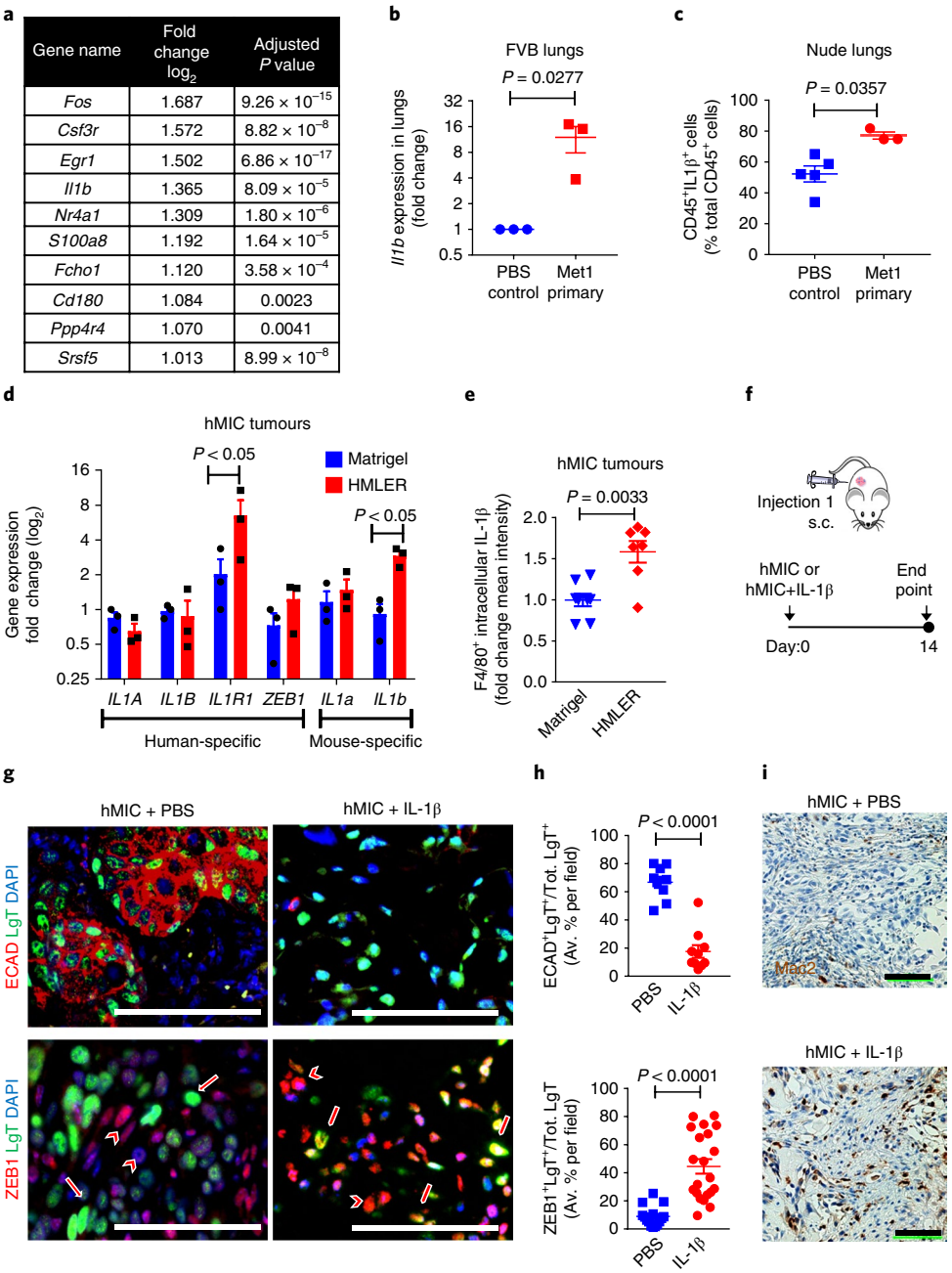

Fig. 4 | Myeloid cell-derived IL-1β is sufficient to prevent MIC differentiation. a, Top 10 differentially upregulated genes (RNA-seq) in lungs from Met1 primary tumour-bearing FVB mice relative to control lungs at day 14 ($n=4$ mice per cohort). **b**, qPCR on lungs 14 days following tail vein injection of mMICs into FVB mice bearing Met1 primary tumours or PBS control (per Fig. 1a). IL-1β normalized relative to β-actin ($n=3$ lungs per cohort, in triplicate). **c**, Flow cytometry analysis of intracellular IL-1β in CD45$^+$ cells from a subset of lungs of nude mice bearing Met1 primary tumours ($n=3$ animals) or PBS control ($n=5$ animals). **d**, qPCR results of hMIC tumours after 14 days of growth using indicated human- and mouse-specific primers. $n=3$ tumours per cohort, analysed in triplicate. **e**, Flow cytometry analysis of intracellular IL-1β in cells positive for both CD11b and F4/80 harvested from hMIC tumours grown opposite Matrigel control ($n=8$ tumours) or HMLER primary tumours ($n=7$ tumours); per Supplementary Fig. 2e. **f**, Schematic showing single injection xenograft model (applies to **g-i**). **g**, Merged immunofluorescence images of hMIC tumours injected in Matrigel containing PBS (hMIC + PBS) or 10 pg ml^{-1} IL-1β (hMIC + IL-1β) representing 2 independent experiments. Block arrows indicate examples of ZEB1$^+$ tumour cells. Long arrows indicate examples of ZEB1$^-$ tumour cells. Arrowheads indicate ZEB1$^+$ stromal cells. **h**, ECAD$^+$LgT$^+$ cells (hMIC + PBS, $n=10$ independent images representing 7 tumours; hMIC + IL-1β, $n=9$ independent images representing 6 tumours) or ZEB1$^+$LgT$^+$ cells (hMIC + PBS, $n=15$ independent images representing 5 tumours; hMIC + IL-1β, $n=21$ independent images representing 7 tumours) as the percentage of the total number LgT$^+$ tumour cells per microscopy field. **i**, Representative tumours stained with Mac2 (macrophages; brown) or haematoxylin (nuclei; blue), representing two independent experiments. All scale bars, 100 μm. Source data for **b**, **c**, **d**, **e** and **h** are provided in Supplementary Table 1. One-sided *t*-test (**b**); two-sided Mann–Whitney (**c**,**h**); two-sided Welch's *t*-test (**e**); two-way ANOVA followed by Sidak's multiple comparison test (**d**).

the systemic cascade of events that resulted in MIC suppression at distant sites. Therefore, we analysed the primary tumours for pro-inflammatory factors that we could interrogate.

An expression analysis of Met1 primary tumours relative to control tissues (GSE111157) showed enhancement of gene terms related to inflammation and neutrophil recruitment. Some of these

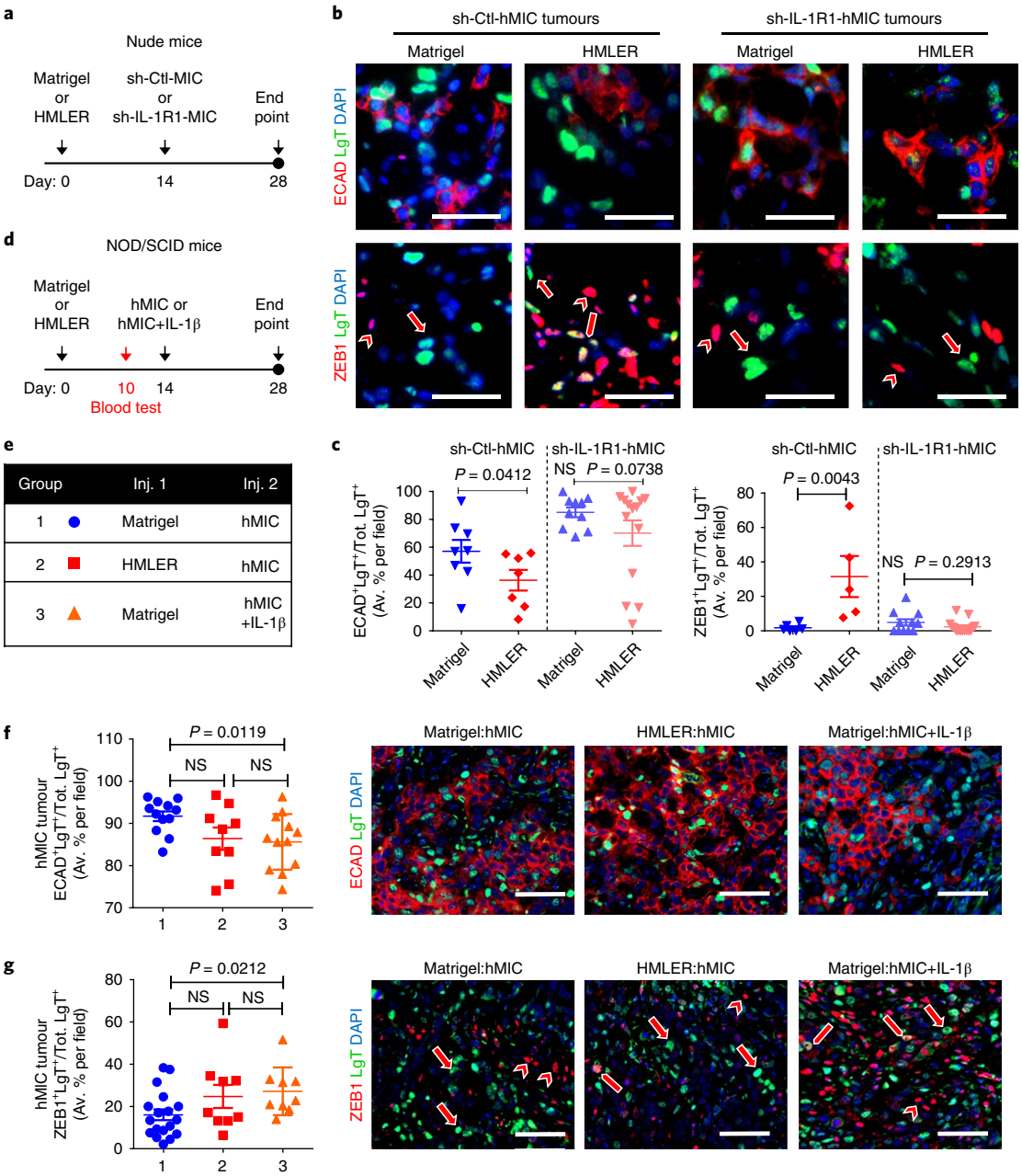

Fig. 5 | IL-1R1 signalling is necessary for preventing MIC differentiation. a, Experimental schematic of hMICs with or without IL-1R1 suppression (sh-IL-1R1-hMIC and sh-Ctl-hMIC) injected opposite Matrigel control or HMLER primary tumour in nude mice (applies to **b** and **c**). **b**, Immunofluorescence images of hMIC tumours. Long arrows indicate examples of ZEB1$^-$ tumour cells. Block arrows indicate ZEB1$^+$ tumour cells. Arrowheads indicate ZEB1$^+$ stromal cells. Scale bar, 50 μm. sh-Ctl-hMIC opposite Matrigel control, $n=7$ tumours; opposite HMLER primary tumour, $n=8$ tumours. sh-IL-1R1-hMIC opposite Matrigel control and HMLER primary tumour, $n=8$ tumours per cohort. **c**, Left: Quantification of ECAD$^+$LgT$^+$ cells. sh-Ctl-hMIC: Matrigel, $n=8$ and HMLER, $n=7$ independent images representing 3 tumours per cohort. sh-IL-1R1-hMIC: Matrigel, $n=10$ and HMLER, $n=14$ independent images representing 5 tumours per cohort as the percentage of the total number of LgT$^+$ human tumour cells per microscopy field. Right: Quantification of ZEB1$^+$LgT$^+$ cells. sh-Ctl-hMIC: Matrigel, $n=6$ and HMLER, $n=5$ independent images representing 3 tumours per cohort. sh-IL-1R1-hMIC: Matrigel, $n=11$ and HMLER, $n=15$ independent images representing 5 tumours per cohort as the percentage of the total number of LgT$^+$ human tumour cells per microscopy field. **d**,**e**, Experimental schematic modelling the early stages of hMIC secondary tumour formation in NOD/SCID mice with HMLER primary tumours or PBS control. Secondary injections involve hMICs or hMICs + 10 pg ml^{-1} rIL-1β (**d**). Indicated cohorts: Group 1 ($n=7$ animals); Group 2 ($n=7$ animals); Group 3 ($n=6$ animals) (**e**). Applies to **f** and **g**. **f**,**g**, Left: Positive staining represented as the percentage of the total number of LgT$^+$ human tumour cells per microscopy field. Right: Immunofluorescence of hMIC tumours, with arrows indicating ZEB1$^-$ tumour cells, block arrows indicating ZEB1$^+$ tumour cells, and arrowheads indicating ZEB1$^+$ stromal cells. ECAD$^+$LgT$^+$ cells in hMIC tumours (4 tumours per cohort) opposite Matrigel control ($n=12$ independent images), HMLER ($n=9$ independent images) or hMIC + IL-1β tumours opposite Matrigel ($n=12$ independent images) (**f**). ZEB1$^+$LgT$^+$ cells in hMIC tumours (3 tumours per cohort) opposite Matrigel ($n=18$ independent images), HMLER ($n=9$ independent images), or hMIC + IL-1β tumours opposite Matrigel ($n=9$ independent images) (**g**). Scale bars, 100 μm. Source data for **c**, **f** and **g** are provided in Supplementary Table 1. One-sided Welch's *t*-test (**c**, left); two-sided Mann–Whitney test (**c**, right); two-sided Welch's *t*-test (**f**,**g**).

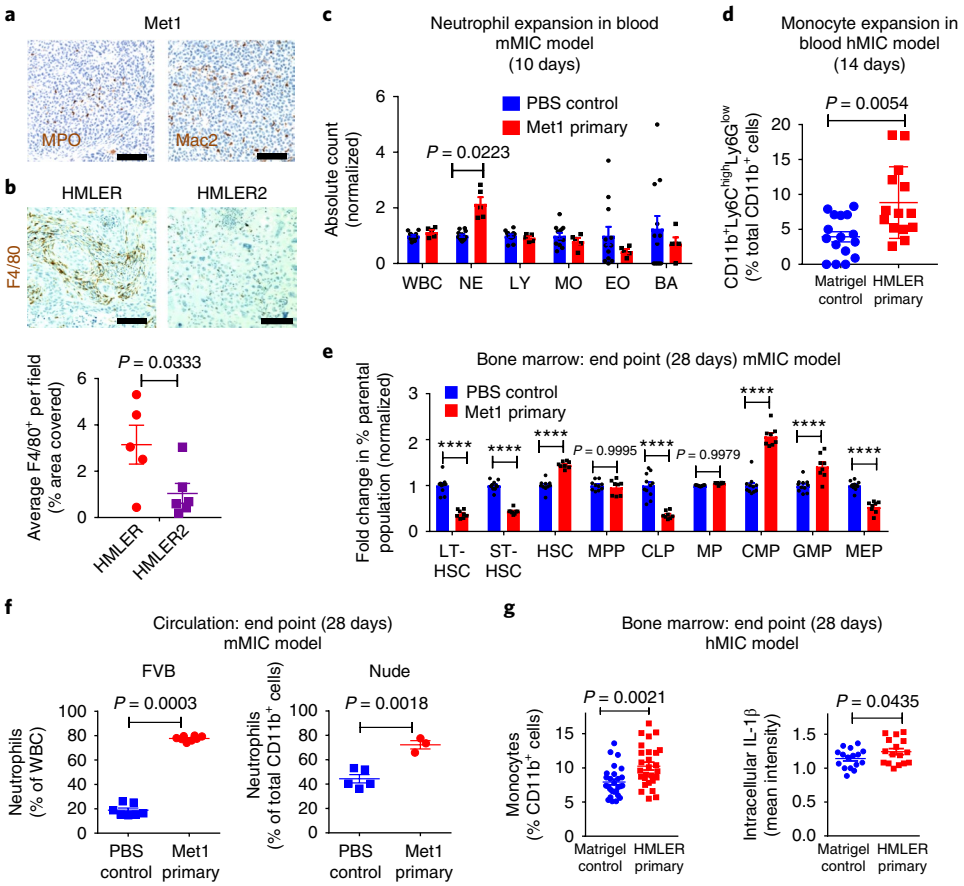

Fig. 6 | Primary tumours initiate a sustained systemic inflammatory response. a,**b**, Met1 primary tumours (per Fig. 1a schematic) stained for MPO (brown) to detect neutrophils and Mac2 (brown) to detect macrophages; haematoxylin (nuclei; blue) (**a**). HMLER and HMLER2 tumours (per Fig. 1h schematic) stained for F4/80 (macrophages; brown) and haematoxylin (nuclei; blue); quantified in the graph below (**b**). HMLER, $n=5$ tumours; HMLER2 $n=6$ tumours. Scale bars, 100 µm. **c**, Absolute blood counts (hemavet) in circulation (FVB mice) 10 days after orthotopic injection of Met1 primary tumours ($n=5$ animals) or PBS control ($n=12$ animals). WBC, whole blood cells; NE, neutrophils; LY, lymphocytes; MO, monocytes; EO, eosinophils; BA, basophils. **d**, Flow cytometry analysis of circulating monocytes ($CD11b^+Ly6C^{high}Ly6G^{low}$) from nude mice 14 days after injection of Matrigel control ($n=16$ independent images representing 8 tumours) or HMLER primary tumours ($n=14$ independent images representing 7 tumours), representing 2 independent experiments. **e**, Fold changes (percentage of the parental population) in bone marrow of FVB mice bearing orthotopic Met1 primary tumours ($n=8$ animals) or PBS control ($n=10$ animals) after 28 days. $^{****}P<0.001$. **f**, Quantification of circulating neutrophils ($CD11b^+Ly6G^+Ly6C^{low}$) at 4-week experimental end points from indicated strains of mice bearing mMIC lung metastases with concurrent orthotopic Met1 primary tumours or PBS control. FVB mice: control, $n=7$ animals; Met1 primary, $n=8$ animals. Nude mice: control, $n=5$ animals; Met1 primary, $n=3$ animals. Representative of three (FVB) and one (nude) experiments. **g**, Monocytes ($CD11b^+Ly6C^{high}Ly6G^{low}$, $n=27$ samples per cohort representing 11 tumours, 3 independent experiments) as the percentage of the total $CD11b^+$ cells in the bone marrow of nude mice bearing hMIC tumours grown opposite Matrigel control or HMLER primary tumours at 28-day end point (left). Intracellular IL-1β in bone marrow monocytes ($n=16$ samples per cohort, representing 8 tumours, 2 independent experiments) (right). Source data for **b**, **c**, **d**, **e**, **f** and **g** are provided in Supplementary Table 1. One-sided Welch's *t*-test (**b**,**g** (right)); two-sided Welch's *t*-test (**d**,**f** (right),**g** (left)); two-way ANOVA Tukey's multiple comparison test (**c**,**e**); two-sided Mann–Whitney test (**f**,left).

included IL-1β, lipocalin 2 (LCN2), granulocyte colony stimulating factor (G-CSF), chemokine (C–C motif) ligand 2 (CCL2, also known as monocyte chemoattractant protein 1), and tumour necrosis factor-α (TNF-α) (Supplementary Fig. 7a). A cytokine analysis also revealed a number of pro-inflammatory cytokines that were secreted at significantly higher levels (≥threefold) by the HMLER cells than the non-inhibitory HMLER2 cells, including IL-1α and LCN2 (Fig. 7a). A number of these same cytokines, including IL-1α , LCN2 and G-CSF, were secreted at significantly higher levels (≥ twofold) by the HMLER cells than hMICs (Supplementary Fig. 7b).

Our earlier results (Figs. 3–5) established that neutrophil neutralization or IL-1R1 suppression within the metastatic niche affects MIC differentiation and colonization; therefore, therapeutic approaches designed to systemically inhibit inflammation would not reveal the necessity or exclusivity of primary tumours in initiating the MIC-inhibitory cascade. Therefore, we sought strategies to inhibit inflammation proximal to the primary tumour. Among the various pro-inflammatory cytokines secreted by primary tumours, IL-1α stood out due to its prominence as a local initiator of systemic inflammatory responses[33]. Importantly, IL-1R activation triggers the induction of some of the pro-inflammatory cytokines that we had observed, including TNF-α[38], LCN2[39] and CCL2[40,41]. Indeed, IL-1α was greater than sixfold more abundant in conditioned medium from HMLERs than from hMICs (Fig. 7b).

To determine whether primary tumour IL-1R1 signalling initiates the pro-inflammatory cascade, we used a recombinant IL-1 receptor antagonist (IL-1Ra)[42]. We implanted Matrigel control, HMLER cells or HMLER cells mixed with IL-1Ra (HMLER+IL-1Ra) into mice and collected blood 13 days later (Fig. 7c). At this time point, circulating monocytes were 2.4-fold elevated in the primary

tumour-bearing cohort relative to the Matrigel controls (Fig. 7d). However, in the cohort bearing HMLER+IL-1Ra tumours, circulating monocytes were reduced to that of the control cohort (Fig. 7d). Murine inflammatory plasma cytokines that are commonly triggered by IL-1R1 signalling (for example, TNFα, G-CSF and CCL1) were also elevated in mice with HMLER primary tumours but not in the cohort bearing HMLER+IL-1Ra tumours (Supplementary Fig. 7c).

Having confirmed an IL-1-dependent host inflammatory response at day 13, we initiated hMIC secondary tumours in all 3 cohorts the following day (day 14) and continued the experiment for another 2 weeks (Fig. 7c). Primary tumour masses were equivalent, yet myeloid infiltration into primary HMLER+IL-1Ra tumours was reduced 6.4-fold compared to HMLER controls (Fig. 7e, Supplementary Fig. 7d–g). Macrophages were also less abundant in the secondary hMIC tumours from mice bearing the distant HMLER+IL-1Ra primary tumours (Supplementary Fig. 7h). Confirming earlier findings, hMICs from mice bearing primary tumours were predominantly ZEB1^{+}ECAD^{low}. In contrast, when IL-1R1 signalling was inhibited at the primary tumour site, hMIC secondary tumours acquired the ZEB1^{low}ECAD^{high} epithelial phenotype (Fig. 7f,g, Supplementary Fig. 7i,j).

Low IL-1β expression in primary breast cancer correlates with reduced metastasis-free survival. Our studies demonstrated that innate immune cells secreting IL-1β, mobilized by the primary tumour, compromise MIC colonization at secondary sites by preventing their differentiation into epithelial progeny, which is essential for forming actively growing tumours (Fig. 8a). Given that this cascade of events depends on the continued presence of the primary tumour, clinical validation relied on careful selection of appropriate patient populations. Indeed, hMIC-derived metastases were not inhibited if the IL-1β-dependent inflammatory cascade was instigated after MIC dissemination and growth initiation (Fig. 8b,c). hMIC tumours that were <2 mm (low mitotic index) at the time of HMLER implantation were significantly suppressed. However, if hMIC tumours had already entered an active growth phase (>2 mm) at the time of primary tumour implantation, MIC-derived tumours sustained continued growth (Fig. 8c). These data provided preliminary indication that HMLER tumours do not cause regression of robustly growing hMIC tumours but instead exert their inhibitory effects at early stages of secondary tumour establishment when MICs are still in the ZEB1^{+} state.

We therefore compared primary tumour IL-1β expression in breast cancer patients with lymph node-positive (LN^{+}) and LN-negative (LN^{-}) disease by retrospective gene set analyses using a database of Affymetrix microarray profiles[43]. Among 508 patients with LN^{-} disease, IL-1β expression did not stratify for overall survival (Fig. 8d). However, among 215 patients with LN^{+} breast cancer, those with high IL-1β expression had improved overall survival relative to those with low IL-1β expression (Fig. 8e). Interestingly, patients whose primary tumours expressed high IL-1β had improved outcomes (distant metastasis-free survival) when we interrogated the entire cohort of 1,379 patients (Supplementary Fig. 8a).

We also analysed correlations between IL-1R1 and the markers of differentiation status that we had observed. In an analysis of 818 tumour tissue samples from patients with invasive breast carcinoma, IL-1R1 expression was positively correlated with ZEB1 expression[44–46] (Fig. 8f).

Discussion

The present work demonstrates that MIC plasticity determines metastatic success and agrees with a clinical report that mesenchymal markers are downregulated in metastases relative to matched primary tumours[47]. An important implication of our study is that therapies designed to prevent disseminated MIC differentiation compromise their ability to form lethal metastases. Another distinction of our work is that MICs are specifically susceptible to growth inhibition. Interestingly, a recent report indicated that breast carcinomas enriched for mesenchymal markers, similar to our MICs, give rise to immunosuppressive tumours, unlike their more epithelial counterparts[48]. However, we did not specifically examine hallmarks of immunosuppression, as the MIC-suppressive cascade occurred in a T cell-independent manner.

It is becoming increasingly clear that modulating innate immunity must be included in efforts to improve patient outcomes[13,27,49–51]. Tumour-associated lung neutrophils that suppressed MIC colonization in our study appear to be entrained differently to that of metastasis-promoting neutrophils that have been reported in the circulation[13] and of pre-metastatic lungs[11] in other models. At first glance, the neutrophils in our study may seem antimetastatic (they prevented MIC colonization) but at the same time, they may also be considered pro-metastatic (they fortified the MIC potential to generate lethal metastases and did not limit primary tumour growth).

Inflammatory processes that initiate primary disease and drive EMT in primary breast cancers, thus causing MICs to disseminate, are not necessarily productive for MIC colonization. For example, IL-1β aids the growth of some primary tumours[33,52] and facilitates invasion and extravasation in early stages of metastasis[53], findings that are consistent with the idea that IL-1β promotes the EMT[17]. However, by specifically examining the role of IL-1β after MIC dissemination, we learned that sustained IL-1β-mediated inflammation or MIC IL-1R signalling prevents colonization and must be shut down for secondary tumour formation. We therefore consider that IL-1β has both dissemination-supportive and colonization-suppressive functions. These findings are consistent with a recent study showing that IL-1R inhibition, in combination with paclitaxel, moderately reduced primary breast tumour growth but significantly increased metastasis[54]. Identifying the appropriate setting to inhibit inflammation is also necessary. For example, a recent study demonstrated that neoadjuvant inhibition of inflammation (achieved by CCL2 blockade) resulted in significantly enhanced mammary carcinoma lung metastasis[55].

Such spatial and temporal considerations seem crucial, as phase I clinical trials using IL-1R blockade for metastatic disease are being initiated, predominantly supported by preclinical studies demonstrating primary tumour inhibition[56]. Our findings indicate that clinical success of IL-1R inhibition rests upon understanding its role at various stages of disease progression. Hence, IL-1R inhibition therapy may not always confer beneficial effects, and further research is required in order to identify appropriate contexts for administering such therapy.

The evolving paradigm of systemic instigation[57–61] or inhibition of breast cancer metastasis suggests new directions from which to investigate the interactions between primary tumours and systemic environment during metastatic progression. The fact that inflammatory hallmarks resolved primary tumours that inhibited secondary disease from those that did not, suggests that using primary tumour tissue to better predict metastatic behaviour may enable more accurate identification of patients with a high likelihood of relapse. It is therefore reasonable to think that a primary tumour expressing pro-inflammatory cytokines resulting in activation of an IL-1β-dependent innate immune response in the metastatic niche might keep secondary disease at bay and conversely, that primary tumour removal might prompt recurrence. Such concepts are underscored by our clinical finding that among patients with breast cancer and LN^{+} disease, those whose primary tumour expressed high IL-1β had improved outcomes relative to those with low IL-1β expression. Moreover, IL-1R1 was associated with the expression of mesenchymal factors in our study and in a report on patient circulating tumour cells[62]. The implications of our findings for other cancers[26] and for patients whose disease mimics the biology we have discovered here remain to be determined.

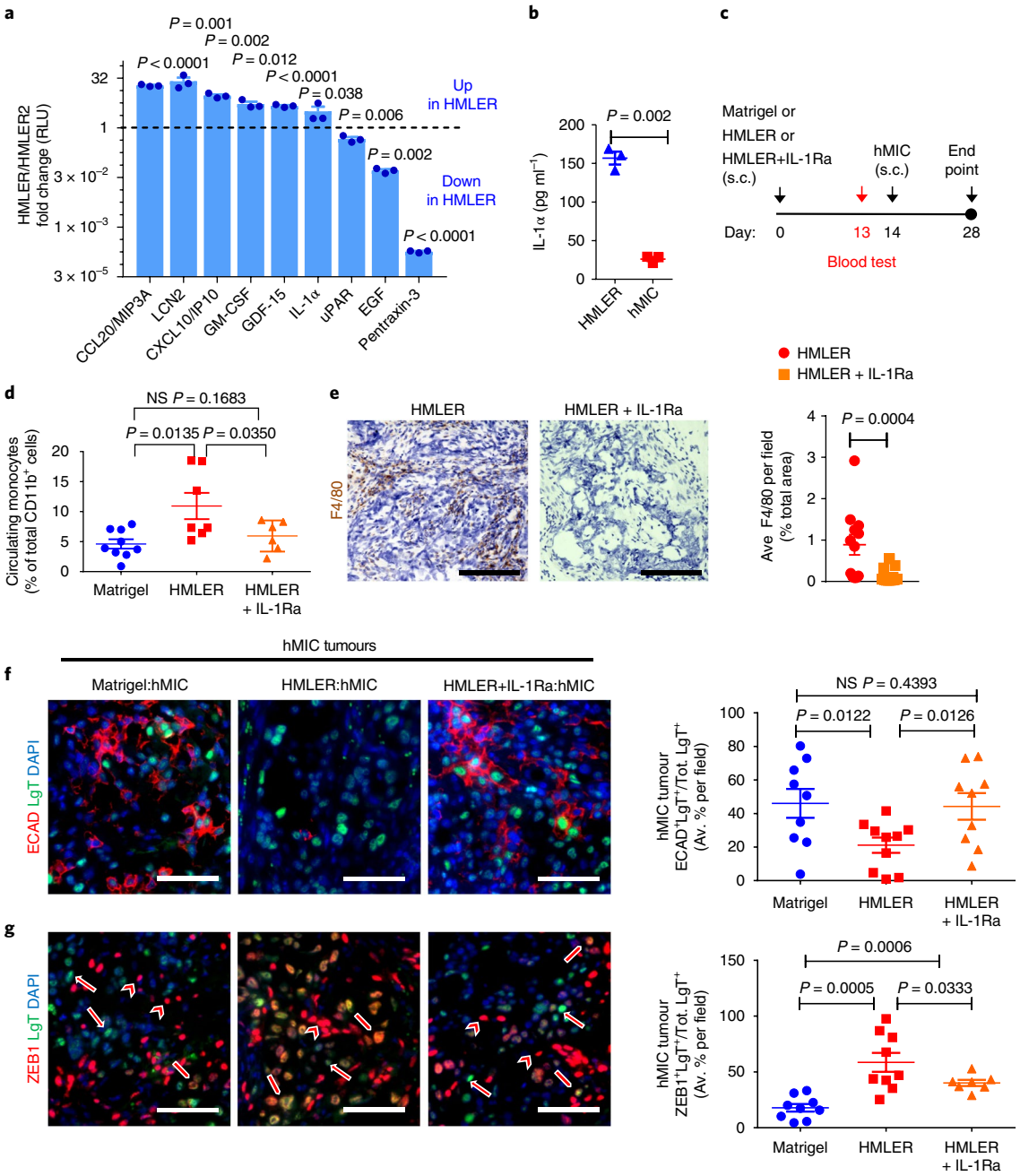

Fig. 7 | Inhibiting inflammation at the primary tumour site results in differentiation of disseminated MICs. a, Inflammatory cytokine array analysis of conditioned media from HMLER and the non-inhibitory primary tumour, HMLER2 cells, 3 days in culture ($n=2$ biological replicates, 3 technical replicates each). Results are fold change ($\log_2$) HMLER/HMLER2. **b**, ELISA for IL-1α in conditioned media from HMLER and hMIC cells, 3 days in culture ($n=3$ biological replicates, 5 technical replicates each). **c**, Experimental schematic modelling the early stages of hMIC colonization (nude mice) with Matrigel control, HMLER primary tumour, or HMLER primary tumour + IL-1Ra. **d**, Flow cytometry analysis of $CD11b^+Ly6C^+Ly6G^{low}$ circulating monocytes (day 13), before contralateral injection of hMIC cells, in mice bearing Matrigel control ($n=9$ animals), HMLER tumours ($n=7$ animals) or HMLER + IL-1Ra (100 ng ml^{-1}) tumours ($n=6$ animals). **e**, Left: HMLER and HMLER + IL-1Ra tumours stained with F4/80 (macrophages; brown) and haematoxylin (nuclei; blue). Scale bars, 100 µm. Right: Area positively stained for F4/80 macrophages in HMLER and HMLER + IL-1Ra tumours ($n=12$ independent images representing 4 tumours per cohort). **f**,**g**, Left: Indicated immunohistochemical staining of various hMIC tumours. Arrows indicate ZEB1$^-$ tumour cells. block arrows indicate ZEB1$^+$ tumour cells, and arrowheads indicate ZEB1$^+$ stromal cells. Scale bars, 100 µm. Right: Quantification of $ECAD^+LgT^+$ cells in hMIC tumours opposite Matrigel ($n=9$ independent images), HMLER ($n=10$ independent images), HMLER + IL-1Ra ($n=9$ independent images), 3 tumours per cohort as the percentage of the total number of LgT^+ human tumour cells per microscopy field (**f**). Quantification of $ZEB1^+LgT^+$ cells in hMICs tumours opposite Matrigel ($n=9$ independent images), HMLER ($n=9$ independent images), HMLER + IL-1R ($n=7$ independent images) 3 tumours per cohort) as the percentage of the total number of LgT^+ human tumour cells per microscopy field (**g**). Source data for **a**, **b**, **d**, **e**, **f** and **g** are provided in Supplementary Table 1. Multiple two-sided *t*-tests (**a**); two-sided Welch's *t*-test (**b**); one-sided Welch's *t*-test (**d**,**f**,**g**); two-sided Mann–Whitney test (**e**).

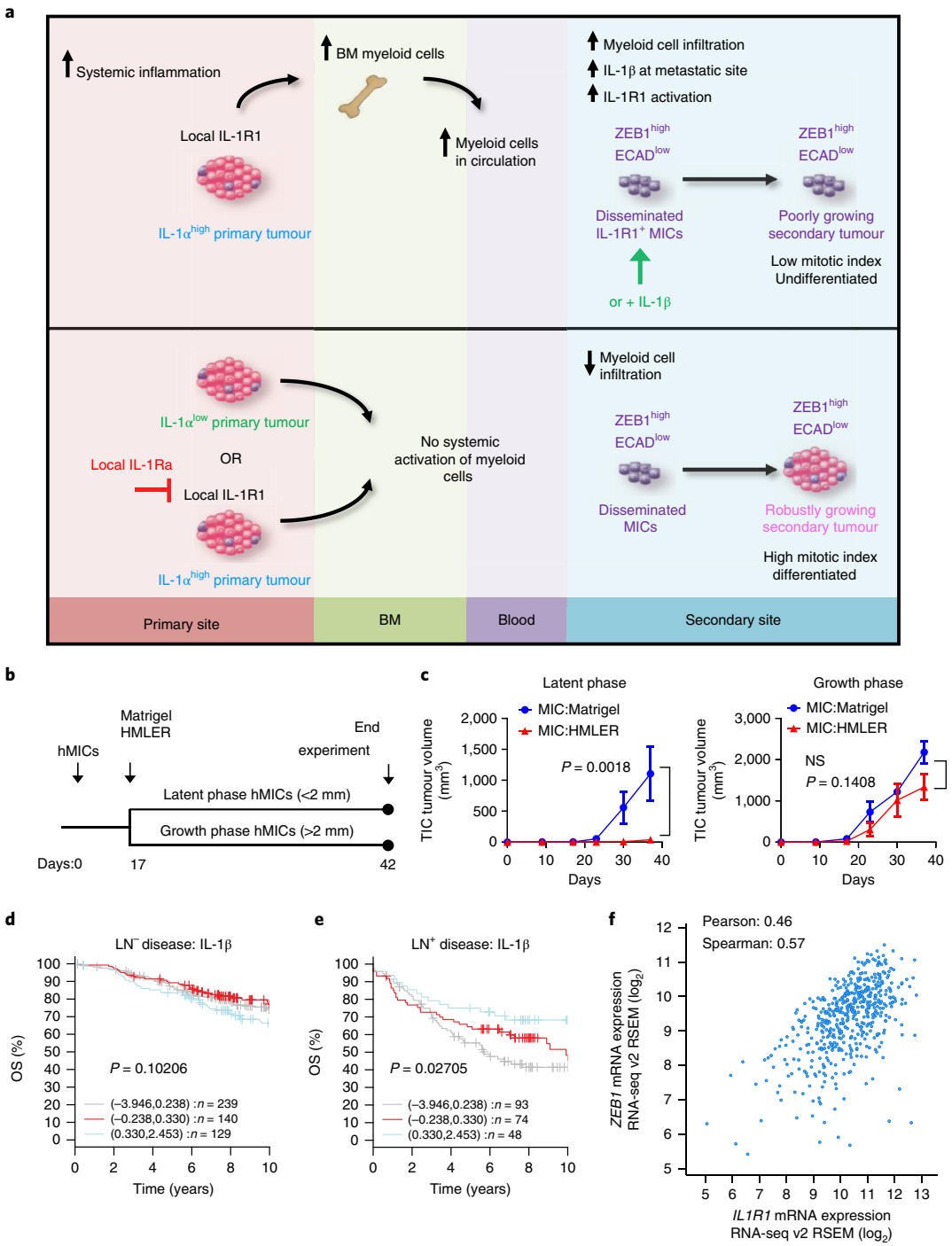

Fig. 8 | Low primary tumour IL-1β correlates with reduced overall survival in breast cancer. a, Model illustrating the systemic mechanism by which primary tumours elicit an IL-1β-dependent inflammatory response to suppress MIC colonization. Top: Primary tumours that secrete high levels of pro-inflammatory cytokines, for example, IL-1α, elicit a systemic innate immune response that expands bone marrow (BM) and circulating myeloid cells, culminating in increased immune infiltrate into tissues where MICs disseminate. In the metastatic microenvironment, IL-1β acts in a paracrine fashion on IL-1R-expressing MICs, causing the MICs to maintain their mesenchymal phenotype of high ZEB1 and/or low ECAD, thereby preventing MIC differentiation and proliferation. Bottom: Preventing inflammation at the primary tumour site or inhibiting IL-1R1 with the antagonist IL-1Ra in the metastatic microenvironment causes MICs to differentiate, proliferate and thereby establish robustly growing secondary tumours and metastases. **b**, Schematic of experiments to test the effect of primary HMLER tumours on established hMIC tumours in nude mice. **c**, Growth kinetics of hMIC tumours that were either in latent phase (left) or growth phase (right) at day 17 when Matrigel control or HMLER tumour cells were injected contralaterally. Latent phase: Matrigel, $n=6$ tumours; HMLER, $n=5$ tumours. Growth phase: Matrigel, $n=4$ tumours; HMLER, $n=5$ tumours. One experiment was performed. Two-way ANOVA and Sidak's multiple comparisons test. **d**,**e**, Kaplan–Meier analysis using overall survival (OS) as the end point with 10-year censoring, based on *IL1B* gene expression (log_2, stratified into three indicated quantiles) in primary tumour tissues from patients with LN^- ($n=508$ patients) (**d**) or LN^+ ($n=215$ patients) (**e**) disease. logrank *P* values are shown. Data and analysis obtained from the GOBO database (http://co.bmc.lu.se/gobo/gsa.pl). **f**, Correlation between *IL1R1* and *ZEB1* mRNA expression in 818 tumour tissue samples from patients with invasive breast carcinoma (RSEM, RNA-seq by expectation maximization). Data and analysis obtained from the cBioPortal database (http://www.cbioportal.org/index.do).

Methods

Methods, including statements of data availability and any associated accession codes and references, are available at https://doi.org/10.1038/s41556-018-0173-5.

Received: 21 March 2017; Accepted: 19 July 2018;
Published online: 27 August 2018

References

1. Siegel, R. L., Miller, K. D. & Jemal, A. Cancer statistics, 2016. *CA Cancer J. Clin.* **66**, 7–30 (2016).
2. Klein, C. A. Parallel progression of primary tumours and metastases. *Nat. Rev. Cancer* **9**, 302–312 (2009).
3. Pantel, K., Brakenhoff, R. H. & Brandt, B. Detection, clinical relevance and specific biological properties of disseminating tumour cells. *Nat. Rev. Cancer* **8**, 329–340 (2008).
4. Luzzi, K. J. et al. Multistep nature of metastatic inefficiency: dormancy of solitary cells after successful extravasation and limited survival of early micrometastases. *Am. J. Pathol.* **153**, 865–873 (1998).
5. Cameron, M. D. et al. Temporal progression of metastasis in lung: cell survival, dormancy, and location dependence of metastatic inefficiency. *Cancer Res.* **60**, 2541–2546 (2000).
6. Chambers, A. F., Groom, A. C. & MacDonald, I. C. Dissemination and growth of cancer cells in metastatic sites. *Nat. Rev. Cancer* **2**, 563–572 (2002).
7. Celia-Terrassa, T. & Kang, Y. Distinctive properties of metastasis-initiating cells. *Genes Dev.* **30**, 892–908 (2016).
8. Ghajar, C. M. Metastasis prevention by targeting the dormant niche. *Nat. Rev. Cancer* **15**, 238–247 (2015).
9. Redig, A. J. & McAllister, S. S. Breast cancer as a systemic disease: a view of metastasis. *J. Intern. Med.* **274**, 113–126 (2013).
10. Finisguerra, V. et al. MET is required for the recruitment of anti-tumoural neutrophils. *Nature* **522**, 349–353 (2015).
11. Wculek, S. K. & Malanchi, I. Neutrophils support lung colonization of metastasis-initiating breast cancer cells. *Nature* **528**, 413–417 (2015).
12. Granot, Z. et al. Tumor entrained neutrophils inhibit seeding in the premetastatic lung. *Cancer Cell* **20**, 300–314 (2011).
13. Coffelt, S. B. et al. IL-17-producing gammadelta T cells and neutrophils conspire to promote breast cancer metastasis. *Nature* **522**, 345–348 (2015).
14. Murgai, M., Giles, A. & Kaplan, R. Physiological, tumor, and metastatic niches: opportunities and challenges for targeting the tumor microenvironment. *Crit. Rev. Oncog.* **20**, 301–314 (2015).
15. McAllister, S. S. & Weinberg, R. A. The tumour-induced systemic environment as a critical regulator of cancer progression and metastasis. *Nat. Cell Biol.* **16**, 717–727 (2014).
16. de Visser, K. E. & Coussens, L. M. The inflammatory tumor microenvironment and its impact on cancer development. *Contrib. Mirobiol.* **13**, 118–137 (2006).
17. Chaffer, C. L., San Juan, B. P., Lim, E., & Weinberg, R. A. EMT, cell plasticity and metastasis. *Cancer Metastasis Rev.* **35**, 645–654 (2016).
18. Borowsky, A. D. et al. Syngeneic mouse mammary carcinoma cell lines: two closely related cell lines with divergent metastatic behavior. *Clin. Exp. Metastasis* **22**, 47–59 (2005).
19. Werbeck, J. L. et al. Tumor microenvironment regulates metastasis and metastasis genes of mouse MMTV-PymT mammary cancer cells in vivo. *Vet. Pathol.* **51**, 868–881 (2014).
20. Olive, J. F. et al. Accounting for tumor heterogeneity when using CRISPR-Cas9 for cancer progression and drug sensitivity studies. *PLoS ONE* **13**, e0198790 (2018).
21. Chaffer, C. L. et al. Normal and neoplastic nonstem cells can spontaneously convert to a stem-like state. *Proc. Natl Acad. Sci. USA* **108**, 7950–7955 (2011).
22. Bierie, B. et al. Integrin-beta4 identifies cancer stem cell-enriched populations of partially mesenchymal carcinoma cells. *Proc. Natl Acad. Sci. USA* **114**, E2337–E2346 (2017).
23. Naumov, G. N., Folkman, J. & Straume, O. Tumor dormancy due to failure of angiogenesis: role of the microenvironment. *Clin. Exp. Metastasis* **26**, 51–60 (2009).
24. Ye, X. & Weinberg, R. A. Epithelial–mesenchymal plasticity: a central regulator of cancer progression. *Trends Cell Biol.* **25**, 675–686 (2015).
25. Pattabiraman, D. R. et al. Activation of PKA leads to mesenchymal-to-epithelial transition and loss of tumor-initiating ability. *Science* **351**, aad3680 (2016).
26. Wellner, U. et al. The EMT-activator ZEB1 promotes tumorigenicity by repressing stemness-inhibiting microRNAs. *Nat. Cell Biol.* **11**, 1487–1495 (2009).
27. Palucka, A. K. & Coussens, L. M. The basis of oncoimmunology. *Cell* **164**, 1233–1247 (2016).
28. Hagerling, C. & Werb, Z. Neutrophils: critical components in experimental animal models of cancer. *Semin. Immunol.* **28**, 197–204 (2016).
29. DeNardo, D. G. et al. Leukocyte complexity predicts breast cancer survival and functionally regulates response to chemotherapy. *Cancer Discov.* **1**, 54–67 (2011).
30. Mantovani, A., Cassatella, M. A., Costantini, C. & Jaillon, S. Neutrophils in the activation and regulation of innate and adaptive immunity. *Nat. Rev. Immunol.* **11**, 519–531 (2011).
31. Gordon, S. Alternative activation of macrophages. *Nat. Rev. Immunol.* **3**, 23–35 (2003).
32. Muir, A. B. et al. Esophageal epithelial and mesenchymal cross-talk leads to features of epithelial to mesenchymal transition in vitro. *Exp. Cell Res.* **319**, 850–859 (2013).
33. Apte, R. N. et al. The involvement of IL-1 in tumorigenesis, tumor invasiveness, metastasis and tumor–host interactions. *Cancer Metastasis Rev.* **25**, 387–408 (2006).
34. Hou, Z., Falcone, D. J., Subbaramaiah, K. & Dannenberg, A. J. Macrophages induce COX-2 expression in breast cancer cells: role of IL-1β autoamplification. *Carcinogenesis* **32**, 695–702 (2011).
35. Bellehumeur, C., Blanchet, J., Fontaine, J. Y., Bourcier, N. & Akoum, A. Interleukin 1 regulates its own receptors in human endometrial cells via distinct mechanisms. *Hum. Reprod.* **24**, 2193–2204 (2009).
36. Windheim, M. & Hansen, B. Interleukin-1-induced activation of the small GTPase Rac1 depends on receptor internalization and regulates gene expression. *Cell Signal.* **26**, 49–55 (2014).
37. Shultz, L. D. et al. Multiple defects in innate and adaptive immunologic function in NOD/LtSz-scid mice. *J. Immunol.* **154**, 180–191 (1995).
38. Garlanda, C., Dinarello, C. A. & Mantovani, A. The interleukin-1 family: back to the future. *Immunity* **39**, 1003–1018 (2013).
39. Hu, Y. et al. Lipocalin 2 upregulation protects hepatocytes from IL1-β -induced stress. *Cell. Physiol. Biochem.* **36**, 753–762 (2015).
40. Deshmane, S. L., Kremlev, S., Amini, S. & Sawaya, B. E. Monocyte chemoattractant protein-1 (MCP-1): an overview. *J. Interferon Cytokine Res.* **29**, 313–326 (2009).
41. Pei, X. et al. The PSMP-CCR2 interactions trigger monocyte/macrophage-dependent colitis. *Sci. Rep.* **7**, 5107 (2017).
42. Dinarello, C. A. Immunological and inflammatory functions of the interleukin-1 family. *Annu. Rev. Immunol.* **27**, 519–550 (2009).
43. Ringner, M., Fredlund, E., Hakkinen, J., Borg, A. & Staaf, J. GOBO: gene expression-based outcome for breast cancer online. *PLoS ONE* **6**, e17911 (2011).
44. Cerami, E. et al. The cBio cancer genomics portal: an open platform for exploring multidimensional cancer genomics data. *Cancer Discov.* **2**, 401–404 (2012).
45. Gao, J. et al. Integrative analysis of complex cancer genomics and clinical profiles using the cBioPortal. *Sci. Signal.* **6**, pl1 (2013).
46. Ciriello, G. et al. Comprehensive molecular portraits of invasive lobular breast cancer. *Cell* **163**, 506–519 (2015).
47. Cejalvo, J. M. et al. Intrinsic subtypes and gene expression profiles in primary and metastatic breast cancer. *Cancer Res.* **77**, 2213–2221 (2017).
48. Dongre, A. et al. Epithelial-to-mesenchymal transition contributes to immunosuppression in breast carcinomas. *Cancer Res.* **77**, 3982–3989 (2017).
49. Guerriero, J. L. et al. Class IIa HDAC inhibition reduces breast tumours and metastases through anti-tumour macrophages. *Nature* **543**, 428–432 (2017).
50. Ruffell, B. & Coussens, L. M. Macrophages and therapeutic resistance in cancer. *Cancer Cell* **27**, 462–472 (2015).
51. Lu, H. et al. A breast cancer stem cell niche supported by juxtacrine signalling from monocytes and macrophages. *Nat. Cell Biol.* **16**, 1105–1117 (2014).
52. Schmid, M. C. et al. Combined blockade of integrin-alpha4beta1 plus cytokines SDF-1alpha or IL-1beta potently inhibits tumor inflammation and growth. *Cancer Res.* **71**, 6965–6975 (2011).
53. Spiegel, A. et al. Neutrophils suppress intraluminal NK cell-mediated tumor Cell clearance and enhance extravasation of disseminated carcinoma cells. *Cancer Discov.* **6**, 630–649 (2016).
54. Voloshin, T. et al. Blocking IL1beta pathway following paclitaxel chemotherapy slightly inhibits primary tumor growth but promotes spontaneous metastasis. *Mol. Cancer Ther.* **14**, 1385–1394 (2015).
55. Kersten, K. et al. Mammary tumor-derived CCL2 enhances pro-metastatic systemic inflammation through upregulation of IL1beta in tumor-associated macrophages. *Oncoimmunology* **6**, e1334744 (2017).
56. Dinarello, C. A. Why not treat human cancer with interleukin-1 blockade? *Cancer Metastasis Rev.* **29**, 317–329 (2010).
57. Castano, Z. et al. Stromal EGF and igf-I together modulate plasticity of disseminated triple-negative breast tumors. *Cancer Discov.* **3**, 922–935 (2013).
58. Elkabets, M. et al. Human tumors instigate granulin-expressing hematopoietic cells that promote malignancy by activating stromal fibroblasts in mice. *J. Clin. Invest.* **121**, 784–799 (2011).
59. Kuznetsov, H. S. et al. Identification of luminal breast cancers that establish a tumor-supportive macroenvironment defined by proangiogenic platelets and bone marrow-derived cells. *Cancer Discov.* **2**, 1150–1165 (2012).

60. McAllister, S. S. et al. Systemic endocrine instigation of indolent tumor growth requires osteopontin. *Cell* **133**, 994–1005 (2008).
61. De Cock, J. M. et al. Inflammation triggers Zeb1-dependent escape from tumor latency. *Cancer Res.* **76**, 6778–6784 (2016).
62. Yu, M. et al. Circulating breast tumor cells exhibit dynamic changes in epithelial and mesenchymal composition. *Science* **339**, 580–584 (2013).

Acknowledgements

This work was supported by funding from the following: International Mentoring Foundation for the Advancement of Higher Education (IMFAHE) (A.G.R.); Center for Stem Cell Bioinformatics at the Harvard Stem Cell Institute (J.N.H.); Samuel Waxman Cancer Research Foundation, Breast Cancer Research Foundation, and Ludwig Center for Molecular Oncology (R.A.W.); Advanced Medical Research Foundation and Nelune Foundation (C.L.C.); National Institutes of Health (NCI) RO1 CA166284, Presidential Early Career Award for Scientists and Engineers, American Cancer Society Research Scholar award, and Department of Defense BCMRP Era of Hope Scholar Award W81XWH-14-1-0191 (S.S.M.). We thank the following: J. Joyce for the Met1 cell line (with permission from A. Borowsky); J. Sceneay, B. Bierie, Y. Qin and K. Tracy for technical expertise; J. Olive for editorial assistance; E. Frank and the Dana-Farber/Harvard Cancer Center Breast Cancer Advocate group for critical discussion and input; Z. Herbert of the Molecular Biology Core Facilities, Dana-Farber Cancer Institute; G. Bell and B. Rosner for statistical advice; The Specialized Histopathology Core at Dana-Farber/Harvard Cancer Center (supported in part by a NCI Cancer Center Support Grant no. NIH 5 P30 CA06516); the Histology Core Facility at the KI Swanson Biotechnology Center, MIT; and the Flow Cytometry Core Facility at the Whitehead Institute for Biomedical Research. Finally, we thank GG Bernath, A. Bernath, J. Bernath, Z. Corsino-Gupta, P. Nguyen, B. Nguyen and K. Nguyen for their support during the preparation of this manuscript.

Author contributions

Z.C., C.L.C. and S.S.M designed and performed experiments, analysed data and wrote the manuscript. R.A.W., C.L.C and S.S.M. supervised the study and edited the manuscript. B.P.S.J., A.S., A.P., M.J.D., T.L., J.M.U., S.R.J., A.D., F.R., A.H., A.G.R. and A.M.G. performed experiments. J.N.H. and Z.T.H. performed the computational and statistical analyses. R.A.W., C.L.C., and S.S.M. acquired funding support.

Competing interests

The authors declare no competing interest.

Additional information

Supplementary information is available for this paper at https://doi.org/10.1038/s41556-018-0173-5.

Correspondence and requests for materials should be addressed to C.L.C. or S.S.M.

Methods

Cell lines and general reagents. HMLER, HMLER2 and hMIC were derived from HMECs originally obtained from ATCC. Cell lines were maintained as previously described[21]. MDA-MB-231 human breast epithelial tumour cells were originally obtained from ATCC and maintained in DMEM containing 10% fetal bovine serum (FBS), and their identity was verified by short tandem repeat analysis (Molecular Diagnostics Laboratory at Dana-Farber Cancer Institute). Met1 murine mammary carcinoma cells were a gift from J. Joyce, with permission from A. Borowsky, and maintained as previously described[18]. Their murine strain of origin was confirmed by short tandem repeat analysis (Bioassay Methods Group, NIST). MT2 and MT3-Met1 derived clones were obtained by expansion of plated 0.5 cells per well[20]. All cell lines were routinely tested to confirm the absence of mycoplasma contamination. The following reagents were used: recombinant human IL-1α and IL-1β (R&D Systems); IL-1Ra (CYT-203; ProSpec); BD Matrigel Basement Membrane Matrix (CB40230; BD Biosciences), dox-inducible lentiviral ZEB1-IRES-GFP construct (pTK380).

Animal experiments. Female FVB mice 7 weeks of age and NCR-Nu (nude) mice 6–8 weeks of age were purchased from Taconic Biosciences. Female NOD/SCID mice were bred in-house. Mice were 8–9 weeks of age at the time of injections. For orthotopic injections, cells (5.0×10^5 hMICs; 2.5×10^5 mMICs) were prepared in PBS (20 µl) and injected into the inguinal mammary fat pads. For intravenous injections, cells (2.5×10^5 hMICs; 7.5×10^5 mMICs) were prepared in PBS (100 µl) and injected into the tail vein. For subcutaneous injections, tumour cells (5.0×10^5 hMICs; 2.5×10^5mMICs) were resuspended in 20% Matrigel/MEGM (100 µl). For in vivo experiments, sample sizes were determined based on previous experience with the models utilized, including experience in variabilities in tumour growth. Animals were randomly assigned to groups. In experiments for which the analysis of secondary tumour biology was dependent on the growth of primary tumours, animals were excluded from subsequent analysis if primary tumours did not grow. Investigators were not blinded to allocation during experiments; however, for downstream analyses of mouse tissue (immunohistochemistry, image analysis and flow cytometry), all experiments were performed in a blinded fashion. Tumour volumes were calculated as follows: $(l\times w^2)/2$. Tumours were measured by caliper 2–3 times per week. For tumour growth curve analysis, we performed one-way ANOVA tests with correction for multiple comparisons using Sidak's multiple comparisons test. The study was compliant with all relevant ethical regulations regarding animal research. All experiments were conducted in compliance with federal laws and institutional guidelines as approved by the Institutional Animal Care and Use Committees of the MIT (protocol no. 1005-076-08), the Children's Hospital Boston (protocol no. 15-11-3062R), and the Brigham and Women's Hospital (protocol no. 2017N000056).

Tumour digests. Tumours were chopped into small pieces in sterile conditions then incubated at 37 °C for 4 h in DME containing collagenase A and hyaluronidase. Following digestion, tumour cell suspensions were pelleted, the DME removed and then resuspended in 0.15% trypsin for 3 min. Trypsin was quenched with 10% IFS in DME. Cells were spun down then analysed by flow cytometry or stored in freezing medium (10% DMSO, 90% calf serum).

Lung metastasis quantification. Pulmonary metastases were scored blindly using two methods. First, visible metastases were counted on whole lung tissue under a dissecting microscope. Second, lesions were counted on haematoxylin and eosin (H&E)-stained tissue sections under high power on a Nikon Eclipse 90i microscope.

Neutrophil depletion. Mice were injected intraperitoneally with 12.5, 50 or 100 µg per 20 g body weight of rat anti-mouse Ly6G antibody (clone 1A8, BioXCell) or rat IgG2a (BioXCell) every other day until indicated experimental end points. The efficiency of neutrophil depletion in blood and lungs was assessed by flow cytometry.

RNA extraction for RNA-seq. Approximately 20-mg samples of lung tissue were excised and immediately snap frozen in liquid nitrogen. Frozen samples were incubated with 600 µl of lysis buffer (RNeasey Plus Mini Kit, Qiagen) and 20 U of RNAse inhibitors per sample (Applied Biosystems), and immediately disrupted and homogenized with a rotor-stator homogenizer. RNA was extracted using the RNeasey Plus Mini Kit, according to the manufacturer's instructions. Final RNA was resuspended in 50 µl of RNase-free water and 20 U of RNAse inhibitors per sample.

Library preparation and RNA-seq. Purified total RNA samples were evaluated for quality using an Agilent Bioanalyzer to calculate the RNA integrity number (RIN) score and percentage of RNA fragments > 200 nucleotides (DV_{200}). RNA samples with a RIN score >7 as well as RNA samples with a RIN score <7 but DV_{200} score >50% were fragmented at 94 °C for 8 min according to the manufacturer's recommendation. RNA samples with a RIN score <7 and DV_{200} score <50% were not fragmented and reverse transcription (RT) primers were annealed at 65 °C for 1 min. Libraries were prepared using Roche Kapa Biosystems RiboErase and RNA HyperPrep sample preparation kits from 100 ng of RNA. The finished dsDNA libraries were quantified using a Qubit fluorometer, a Agilent TapeStation 2200 and by RT-qPCR using the Roche Kapa Biosystems library quantification kit according to manufacturer's protocols. Uniquely indexed libraries were pooled in equimolar ratios and sequenced on an Illumina NextSeq500 with single-end 75 bp reads by the Dana-Farber Cancer Institute Molecular Biology Core Facilities.

RNA-seq differential expression and functional enrichment analysis. All samples were processed and analysed using an RNA-seq pipeline implemented in the bcbio-nextgen project (https://bcbio-nextgen.readthedocs.org/en/latest/) and the bcbioRNASeq R package (https://github.com/hbc/bcbioRNASeq)[63]. Reads were aligned to the Genome Reference Consortium Mouse Reference build number 38 (GRCm38) of the mouse genome (aka mm10) augmented with transcript information from Ensembl using STAR[64] with soft trimming enabled to remove adapter sequences, other contaminant sequences such as poly-A tails and low Phred quality score sequences. Counts of reads aligning to known genes were generated by featureCounts[65] for use in quality control measures. In parallel, transcripts per million measurements per isoform were generated by quasialignment using Salmon[66] for use in clustering and differential expression analyses. STAR alignments were checked for evenness of coverage, ribosomal RNA content, genomic context of alignments (for example, alignments to exons and introns), complexity and other quality checks using a combination of FastQC, Qualimap[67], MultiQC (https://github.com/ewels/MultiQC) and custom tools. Samples were clustered in an unsupervised manner by both principal component analysis and hierarchical means using rlog transformed reads to identify potential outliers and technical artefacts. Outlier samples with low mapping rates (<70%) or low RIN values and 5'>3' biases were removed from the analysis. Only data for Ensembl annotated protein coding and long intergenic noncoding RNA genes were retained for further analysis. Differential expression at the gene level was called with DESeq2[68], using the counts per gene estimated from the Salmon quasialignments by tximport[69] as quantitating at the isoform level has been shown to produce more accurate results at the gene level. Lists of DEGs were examined for GO and Kyoto Encyclopedia of Genes and Genomes (KEGG) term enrichment with clusterProfiler[70]. In addition, cut-off-free gene set enrichment analyses (GSEA) were performed with clusterProfiler, the fast GSEA pre-ranked algorithm[71] and the fold change calculations from DESeq2. Functional gene sets were considered enriched if their false discovery rate-adjusted P value was less than 0.05.

RNA-seq cell signature analysis. For the Coffelt signature[13], DEGs from their KEP versus wild-type analysis were selected and subset to those with a P value <0.1. Genes were split into two sets of signature genes: those upregulated in KEP neutrophils and those downregulated. For each signature's genes, the geometric means of expression were determined for samples within our dataset (using data from the transcripts per million count matrix) and the ratio of these values determined. Significance was assessed by simple t-test. Samples with RIN values <3 were removed from the analysis.

RNA extraction and RT-qPCR. Fresh tumours (up to 150 mg) were homogenized in 1 ml of TRIzol (Ambion, Life Technologies, catalogue no. 15596018) with a tissue homogenizer in a 5-ml BD Falcon polypropylene tube. Cultured cells were collected using a cell lifter (Costar cell lifter, polyethylene, catalogue no. 3008) in 1 ml of TRIzol. Samples were incubated in TRIzol for 5 min at room temperature. Chloroform (0.2 ml; Sigma, catalogue no. 366927) was added to homogenates and the samples were shaken vigorously for 15 s. Samples were incubated at room temperature for 3 min and centrifuged at 13,000×g for 15 min at 4 °C. The aqueous phase was carefully removed and applied to a genomic DNA elimination column (approximately 350 µl) (Qiagen RNeasy Plus kit, catalogue no. 74136). The column was centrifuged for 30 s at 13,000×g. An equal volume of 100% RNA-free ethanol was added to the RNA in the collection tube and mixed with a pipette tip. The sample (700 µl) was loaded onto an RNeasy column (Qiagen RNeasy Plus kit, catalogue no. 74136) seated in a collection tube and centrifuged for 30 s at 8,000×g. Columns were washed with Buffer RW1 (700 µl), then centrifuged for 30 s at 8,000×g, then washed and centrifuged with buffer RPE (500 µl) two times. To eliminate the remaining buffer, columns were centrifuged again for 1 min at 8,000×g. The column was transferred into a new 1.5-ml collection tube and 50 µl of RNase-free water was pipetted directly onto the column membrane. The sample was incubated for 2 min at room temperature and centrifuged for 1 min at 8,000×g to elute RNA. The RNA concentration was measured using a Nanodrop (Thermo Scientific). RNA was stored at −80 °C. The miScript II RT kit (Qiagen, catalogue no. 218161) was used to synthesize complementary DNA from total RNA. Therefore, a 20-µl reaction was prepared containing 4 µl of 5× miScript Hiflex buffer, 2 µl of 10× miScript Nucleics mix, 2 µl Reverse Transcriptase mix and 1 µg of purified RNA in 12 µl of RNase-free water. According to the manufacturer's protocol, the samples were amplified using a Biorad Mycycler at 37 °C for 60 min, 95 °C for 5 min and cooled to 4 °C. RNase-free water (80 µl) was added to each cDNA sample (20 µl) to obtain a concentration of 10–15 ng µl^{-1}. cDNA was stored at −20 °C. Relative gene expression was determined using a QuantiFast SYBR Green PCR kit (Qiagen) and Quantitect Primer Assays (Qiagen). qPCR amplifications were carried out in 384-well plates using a Lightcycler 480 (Roche). The following human-specific

Quantitect Primer Assays were used: β-actin (ACTB; QT01680476), IL-1A (QT00001127), ZEB1 (QT01888446), IL-1R1 (QT00081263), IL-1B (QT00021385), and IL-1RN (QT00014238). The following mouse-specific Quantitect Primer Assays were used: IL-1β (QT01048355), IL-1α (QT00113505), and Actb (QT01136772). Other primers used for gene expression quantification were as follows: murine IL-1β (F: 5′-CTTCAGGCAGGCAGTATCACTC-3′, R: 5′-GCAGTTGTCTAATGGGAACGTC-3′) and murine β-actin (F: 5′-CCACTGCCGCATCCTCTTCCT-3′, R:5′-CACACAGAGTACTTGCGCTCAGG-3′). mRNA expression levels were normalized to the mRNA levels of the housekeeping gene *ACTB*. All qPCR reactions were run in triplicate.

Immunofluorescence, immunohistochemistry, image analysis and antibodies. Dissected tissues were fixed in 4% (w/v) paraformaldehyde for 24 h, stored in 70% ethanol for 24 h, embedded in paraffin, and sectioned onto ProbeOn Plus slides (Fisher Scientific) for immunohistochemistry using Vectastain Elite ABC kits (Vector Laboratories) as previously described[57,72]. Details and antibodies are provided in the Reporting Summary. Myeloperoxidase staining was run on a Leica Bond III autostaining platform using a Bond Polymer Refine Detection kit. Antigen retrieval was performed using Bond Epitope Retrieval 2 for 20 min. For immunofluorescence, an Enhancer TSA Plus Cyanine 3 System (Perkin Elmer) was used for ZEB1, CK14 and ECAD stains. Nuclei were stained and mounted with ProLong Gold Antifade Mountant with 4,6-diamidino-2-phenylindole (DAPI; ThermoFisher Scientific). Images were captured under indicated the magnification, and with identical exposure and gain for any given experiment, using a Nikon Eclipse 90i microscope. Staining was quantified using NIH ImageJ software (http://imagej.nih.gov/ij/).

ELISA and cytokine array. Cells (1×10^6) were plated in triplicate into 10-cm plates with 10 ml of medium. After 72 h, media were collected, centrifuged at 413 × g for 10 min at 4 °C, and supernatant was used for ELISAs. The number of cells and viability were measured in each plate in order to normalize the levels of protein secretion based on the final number of cells. The following ELISAs and cytokine arrays were carried out according to the manufacturer's instructions: human IL-1α/IL-1F1, human IL-1β/IL-1F2, and mouse IL-1β/IL-1F2 Quantikine ELISA Kits; human XL Cytokine Array Kit ARY022; and mouse cytokine Antibody Array ARY006 (R&D Systems).

Isolation of blood and bone marrow cells. Blood was collected into EDTA tubes (BD Microtainer), and red blood cell lysis was performed using BD Pharm Lyse Lysing Buffer (BD Biosciences) following the manufacture's protocol. Bone marrow cells were harvested from donor mice by flushing femurs with PBS–2% FBS. Cells were washed with PBS, dissociated with 18 gauge needles, and filtered through 70-μm nylon mesh[58,60].

Flow cytometry. Cell suspensions were blocked with anti-CD16/32 F_cY III/II receptor antibody (BioLegend) used at a concentration of 250 ng per 1×10^6 cells for 20 min on ice. After washing, cells were incubated with anti-IL-1β-APC (clone 166931) used at a concentration of 10 μl per 1×10^6 cells and rat anti-IgG2B isotype control-APC (clone 141945; R&D Systems). Anti-mouse CD45-PerCy5.5, anti-mouse Ly-6C-PE, anti-mouse PE-Gr1, anti-mouse Ly-6G-488 and anti-mouse CD11b PE-Cy7 (eBioscience) were used at a concentration of 0.2 μg per 1×10^6 cells. Intracellular fluorescence-activated cell sorting (FACS) staining required BD Cytofix/Cytoperm Plus (BD Biosciences) and was used according to the manufacturer's instructions. Samples were analysed on a BD LSRII using FACSDiva Software (BD Biosciences). The following antibodies (purchased from BioLegend unless otherwise stated) were used to characterize haematopoietic stem and progenitor populations: BV605 Sca1 (clone D7); BV786 cKit (BD, clone 2B8); APC CD150 (clone TC15); APC Cy7 CD48 (clone HM48-1); AF488 CD34 (eBioscience, clone RAM34); PE Cy7 IL7Ra (clone A7R34); PE FcgRII/III (clone 93); PE Flt3 (clone A2F10); PB Lineage cocktail (catalogue no. 133310); APC Cy7 NK1.1 (clone PK136); Brilliant violet 785 B220 (clone RA3-6B2); and PE cd11c (clone N418). Cell populations were characterized using the following cell surface markers: Lin^-, $Sca1^+$, $cKit^+$, $CD150^+$, $CD48^+$, $CD45^-$ and $Flt3^-$ for HSCs; Lin^-, $Sca1^+$, $cKit^+$, $CD34^-$ and $Flt3^-$ for LT-HSCs; Lin^-, $Sca1^+$, $cKit^+$, $CD34^-$ and $Flt3^+$ for ST-HSCs; Lin^-, $Sca1^+$, $cKit^+$, $CD150^-$ and $CD48^+$ for multipotent progenitors (MPPs); Lin^-, $Sca1^+$, $cKit^+$ and $IL\text{-}7Ra^+$ for CLPs; Lin^-, $Sca1^-$, $cKit^+$ and $IL\text{-}7Ra^-$ for myeloid progenitors; Lin^-, $Sca1^-$, $cKit^+$, $IL\text{-}7Ra^-$, $CD34^+$ and $FCgRII/III^-$ for CMPs; Lin^-, $Sca1^-$, $cKit^+$, $IL\text{-}7Ra^-$, $CD34^+$ and $FCgRII/III^+$ for GMPs; and Lin^-, $Sca1^-$, $cKit^+$, $IL\text{-}7Ra^-$, $CD34^-$ and $FCgRII/III^-$ for MEPs. Dead cells were excluded using 7AAD (BioLegend). CountBright absolute counting beads (Molecular Probes, ThermoFisher) were added to samples to determine absolute cell numbers. Flow cytometry was performed on a LSRII (BD Biosciences), and data were analysed using FlowJo (TreeStar).

Tumourspheres. Met1 cells (2.0×10^3 or 4.0×10^3) were plated on ultralow attachment plates (Corning, Costar) in DMEM/F-12 HAM medium (Sigma) containing 20 ng ml^{-1} basic fibroblast growth factor (Sigma), 20 ng ml^{-1} epidermal growth factor (EGF; Sigma) and B-27 supplement (1:50 dilution, Life Technologies), and cultured at 37 °C, 5% CO_2. Fresh media with or without IL-1β or anakinra treatments were added every 48 h. Seven days later, spheres were counted based on size (small considered > 5 < 20 cells per sphere; large considered > 20 cells per sphere). Tumoursphere formation is represented as a percentage of control.

Western blot analysis. Protein was extracted from cell lysates using RIPA lysis buffer (sc-24948) or specific lysis buffer for phospho-protein detection (20 mM Tris-HCl pH 7.6, 137 mM NaCl, 1% NP40, 0.5% Na-deoxycholate, 10 mM NaF, 20 mM β-glycerophosphate, 1 mM Na-orthovanadate and 1:200 complete protease inhibitors). A total of 10 μg of proteins and precision plus protein dual colour standard (Bio-Rad, 161-0374) were run in a 4–12% Bis-Tris gel (Invitrogen). Proteins were transferred to a polyvinylidene fluoride membrane and incubated overnight with VIM (diluted 1:500; Dako, clone Vim3B4), ECAD (diluted 1:500; Cell Signaling, clone 24E10), P-NF-κB p65 (diluted 1:1,000; Cell Signaling, clone S536), NF-κB p65 (diluted 1:1,000; Cell Signaling, clone D14E12) and GAPDH (diluted 1:1,000; Santa Cruz Biotechnology) or β-actin (diluted 1:10,000, ab20272). Horseradish peroxidase-conjugated secondary antibodies (diluted 1:5,000) were used (Jackson Immunoresearch). Blots were developed using ECL (Dura or Femto, Pierce). Blots were re-probed after stripping the membranes with 1-min Western Blot stripping buffer (GN6002, GM Biosciences).

Cell proliferation assay. Cell proliferation was measured using a CyQuant Cell Proliferation Assay Kit (ThermoFisher Scientific). Cells were plated in triplicate at a density of 1.0×10^3 cells per well in a 96-well plate. Cells were harvested daily for 5 days by removing the culture medium and storing at −20 °C. All plates were processed at the end of the experiment on the same day. Cell number was determined by measuring fluorescence using a microplate reader with ~480 nm excitation and ~520 nm emission.

Suppression of IL-1R using shRNA constructs. IL-1R1-shRNA constructs were purchased from Openbiosystems (RHS4531-NM_000877). pLenti-based constructs were packaged with the pMD2.G (VSVG) and psPAX2 plasmids. Viral infections were performed using 6 μg ml^{-1} protamine sulfate for 8 h.

Statistics and reproducibility. Statistical analyses were performed as described in the figure legend for each experiment. All statistical tests were two-sided unless otherwise indicated. D'Agostino Pearson omnibus and Shapiro–Wilk normality tests were used to test datasets for Gaussian distribution. All data are presented as the mean ± s.e.m. Differences were considered statistically significant at $P \leq 0.05$. All data shown are representative of two or more independent experiments, unless indicated otherwise. All attempts at replication were successful. No data points were excluded from analysis.

Reporting Summary. Further information on experimental design is available in the Nature Research Reporting Summary linked to this article.

Code availability. Scripts and auxiliary data needed to reconstruct analysis files are available in a git repository (https://github.com/hbc/sandra_mcallister_lung_distal_tumor) and under a DOI (https://doi.org/10.5281/zenodo.1172004).

Data availability. Transcriptomic data that support the findings of this study have been deposited in the Gene Expression Omnibus under primary accession code GSE111157. Previously published RNA-seq data that were re-analysed are available under the origin accession code GSE55633 (Coffelt dataset). *IL1B* gene expression-based outcomes for patients with breast cancer were based on the online tool GOBO (http://co.bmc.lu.se/gobo/), and correlation studies between IL-1R and EMT genes on the cBio Cancer Genomics Portal (http://cbioportal.org). Source data are provided in Supplementary Table 1, and unprocessed blots are provided in Supplementary Fig. 9. All other data are available from the corresponding authors upon reasonable request.

References

63. Steinbaugh, M. J. bcbioRNASeq: R package for bcbio RNA-seq analysis. *F1000Res* **6**, 28 (2017).
64. Dobin, A. et al. STAR: ultrafast universal RNA-seq aligner. *Bioinformatics* **29**, 15–21 (2013).
65. Liao, Y., Smyth, G. K. & Shi, W. featureCounts: an efficient general purpose program for assigning sequence reads to genomic features. *Bioinformatics* **30**, 923–930 (2014).
66. Patro, R., Duggal, G., Love, M. I., Irizarry, R. A. & Kingsford, C. Salmon provides fast and bias-aware quantification of transcript expression. *Nat. Methods* **14**, 417–419 (2017).
67. Garcia-Alcalde, F. et al. Qualimap: evaluating next-generation sequencing alignment data. *Bioinformatics* **28**, 2678–2679 (2012).
68. Love, M. I., Huber, W. & Anders, S. Moderated estimation of fold change and dispersion for RNA-seq data with DESeq2. *Genome Biol.* **15**, 550 (2014).

69. Soneson, C., Love, M. I. & Robinson, M. D. Differential analyses for RNA-seq: transcript-level estimates improve gene-level inferences. *F1000Res* **4**, 1521 (2015).
70. Yu, G., Wang, L. G., Han, Y. & He, Q. Y. clusterProfiler: an R package for comparing biological themes among gene clusters. *OMICS* **16**, 284–287 (2012).
71. Sergushichev, A. An algorithm for fast preranked gene set enrichment analysis using cumulative statistic calculation. Preprint at https://doi.org/10.1101/060012 (2016).
72. Sendobry, S. M. et al. Attenuation of diet-induced atherosclerosis in rabbits with a highly selective 15-lipoxygenase inhibitor lacking significant antioxidant properties. *Br. J. Pharmacol.* **120**, 1199–1206 (1997).

nature research

Corresponding author(s): C. Chaffer, S. McAllister
NCB-C33621

Reporting Summary

Nature Research wishes to improve the reproducibility of the work that we publish. This form provides structure for consistency and transparency in reporting. For further information on Nature Research policies, see Authors & Referees and the Editorial Policy Checklist.

Statistical parameters

When statistical analyses are reported, confirm that the following items are present in the relevant location (e.g. figure legend, table legend, main text, or Methods section).

n/a	Confirmed	
☐	☒	The exact sample size (*n*) for each experimental group/condition, given as a discrete number and unit of measurement
☐	☒	An indication of whether measurements were taken from distinct samples or whether the same sample was measured repeatedly
☐	☒	The statistical test(s) used AND whether they are one- or two-sided *Only common tests should be described solely by name; describe more complex techniques in the Methods section.*
☐	☒	A description of all covariates tested
☐	☒	A description of any assumptions or corrections, such as tests of normality and adjustment for multiple comparisons
☐	☒	A full description of the statistics including central tendency (e.g. means) or other basic estimates (e.g. regression coefficient) AND variation (e.g. standard deviation) or associated estimates of uncertainty (e.g. confidence intervals)
☐	☒	For null hypothesis testing, the test statistic (e.g. *F*, *t*, *r*) with confidence intervals, effect sizes, degrees of freedom and *P* value noted *Give P values as exact values whenever suitable.*
☒	☐	For Bayesian analysis, information on the choice of priors and Markov chain Monte Carlo settings
☐	☒	For hierarchical and complex designs, identification of the appropriate level for tests and full reporting of outcomes
☐	☒	Estimates of effect sizes (e.g. Cohen's *d*, Pearson's *r*), indicating how they were calculated
☐	☒	Clearly defined error bars *State explicitly what error bars represent (e.g. SD, SE, CI)*

Our web collection on statistics for biologists may be useful.

Software and code

Policy information about availability of computer code

Data collection	For RNA library preparation Qubit fluorometer, Agilent TapeStation 2200 was used. For images capture Nikon NIS Elements v4.3 software was use, for flow cytometric capture FACSDiva software (BD Biosciences) was used.
Data analysis	Prism, NIH ImageJ (http://imagej.nih.gov/ij/), FlowJo, CellProfiler, GOBO database (http://co.bmc.lu.se/gobo/gsa.pl), and cBioPortal database (http://www.cbioportal.org/index.do). All the information related to software and codes used for RNAseq analysis are available on DOI (https://doi.org/10.5281/zenodo.1172004).

For manuscripts utilizing custom algorithms or software that are central to the research but not yet described in published literature, software must be made available to editors/reviewers upon request. We strongly encourage code deposition in a community repository (e.g. GitHub). See the Nature Research guidelines for submitting code & software for further information.

Data

Policy information about availability of data

All manuscripts must include a data availability statement. This statement should provide the following information, where applicable:

- Accession codes, unique identifiers, or web links for publicly available datasets
- A list of figures that have associated raw data
- A description of any restrictions on data availability

There are no restrictions on availability of materials.

Field-specific reporting

Please select the best fit for your research. If you are not sure, read the appropriate sections before making your selection.

☒ Life sciences ☐ Behavioural & social sciences

For a reference copy of the document with all sections, see nature.com/authors/policies/ReportingSummary-flat.pdf

Life sciences

Study design

All studies must disclose on these points even when the disclosure is negative.

Sample size	Sample sizes were chosen based on previous experience with the models and methods used in this study. Online Methods - Animals
Data exclusions	No data were excluded from analysis Online Methods - Statistical Analysis.
Replication	Biological experiments were repeated at least twice whenever possible. In vitro experiments were run with at least 2 biological replicates and 3 technical replicates. All attempts at replication were successful. Online Methods - Statistical Analysis.
Randomization	Animals were randomly assigned to groups. Online Methods - Animals
Blinding	The investigators were not blinded to allocation during experiments, however, for downstream analyses of mouse tissue (metastasis quantification, immunohistochemistry, image analysis, flow cytometry) all experiments were performed in a blinded fashion. Online Methods - Animals

Materials & experimental systems

Policy information about availability of materials

n/a	Involved in the study
☒	☐ Unique materials
☐	☒ Antibodies
☐	☒ Eukaryotic cell lines
☐	☒ Research animals
☒	☐ Human research participants

Antibodies

Antibodies used	For IHC/IF: anti-Meca32 (129501, BioLegend) anti-Myeloperoxidase (A0398, Dako, Dil 1:3500) anti-MAC-2 (CL8942AP, Cederlane, Dil 1:8000) anti-ECAD (clone 24E10, Cell Signaling, Dil 1.50, Lot 13) anti-Zeb1 (sc-25388, Santa Cruz Biotechnology, Dil 1:150, Lot K1615) anti-SV40TAg (Pab101, Santa Cruz Biotechnology, Dil 1:75, Lot I1212) anti-Cleaved Caspase3 (9664, Cell Signaling, Dil 1:50, Lot 20) anti-Ki67 (SP6, ThermoFisher Scientific, Dil 1:200, Lot 9106S) anti-CK14 (PRP-155P, Biolegend, Dil 1: 50, Lot B237273) anti-CK8 (TROMA-I, DSHB, Dil 1:50) anti-human mitochondria (MAB1273, Millipore, Dil 1:50, Lot NG1924059) anti-PyMT (ab15085, Abcam, Dil 1:50, Lot GR108140-23) anti-IL-1R (sc393998, Santa Cruz, Dil 1:50, Lot D1117)

Alexa Fluor 488 goat anti-mouse (A11001, Invitrogen, Dil 1:200, Lot 1110070)
Alexa Fluor 594 goat anti-rabbit (A11012, Invitrogen, Dil 1:200, Lot 1745478)
Alexa Fluor 647 goat anti-rat (A21247, Invitrogen, Dil 1:200, Lot 1810934)

For Western blot:
anti-Vimentin (Dil 1:500; Dako clone Vim3B4)
anti-ECAD (Dil 1:500; Cell Signaling clone 24E10, Lot 13)
anti-Phospho-NF-Kappa B p65 (Dil 1: 1000; Cell Signaling clone S536, Lot 16)
anti-NF-Kappa B p65 (Dil 1: 1000; Cell Signaling clone D14E12, Lot 9)
anti-GAPDH (Dil 1:1000; santa cruz biotechnology)
anti-ACTB (Dil 1:10,000, ab20272, Lot GR256141-5)

Validation

For Western blot, antibodies were validated as noted on manufacturer's website. Specifically VIM, ECAD, P-NF-Kappa B p65, NF-Kappa B p65, GAPDH and ACTB were demonstrated to work for western blot by previous publications of others and our own groups in the species tested. Positive and negative controls were included, when possible.
For flow cytometry and immunofluorescence, antibodies were validated as noted on manufacturer's website, and most of antibodies specificity was confirmed in the literature. In addition, the stainings were consistent with the predicted cellular localization of the protein.
Antibodies were further validated by using positive and negative controls in our studies.

Eukaryotic cell lines

Policy information about cell lines

Cell line source(s)

HMLER, HMLER2 and hMIC were derived from human mammary epithelial cells (HMEC) originally obtained from ATCC. MDA-MB-231 were obtained from ATCC. Met1 cells were a gift from Dr. Johanna Joyce, with permission from A. Borowsky. MT2 and MT3 were Met1 derived clones obtained by expansion of plated 0.5 cells/well. More details about cell lines used in this study are described in online methods

Authentication

The murine strain of origin from Met1, was confirmed by short tandem repeat analysis (Bioassay Methods Group, NIST). MDA-MB-231 cells were validated by short tandem repeat analysis (Molecular Diagnostics Laboratory at Dana-Farber Cancer Institute, Boston, MA). HMLER, HMLER2, and hMIC cells were not authenticated.

Mycoplasma contamination

All cell lines were routinely tested to confirm the absence of mycoplasma contamination.

Commonly misidentified lines
(See ICLAC register)

No commonly misidentified cell lines were used.

Research animals

Policy information about studies involving animals; ARRIVE guidelines recommended for reporting animal research

Animals/animal-derived materials

Female FVB mice 7 weeks of age and NCR-Nu (Nude) mice 6-8 weeks of age were purchased from Taconic Biosciences (Hudson, NY). Female NOD/SCID mice were bred in-house. All experiments were conducted in accordance with regulations of the MIT committee on animal care protocol (1005-076-08), Children's Hospital institutional animal care and use committee (protocol 15-11-3062R) and Brigham and Women's Hospital animal care protocol committee (2017N000056).
Online Methods - Animals

Method-specific reporting

n/a	Involved in the study
☒	☐ ChIP-seq
☐	☒ Flow cytometry
☒	☐ Magnetic resonance imaging

Flow Cytometry

Plots

Confirm that:

☒ The axis labels state the marker and fluorochrome used (e.g. CD4-FITC).

☒ The axis scales are clearly visible. Include numbers along axes only for bottom left plot of group (a 'group' is an analysis of identical markers).

☒ All plots are contour plots with outliers or pseudocolor plots.

☒ A numerical value for number of cells or percentage (with statistics) is provided.

Methodology

Sample preparation

Cell suspensions were blocked with anti-CD16/32 FcγIII/II receptor antibody (BioLegend) used at a concentration of 250 ng/106

Sample preparation	cells for 20 minutes on ice. After washing, cells were incubated with anti-IL-1β-APC (Clone: 166931) used at a concentration of 10uL / 10^6 cells and Rat anti-IgG2B Isotype Control-APC (Clone: 141945; R&D Systems); Anti-Mouse CD45-PerCy5.5, Anti-Mouse Ly-6C-PE, Anti-Mouse PE-Gr1, Anti-Mouse Ly-6G-488, and Anti-Mouse CD11b PE-Cy7 (eBioscience) were used at a concentration of 0.2ug / 10^6 cells). Intracellular FACS staining required BD Cytofix/Cytoperm™ Plus (BD Biosciences) and was used according to the manufacturer's instructions. Samples were analyzed on a BD LSRII using FACSDiva Software (BD Biosciences). Antibodies used to characterize hematopoietic stem and progenitor populations (represented in Table S2) were purchased from Biolegend unless otherwise noted: BV605 Sca1 (clone D7), BV786 cKit (BD, clone 2B8), APC CD150 (clone TC15), APC Cy7 CD48 (clone HM48-1), AF488 CD34 (eBioscience, clone RAM34), PE Cy7 IL7Ra (clone A7R34), PE FcgRII/III (clone 93), PE Flt3 (clone A2F10), PB Lineage cocktail (catalog #133310), APC Cy7 NK1.1 (clone PK136), Brilliant violet 785 B220 (clone RA3-6B2), and PE cd11c (clone N418). Dead cells were excluded using 7AAD (Biolegend). To determine absolute numbers of cells, CountBright absolute counting beads (Molecular Probes, ThermoFisher) were added to samples.
Instrument	BD FACSCanto II Flow Cytometer (BD Biosciences, Ref. 338960).
Software	FlowJo (TreeStar).
Cell population abundance	No FACS sorting was performed for this work.
Gating strategy	For all experiments, debris was first excluded by a morphology gate based on FSC-A and SSC-A. Then, non-singlets were eliminated from analysis by a single cell gate based on FSC-H and FSC-A. Next, dead cells were eliminated by an appropriate viability gate: 7AAD was used to distinguish live/dead cells, except in cases requiring intracellular staining in which case eFluor 450 (eBioscience) fixable viability dyes were used. When appropriate, all lymphocytes were identified using a CD45+ gate.

☒ Tick this box to confirm that a figure exemplifying the gating strategy is provided in the Supplementary Information.

Published OnlineFirst July 31, 2018; DOI: 10.1158/0008-5472.CAN-18-0548

Tumor Biology and Immunology

Cancer Research

Modulating Bone Marrow Hematopoietic Lineage Potential to Prevent Bone Metastasis in Breast Cancer

Jessalyn M. Ubellacker[1,2], Ninib Baryawno[3,4,5], Nicolas Severe[3,4,5], Molly J. DeCristo[1,2], Jaclyn Sceneay[1,2], John N. Hutchinson[6], Marie-Therese Haider[7], Catherine S. Rhee[3,4,5], Yuanbo Qin[1,2], Walter M. Gregory[8], Ana C. Garrido-Castro[9], Ingunn Holen[7], Janet E. Brown[7], Robert E. Coleman[7], David T. Scadden[3,4,5,10], and Sandra S. McAllister[1,2,5,10]

Abstract

The presence of disseminated tumor cells in breast cancer patient bone marrow aspirates predicts decreased recurrence-free survival. Although it is appreciated that physiologic, pathologic, and therapeutic conditions impact hematopoiesis, it remains unclear whether targeting hematopoiesis presents opportunities for limiting bone metastasis. Using preclinical breast cancer models, we discovered that marrow from mice treated with the bisphosphonate zoledronic acid (ZA) are metastasis-suppressive. Specifically, ZA modulated hematopoietic myeloid/osteoclast progenitor cell (M/OCP) lineage potential to activate metastasis-suppressive activity. Granulocyte-colony stimulating factor (G-CSF) promoted ZA resistance by redirecting M/OCP differentiation. We identified M/OCP and bone marrow transcriptional programs associated with metastasis suppression and ZA resistance. Analysis of patient blood samples taken at randomization revealed that women with high-plasma G-CSF experienced significantly worse outcome with adjuvant ZA than those with lower G-CSF levels. Our findings support discovery of therapeutic strategies to direct M/OCP lineage potential and biomarkers that stratify responses in patients at risk of recurrence.

Significance: Bone marrow myeloid/osteoclast progenitor cell lineage potential has a profound impact on breast cancer bone metastasis and can be modulated by G-CSF and bone-targeting agents. *Cancer Res; 78(18); 5300–14. ©2018 AACR.*

Introduction

The majority of patients with breast cancer have no evidence of metastatic disease at the time of diagnosis, yet approximately 30% of patients experience recurrent breast cancer in the form of metastasis, of which the most prominent site is bone (1). Moreover, bone is the most frequent site of *de novo* metastasis for all breast cancer molecular subtypes (2). At present, little is known about what promotes tumor cell survival and outgrowth into incurable disease in the bone (1, 3). Disseminated tumor cells (DTC) are frequently detected in bone marrow aspirates of patients with breast cancer, regardless of breast cancer subtype and even in those who have early-stage disease, and are predictive of decreased recurrence-free survival (4). These and other such findings support the idea that DTCs find a hospitable niche in the bone marrow (4–6).

Bone metastatic niches in which DTCs reside have been defined as microdomains within the bone that support tumor cell seeding and outgrowth and are predominantly comprised of hematopoietic cells, mesenchymal stromal cells, osteoblasts, osteoclasts, and/or vascular cells (5, 6). Paracrine interactions between DTCs and these various stromal cells disrupt bone homeostasis, which is normally tightly controlled, to fuel metastatic progression. For example, it is well established that DTCs secrete a variety of cytokines that promote osteoclast activity, which in turn, causes release of a variety of tumor-promoting growth factors from the bone, thus propagating a vicious cycle of tumor outgrowth and osteolytic bone breakdown (6).

Although results from studies that focused on mesenchymal stromal cells, osteoblasts, osteoclasts, and vascular cell activity have yielded significant insights into cellular and molecular processes that influence DTC outgrowth and dormancy in the bone (5, 6), surprisingly little is known about whether or how hematopoietic cells in the marrow compartment impact bone

[1]Hematology Division, Brigham & Women's Hospital, Boston, Massachusetts. [2]Department of Medicine, Harvard Medical School, Boston, Massachusetts. [3]Department of Stem Cell and Regenerative Biology, Harvard University, Cambridge, Massachusetts. [4]Center for Regenerative Medicine and the Cancer Center, Massachusetts General Hospital, Boston, Massachusetts. [5]Harvard Stem Cell Institute, Cambridge, Massachusetts. [6]Department of Biostatistics, Harvard T.H. Chan, School of Public Health, Boston, Massachusetts. [7]Academic Unit of Clinical Oncology, Department of Oncology & Metabolism, Weston Park Hospital, University of Sheffield, Sheffield, United Kingdom. [8]Clinical Trials Research Unit, University of Leeds, Leeds, United Kingdom. [9]Department of Medical Oncology, Dana-Farber Cancer Institute, Boston, Massachusetts. [10]Broad Institute of Harvard and MIT, Cambridge, Massachusetts.

Note: Supplementary data for this article are available at Cancer Research Online (http://cancerres.aacrjournals.org/).

Corresponding Author: Sandra S. McAllister, Harvard Medical School, Brigham & Women's Hospital, 4 Blackfan Circle, HIM 742, Boston, MA 02215. Phone: 617-525-4929; Fax: 617-355-9093; E-mail: smcallister1@bwh.harvard.edu

doi: 10.1158/0008-5472.CAN-18-0548

Published OnlineFirst July 31, 2018; DOI: 10.1158/0008-5472.CAN-18-0548

metastases. Clinical studies indicate that the presence of DTCs in patient with breast cancer bone marrow correlates with metastatic relapse and poor outcome (7). In the preclinical setting, it is becoming increasingly apparent that various physiologic and pathologic processes as well as certain drugs and chemotherapies alter hematopoietic cells in the marrow in ways that impact cancer progression (7–10); however, it is not yet clear how DTCs are impacted when they first encounter such hematopoietic cells in the marrow.

Hematopoiesis relies on precise regulation of quiescence, proliferation, and differentiation of hematopoietic progenitor cells within specialized niches (11, 12). For example, within the osteoblastic niche, mature osteoclasts influence hematopoiesis by releasing bone-matrix proteins essential for hematopoietic cell maintenance (13, 14). It is reasonable therefore to hypothesize that modulating osteoclast activity would have an impact on hematopoiesis in ways that affect DTC behavior.

We previously established that bisphosphonate treatment, which is a widely used osteoclast inhibitor therapy for effective treatment of osteolytic diseases, induces subclinical changes in the composition of bone marrow hematopoietic progenitor populations (15). We reported that bone marrow cells isolated from zoledronic acid (ZA)-treated animals suppress mammary carcinoma formation in the absence of a direct effect of ZA on tumor cells, indicating that the bone marrow harbors the majority of ZA's tumor-suppressive capacity (15). However, whether such modulation of the marrow affects breast cancer bone metastasis independently of the effects on mature osteoclasts in the endosteal niche and whether a specific subpopulation of hematopoietic cells has metastasis-suppressive capacity remained undetermined. A better understanding of the bone marrow microenvironment and processes that influence tumor cell maintenance and growth in the bone should present opportunities for targeting hematopoietic cell populations as part of anticancer therapy.

Materials and Methods

Cell lines

MDA-MB-231 B1 cells (gift from Dr. Gabri van der Pluijm, Leiden University Medical Centre, Leiden, South Holland, Netherlands), a clonal bone-tropic human breast cancer cell line expressing luciferase, was maintained under selection in 1 mg/mL gentamicin, (G418, Life Technologies, 15750060) in DMEM with 10% FBS. MDA-MB-231 B2 bone-tropic human breast cancer cells (gift from Dr. Penelope Ottewell, Department of Onocology and Metabolism, University of Sheffield, Sheffield, United Kingdom) were transfected with luciferase and maintained in 10% FBS in DMEM. Cells were not used beyond passage five post-thawing. All cells tested negative for *Mycoplasma* (Lonza Kit: LT07-118) every 6 months (last test: June 2017) and were validated using short tandem repeat (STR) profiling (Molecular Diagnostics Laboratory at Dana-Farber Cancer Institute, Boston, MA).

Mice

Six to 7-week-old female CrTac:NCr-*Foxn1*^{nu} (nude) female mice were purchased from Taconic Laboratories. C57BL/6J female mice were purchased from The Jackson Laboratory. All animal procedures were performed in accordance with the ethics and regulations of Brigham & Women's Hospital Institutional Animal Care and Use Committee (protocol approval 2017N000056), Boston Children's Hospital Institutional Animal Care and Use Committee (protocol approval 12-11-2308R), and Massachusetts General Hospital (protocol approval 2017N000023).

Drug administration

ZA [1-hydroxy-2-(1H-imidazole-1-yl)ethylidene-bisphosphonic acid] (Novartis Pharmaceuticals) was dissolved in 1× Hank balanced buffer solution (Gibco) and stored at 4°C until use. ZA was administered to mice at a dose of 100 μg/kg (i.p.). Recombinant human granulocyte-colony stimulating factor (G-CSF; carrier-free, BioLegend #578604) was administered to nude mice each day for 3 days at a dose of 50 μg/kg (i.p.) beginning one day after administration of ZA, and C57BL/6 mice each day for 3 days at a dose of 50 μg/kg (i.p.) beginning 2 days after administration of ZA. For G-CSF depletion experiments, nude mice were treated with 100 μg/kg (i.p.) G-CSF antibody (R&D Systems, MAB414100) or the 100 μg/kg (i.p.) isotype control IgG (R&D Systems, MAB005) 6 hours prior to intracardiac injection of tumor cells.

Blood and plasma

At experimental endpoints, blood was collected by intracardiac puncture with a 27-gauge needle into ethylenediaminetetraacetic acid (EDTA) Microtainer tubes (BD Pharmingen). Complete blood counts were obtained using a HEMAVET hematology analyzer (Drew Scientific). Plasma was prepared by centrifugation of whole blood at 1.5 g × 1,000 for 8 minutes at 4°C.

Experimental bone metastasis

Mice were anesthetized with isoflurane, and 1×10^5 luciferase-tagged bone-tropic cell lines (B1, B2, B1-G, B2-shG) were suspended in 100 μL of PBS and injected into the left cardiac ventricle. Tumor growth was monitored by bioluminescence imaging, and by Vybrant CM-Dil cell-labeling solution by florescence imaging (Life Technologies, V22888). For intratibial injections, mice were anesthetized with isoflurane and 5×10^4 cells in 10 μL of PBS were injected directly into both tibiae. Tumor growth was monitored by bioluminescence imaging. In indicated experiments, mice were treated with 100 μg/kg of ZA or equivalent volume of vehicle control 72 hours prior to injection of tumor cells.

Bone marrow cell preparations

Femora and tibiae were dissected free into 2% FBS in PBS and centrifuged at 6.0–7.0 g ×1,000 for 4 minutes at 4°C to collect whole bone marrow cells (BMC; WBM). Cells were then incubated with red blood cell (RBC) lysis solution (BioLegend, 420301) for 5 minutes on ice, washed once with 2% FBS in PBS, resuspended in 0.5 mL of sterile BMC buffer, and passed through a 5-mL polystyrene round-bottom tube with a cell-strainer cap (Corning, 352235).

Flow cytometry and FACS

BMCs were prepared for flow cytometry by suspension in sterile PBS containing 2% FBS. Cells were labeled with appropriate antibodies for 30 minutes at 4°C. Gating was used to exclude debris, cell clumps, and dead cells (using 7-aminoactinomycin D; 7-AAD Viability Staining Solution (BioLegend, 420404). Myeloid/osteoclast progenitor cell (M/OCP) populations were defined as Lineage$^-$ CD115$^+$. Antibody panel includes Pacific Blue anti-mouse Lineage Cocktail (BioLegend, 133310: CD3$^-$, Ly-6G/Ly6-C$^-$, Cd11b$^-$, CD45R$^-$, TER119$^-$) and Alexa Fluor 488

Published OnlineFirst July 31, 2018; DOI: 10.1158/0008-5472.CAN-18-0548

anti-mouse CD115 (CSF-1R; BioLegend, 135511). Cells were acquired on a FACSCanto II or a FACSAria IIu/FACSDiva (BD Biosciences). At the endpoint of the osteoclast differentiation assays, macrophages were defined as $MHCII^+/F4/80^+/Cd11b^+$ (MHCII: APC-Cy7 (BioLegend 107627), F4/80: PE-Cy-7 (BioLegend 123113), Cd11b:Alexa Fluor-488 (BioLegend 101205) and dendritic cells were defined as $MHCII^+/Cd11b^+/Cd11c^+$ [MHCII: APC-Cy7 (BioLegend 107627), Cd11c: PE (BioLegend 117307), Cd11b:Alexa Fluor-488 (BioLegend 101205)]. Analyses were performed using FlowJo software (FlowJo, LLC). CountBright Absolute Counting Beads (Life Technologies, C36950) were used to quantify absolute cell numbers. For cell sorting of the M/OCP populations and for isolation of Lin^- and Lin^+ populations, the Murine Direct Lineage Cell Depletion Kit (Miltenyi Biotec Inc., 130-110-470) was used to enrich for Lin^- populations, which was confirmed by flow cytometry for the markers in the lineage cocktail.

Bone marrow tumor support functional assay

Donor mice were treated via intraperitoneal injection with vehicle (1× HBBS) or ZA (100 μg/kg) and sacrificed 3 days (nude mice) or 5 days (C57BL/6 mice) following treatment. BMCs were harvested as described above. For WBM assays, 7.5×10^5 donor BMCs were mixed with 2.5×10^5 of the appropriate tumor cells in 100 μL DMEM with 10% basement membrane matrix, Corning Matrigel Growth Factor Reduced (low growth; Westnet Inc., 354230) immediately prior to injection. To test the tumor support function of various FACS-isolated marrow subpopulations, 2.5×10^5 tumor cells were mixed with either 2.5×10^5 Lin^- BMCs, 7.5×10^5 Lin^+ BMCs, or 1×10^5 M/OCPs. Admixtures were injected subcutaneously into host nude mice. During the 14-day time courses, no graft versus host disease was observed for nude mice receiving C57BL/6 donor marrow. Each donor BMC sample was distributed into a minimum of 3 host nude mice. Tumor growth was monitored by bioluminescent imaging.

Osteoclast differentiation assay

Bone marrow cells were prepared as previously described, and 1,000 WBM cells or 250 M/OCP cells were plated in 24-well plates with 15% FBS in αMEM with 10 ng/mL of recombinant M-CSF (R&D Systems, 416ML010). After 3 days, recombinant RANKL (5 ng/mL R&D Systems, 462TEC010CF) or vehicle control were added to the assay. At the 5-day endpoint, Tartrate Resistant Acid Phosphatase, Leukocyte (TRAP) Kit (Sigma Aldrich, 387A) was used and TRAP-positive osteoclasts were counted and flow cytometry was performed to quantify the numbers of macrophages and dendritic cells in the resultant cultures. To test phagocytic function of the resulting cultures, tumor cells were stained with Vibrant CM-Dil (Life Technologies) at a concentration of 5 μL CM-Dil solution per 1 million cells/mL for 5 minutes at 37°C. Cells were washed twice with PBS, and then 1,000 tumor cells were added into the wells at the endpoint of the osteoclast differentiation assay. After two hours, wells were washed with PBS and prepared for flow cytometry. Cells within the macrophage gate that were $CM\text{-}Dil^+$ were reported as a percentage of the total macrophage population.

Patient plasma samples

Breast cancer patient plasma samples ($n = 392$) were obtained from the AZURE clinical trial sample database (ISRCTN79831382, University of Sheffield, Sheffield, United Kingdom; ref. 16). The AZURE study was performed in accordance with the Declaration of Helsinki, and was performed after approval by an institutional review board (West Midlands Research Ethics Committee). Patients were randomized to either standard adjuvant therapy alone (control, Ctl) or with ZA (Novartis Pharmaceuticals) and written informed consent was received from all patients prior to inclusion in the study. To reduce possible imbalances in tumor and treatment characteristics, a minimization process was used that took into account the number of involved axillary lymph nodes, clinical tumor stage, estrogen receptor status, type and timing of systemic therapy, menopausal status, statin use, and treating center. Eligible patients were randomized to receive (neo) adjuvant chemotherapy and/or endocrine therapy ± ZA 4 mg i.v. every 3–4 weeks for 6 doses, then 3 monthly ×8 and 6 monthly ×5 to complete 5 years of treatment. Secondary prophylaxis with G-CSF to prevent neutropenic sepsis or treatment delays due to neutropenia was allowed but primary G-CSF prophylaxis was not used. Both the use of adjuvant systemic treatments and locoregional radiotherapy were given in accordance with standard protocols at each participating institution. The date of recurrence was defined as the date on which relapse was first suspected. Subjects were followed up on an annual basis after completion of the 5-year treatment phase (ZA or Ctl) for both disease and relevant safety endpoints (16). Patient samples to be used in this study were selected on the basis of: (i) menopausal status [postmenopausal women ($n = 164$); non-postmenopausal women ($n = 226$); unknown menopausal status ($n = 2$)], (ii) whether or not the patient had recurrence of breast cancer (disease-free or recurrence in bone only or bone as well as other distant sites), and (iii) whether or not the patient received adjuvant ZA treatment. These three parameters were used to power the sample size estimation using the reported HR of 0.81, and a standardized effect size of 0.80 (16). Plasma G-CSF levels were analyzed by ELISA.

Statistical analysis

All experiments were performed with three independent replications, unless otherwise indicated. Sample size for *in vivo* experiment was based on outcomes from pilot experiments and was calculated at a statistical significance level of 0.05, and powered at 0.80. All data were analyzed with the use of GraphPad Prism Software (Version 7). Data are expressed as mean ± SEM with n denoting the number of independent data points (i.e., mice, cell wells, etc.). Statistics were determined using the unpaired, two-tailed Student t test unless otherwise indicated. Results were considered statistically significant if $P < 0.05$ (*), $P < 0.01$ (**), and $P < 0.001$ (***).

ELISAs and cytokine array

Plasma was obtained from the mice as previously described, and ELISA assays were performed according to manufacturer's instructions: Murine G-CSF ELISA Kit (R&D Systems, MCS00); Murine RANKL ELISA Kit (Innovative Research, IRKTAH5466); Murine NTX ELISA (Biotang Inc., 50154363). For the human cytokine array, 1×10^5 cells of B1 or B2 were plated and conditioned media from 5 different wells was obtained 24 hours after plating, was pooled and then assessed using Human Cytokine Array, Panel A per manufacturer's instructions (R&D Systems,

Published OnlineFirst July 31, 2018; DOI: 10.1158/0008-5472.CAN-18-0548

ARY005). For the patient plasma samples, 100 μL of sample was used and ELISA assays were performed according to manufacturer's instructions (Human G-CSF QKIT HS ELISA; R&D Systems, HSTCS0). Plates were analyzed using Softmax Pro7 Software (Molecular Devices).

Data and software availability

RNA-Sequencing data will be available using the Gene Expression Omnibus (GEO; GSE108250) database.

Results

Identification of therapeutically induced tumor-inhibitory hematopoietic bone marrow cells

We and others have reported that primary cancers, physiologic aging, and drug treatments all affect bone marrow hematopoietic cells in ways that influence disease progression (8–10, 15, 17). To understand whether therapeutic modulation of the bone marrow microenvironment would provide an effective approach for treating breast cancer bone metastasis, we used the nitrogen-containing bisphosphonate, ZA in both immunocompromised and immunocompetent preclinical models of breast cancer.

We treated tumor-free cohorts of C57BL/6 and nude mice with a single dose of either ZA or vehicle control and harvested their bone marrow 5 days (C57BL/6 mice) or 3 days (nude mice) following treatment. These are time points at which osteoclast activity is inhibited by ZA (15). We then used our well-established hematopoietic cell functional assay (15–18) to test the bone marrow for effects on growth of a bone-metastatic human breast tumor cell line, MDA-MB-231-B1 (B1), (Fig. 1A). This assay is designed to test any effects on tumor growth that are exclusively mediated by bone marrow hematopoietic cells and is based on the notion that the outgrowth of DTCs would be affected by any ZA-induced changes to hematopoietic cells. Importantly, mature osteoclasts are of hematopoietic origin but localize to the endosteal niche upon maturation (19). TRAP staining of the bone marrow plugs confirmed that osteoclasts were absent from the bone marrow samples used in these experiments (Supplementary Fig. S1A).

WBM from both strains of Ctl-treated donor mice had no significant effect on subcutaneous B1 tumor growth when compared with B1 tumor cells injected alone—in these cohorts, tumors formed with approximately 80% incidence in both strains of mice (Fig. 1B; Supplementary Fig. S1B). However, WBM from both strains of ZA-treated mice significantly reduced B1 tumor incidence to <30% (Fig. 1B; Supplementary Fig. S1B), indicating that tumor suppression occurred independently of a functional adaptive immune system.

To begin to understand whether tumor-suppressive function is enriched in a particular subpopulation of hematopoietic cells, we sorted the marrow from Ctl or ZA-treated mice into lineage-negative (Lin^-) progenitor populations and mature lineage-positive (Lin^+) populations and assessed B1 tumor growth using the bone marrow functional assay. As before, WBM from the ZA-treated mice suppressed B1 tumor formation; tumor incidence was only 50% of that from the respective Ctl cohort (Fig. 1C). The Lin^+ subpopulation from ZA-treated mice had no effect on tumor incidence, which was equivalent to that of the respective Ctl subpopulation (Fig. 1C). In striking contrast, Lin^- cells from ZA-treated donors significantly reduced B1 tumor incidence to only 14.3% relative to Lin^- cells from the Ctl mice (Fig. 1C).

Osteoclasts differentiate from Lin^- myeloid-committed cells in the marrow (19–21); therefore, we wondered whether ZA imparted its tumor-suppressive effect via osteoclast precursor cells. There is currently no clear consensus on the cell-surface markers that delineate osteoclast precursors (21). However, given our previous report that ZA, in addition to inhibiting osteoclast activity, significantly expands numbers of bone marrow common myeloid progenitor populations (15), we reasoned that an effort to capture functional activity should include multipotent progenitors of the myeloid/osteoclast lineage. We therefore utilized the markers $CD3^-B220^-Ly6G^-Ly6C^-CD11b^-Ter119^-CD115^+$ to define a population we termed "myeloid/osteoclast progenitors" (M/OCP; Supplementary Fig. S1C). We confirmed that this sorted population from Ctl-treated donors gives rise to macrophages, dendritic cells, and osteoclasts in a standard *in vitro* differentiation assay (Supplementary Fig. S1D and S1E; ref. 20).

We treated tumor-free C57BL/6 mice with a single dose of ZA and quantified the numbers of $CD3^-B220^-Ly6G^-Ly6C^-CD11b^-Ter119^-CD115^+$ M/OCPs in the marrow over an experimental time course of 15 days. ZA treatment significantly increased the number of bone marrow M/OCPs in a time-dependent manner (Fig. 1D).

We then investigated M/OCP tumor-suppressive function by sorting $CD3^-B220^-Ly6G^-Ly6C^-CD11b^-Ter119^-CD115^+$ M/OCPs, as well as the M/OCP-depleted population, from the marrow of Ctl or ZA-treated cohorts and subjecting them to the bone marrow functional assay. As a control, we confirmed that WBM from the ZA-treated cohort significantly suppressed tumor growth as expected (Fig. 1E; Supplementary Fig. S1F). M/OCPs isolated 5 days after ZA treatment significantly inhibited tumor incidence and mass relative to the same number of M/OCPs from the Ctl-treated cohort (Fig. 1E; Supplementary Fig. S1F). In contrast, the M/OCP-depleted marrows from Ctl and ZA-treated mice were not significantly different in their tumor-modulating capacity (Fig. 1E).

The results from the *in vivo* BMC functional assays suggested that M/OCPs from ZA-treated mice are qualitatively different than their control counterparts. Hence, we performed RNA sequencing on M/OCPs from Ctl and ZA-treated cohorts. Computational analyses revealed a list of significantly differentially expressed genes (DEG; GEO, GSE108250; Supplementary Table S1). Functionally enriched gene ontology (GO) terms and gene set enrichment analyses (GSEA) among the DEGs revealed biological and cellular processes that were enriched in the ZA-treated M/OCPs. Of these, "organic cyclic compound metabolic process," "cellular aromatic compound metabolic process," "oxidative phosphorylation," "phagosome," "lysosome organization," and "lipid transport" pathways (Fig. 1F; Supplementary Table S2A and S2B) were particularly interesting, as these processes are important for monocyte differentiation and macrophage function (22, 23).

Collectively, these results established that M/OCP transcriptional programs are altered in the marrow and correlate with tumor-suppressive function in response to the bone-targeting agent, ZA, independently of a functional adaptive immune system. Moreover, these results are in agreement with preclinical findings that ZA reduces the risk of breast cancer recurrence independently of its direct action on osteoclast apoptosis (24)

Published OnlineFirst July 31, 2018; DOI: 10.1158/0008-5472.CAN-18-0548

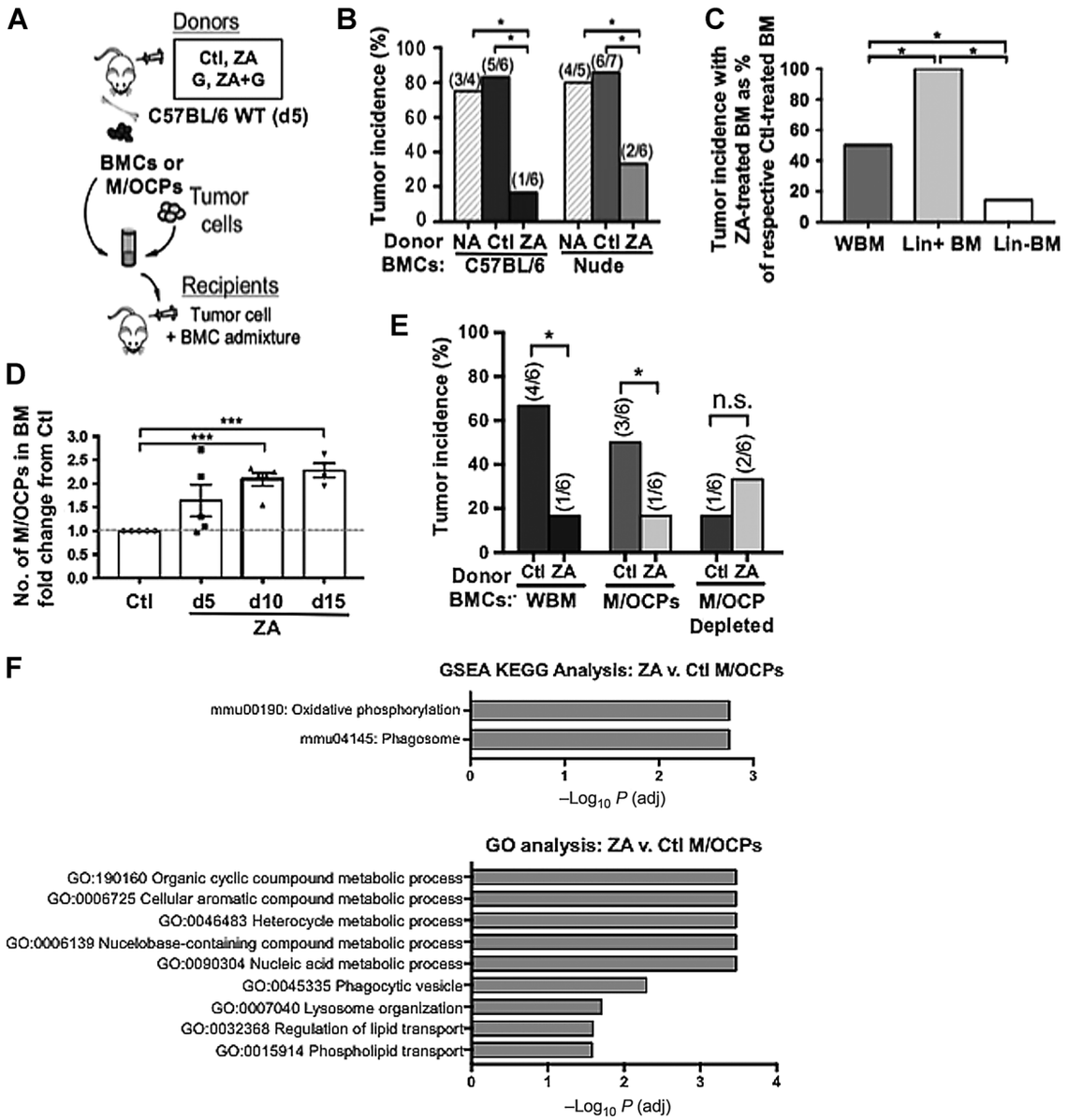

Figure 1.

Identification of therapeutically induced tumor-inhibitory hematopoietic bone marrow cells. **A,** Experimental scheme for assay to test BMC tumor support function. WBM or various FACS-isolated bone marrow populations were harvested from ZA- or vehicle-treated control (Ctl) donor mice at either 5 days (C57BL/6) or 3 days (nude) and mixed with tumor cells immediately prior to injection into recipient mice and tumor incidence and growth kinetics measured over time. **B,** Incidence (%) of subcutaneous tumor formation in nude recipient mice at experimental endpoint (d14) resulting from 2.5×10^5 MDA-MB-231-B1 (B1) cells admixed with Matrigel (NA, no donor BMCs included) or 7.5×10^5 WBM cells from Ctl or ZA-treated nude and C57BL/6 donors ($n = 4$–7 injections per cohort; statistics representative of two biological replicates). **C,** Incidence (%) of subcutaneous tumor formation in nude recipient mice at experimental endpoint (d14) resulting from 2.5×10^5 MDA-MB-231-B1 (B1) cells admixed with 7.5×10^5 WBMs, 7.5×10^5 Lin^+ BMCs, or 2.5×10^5 Lin- BMCs from Ctl- or ZA-treated nude donors. Data for each ZA-treated cohort are represented relative to its respective Ctl-treated cohort; ($n = 20$–24 injections per cohort). Lin^- populations were sorted by gating on $CD3^-$ Ly-6G/Ly6-C^- $Cd11b^-$ $CD45R^-$, and $TER119^-$ and all of the remaining BMCs were used as the Lin^+ populations. **D,** Number of M/OCPs (Lin^-CD115^+) in the bone marrow of C57BL/6 mice at indicated time points after ZA treatment ($n = 4$–5 mice per cohort, representative of three biological replications). **E,** Incidence (%) of tumor formation in nude recipient mice at experimental endpoint (d14) resulting from 2.5×10^5 B1 cells admixed with 7.5×10^5 WBM cells, 10^5 sorted M/OCPs, or 6.5×10^5 M/OCP-depleted BMCs from Ctl- or ZA-treated C57BL/6 donors ($n = 6$ injections per cohort; statistics representative of two biological replications). Controls from different cohorts were not compared due to the fact that different numbers of BMCs were admixed with tumor cells in each case. **F,** GSEA analysis [clusterProfiler tool using Kyoto Encyclopedia of Genes and Genomes (KEGG) gene sets] and gprofileR (GO) analysis of the differentially expressed genes in M/OCPs isolated from ZA-treated mice as compared with M/OCPs isolated from Ctl-treated mice. Significance was determined as described in Materials and Methods: RNA-sequencing. Error bars, mean ± SEM; two-tailed *t* tests (unpaired) were used to determine statistical significance (*, $P < 0.05$; ***, $P < 0.001$). n.s., nonsignificant.

Published OnlineFirst July 31, 2018; DOI: 10.1158/0008-5472.CAN-18-0548

and that bone tumor burden can be modulated in an osteoclast-independent manner (25).

ZA skews lineage potential of myeloid/osteoclast progenitor cells toward macrophages

Our RNAseq analyses suggested that M/OCPs are enriched for transcriptional programs consistent with those of the monocyte/macrophage lineage in response to ZA. Although it is well known that ZA inhibits mature osteoclasts, whether ZA affects myeloid/osteoclast lineage bias is not understood; therefore, we tested the lineage potential of bone marrow samples from control and ZA-treated mice using *in vitro* differentiation assays (20; Fig. 2A). In these assays, macrophage-colony stimulating factor (M-CSF; CSF1) is necessary for sustaining M/OCP populations (26) and in the absence of receptor activator of nuclear factor kappa-B ligand (RANKL), these progenitors normally differentiate into macrophages and dendritic cells (DC) whereas in the presence of RANKL, they differentiate into osteoclasts (27).

Interestingly, when WBM samples from ZA- and Ctl-treated mice were subjected to M-CSF and RANKL *in vitro*, the marrow cells from ZA-treated donors gave rise to significantly fewer numbers of osteoclasts as compared with those of Ctl-treated donors (Fig. 2B), despite having more M/OCPs (Fig. 1D). Instead, the resulting cultures from the ZA-treated cohort had significantly increased numbers of macrophages ($Cd11b^+$/$F4/80^+$/$MHCII^+$) and DCs ($Cd11b^+$/$MHCII^+$/$Cd11c^+$) as compared with those of the Ctl-treated cohort (Fig. 2C; Supplementary Fig. S2A and S2B). In fact, these numbers of macrophages and DCs were comparable with those of bone marrow samples treated only with M-CSF (Fig. 2C).

We next tested the lineage potential of M/OCPs isolated from ZA-treated animals. Thus, we sorted M/OCP populations from the marrow of mice treated with Ctl or ZA and subjected them to the differentiation assay. In the presence of RANKL, M/OCPs from ZA-treated mice gave rise to significantly more macrophages than those of controls and these numbers were comparable to those from cultures that had not been treated with RANKL (Fig. 2D). Although DCs were detected in the resulting cultures, there were no significant differences in their numbers between ZA and Ctl treated mice (Fig. 2D; Supplementary Fig. S2B).

Collectively, these findings indicated that ZA inherently changes the lineage potential of M/OCPs by skewing their differentiation potential toward macrophages, even in the presence of RANKL. Moreover, the marrow of ZA-treated cohorts harbor significantly more of these differently poised M/OCPs than that of the control counterparts.

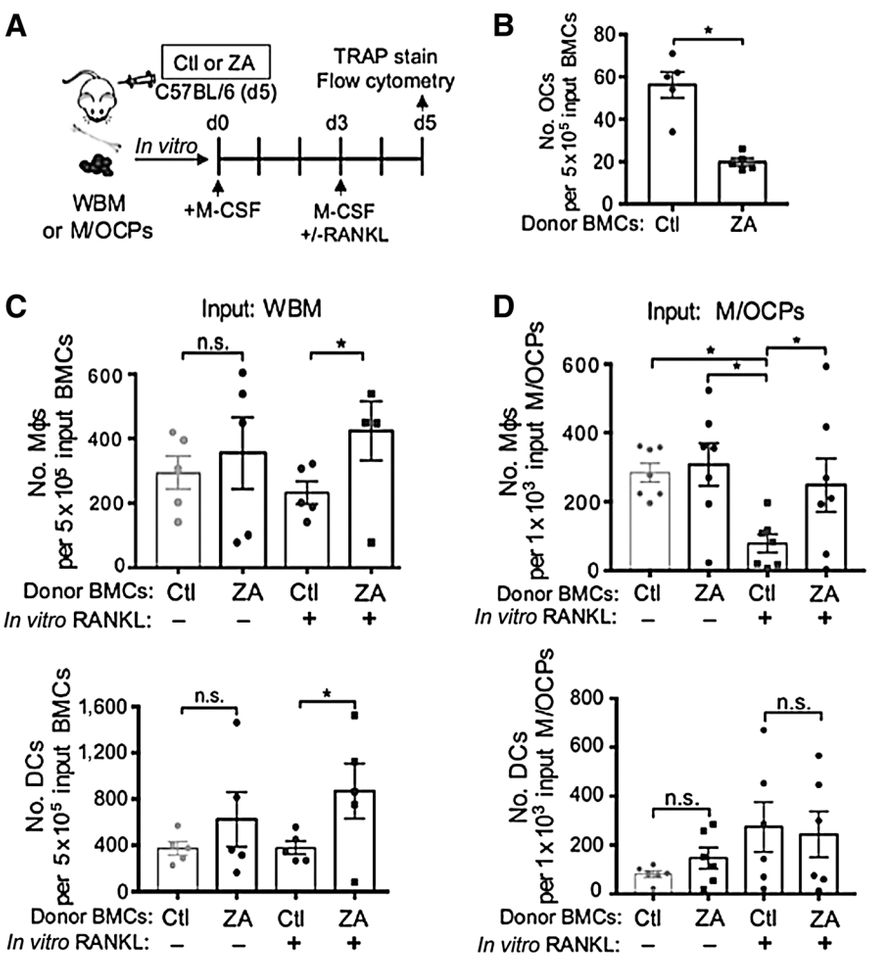

Figure 2.

ZA skews lineage potential of myeloid/osteoclast progenitor cells toward macrophages. **A,** Experimental scheme for *in vitro* osteoclast differentiation assay with WBM or M/OCPs from Ctl- or ZA-treated C57BL/6 donors. **B,** Quantification of osteoclasts (OC) ($TRAP^+$, multinucleated cells) at endpoint of *in vitro* osteoclast differentiation assay (d5) with WBM from Ctl- or ZA-treated C57BL/6 donors ($n = 5$ donor samples/cohort; representative of three biological replicates). **C** and **D,** Flow cytometric quantification of macrophages (Mϕs; $Cd11b^+$/$F4/80^+$/$MHCII^+$) and DCs ($Cd11b^+$/$MHCII^+$/$Cd11c^+$) from sorted WBM populations (**C**; $n = 5$ donor samples/cohort; representative of three biological replicates) or M/OCPs (**D**; $n = 6$–7 donor samples/cohort; representative of three biological replicates) from Ctl- or ZA-treated C57BL/6 donors at endpoint (d5) of osteoclast differentiation assay. Error bars, mean ± SEM; two-tailed *t* tests (unpaired) were used to determine statistical significance (*, $P < 0.05$). n.s., nonsignificant.

Published OnlineFirst July 31, 2018; DOI: 10.1158/0008-5472.CAN-18-0548

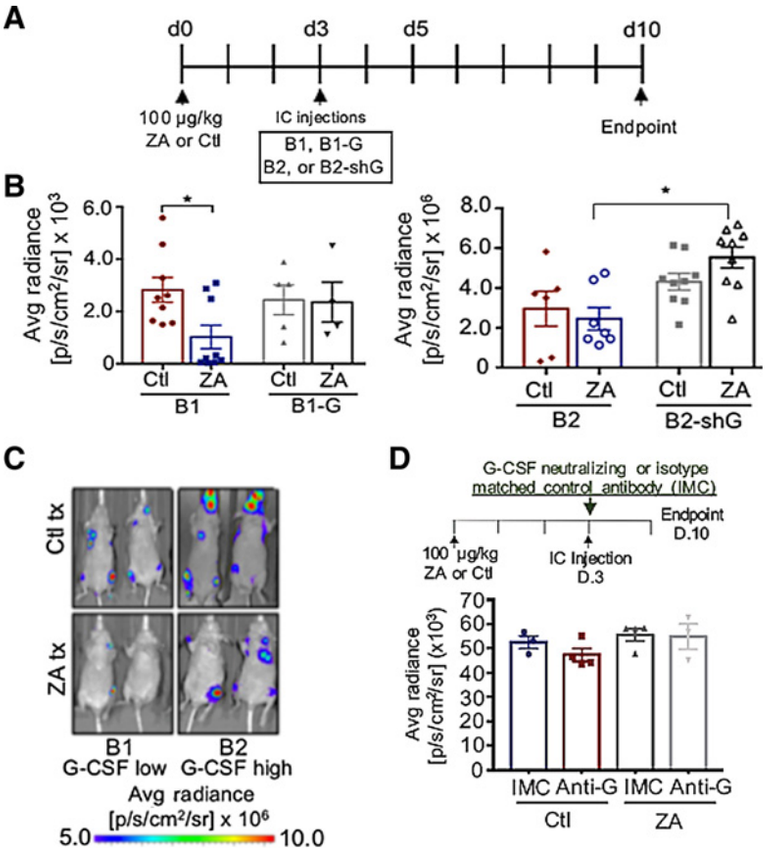

Figure 3.
ZA inhibits breast cancer metastasis in a manner that is counteracted by G-CSF. **A,** Experimental scheme for intracardiac (IC) injections of indicated breast tumor cells into Ctl or ZA pretreated nude mice. **B,** Total tumor burden at experimental endpoint as quantified by bioluminescence imaging (n = 4–9/cohort); representative of three biological replicates. **C,** Representative bioluminescence images from indicated cohorts in **B** at experimental endpoint. **D,** Experimental scheme for intracardiac injections of B2 cell line following pretreatment with Ctl or ZA and a G-CSF neutralizing antibody or isotype-matched control antibody (IMC; top). Graph represents total tumor burden at experimental endpoint (d10) as quantified by bioluminescence imaging of the luciferase$^+$ B2 cell line. All mice had signal present (d10; n = 4–5/cohort). Error bars, mean ± SEM; two-tailed t tests (unpaired) were used to determine statistical significance (*, $P < 0.05$).

ZA inhibits breast cancer metastasis in a manner that is counteracted by G-CSF

The ability to therapeutically generate tumor-suppressive bone marrow has important implications for bone metastasis; therefore, we tested whether pretreating nude mice with ZA three days prior to intracardiac injection of breast tumor cells would affect subsequent bone metastasis (Fig. 3A). We used two derivative bone-tropic subpopulations, B1 (28) and B2 (29), of the parental MDA-MB-231 breast cancer cell line.

Interestingly, while B1 bone metastatic burden was significantly lower following ZA pretreatment (63.7% lower than the control cohort, $P < 0.05$), B2 metastatic burden was unaffected (Fig. 3B and C; Supplementary Fig. S3A). Likewise, ZA pretreatment decreased outgrowth of B1, but not B2, bone tumors when cells were directly injected into the tibia (Supplementary Fig. S3B). Moreover, WBM from ZA-treated mice did not suppress B2-derived tumor growth in the bone marrow functional assay (Supplementary Fig. S3C), indicating that the B2 cell line is resistant to the tumor-suppressive effect of ZA-treated bone marrow.

Comparative cytokine analysis revealed that the ZA-resistant B2 cell line expressed higher levels of G-CSF, GM-CSF, CXCL1, and IL18 than the ZA-responsive B1 cell line (Supplementary Fig. S3D). Various tumor-derived factors have been previously shown to induce osteoclastogenesis and osteoclast activity, including cell surface ligand Jagged1 and secreted factors RANKL, G-CSF, GM-CSF, MIP-1α, PTHrP, IL8, IL6, ICAM1 (30, 31). In particular, elevated plasma levels of G-CSF have been correlated with poor prognosis for patients with triple-negative breast cancer (32) and enhanced osteoclast activity has been reported in mice with elevated G-CSF levels (33–35). Although it is well established that G-CSF leads to increased numbers of myeloid cells in the bone marrow (35), whether G-CSF directly affects osteoclastogenesis or response to ZA is not well understood.

To assess whether G-CSF plays a role in resistance to ZA treatment that we had observed, we overexpressed G-CSF in the B1 cell line, which has endogenously low G-CSF expression, to generate a G-CSF–high cell line (B1-G) (Supplementary Fig. S3E). Unlike the B1 bone metastases that were significantly reduced following ZA pretreatment (~3-fold reduction; $P < 0.05$), the B1-G metastatic burden was no different from that of the control cohort and significantly higher than that of B1 cells treated with ZA (Fig. 3B and C). ZA also failed to suppress B1 metastases when G-CSF was administered systemically (Supplementary Fig. S3F), even though the systemic efficacy of G-CSF was confirmed by an expected increase in peripheral neutrophil counts (Supplementary Fig. S3G). Of note, neutrophil numbers in the bone marrow of B1 tumor-bearing mice was unchanged after ZA, G-CSF, or ZA+G-CSF administration (Supplementary Fig. S3H) and G-CSF did not alter osteoclast activity relative to Ctl treatment, as measured by plasma NTX (Supplementary Fig. S3I).

To determine whether G-CSF suppression is sufficient to confer ZA response, we used two different shRNA constructs to suppress G-CSF in the B2 cell line, which has endogenously

Published OnlineFirst July 31, 2018; DOI: 10.1158/0008-5472.CAN-18-0548

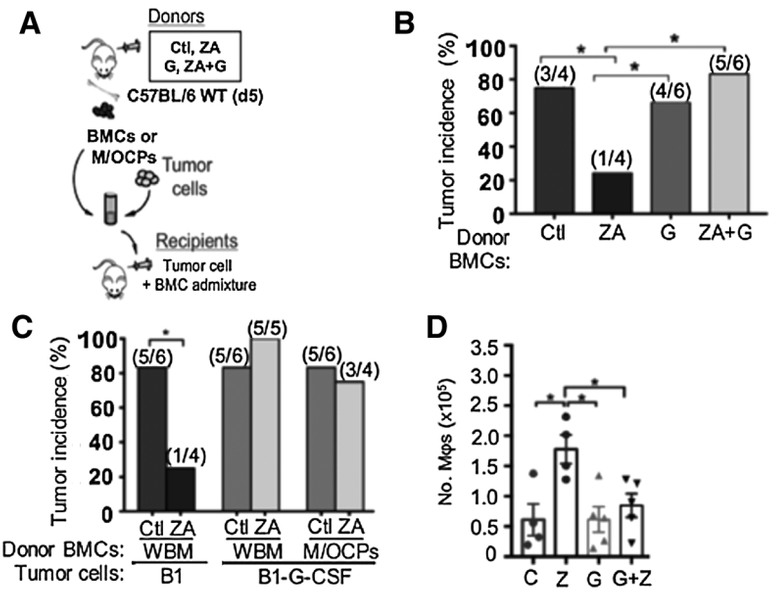

Figure 4.

G-CSF prevents generation of tumor-suppressive M/OCPs. **A,** Experimental scheme for assay to test tumor support function of BMCs from indicated donor mice. **B,** Incidence (%) of subcutaneous tumor formation in nude recipient mice at experimental endpoint (d14) resulting from B1 cells admixed with WBM from Ctl-, ZA-, G-CSF (G)-, or ZA+G-CSF (ZA+G)-treated C57BL/6 donors ($n = 4$–6 tumors per cohort; statistics representative of two biological replicates). **C,** Incidence (%) of tumor formation in nude recipient mice at experimental endpoint (d14) resulting from B1 or B1-G cells admixed with WBM or sorted M/OCPs from Ctl- or ZA-treated C57BL/6 donors ($n = 4$–6 tumors per cohort; statistics representative of two biological replicates). **D,** Quantitative flow cytometric analysis of WBM from indicated mice for number of macrophages ($Cd11b^+/F4/80^+/MHCII^+$) 3 days after Ctl (C), ZA (Z), G-CSF (G), or G-CSF+ZA (G+Z) treatment ($n = 4$-5/cohort; representative of three biological replications). Error bars, mean ± SEM; two-tailed *t*- ests (unpaired) were used to determine statistical significance (*, $P < 0.05$).

high G-CSF expression, to generate G-CSF–low cell lines (B2-shG1 and B2-shG2; Supplementary Fig. S3E). At this time point, metastatic burden was not significantly affected following ZA pretreatment regardless of G-CSF status in the B2 cells (Fig. 3B and C; Supplementary Fig. S3J). Likewise, neutralizing G-CSF *in vivo* prior to IC injection of the B2 cell line did not significantly reduce metastases following ZA pretreatment (Fig. 3D).

Together, these findings demonstrated that elevating G-CSF levels is sufficient to confer ZA resistance, but that suppression of G-CSF is not sufficient to induce ZA response. Moreover, these data indicated that G-CSF alone does not necessarily enhance metastatic burden above that of controls, but suggested that in the context of ZA treatment, G-CSF increases metastatic burden.

G-CSF prevents generation of tumor-suppressive M/OCPs

We next wondered whether resistance to ZA under G-CSF–high conditions was due to counteracting effects of G-CSF on bone marrow hematopoietic cells. We started by analyzing the function of WBM harvested from C57BL/6 mice 5 days following administration of ZA, G-CSF, combination ZA+G-CSF, or vehicle control (Fig. 4A).

As we observed repeatedly, WBM from ZA-treated mice inhibited B1 tumor formation *in vivo* (Fig. 4B; Supplementary Fig. S4A). We also confirmed that, as expected, ZA decreased osteoclast activity in these mice (Supplementary Fig. S4B). While WBM from mice treated systemically with G-CSF did not significantly alter tumor growth relative to that of the control cohort, when mice were treated systemically with combination ZA+G-CSF, their WBM was no longer tumor suppressive (Fig. 4B; Supplementary Fig. S4A). Importantly, both WBM and M/OCPs harvested from ZA-treated mice, which inhibited outgrowth of B1 tumor cells, were unable to inhibit growth of B1 tumor cells that overexpressed G-CSF (B1-G; Fig. 4C; Supplementary Fig. S4C).

In concordance with our findings from the *in vitro* differentiation assays (Fig. 2C and D), ZA significantly increased the numbers of macrophages in the marrow relative to vehicle control *in vivo* (Fig. 4D). In contrast, WBM from mice treated systemically with G-CSF or with ZA+G-CSF contained similar numbers of macrophages as those of the Ctl cohort (Fig. 4D).

These results suggested that G-CSF itself does not generate a marrow environment that enhances tumor growth relative to the control cohorts. Instead, G-CSF appeared to render ZA ineffective to generate tumor-suppressive marrow.

G-CSF counteracts ZA's ability to push differentiation of myeloid/osteoclast progenitors toward phagocytic macrophages

Our results thus far established that ZA alters the lineage potential of M/OCPs and renders them tumor-suppressive, while G-CSF mediates resistance to their tumor-suppressive effect. We therefore wished to know whether G-CSF alters the lineage potential of the M/OCP population.

We first isolated WBM from Ctl-, ZA-, G-CSF, and ZA+G-CSF–treated mice and then treated the cells *in vitro* with M-CSF and RANKL (Fig. 5A). As we repeatedly observed, in the absence of G-CSF, WBM from the ZA-treated cohort gave rise to significantly fewer osteoclasts than those from the control cohorts (Fig. 5B). However, WBM from G-CSF–treated animals gave rise to significantly more osteoclasts, even in the context of ZA treatment (Fig. 5B).

We also isolated M/OCPs from Ctl- or ZA-treated mice and then treated the cells *in vitro* with M-CSF and RANKL in the presence or absence of G-CSF (Fig. 5C). In the presence of G-CSF, M/OCPs from both Ctl- and ZA-treated mice gave rise to increased numbers of osteoclasts and decreased numbers of macrophages *in vitro* relative to M/OCPs in the absence of G-CSF (Fig. 5D and E; Supplementary Fig. S5A and S5B).

Our RNAseq analyses of M/OCPs from Ctl and ZA-treated mice (Fig. 1F) had suggested that ZA induces transcriptional changes consistent with monocyte/macrophage lineage bias. Therefore, to test potential functional consequences of altered M/OCP lineage potential, we added fluorescently labeled B1 tumor cells to the cultures resulting from M/OCP differentiation under various conditions, thus enabling us to assess

Published OnlineFirst July 31, 2018; DOI: 10.1158/0008-5472.CAN-18-0548

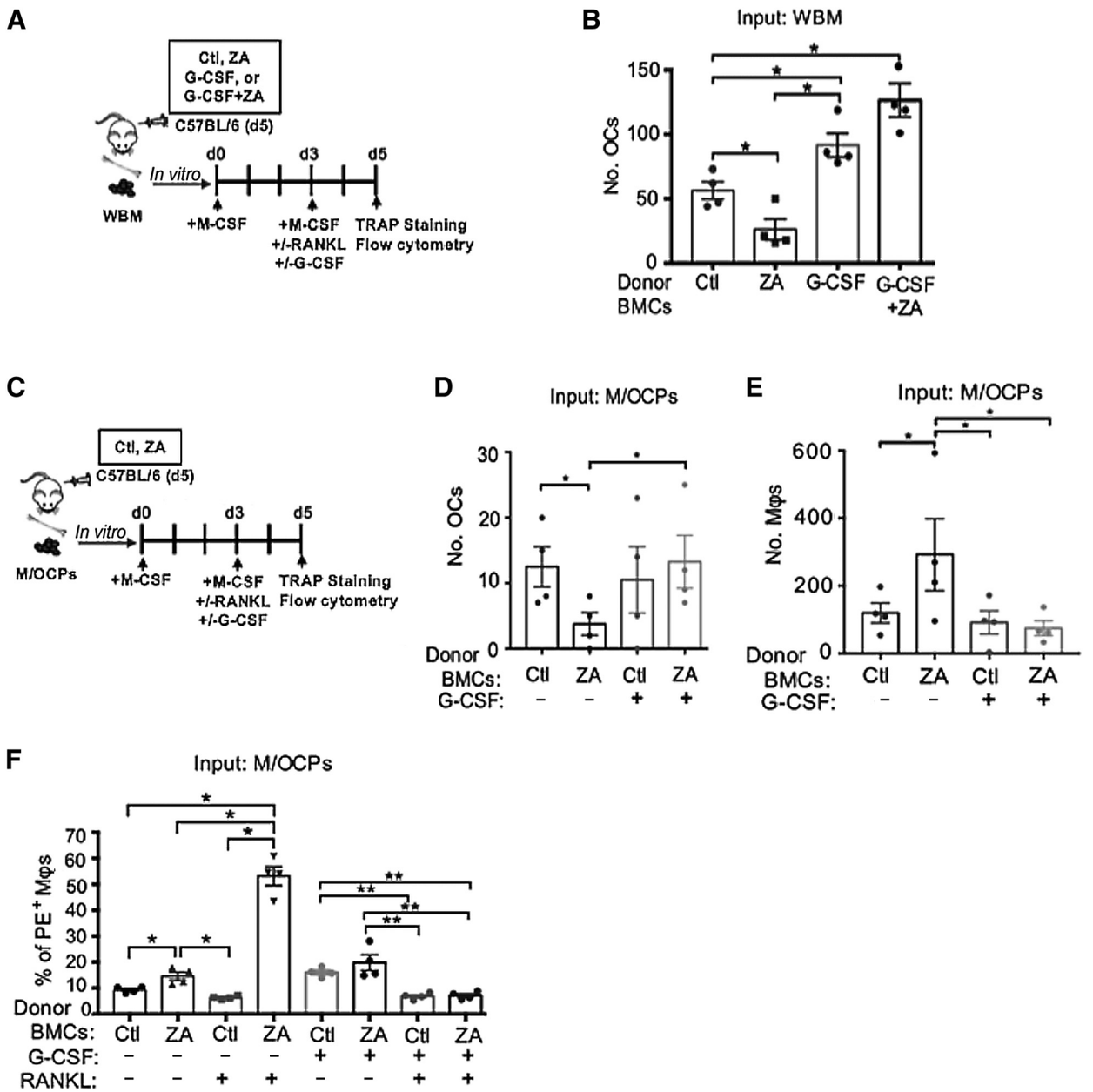

Figure 5.

G-CSF counteracts ZA's ability to push differentiation of myeloid/osteoclast progenitors toward phagocytic macrophages. **A,** Experimental scheme for *in vitro* osteoclast differentiation assay using bone marrow from Ctl-, ZA-, G-CSF- or ZA+G-CSF-treated C57BL/6 donors. **B,** Quantification of osteoclasts (OC; $TRAP^+$, multinucleated cells) at endpoint (d5) of *in vitro* osteoclast differentiation assay with 1,000 WBM per well from Ctl-, ZA-, G-CSF-, or ZA+G-CSF–treated C57BL/6 donors ($n = 4$ donor samples/cohort; representative of three biological replicates). **C,** Experimental scheme for *in vitro* osteoclast differentiation assay using bone marrow from Ctl- or ZA-treated C57BL/6 donors that were subsequently treated with Ctl or recombinant hG-CSF *in vitro* at d3. **D,** Quantification of osteoclasts ($TRAP^+$, multinucleated cells) at endpoint (d5) of *in vitro* osteoclast differentiation assay with 250 M/OCPs per well from Ctl- or ZA-treated C57BL/6 donor mice; M/OCPs were treated *in vitro* with RANKL ± G-CSF ($n = 4$ donor samples per cohort; representative of three biological replications). **E,** Flow cytometric quantification of macrophages ($Cd11b^+$/F4/80 $MHCII^+$) at endpoint of *in vitro* osteoclast differentiation assay (d5) using sorted M/OCPs from Ctl- or ZA-treated C57BL/6 mice; M/OCPs were subsequently treated *in vitro* with M-CSF and RANKL ± G-CSF ($n = 4$ donor samples per cohort; representative of three biological replicates). **F,** Percent of phycoerythrin (PE)-positive M/OCP-derived macrophages ($Cd11b^+$ $F4/80^+$ $MHCII^+$) at endpoint (d5), indicating phagocytosis of Did-Cm (PE)-labeled B1 tumor cells ($n = 4$ donor samples per cohort; representative of three biological replicates). Error bars, mean ± SEM; two-tailed *t* tests (unpaired) were used to determine statistical significance (*, $P < 0.05$; **, $P < 0.01$).

Published OnlineFirst July 31, 2018; DOI: 10.1158/0008-5472.CAN-18-0548

macrophage phagocytic capacity by scoring their uptake of fluorescence. In the absence of G-CSF, macrophages derived from M/OCPs of ZA-treated mice had significantly enhanced phagocytic capacity relative to those from Ctl-treated mice, irrespective of adding RANKL to the culture (Fig. 5F). In contrast, G-CSF significantly decreased the phagocytic capacity of the resulting culture from ZA-treated M/OCPs in both the undifferentiated (without RANKL) and differentiated (with RANKL) cultures (Fig. 5F). Consistent with the phagocytic phenotype, numbers of F4/80 MHCII+ macrophages in the bone marrow of ZA-treated mice was approximately 3-fold higher than in the control cohort, and G-CSF prevented this increase (Supplementary Fig. S5C).

Collectively, these findings suggested that G-CSF counteracts the effect of ZA on M/OCP function and lineage potential at least in part by preventing ZA from inducing M/OCP differentiation toward phagocytic macrophages. Moreover, these results provide additional evidence to suggest an association between lineage potential and the tumor-inhibitory function of the bone marrow.

Bone marrow transcriptome and gene ontology processes that correlate with function

The results from our preclinical metastasis models thus far indicated that the status of the bone marrow at the time metastatic tumor cells encounter it has a profound influence on metastatic success. As such, we wanted to gain insights into how the whole bone marrow hematopoietic microenvironment is affected by ZA and how G-CSF may alter the ZA signature. We therefore characterized transcriptional programs (RNA-seq) on whole bone marrow from mice treated with Ctl, ZA, G-CSF, or combination ZA+G-CSF (GSE108250).

We first analyzed the RNA-seq data by identifying enriched gene ontology processes (36) within the lists of DEGs from each treatment condition (ZA, G-CSF, or ZA+G-CSF) as compared with Ctl-treated bone marrow (Supplementary Fig. S6A–S6C; Supplementary Table S3A–S3F). In the ZA-treated cohort, significantly enriched processes were related primarily to metabolic process whereas in the G-CSF–treated cohorts, as well as in the ZA+G-CSF–treated cohorts, significantly enriched processes were dominated by immune processes (Supplementary Fig. S6C).

A global analysis of gene expression differences between each of the 3 treatment cohorts (ZA, G-CSF, and ZA+G-CSF) and the control cohort (Ctl) provided insights into the effect of each treatment on WBM and M/OCPs. For WBM, the comparisons identified 56, 1,445, and 1,054 DEGs (modified BH adjusted P value <0.01) in the ZA, G-CSF, and ZA+G-CSF cohorts, respectively (Fig. 6A; Supplementary Fig. S6A and S6B; Supplementary Table S4A–S4C). A total of 779 DEGs were common to both the G-CSF and ZA+G-CSF comparisons, only 28 of which were also shared with the ZA comparison (Fig. 6A). The 28 DEGs that were affected by all 3 treatments were the only DEGs shared between the ZA and ZA+G-CSF comparisons (Fig. 6A). Importantly, 16 DEGs were affected exclusively by ZA treatment (i.e., not identified in the combined treatment comparison) and included genes involved in phagocytosis such as *Slc15a4*, *Usp37*, and *Ipo13* (Fig. 6A; Supplementary Table S4A). Interestingly, approximately 25% of the DEGs resulting from combination ZA+G-CSF were unique to that treatment cohort (Fig. 6A).

In the M/OCPs, 165 DEGs resulted from ZA treatment, 314 from G-CSF treatment, and 151 from combination ZA+G-CSF (Fig. 6A; Supplementary Table S5A–S5C). As observed with WBM, a number of DEGs (~38%) were unique to the combination treatment. 103 DEGs were affected exclusively by ZA treatment (Fig. 6A). Interestingly, *Mapk8ip2* was one of the most significantly upregulated DEGs in the ZA-treated cohort ($P = 3.39 \times 10^{-14}$), but was down-regulated in both G-CSF–treated ($P < 8.48 \times 10^{-4}$), and ZA+G-CSF–treated cohorts ($P = 4.31 \times 10^{-6}$). *Mapk8ip2* is involved in monocyte differentiation into macrophages when activated (Supplementary Table S5A; ref. 37).

These analyses revealed that both G-CSF and ZA significantly and uniquely affect transcriptional programs in the WBM and that combined treatment yields yet a different transcriptional profile from either treatment alone. Moreover, ZA treatment appeared to have a larger impact on M/OCPs than on WBM, while G-CSF appeared to dominate the effect on WBM.

Effects of ZA that are lost or significantly changed in the presence of G-CSF

We considered the transcriptional effects we observed with each treatment and the fact that ZA treatment generated metastasis-suppressive marrow while G-CSF alone had no effect on metastatic burden, yet G-CSF induced resistance to ZA and increased metastatic burden in the context of ZA treatment. In doing so, we speculated that ZA and G-CSF either affect the marrow in opposing directions or that the effects of combination treatment cannot be explained by contributions of either treatment alone.

Our comparative analysis revealed that the DEGs upon combination treatment were not equivalently significant in either the ZA or G-CSF cohorts (Fig. 6A). In other words, none of these genes was expressed in an opposing manner. Indeed, 263 DEGs were unique to WBM and 58 genes unique to the M/OCP population in the ZA+G-CSF cohorts (Fig. 6A). Hence, we employed a regression approach with an interaction term and identified genes for which the effects of G-CSF and ZA statistically interact (Fig. 6B; Supplementary Table S6A and S6B).

GO analysis of these nonadditively differentially expressed genes from WBM revealed processes significantly enriched by the combination treatment that described the difference in response to ZA in the presence of G-CSF (Fig. 6C; Supplementary Table S7). The enrichment list represents gene sets that were either enhanced or ablated relative to the cumulative effects expected from adding together the effects of ZA and G-CSF treatments alone, including those newly emerging with combination treatment. Of these, "immune response" and "phagocytosis" were particularly intriguing to us, as these were predominantly suppressed by combination treatment. For example, a number of genes involved in antigen processing and lymphocyte activation, including *B2m*, *Vav2*, and a number of histocompatibility genes (*H2-K1*, *H2-D1*, *H2-Q5*, *H2-Q7*) were uniquely suppressed with ZA+G-CSF combination treatment relative to Ctl treatment (Supplementary Table S6A). Moreover, *Axl*, which suppresses myeloid cell immune function and dampens NK-cell activity (38), was significantly suppressed by ZA treatment [$\log_2$ (fold change) $= -1.20$, $P = 1.25 \times 10^{-4}$] but significantly enhanced with ZA+G-CSF treatment [$\log_2$ (fold change) $= 1.68$, $P = 2.7 \times 10^{-5}$; Supplementary Table S6A].

Together with our preclinical modeling, these analyses indicated that in the marrow of animals treated with combination

Published OnlineFirst July 31, 2018; DOI: 10.1158/0008-5472.CAN-18-0548

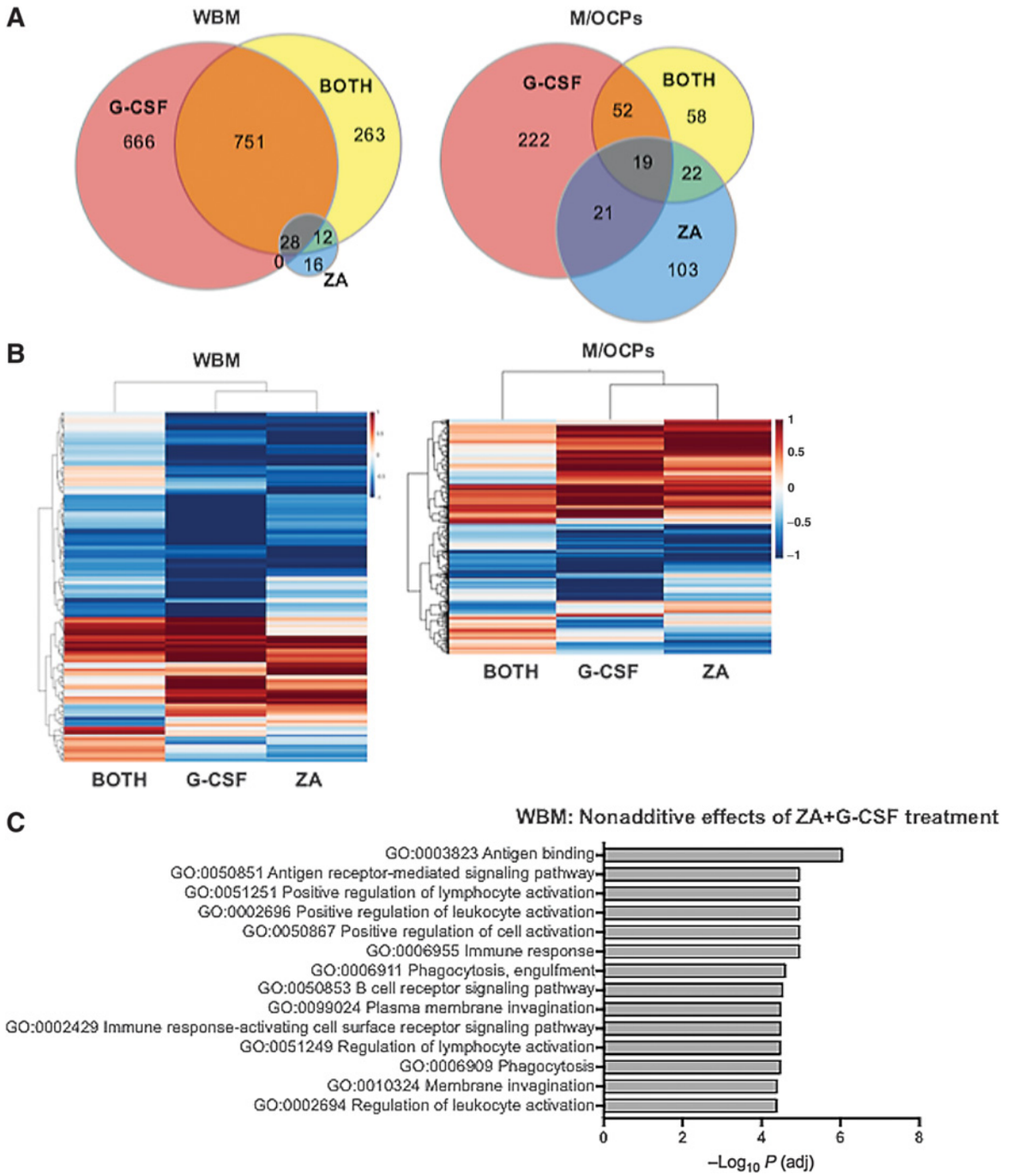

Figure 6.

Bone marrow transcriptome and gene ontology processes that correlate with function. **A,** Venn diagrams for distinct and nondistinct differentially expressed genes in the bone marrow (left) or M/OCPs (right) from mice treated with ZA (blue), G-CSF (red), or ZA+G-CSF ("Both"; yellow), as normalized to Ctl-treated bone marrow or M/OCPs (modified BH adjusted *P* value less than 0.01). **B,** Heatmap of expression levels of genes identified from a regression analysis of the interaction between G-CSF and ZA effects on gene expression for WBM (left) or M/OCPs (right). Individual sample expression levels are shown for genes with a modified BH-adjusted *P* value of less than 0.01 from the regression. Values represent normalized counts after centering on the mean expression levels of the control samples and scaling to the range of gene expression across all samples (so that −1 represents the lowest expression level for all samples and 1 the highest). **C,** Enriched gene ontology categories for genes for which the simultaneous effects of G-CSF and ZA treatment on expression were not additive in a comparative analysis model for WBM. Categories for each indicated cohort were compared with control using the nonadditive genes (as ordered by absolute $\log_2$-fold change; modified BH-adjusted *P* value less than 0.01). A list of the statistically enriched GO terms for biological processes was generated using the methods described in **A**.

Published OnlineFirst July 31, 2018; DOI: 10.1158/0008-5472.CAN-18-0548

ZA + G-CSF, the transcriptional effects of ZA are negated and/or significantly changed by G-CSF in a manner that associates with metastatic progression.

High plasma G-CSF correlates with worse outcome for patients with breast cancer treated with adjuvant ZA

Our preclinical data established that G-CSF mediates resistance to ZA, and in fact, ZA+G-CSF combination treatment had unexpected effects on the metastatic microenvironment, resulting in enhanced metastasis relative to ZA treatment alone. Hence, we sought to understand whether patient plasma G-CSF levels correlate with response to ZA. In the clinical setting, bisphosphonates have suggested benefit, as demonstrated by results from a meta-analysis in which patients who had received adjuvant bisphosphonate treatment observed a significant reduction in breast cancer recurrence in the bone (39). Nevertheless, responses have been limited for unknown reasons and biomarkers that can be used to guide treatment decisions are lacking.

We analyzed patient plasma samples (n = 392) from the AZURE clinical trial in which women with stage II/III breast cancer were randomized to receive standard systemic treatment (>95% of the patients received chemotherapy) with or without adjuvant ZA (Fig. 7A; ref. 16). In the AZURE trial, postmenopausal (natural or induced with ovarian suppression) patients observed a significant decrease in overall breast cancer recurrence (16). Importantly, primary G-CSF prophylaxis was not used in these patients. We verified that the magnitude of effect of ZA in reducing the development of bone metastasis at any time during the 10-year follow-up in our patient subset was similar to that of the overall trial [trial total n = 3,360, HR = 0.81, 95% confidence interval (CI) 0.68–0.97 (16); our subset n = 392, HR = 0.89, 95% CI 0.62–1.3; Fig. 7A].

We utilized an analytic approach that adjusts for an optimal plasma G-CSF concentration cut-off point and enables us to accurately determine DFS and significance levels in an unbiased fashion (See Materials and Methods, Supplementary Fig. S7A–S7D; ref. 40). On the basis of these previously published methods, we determined that a plasma G-CSF concentration of 23 pg/mL was the optimum cut-off point for assessing disease-free survival (DFS) events in ZA-treated patients (40).

Patients receiving adjuvant ZA whose plasma G-CSF levels were > 23 pg/mL at the time of randomization had significantly reduced DFS when compared with patients with plasma G-CSF levels < 23 pg/mL ($P_{adjusted}$ = 0.02) as assessed over a 10-year period (Fig. 7B). However, in the cohort that did not receive ZA, plasma G-CSF levels did not predict a significant difference in DFS (Supplementary Fig. S7B). Cox model analysis

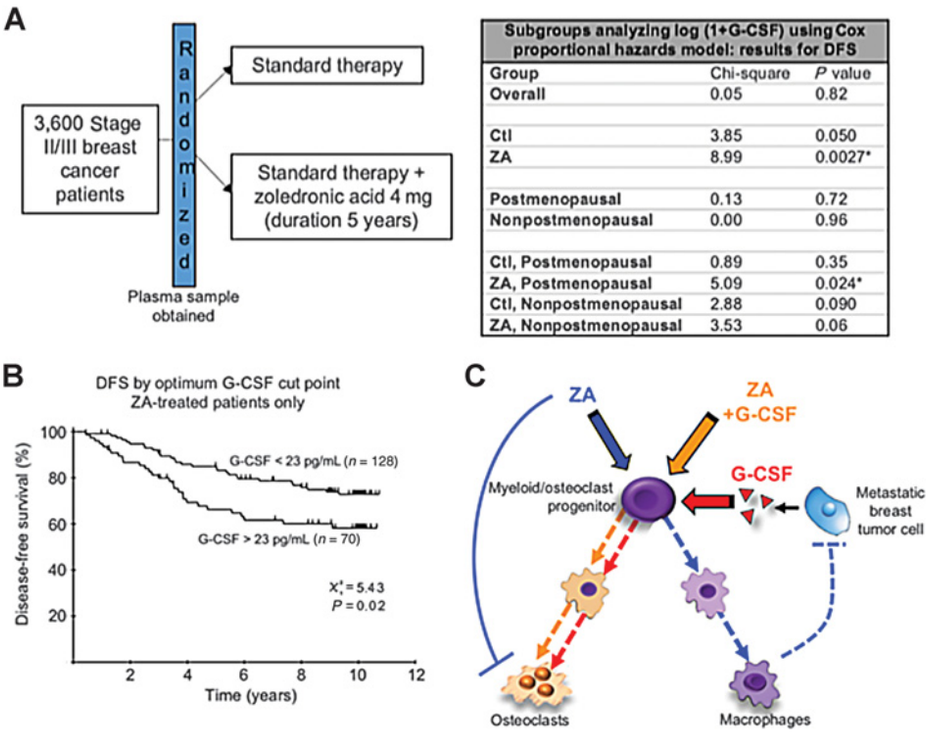

Subgroups analyzing log (1+G-CSF) using Cox proportional hazards model: results for DFS		
Group	Chi-square	P value
Overall	0.05	0.82
Ctl	3.85	0.050
ZA	8.99	0.0027*
Postmenopausal	0.13	0.72
Nonpostmenopausal	0.00	0.96
Ctl, Postmenopausal	0.89	0.35
ZA, Postmenopausal	5.09	0.024*
Ctl, Nonpostmenopausal	2.88	0.090
ZA, Nonpostmenopausal	3.53	0.06

Figure 7.

High plasma G-CSF correlates with worse outcome for patients with breast cancer treated with adjuvant ZA. **A,** AZURE clinical trial randomization scheme from Coleman and colleagues, 2014 (16) and Cox proportional hazards model analysis of subgroup from AZURE trial (n = 392) for DFS by Ctl and ZA cohorts, menopausal status, and by menopausal status for treatment group (*, P < 0.05). **B,** DFS outcome (derived from cut-off point analysis—see Materials and Methods) defined in terms of number of DFS events avoided/saved over the 10-year period post randomization among ZA-treated patients; optimal cut-off point was at 23 pg/mL G-CSF. **C,** Proposed model. ZA inhibits mature osteoclasts and also increases the numbers of M/OCPs in the bone marrow, altering their gene expression profile to drive them toward tumor suppressive phagocytic macrophages. Tumor-derived or systemic G-CSF counteracts the effects of ZA by driving the lineage potential of M/OCPs toward osteoclasts.

Published OnlineFirst July 31, 2018; DOI: 10.1158/0008-5472.CAN-18-0548

demonstrated that the relationship between high plasma G-CSF levels and DFS in ZA-treated patients could not be explained by imbalances in other key prognostic variables, namely number of involved lymph nodes affected, tumor size (T stage), and breast cancer receptor status (ER/PR/Her2). Moreover, in support of the retrospective analyses demonstrating that postmenopausal patients observed significant benefit with adjuvant ZA, plasma G-CSF levels were significantly lower in postmenopausal patients than premenopausal patients in our cohort ($P = 1.14 \times 10^{-4}$).

Discussion

This work revealed that bone marrow hematopoietic cell states, particularly M/OCP lineage potential, have a profound impact on breast cancer bone metastasis and that the hematopoietic microenvironment, which serves as a niche for disseminated tumor cells, can be modulated by bone-targeting agents and cytokines to alter disease outcome. Specifically, the bisphosphonate, ZA, directs M/OCP lineage potential toward tumor-suppressive macrophages and prevents metastatic growth in the bone; systemic or tumor-derived G-CSF promotes resistance to the metastasis-suppressive effect of ZA by skewing M/OCP differentiation toward osteoclasts and away from the phagocytic myeloid lineage (Fig. 7C).

Further mechanistic investigation into the newly identified biology that we report here is warranted to understand how best to capitalize on bone marrow and M/OCP function and differentiation potential to prevent or limit metastatic disease in the bone. The novel, perhaps unexpected effect of ZA on the bone microenvironment may provide one such avenue. From a clinical perspective, targeting osteoclast activity with bone-modifying agents, such as bisphosphonates or the RANK-ligand inhibitor denosumab, has significantly reduced skeletal-related events patients with metastatic breast cancer to the bone (i.e., bone fractures, bone pain requiring radiotherapy, spinal cord compression, and hypercalcemia; ref. 41). Thus, current NCCN guidelines support the administration of these agents in combination with chemotherapy or endocrine therapy for patients with bone metastases (category 1 recommendation; refs. 42, 43). Results from a meta-analysis of individual patient data from 18,766 women—enrolled over 26 randomized trials that evaluated the benefits of adjuvant bisphosphonate treatment—showed a significant reduction in bone recurrence and improvement in breast cancer–specific survival (44).

Subgroup analyses have suggested that postmenopausal status, but not hormone receptor (ER/PR) or growth factor receptor (Her2) expression, predisposes patients who are more likely to benefit from bisphosphonates, and this is reflected in the recently published guidelines by Cancer Care Ontario and the American Society of Clinical Oncology that recommend consideration of ZA or clodronate for postmenopausal (natural or induced with ovarian suppression) patients deemed candidates for adjuvant systemic therapy (43). Other meta-analyses revealed that adjuvant therapy with ZA increases overall survival in early-stage breast cancer (44). In addition, ZA decreased the number of DTCs in the bone marrow of stage II/III patients with breast cancer in a randomized clinical trial (45). ZA has also been demonstrated to increase disease-free survival when it is administered with neoadjuvant chemotherapy, particularly in postmenopausal patients (46). Nevertheless, an underlying biological explanation for the protective effect of bisphosphonates in breast cancer, in terms of reduction of disease recurrence, had remained elusive.

Although meta-analyses of the clinical studies highlighted efficacy of ZA, no overall survival benefit has been reported to date in individual randomized controlled trials in breast cancer. Consequently, even considering pre- or post-menopausal status, it remained unclear how to identify which patients would observe benefit with ZA (16). Our findings provide new insights into why certain patients may not see reduction in breast cancer recurrence with ZA. Our preclinical findings are underscored by the fact that patients in the AZURE trial (16) with higher plasma G-CSF levels experienced worse outcome from adjuvant ZA treatment and provide preliminary evidence to caution against the use of ZA in patients with high plasma G-CSF. High plasma G-CSF, however, has been correlated with poor prognosis in patients with breast cancer, specifically those with triple-negative breast cancer (32). However, in our study, plasma G-CSF levels alone, in the absence of ZA treatment, did not predict worse survival.

Unfortunately, our findings provide a preliminary indication that suppression of G-CSF may not be an effective strategy for improving responses to ZA, as neither genetic nor pharmacologic inhibition of G-CSF was sufficient to confer response. It is possible that the balance between tumor-promoting (8) and tumor-suppressive cells in the marrow, or other cytokines (such as GM-CSF) must be considered in the appropriate contexts. Further studies to evaluate our findings will therefore require well-designed preclinical and clinical trials to determine patient benefit with adjuvant ZA in the presence or absence of G-CSF administration. Our analyses suggest other ways to achieve this goal may be to include combinations with other bone-targeting agents or immunotherapies. Further studies based on results of our gene expression profiling under these various conditions may reveal factors, pathways, and processes that are necessary and/or sufficient for the tumor-inhibitory function of the bone marrow. Some of the newly identified gene products presented here may be considered as candidate targets for future combination therapies and preclinical research.

Likewise, additional work will be necessary to determine the translatability of G-CSF as a biomarker for selection of patients who should/should not receive ZA treatment, given that many patients also receive G-CSF at the time of chemotherapy and adjuvant ZA treatment (the patients in our study did not receive primary G-CSF prophylaxis and less than 10% received secondary G-CSF treatment). Identifying biomarkers that better stratify patient risk and responses to ZA hold the potential of using bone-modulating drugs to improve patient outcomes.

Identification of a tumor-suppressive population in the bone marrow provides opportunities for exploring new therapeutic strategies that could generate such cells to halt metastatic progression or overcome the adverse effects of G-CSF. The ability to use relatively safe bone-modulating therapeutics to capitalize on the tumor-suppressive function of the bone marrow, particularly M/OCP populations, provides a foundation for potentially curative treatments during the time when metastatic breast cancer can still be controlled.

Published OnlineFirst July 31, 2018; DOI: 10.1158/0008-5472.CAN-18-0548

Disclosure of Potential Conflicts of Interest

J.E. Brown has received speakers bureau honoraria from Amgen and Novartis and is a consultant/advisory board member for Amgen and Novartis. R.E. Coleman is a medical director at prIME Oncology, has ownership interest (including stock, patents, etc.) in Inbiomotion, and is a consultant/advisory board member for Amgen. No potential conflicts of interest were disclosed by the other authors.

Authors' Contributions

Conception and design: J.M. Ubellacker, J.E. Brown, Y. Qin, S.S. McAllister
Development of methodology: J.M. Ubellacker, J.E. Brown, S.S. McAllister
Acquisition of data (provided animals, acquired and managed patients, provided facilities, etc.): J.M. Ubellacker, N. Baryawno, N. Severe, M.J. DeCristo, M.-T. Haider, C.S. Rhee, Y. Qin, I. Holen, R.E. Coleman
Analysis and interpretation of data (e.g., statistical analysis, biostatistics, computational analysis): J.M. Ubellacker, N. Severe, J. Sceneay, J.N. Hutchinson, M.-T. Haider, C.S. Rhee, W.M. Gregory, A.C. Garrido-Castro, J.E. Brown, D.T. Scadden, S.S. McAllister
Writing, review, and/or revision of the manuscript: J.M. Ubellacker, N. Baryawno, N. Severe, J.N. Hutchinson, W.M. Gregory, A.C. Garrido-Castro, I. Holen, J.E. Brown, R.E. Coleman, D.T. Scadden, S.S. McAllister
Administrative, technical, or material support (i.e., reporting or organizing data, constructing databases): J.N. Hutchinson
Study supervision: S.S. McAllister

Acknowledgments

This work was supported by funds from NIH T32 GM007226 and NCI F31CA195797 (to J. Ubellacker); NIH R01DK107784 and U54CA163191 (to D. Scadden); DOD Era of Hope W81XWH-14-1-0191 and NIH NCI RO1 CA166284 Presidential Early Career Award for Scientists and Engineers (to S. McAllister). We are grateful to the patients who participated in the AZURE trial. We thank P. Ottewell and G. van der Plujm for generous donation of MDA-MB-231 bone-tropic cell lines; J. Brown, H. Shulver, and J. Horsman for assistance with obtaining clinical trial samples; and the Boston Children's Hospital Heme/Onc-HSCI Flow Cytometry facility (Boston, MA). We thank members of the McAllister and Scadden laboratories and Drs. Bruce Zetter, Karen Cichowski and Nancy Lin for helpful discussion; L. Rooney, J. Olive, Z. Castano for technical review of the manuscript; J. Ferlic for biostatistics assistance; R. Tadipatri for technical assistance; A. Molineaux and M. Petit for administrative assistance. We are also grateful to N. Tung and J. Garber for helpful discussion in early stages of the project.

The costs of publication of this article were defrayed in part by the payment of page charges. This article must therefore be hereby marked *advertisement* in accordance with 18 U.S.C. Section 1734 solely to indicate this fact.

Received February 20, 2018; revised June 12, 2018; accepted July 23, 2018; published first July 31, 2018.

References

1. Colleoni M, Sun Z, Price KN, Karlsson P, Forbes JF, Thurlimann B, et al. Annual hazard rates of recurrence for breast cancer during 24 years of follow-up: results from the International breast cancer study group trials I to V. J Clin Oncol 2016;34:927–935.
2. Press DJ, Miller ME, Liederbach E, et al. De novo metastasis in breast cancer: occurrence and overall survival stratified by molecular subtype. Clin Ex Metastasis 2017;1573–7276.
3. Gnant M, Hadji P. Prevention of bone metastases and management of bone health in early breast cancer. Breast Cancer Res 2010;12:216.
4. Tjensvoll K, Oltedal S, Heikkila R. Persistent tumor cells in bone marrow of non-metastatic breast cancer patients after primary surgery are associated with inferior outcome. BMC Cancer 2012;12:190. doi: 10.1186/1471-2407-12-190.
5. Ren G, Esposito M, Kang Y. Bone metastasis and the metastatic niche. J Mol Med 2015;93:1203–12.
6. Guise T. Examining the metastatic niche: targeting the microenvironment. Semin Oncol 2010;37:S2–S14.
7. Rack B, Junckstock J, Gunthner-Biller M, Andergassen U, Neugebauer J, Hepp P, et al. Trastuzumab Clears HER2/neu-positive isolated tumor cells from bone marrow in primary breast cancer patients. Arch Gynecol Obstet 2011;285:485–92.
8. McAllister SS, Weinberg RA. The tumour-induced systemic environment as a critical regulator of cancer progression and metastasis. Nat Cell Biol 2014;16:717–27.
9. Engblom C, Pfirschke C, Pittet MJ. The role of myeloid cells in cancer therapies. Nature Rev Cancer 2016;16:447–62.
10. Gao D, Mittal V. The role of bone-marrow-derived cells in tumor growth, metastasis initiation and progression. Trends Mol Med 2009;15:333–43.
11. Morrison SJ, Scadden DT. The bone marrow niche for haematopoietic stem cells. Nature 2014;505:327–34.
12. Kollet O, Dar A, Shivtiel S, Kalinkovich A, Lapid K, Sztainberg Y, et al. Osteoclasts degrade endosteal components and promote mobilization of hematopoietic progenitor cells. Nat Med 2006;12:657–64.
13. Nilsson SK, Johnston HM, Whitty GA, Williams B, Webb RJ, Denhardt DT, et al. Osteopontin, a key component of the hematopoietic stem cell niche and regulator of primitive hematopoietic progenitor cells. Blood 2005;106:1232–9.
14. Stier S, Ko Y, Forkert R, Lutz C, Neuhaus T, Grunewald E, et al. Osteopontin is a hematopoietic stem cell niche component that negatively regulates stem cell pool size. J Exp Med 2005;201:1781–91.
15. Ubellacker JM, Haider MT, DeCristo MJ, Allocca G, Brown NJ, Silver DP, et al. Zoledronic acid alters hematopoiesis and generates breast tumor-suppressive bone marrow cells. Breast Cancer Res 2017;19:23.
16. Coleman R, Cameron D, Dodwell D, Bell R, Wilson C, Rathbone E, et al. Adjuvant zoledronic acid in patients with early breast cancer: final efficacy analysis of the AZURE (BIG 01/04) randomised open-label phase 3 trial. Lancet Oncol 2014;15:997–1006.
17. Marsh T, Wong I, Sceneay J, Barakat A, Qin Y, Sjodin A, et al. Hematopoietic age at onset of triple-negative breast cancer dictates disease aggressiveness and progression. Cancer Res 2016;76:2932–43.
18. McAllister SS, Gifford AM, Greiner AL, Kelleher SP, Saelzler MP, Ince TA, et al. Systemic endocrine instigation of indolent tumor growth requires osteopontin. Cell 2008;133:994–1005.
19. Boyle WJ, Simonet WS, Lacey DL. Osteoclast differentiation and activation. Nature 2003;423:337–42.
20. Jacome-Galarza CE, Lee SK, Lorenzo JA, Aguila JA. Identification, characterization and isolation of common progenitor for osteoclasts, macrophages, and dendritic cells from murine bone marrow and periphery. J Bone Miner Res 2013;28:203.
21. Miyamoto T. Identification and characterization of osteoclast precursor cells. BoneKEy 2013;346. doi: 10.1038/bonekey.2013.80.
22. Zhu L, Zhao Q, Yang T, Ding W, Zhao Y. Cellular metabolism and macrophage functional polarization. Int Rev Immunol 2015;34:82–100.
23. Martinez F, Gordon S, Locati M, Mantovani A. Transcriptional profiling of the human monocyte-to-macrophage differentiation and polarization: new molecules and patterns of expression. J Immunol 2006;177:7303–11.
24. Hirbe AC, Roelofs AJ, Floyd DH, Deng H, Becker SN, Lanigan LG, et al. The bisphosphonate zoledronic acid decreases tumor growth in bone in mice with defective osteoclasts. Bone 2009;44:908–16.
25. Zhang K, Kim S, Cremasco V, Hirbe AC, Novack DV, Weilbaecher K, et al. CD8+ T cells regulate bone tumor burden independent of osteoclast resorption. Cancer Res 2011;71:4799–808.
26. Dougall WC, Glaccum M, Charrier K, Rohrbach K, Brasel K, De Smedt T, et al. RANK is essential for osteoclast and lymph node development. Genes Dev 1999;13:2412–24.
27. Ari F, Miyamoto T, Ohneda O, Inada T, Sudo T, Brasel K, et al. Commitment and differentiation of osteoclast precursor cells by the sequential expression of c-fms and RANK receptors. J Exp Med 1999;190:1741–1754.

28. Wetterwald A, van der Pluijm G, Que I, Sijmons B, Buijs J, Kaperien M, et al. Optical imaging of cancer metastasis to bone: a mouse model of minimal residual disease. Am J Pathol 2002;160:1143–53.
29. Nutter F, Holen I, Brown HK, Cross SS, Evans CA, Walker M, et al. Different molecular profiles are associated with breast cancer cell homing compared to colonisation of bone—evidence using a novel bone-seeking cell line. Endocr Relat Cancer 2014;21:327–41.
30. Ell B, Kang Y. Bone Metastasis. Cell 2012;151:690.
31. Weilbaecher KN, Guise TA, McCauley LK. Cancer to bone: a fatal attraction. Nat Rev Cancer 2011;11:411–25.
32. Hollmén M, Karaman S, Schwager S, Lisibach A, Christiansen AJ, Maksimow M, et al. G-CSF regulates macrophage phenotype and associates with poor overall survival in human triple-negative breast cancer. Oncoimmunology 2015;5:e1115177.
33. Takahashi T, Wada T, Mori M, Kokai Y, Ishii S. Overexpression of the granulocyte colony-stimulating factor gene leads to osteoporosis in mice. Lab Invest 1996;74:827–34.
34. Hirbe AC, Uluckan O, Morgan EA, Eagleton MC, Prior JL, Piwnica-Worms D, et al. Granulocyte colony-stimulating factor enhances bone tumor growth in mice in an osteoclast-dependent manner. Blood 2007;109:3424–31.
35. Christopher MJ, Link DC. Granulocyte colony-stimulating factor induces osteoblasts apoptosis and inhibits osteoblast differentiation. J Bone and Miner Res 2008;23:1765–74.
36. Reimand J, Kull M, Peterson H, Hansen J, Vilo J. G:Profiler-a web-based toolset for functional profiling of gene lists from large-scale experiments. Nucleic Acids Res 2007;35:W193–W200.
37. Hale KK, Trollinger D, Rihanek M, Manthey CL. Differential expression and activation of p38 mitogen-activated protein kinase α, β, γ and δ in inflammatory cell lineage. J Immunology 1999;162:4246–52.
38. Ludwig KF, Du W, Sorrelle NB, Wnuk-Lipinska K, Topalovski M, Toombs JE, et al. Small molecule inhibition of Axl targets tumor immune suppression and enhances chemotherapy in pancreatic cancer. Cancer Res 2018;78:246–55.
39. Early Breast Cancer Trialists' Collaborative Group (EBCTCG). Adjuvant bisphosphonate treatment in early breast cancer: meta-analyses of individual patient data from randomised trials. Lancet 2015;386:1353–61.
40. Viprey VF, Gregory VM, Corrias MV, Tchirkov A, Swerts K, Vicha A, et al. Neuroblastoma mRNAs predict outcome in children with stage 4 Neuroblastoma: a European HR-NBL1/SIOPEN Study. J Clin Oncol 2014;32:1074–83.
41. Stopeck AT, Lipton A, Body JJ, Steger GG, Tonkin K, de Boer RH, et al. Denosumab compared with zoledronic acid for the treatment of bone metastases in patients with advanced breast cancer: a randomized, double-blind study. J Clin Oncol 2010;28:5132–9.
42. Gradishar WJ, Anderson BO, Balassanian R, Blair SL, Burstein HJ, Cyr A, et al. Breast cancer, version 1.2017. NNCN guidelines insights. J Natl Compr Canc Netw 2017;15:433–51.
43. Dhesy-Thind S, Fletcher GG, Blanchette PS, Clemons MJ, Dillmon MS, Frank ES, et al. Use of adjuvant bisphosphonates and other bone-modifying agents in breast cancer: a cancer care ontario and american society of clinical oncology clinical practice guideline. J Clin Oncol 2017;35:2062–80.
44. Valachis A, Polyzos NP, Coleman RE, Gnant M, Eidtmann H, Brufsky AM, et al. Adjuvant therapy with zoledronic acid in patients with breast cancer: a systemic review and meta-analysis. Oncologist 2013;18:353–61.
45. Aft RL, Naughton M, Trinkaus K, Watson M, Ylagan L, Chavez-MacGregor, et al. Effect of zoledronic acid on disseminated tumour cells in women with locally advanced breast cancer: an open label, randomized, phase 2 trial. Lancet Oncol 2010;11:421–28.
46. Kroep JR, Charehbili A, Coleman RE, Aft RL, Hasegawa Y, Winter MC, et al. Effects of neoadjuvant chemotherapy with or without zoledronic acid on pathological response: a meta-analysis of randomized trials. Eur J Cancer 2016;54:57–63.

Cancer Research
The Journal of Cancer Research (1916–1930) | The American Journal of Cancer (1931–1940)

AACR American Association for Cancer Research

Modulating Bone Marrow Hematopoietic Lineage Potential to Prevent Bone Metastasis in Breast Cancer

Jessalyn M. Ubellacker, Ninib Baryawno, Nicolas Severe, et al.

Cancer Res 2018;78:5300-5314. Published OnlineFirst July 31, 2018.